Numerical Investigation of Heat Transfer from a Heated Square Cylinder due to Nanofluids in the Presence of an Upstream Rectangular Cylinder

THESIS

Submitted in partial fulfilment

of the requirements for the degree of

DOCTOR OF PHILOSOPHY

by

SWATI SHARMA

Under the Supervision of

Prof. BHUPENDRA K. SHARMA

and the Co-supervision of

Prof. DILIP K. MAITI

BIRLA INSTITUTE OF TECHNOLOGY AND SCIENCE, PILANI

2019

BIRLA INSTITUTE OF TECHNOLOGY AND SCIENCE, PILANI

CERTIFICATE

This is to certify that the thesis titled **"Numerical Investigation of Heat Transfer from a Heated Square Cylinder due to Nanofluids in the Presence of an Upstream Rectangular Cylinder"** submitted by **Ms. Swati Sharma**, **ID No. 2014PHXF0418P** for award of Ph.D. of the institute embodies original work done by her under our supervision.

Signature of the Supervisor	**Signature of the Co-supervisor**
Name : **BHUPENDRA K. SHARMA**	Name : **DILIP K. MAITI**
Designation : **Associate Professor**	Designation : **Professor**

Date: May 9, 2019

DEDICATED TO MY LOVING

FATHER

Acknowledgements

Undertaking this PhD has been a truly life-changing experience for me and it would not have been possible to do without the support and guidance that I received from many people.

With immense pleasure and deep sense of gratitude, I wish to express my sincere thanks to my supervisor **Prof. Bhupendra K. Sharma**, Associate Professor and Head, BITS PILANI, Pilani Campus, without his motivation and continuous encouragement, this research would not have been successfully completed. He has supported me when I needed it the most.

My special words of thanks should also go to my co-supervisor, **Prof. Dilip K. Maiti**, Professor and Head, Vidyasagar University, Midnapore, WB, for always being so kind, helpful and motivating. He has taught me another aspect of life, that, "goodness can never be defied and good human beings can never be denied". His constant guidance, cooperation and support has always kept me going ahead. I owe a lot of gratitude to him for always being there for me and I feel privileged to be associated with a person like him during my life.

I would like to extend my indebtedness to the Vice Chancellor, Director, Deputy Director, BITS Pilani, Pilani Campus, for providing me an opportunity to use infrastructural facilities and a comfortable research environment. I express my gratitude to Prof. Srinivas Krishnaswamy, Dean, AGSRD, Prof Jitendra Panwar, Associate Dean, AGSRD for the arrangement of administrative matters.

A very special thanks to the members of my DAC committee Dr. Ashish Tiwari and Dr. Sangeeta Yadav who spent their valuable time in explaining concepts and giving suggestions for improvement.

I thank all the faculty members and staff of our department who helped me in the compilation of this work successfully. Their support and guidance contributed decisively to improve my academic maturity.

The financial support provided by BITS PILANI and CSIR, which made this study

possible, gratefully acknowledged.

I express my gratitude towards my colleagues, friends and staff who provded support, encouragement and references whenever required to attain this stage of academic achievement. I am grateful to the affectionate co-operation made by them.

I thank the Almighty for giving me the strength and patience to work through all these years so that today I can stand proud with my head held high.

Finally, I would like to acknowledge the people who mean world to me, my family. I extend my respect to all elders in the family. I don't imagine a life without their love and blessings. Thank you father (**Mr. D.P. Sharma**), brother (**Mr. Gaurav Sharma**) and sister-in-law (**Mrs. Rohini Sharma**) for showing faith in me and giving me liberty to choose what I desired. I consider myself the luckiest in the world to have such a supportive family, standing behind me with their love and support. My special love to my two little nephews **Hanu** (**Aarav**) and **Maan** for making me smile always.

Place: PILANI

Date: May 9, 2019 **SWATI SHARMA**

ABSTRACT

Heat Transfer is an important phenomenon involves in various industrial sectors such as automobile, electronic, power generation etc. In the past, conventional fluids such as water, ethylene gylcol and oil had been used as the heat transfer fluids. Due to their poor conductivity, a significant need to innovate another generation of heat transfer fluids for better efficiency is required. Fluids with colloidal suspension of nanoparticles in them are known as nanofluids and represent advanced heat transfer fluids.

This research is focussed on the enhancement of heat transfer from a heated square cylinder placed in the vicinity of a plane wall utilizing nanofluids. The cylinder is either dissipating constant heat flux (q_w) or maintaining at a constant temperature (T_w). The conventional fluids are chosen as water, and ethylene glycol and water mixture ($EG : W$, $60 : 40$ by weight). The nanoparticle materials are selected as Al_2O_3 and CuO. Nanofluid models which takes care of Brownian motion, temperature of base fluids, the mean nanoparticle diameter, the nanoparticle volume fraction, the nanoparticle density and the base fluids physical properties are considered here. The flow field and heat transfer are computed through a finite volume method (FVM) on a staggered grid system using QUICK scheme for convective terms and SIMPLE algorithm. The resulting equations are then solved by an implicit, time-marching, pressure correction based SIMPLE algorithm. The influence of numerical parameters on the validated code used in this study is demostrated in this work.

Initially, the heat transfer enhancement from the heated square cylinder is investigated by varying the parameters governing the nanofluids: nanoparticle material, nanoparticle size (d_{np}), concentration of nanoparticles (ϕ) in base fluid and the base fluid temperature. This study was performed for four types of nanofluids with particle material are considered as Al_2O_3 and CuO and type of base fluids are selected as water and ethylene glycol-water ($EG : W$) under the incident of Couette flow. The results showed that the increase in the volume fraction promotes the heat transfer. On the other hand, the increase in particle size decreases the heat transfer rate. Further, the increase in the base

fluid temperature was not found preferable from a heat transfer perspective, but the effectiveness of nanoparticles in base fluid is found more at higher temperature. Though the hydrodynamic characteristics of the cylinder are same for both base fluids at a Re due to mechanical similarity, heat transfer characteristics are different due to difference in their Pr values. The classical fluid dynamics relationship among $\overline{Nu}_M$, Reynolds number (Re) and Prandtl number (Pr) is discussed through Colburn $j-$factor, and hence the utility of proposed correlation between $j-$factor and Re towards engineering problems is also explored.

For Couette-Poiseuille flow, the effect of the pressure gradient (P) using nanofluid is investigated thoroughly. This study is performed for two types of thermal boundary conditions (namely, uniform heat flux and constant temperature) at the cylinder's surface. The results showed that the nusselt number increases with the increase in non-linearity of the flow at the inlet. The effect of non-linearity on heat transfer is more pronounced than that of nanoparticle concentration. Heat transfer is found more for the case of uniform heat flux in comparison to constant temperature condition.

In the next phase, flow past a square heated cylinder (of height A^*) near a wall (at a gap height $0.5A^*$) in presence of an adiabatic upstream rectangular cylinders (of different height a^* and width b^*) in a tandem arrangement under the incidence of Couette-Poiseuille flow based non-uniform linear/non-linear velocity profiles is studied. The enhancement of heat transfer from the heated cylinder with constant temperature is explored due to the flow instability by employing the upstream cylinder of rectangular shape of optimum size placed at suitable distance and loading of nanoparticles in the base fluid. The parameters governing the fluid flow are spacing distance D^* between the cylinders, gap height (L^*) of the upstream cylinder from the wall, ratio of heights $r_2 = a^*/A^*$ (≤ 1), aspect ratio $r_1 = b^*/a^*$ (≤ 1), Reynolds number Re and non-dimensional pressure gradient P at the inlet. It is observed that the heat transfer from the downstream cylinder is an increasing function of pressure gradient P and ϕ, while decreasing function of aspect ratio of the upstream cylinder $r_1 = b^*/a^*$. A critical discussion is made on the mechanism of improvement/reduction (due to the presence of the upstream cylinder) of heat transfer

and drag coefficient, in comparison to those of an isolated cylinder. The heat transfer from the rear face of the downstream cylinder can be improved by generating unsteadiness in the flow by increasing P, or decreasing r_1. While looking at the effect of gap height (L^*), the heat transfer from the downstream cylinder is found more in offsetting away from the wall, in comparison to the inline case and offsetting away from the wall for these parameters values. An effort is made to find the optimum position and shape of upstream cylinder for the enhancement of heat transfer.

Contents

List of Figures

List of Tables

NOMENCLATURE

A^*	height of downstream square cylinder $[m]$
a^*	height of upstream rectangular cylinder $[m]$
b^*	width of upstream rectangular cylinder $[m]$
C_D	drag coefficient, $\frac{F_D}{\frac{1}{2}\rho U_1^2 A^*}$
C_{DP}	drag coefficient due to pressure
C_{DSH}	drag coefficient due to shear
C_L	lift coefficient, $\frac{F_L}{\frac{1}{2}\rho U_1^2 A^*}$
C_p	non-dimensional pressure coefficient, $\frac{p-p^*}{\frac{1}{2}\rho U_0^2 A^*}$
D^*	spacing distance between the cylinders $[m]$
d	diameter
DSC	downstream Square Cylinder
$EG:W$	ethylene glycol and water mixture (60:40 by weight)
E_P	effectiveness of pressure gradient
E_ϕ	effectiveness of concentration
F_D	the integrated drag force experienced by the cylinder
F_L	the integrated lift force experienced by the cylinder
h	distance from the lower wall
h_1	convective heat transfer coefficient
L^*	gap height of cylinder from the wall [m]
L	non-dimensional gap height of upstream cylinder from the wall, $\frac{H^*}{A^*}$
Nu	local nusselt number
Nu_M	mean nusselt number
Nu_{avg}	face-wise average nusselt number
$Nu_{M\|_P}$	time-averaged-mean Nusselt number at different pressure gradient
$Nu_{M\|_\phi}$	time-averaged-mean Nusselt number at different concentration
P	non-dimensional pressure gradient at inlet

Pr	prandtl number, $\frac{\nu_f}{\alpha_f}$
q	heat flux
r_2	ratio of heights of cylinders, $\frac{a^*}{A^*}$
r_1	aspect ratio of upstream rectangular cylinder, $\frac{b^*}{a^*}$
Re	reynolds number based on U_1, $\frac{U_1 A^*}{\nu}$
Re_{U_2}	reynolds number based on U_2, $\frac{U_2 A^*}{\nu}$
R^2	coefficient of determination
RSS	residual sum of squares
S	non-dimensional spacing distance between the cylinders, $\frac{D^*}{A^*}$
St	strouhal number, $\frac{fA^*}{U_2}$
T	temperature [K]
t	non-dimensional time, $\frac{t^* U_1}{A^*}$
u	$x-$component of velocity [ms^{-1}]
U_1	inlet velocity at height A^* from the wall [ms^{-1}]
U_2	inlet velocity at height $10A^*$ from the wall [ms^{-1}]
$UREP$	upstream rectangular eddy promoter
v	$y-$component of velocity [ms^{-1}]
W	water
x	horizontal distance [m]
y	vertical distance [m]

Averaged Symbols

$\overline{C}_D$	average drag coefficient, $\frac{\sum_t C_D(t)t}{\sum t}$
$\overline{C}_L$	average lift coefficient, $\frac{\sum_t C_L(t)t}{\sum t}$
$\overline{C}_p$	average pressure coefficient, $\frac{\sum_t C_P(t)t}{\sum t}$
$\overline{Nu}_M$	time- and surface-averaged nusselt number
$\overline{u}$	average x-component of velocity

Greek Symbols

$\triangle t$	time step increment, $[s]$
λ	the prescribed slope of the incident velocity profile
ω	vorticity vector, $\frac{\partial v}{\partial x} - \frac{\partial u}{\partial y}$
α	thermal diffusivity [m^2/s]
κ	thermal conductivity, [W/mK]
μ	dynamic viscosity, [kg/ms]
ν	kinematic viscosity [m^2/s]
ϕ	Volume concentration, [%]
ρ	density, [kg/m^3]
θ	Non-dimensional temperature

Subscripts

f	Base fluid
nf	Nanofluid
np	Nanoparticle
o	Ambient
w	Wall

Superscripts

$*$	Dimensional

Chapter 1

Introduction

1.1 Motivation

In the recent past, there have been a revolutionary advancement in a number of industrial sectors, viz., automotive, telecommunications, electronic and so forth. This development in technology has further pioneered latest products that are amazingly small in physical dimensions but very strong in effectiveness. The reduction in physical dimensions have come up with surprising results: increased functionality on a single device unit thereby not only increases the consumption of power but also of generation of heat. For proper functioning and reduction of failure of the working equipment due to overheating, there is a significant need for compatible cooling arrangement to dissipate excess heat generated within the system.

In order that the efficiency of heat transfer is enhanced, a number of techniques can be used these days. To enumerate some of the methods, we can resort to a change in the flow geometry, introduction of an obstacle in the flow, and also the use of varying shapes and different configurations of heated objects such as square cylinders, flattened plates or other objects with blunt cross sections. Besides this, we can also improve the efficiency of

heat transfer by increasing the thermal conductivity of a particular working fluid. In order to increase the thermal conductivity of conventional heat transfer fluids, for example, engine oil, water and ethylene glycol, scientists have been successful by the suspension of micro particles to the base fluid, on the principle that the thermal conductivity of a solid remains higher than that of a fluid. Nevertheless, given the fact, that these particles are of larger sizes and have high density, there have been a few drawbacks in their endeavours with reference to the resistance of flow, clogging of channels, erosion in channel walls, sedimentation of particles that have proved detrimental in the widespread commercial use of suspension of particles that are more grainy to the base fluids, and consequently these advanced working fluids cannot be used in the heat transfer applications.

1.2 Bluff Body Flows

When the body shape is such that the length is approximately similar or equal to the length perpendicular to the direction of the flow is called bluff body. For example, flow past cylindrical objects and moving vehicles are bluff body flows. In a bluff body flows, separation of flow takes place which results in the formation of wide wake zone. Hence, the shape of the body plays an important role for deciding the bluffness of the body. Based on the location of the separation points, Narasimhamurthy [5] classified the bluff bodies into two categories namely, sharp edged bodies (rectangular, flat plates, polygonal and, triangular cylinders) and rounded corners (elliptical, circular, and arbitrary oval cylinders). When the cylinder is immersed or in close proximity to the wake of another bluff body, the interference in flow completely changes the flow character around bluff bodies. Therefore, the flow attacking on the cylinder is usually totally different from the free stream flow.

1.3 Emergence of Nanofluids

Thanks to the changing technology and the tremendous growth in nanotechnology, we have been able to not only produce but also process the particles of size less than

100nm. Nanofluids, introduced by Stephen Choi, at San Francisco in 1995, can be defined as fluids with a colloidal suspension of highly small particles in them. The concept of nanofluids is prevalent in applications pertaining to advanced heat transfer fluids for the last twenty years. But due to the diverse complexity and huge variety of the nanofluid systems, there has been no concrete understanding on the magnitude of the nanofluids to be applied in the heat transfer applications. There are a number of advantages of using nanofluids compared to conventional solid–liquid suspensions for heat transfer applications. To enumerate some of them:

1. More transfer of heat between fluids and nanoparticles due to high specific surface area.

2. High dispersion stability with reference to the Brownian motion of particles.

3. Compared to the customary slurries, there is found a reduced particle clogging, thereby leading to a better system miniaturization.

4. The thermo-physical properties of nanofluids can be adjusted, by varying nanoparticle concentration and size of nanoparticles in base fluids, which makes these fluids useful for diverse applications.

1.4 Thermo-physical Properties of Nanofluids

Nanofluids exhibit such physical properties that play an unprecedented role in predicting their heat transfer behaviour. These liquids give a new dimension to energy saving perspectives with reference to the industrial and automobile sector. When compared to the conventional suspensions of particle in fluids, varying between millimetre and micrometre, we find that nanofluids have a great power to enhance thermal transport properties. There is no gainsaying that in the last ten years, nanofluids have become the most successful innovation with respect to their excellent thermal properties. In the wake of the experiments, it was found that the viscosity and the thermal conductivity of the nanofluids were depend not only on the volume fraction of nanoparticles but also on various other

such as particle material, particle size, particle shape, base fluid material, and temperature. While comparing the nanofluids with the base fluids, it was found literally that the application of nanofluids resulted in an increase in both the thermal conductivity and viscosity. For convective heat transfer analysis of nanofluids, accurate determination of the thermophysical properties is a key issue. Calculations of density and specific heat of nanofluids are relatively straightforward. But, for thermal conductivity and viscosity of nanofluids, a number of correlations have been proposed after persistent theoretical and experimental observations, but given the absence of consensus of common understanding on the mechanism of nanofluids, we are yet to achieve general correlations.

1.4.1 Density and Specific Heat

The calculation of the density (ρ_{nf}) and the specific heat ($C_{p,nf}$) of a nanofluid can be determined based on the physical principle of the mixture rule as

$$\rho_{nf} = \left(\frac{m}{V}\right)_{nf} = \frac{m_f + m_{np}}{V_f + V_{np}} = \frac{\rho_f V_f + \rho_{np} V_{np}}{V_f + V_{np}} = (1 - \phi_{np})\rho_f + \phi_{np}\rho_{np}, \tag{1.1}$$

and,

$$(\rho C_p)_{nf} = (1 - \phi_{np})(\rho C_p)_f + \phi_{np}(\rho C_p)_{np}, \tag{1.2}$$

which can be rewritten as

$$C_{p,nf} = \frac{(1 - \phi_{np})(\rho C_p)_f + \phi_{np}(\rho C_p)_{np}}{(1 - \phi_{np})\rho_f + \phi_{np}\rho_{np}}. \tag{1.3}$$

In equations (1.1 - 1.3), ϕ is nanoparticle concentration and subscripts f, np and nf refers to base fluid, nanoparticle and nanofluid respectively. The equation (1.1) was proposed by Pak and Cho [6] while equations (1.2 - 1.3) were given by Xuan and Roetzel [7] that assumes thermal equilibrium between the base fluid and the nanoparticles.

1.4.2 Thermal Conductivity

In order to establish a model for determining thermal conductivity of the nanofluids, a vast number of experiments and researches were conducted on the nature as well as

on the literature of the previous theories of nanofluids. All the data derived was based on account of the effective thermal conductivity of a two-component mixture. One of the foremost models was "The Maxwell model" proposed in 1881 by Maxwell [8] for a solid–liquid mixture with relatively large particles. The effective thermal conductivity , k_{eff}, is given by

$$k_{eff} = \frac{k_{np} + 2k_f + 2(k_{np} - k_f)\phi}{k_{np} + 2k_f - 2(k_{np} - k_f)\phi} k_f. \tag{1.4}$$

This model based its propositions on the solution of heat conduction equation through a stationary random suspension of spheres.

Later, Koo and Kleinstreuer [9] proposed a relation that was modified by Vajjha and Das [10] for calculating thermal conductivity as a two terms function (which takes into account the effect of d_{np}, ϕ, temperature T and the properties of the base fluid). It is given by:

$$k_{nf} = \frac{k_{np} + 2k_f - 2(k_f - k_{np})\phi}{k_{np} + 2k_f + (k_f - k_{np})\phi} k_f + 5 \times 10^4 \beta\phi\rho C_{p,f} \times \sqrt{\frac{K_b T}{\rho_{np} d_{np}}} f(T, \phi), \tag{1.5}$$

where,

$f(T, \phi) = (2.8217 \times 10^{-2}\phi + 3.917 \times 10^{-3})\frac{T}{T_0} + (-3.0669 \times 10^{-2}\phi - 3.91123 \times 10^{-3})$.

T_0 is set at 273K and expression for β is taken from Vajjha and Das [10].

Kim et al. [11] experimentally and Ebrahimnia-Bajestan et al. [12] numerically confirmed that the model given by equation (1.5) predicts the thermal conductivity and hence predict the heat transfer coefficient of nanofluids more accurately as compared to the models based on the pure static conditions of the nanofluids.

A remarkable trend observed during all these researches highlights that with a decrease in particle size there is a relative increase in the thermal conductivity of the nanofluids. Two mechanisms of thermal conductivity enhancement substantiate and propound this claim, namely, "Brownian motion of nanoparticles and liquid layering around nanoparticles (Ozerinc et al. [13])." But the experiments have not been without drawbacks in that there has been observed substantial amount of contradiction in the data, a fact that eluci-

dates that sometimes the decrease in the particles size is accompanied in the decrease of thermal conductivity.

What is more confounding is that even for the same base fluid particle and nanoparticle size, published articles offered neither an agreement about the mechanisms for heat transfer enhancement nor a unified possible explanation with reference to these inconsistencies. Although a number of models are used to measure the thermal conductivity of the nanofluids yet a number of anomalies are observed in them. Unfortunately, at present, no model serves an exemplary role with reference to its theoretical observations that can predict the thermal conductivity of a nanofluid accurately.

1.4.3 Viscosity

In the literature of viscosity, we find that the number of rheological studies conducted is far less when compared to the experimentation of thermal conductivity of nanofluids. Researchers use varying models of viscosity to form a realistic model for measuring the effective viscosity of nanofluid as a function of volume fraction. One of the pioneers, in this field, Einstein [14] in 1906, found the effective viscosity of a suspension of spherical solids as a function of volume fraction using the phenomenological hydrodynamic equations. The proposed model was given by:

$$\mu_{eff} = (1 + 2.5\phi_{np})\mu_f. \tag{1.6}$$

This model is valid for nanoparticle volume concentration strictly less than 5%.

Another exemplar was achieved by Brinkman [15] in 1952, who by modifying Einstein's equations to suspensions with mild particle volume fraction as low as 4% established a viscosity correlation. He derived the following equations:

$$\mu_{eff} = \frac{1}{(1 - \phi_{np})^{2.5}}\mu_f. \tag{1.7}$$

It was Batchelor [16] who in 1977 studied the phenomenon of Brownian motion on the effective viscosity in a suspension of rigid spherical particles, thereby creating better

models for measuring the viscosity of nanofluids, given by

$$\mu_{eff} = (1 + 2.5\phi_{np} + 6.2(\phi_{np})^2)\mu_f. \tag{1.8}$$

Later, in 2009, Masoumi et al. [17] developed a theoretical model for the prediction of the effective viscosity of nanofluids based on Brownian motion. Their model is defined as:

$$\mu_{nf} = \mu_f + \frac{\rho_{np} V_B d_{np}}{72C\delta}, \tag{1.9}$$

where, $V_B = \frac{1}{d_{np}}\sqrt{\frac{18K_bT}{\Pi\rho_{np}d_{np}}}$ is the Brownian velocity, C is the correlation factor defined by

$$C = \mu_f^{-1}[a\phi + b], \tag{1.10}$$

with $a = -1.133 * 10^{-6} * d_{np} * 10^9 - 2.771 * 10^{-6}$,

$$b = 90 * 10^{-8} * d_{np} * 10^9 - 3.93 * 10^{-7}, \tag{1.11}$$

and $\delta = (\frac{\pi}{6\phi})^{\frac{1}{3}} d_{np}$ is the distance between the centres of particles.

1.5 Types of Nanofluid Models

Researchers have been using two different approaches to predict the convective heat transfer performance of nanofluids, which can be mainly characterised into the following approaches:

1.5.1 Homogeneous Model (Single Component Model)

Nanofluids can be presumed to function like a single phase fluid containing solid particles that also behave like a fluid. Moreover, the fluid phase and the nanoparticles are in thermal equilibrium and flow with the same local velocity. The convective transport equations of conventional fluids can be extended to nanofluids by using the physical properties of nanofluids as a function of the properties of both constituents (nanoparticles and base fluid) and their concentrations. Therefore, continuity, momentum and energy equations

can be solved as if the fluid were a classical Newtonian fluid by using effective properties of nanofluid.

1.5.2 Non-Homogeneous Model (Two Component Model)

Despite trying to suspend the ultra-fine particles quite uniformly in the base fluid, the researchers find that a number of phenomena, namely brownian motion and thermophoresis, can create an adverse effect on the relative particle motion, thereby leading to particle slip. In order to overcome the particle slip, the researchers use alternative approaches. Working on the lines of Buongiorno [18], who in 2006, proposed a transport phenomenon in the nanofluids, they tend to stimulate the nanofluids by incorporating a two-component non-homogeneous model where solid particles are treated as a solid phase in the base fluids. The foremost model in use is the Eulerian–Mixture model (EMM) which proves very conducive to solving the momentum and energy equations for mixture phase coupled with continuity equation for each phase, and then in relating the phase velocities by empirical correlations. Another model is the Eulerian–Eulerian model (EEM) helps in solving the continuity, momentum, and energy equations for each phase. This method is more apt for flows where interactions between phases are not clearly established.

Apparently, it is the single phase approach that has an edge over the two phase approach in that it is easier in using, calculating computational cost, besides showing a better comparison with the experimental data sets. But it is to be noted that whatever approach is used by the researchers, the outcome eventually depends on the selected thermophysical property models, especially for the thermal conductivity and viscosity. In this thesis, single phase approach has been used.

1.6 Equations Describing the Nanofluid Flow

Under the assumptions of single phase approach that there exist no slip between the nanoparticles and the fluids, the nanofluid can be treated as pure fluid. The equations governing the conventional fluid based on the conservation laws of mass, momentum and energy can thus directly be extended to the nanofluids with the effective thermophysical

properties of the nanofluids. These thermophysical properties can be expressed in terms of the properties of both base fluid and the nanoparticle.

a) **Equation of Continuity**

This equation represents the mass of fluid entering and leaving the control volume is conserved. In other words, the change of mass in a control volume is equal to the mass that enters through its faces minus the total mass leaving its faces. An equation of continuity for nanofluids can be written mathematically as:

$$\frac{\partial \rho_{nf}}{\partial t} + \frac{\partial}{\partial x_i}(\rho_{nf} u_i) = 0. \tag{1.12}$$

b) **Momentum equation**

Momentum is defined as the mass of an object multiplied by the velocity of the object. The conservation of momentum states that the rate of change of a momentum in a domain is equal to the sum of the foces (body force and surface force) acting on that domain. In other words, in the absence of external forces, the momentum is conserved. It can neither be created nor be destroyed, but only changed through the action of forces as described by Newton's second law. Mathematically, this can be written as:

$$\frac{\partial \rho_{nf} u_i}{\partial t} + \frac{\partial}{\partial x_j}((\rho C_p)_{nf} u_i u_j) = -\frac{\partial p}{\partial x_i} + \frac{\partial}{\partial x_j}\Big[\mu_{nf}\Big(\frac{\partial u_i}{\partial x_j} + \frac{\partial u_j}{\partial x_i}\Big)\Big]. \tag{1.13}$$

c) **Energy equation**

This equation is based on conservation of energy (i.e) the rate of change of energy is equal to the sum of rate of heat addition to and work done on fluid particle. Mathematically,

$$\frac{\partial \rho_{nf} T}{\partial t} + \frac{\partial}{\partial x_i}(\rho_{nf} u_i T) = \frac{\partial}{\partial x_i}\Big[k_{nf}\Big(\frac{\partial T}{\partial x_i}\Big)\Big]. \tag{1.14}$$

where,

ρ is the mass per unit volume (density), t is time, **u** is the flow velocity vector field, T is the temperature, and subscript 'nf', 'i' and 'j' denotes nanofluid, flow field in x and y direction respectively.

For the case of incompressible flow (ρ = constant) and therefore, the equation of continuity, momentum and energy, respectively, simplifies as

$$\frac{\partial}{\partial x_i}(\rho_{nf} u_i) = 0, \tag{1.15}$$

$$\frac{\partial u_i}{\partial t} + \frac{\partial}{\partial x_j}(u_i u_j) = -\frac{\partial p}{\partial x_i} + \frac{\partial}{\partial x_j}\Big[\mu_{nf}\Big(\frac{\partial u_i}{\partial x_j} + \frac{\partial u_j}{\partial x_i}\Big)\Big], \tag{1.16}$$

$$\frac{\partial T}{\partial t} + \frac{\partial}{\partial x_i}(u_i T) = \frac{\partial}{\partial x_i}\Big[\alpha_{nf}\Big(\frac{\partial T}{\partial x_i}\Big)\Big]. \tag{1.17}$$

1.7 Dimensionless Parameters

All physical problems related to nanofluids are associated with physical units, which are measured differently on a particular scale. But more often, it is found that these physical problems somehow are dependent on the unit which we use for measuring these quantities. Therefore, using the principle of dimensional analysis, we use the concept of dimensional units while taking the dimensions of the physical quantities, and attain the non-dimensional numbers by arranging, dividing and rearranging the different units. In order to achieve dimensionless parametres we basically rely on two approaches:
(i) The inspectional analysis
(ii) The dimensionless analysis.

For the production of the thesis, the latter model has been used, wherein by using certain dependent and independent characteristic values, we make the basic equations non-dimensional.

It is very important from both the theoretical and computational points of views that the equations related to the fluid flow be made non-dimensional. This non-dimensional scaling helps us to use different methods for acquiring dimensionless groups, which in turn give us an insight into the significance of various terms with reference to equations governing them. These dimensionless forms not only provide us with an opportunity to

treat the solution in a compact way but also prove very useful, computationally, in giving us the added benefit of numerical scaling of the system discrete equations.

1.7.1 Reynolds Number

It is an important dimensionless number, defined as the ratio of inertial forces to viscous forces acting on a fluid. Basically, it signifies whether the flow is viscous dominant or inertial force dominant. Mathematically, it is represented as :

$$Re = \frac{\rho u A}{\mu} = \frac{\mathbf{u} A}{\nu},$$

where,

ν is the kinematic viscosity of the fluid (m^2/s),

μ is the dynamic viscosity of the fluid (kg/ms),

A is a characteristic length dimension (m),

u is the velocity of the fluid with respect to the object (m/s),

ρ is the density of the fluid (SI units: kg/m^3).

1.7.2 Prandtl Number

The Prandtl Number is defined as the ratio of momentum diffusivity to thermal diffusivity. It is useful in the calculation of free and forced convective heat transfer. It depends on the properties of the fluid. It can be expressed as

$$Pr = \frac{\nu}{\alpha} = \frac{\mu/\rho}{k/(C_p \rho)} = \frac{\mu C_p}{k}.$$

1.7.3 Peclet Number

The Peclet number is a dimensionless number used in the calculations of convective heat transfer phenomenon. It is defined as the ratio of thermal energy convective to the fluid to the thermal energy conducted within the fluid. If Pe is small, heat transfer through conduction is important. Conversely, heat transfer through convection is important at

higher Pe. It is the product of Re and Pr (i.e.),

$$Pe = Re \times Pr.$$

1.8 Numerical Methodology

When the flow variables act as functions of space and time, the Navier Stokes equations along with energy equation describes numerically the complete description of the fluid flow. It is a generally accepted convention that Navier-Stokes equations is the most prevalent model and a precise representation of the fluid motion. These equations describe how the pressure, density, velocity and temperature of a moving fluid are related. Given the complexity of the coupled systems of these equations, we find it difficult to solve them computationally and analytically. And with a view to countering the complexity, we have to resort to a number of assumptions to make the mathematical model less complex and more amenable with the exact or the numerical solution. These equations depend upon conservation of mass, momentum and energy. It is also observed that in application to the high Reynolds number flow, the solutions of the incompressible Navier-Stokes equations generally don't reach a stable state, and rather keep oscillating at different lengths and timescales. Furthermore, while analysing the general Navier-Stokes equations for an incompressible fluid, i.e. the general transport equation, it can be shown that there is a set of partial differential equations showing a parabolic time response and an elliptic space behaviour. In consequence of this response and behaviour, it becomes mandatory to give initial conditions at the point of time $t = 0$, while keeping the boundary conditions specified along the entire area of the borders of the flow domain. To solve these partial differential equations, one needs to discretize (to store variables at discrete points) these equation over the computational domain to perform simulations using high speed computers. After discretization, we are left with a system of nonlinear algebraic equations (of a special structure), so, we have to choose appropriate solvers. And in order to treat the nonlinearity, we have to take help of the iterative methods, instead of the expensive direct solver.

1.8.1 Variable Arrangement

We can find the numerical solution of the fluid flow problems when the boundaries and spaces around boundaries of the computational domain are represented in a form comprehensible to the computers. The domain of the solution has a particular time and space domain, which can further be divided in a small non overlapping control volumes called mesh. In order to attain this we use specific arrangement of regular and irregular spaced nodes around the computational domain, and discretise the governing equations on these meshes. Depending on the choice of discretization scheme (finite difference, finite volume or finite element method), there are two possible choices for arrangement of the problem variables on grid nodes:

(a) **Collocated Arrangement**

In this arrangement, all the variables that describe flow are stored in the same positions (i.e. at the center node for finite volume). As can be seen in the Fig. 1.1(a), the arrow going from left to right denotes u-velocity, the arrow from bottom to top denotes v-velocity and the centre nodes denotes storoge of scalar variables (pressure, temperature). This type of variable arrangement are straight forward, easy to code and requires less computational space . Like any other method, this method has also some disadvantages. There is an odd-even decoupling between the pressure and velocity that arises discretization error. The discretization error may lead to oscillation in the pressure field (i.e. checkerboard pressure fields in the solutions).

(b) **Staggered Grid Arrangement**

This type of variable arrangement was first used by Harlow and Welch [19] in 1965. Unlike collocated arrangement, the variables are not defined at the same position. The scalar variables (pressure, temperature) are stored at the center of the control volumes, whereas the velocity components are stored at the cell faces. A staggered storage is mainly used on structured grids for compressible or incompressible flow simulations. Unlike collocated arrangement, there is a natural strong coupling between velocity and pressure, and this avoids oscillations in pressure as well as velocity field. However, due

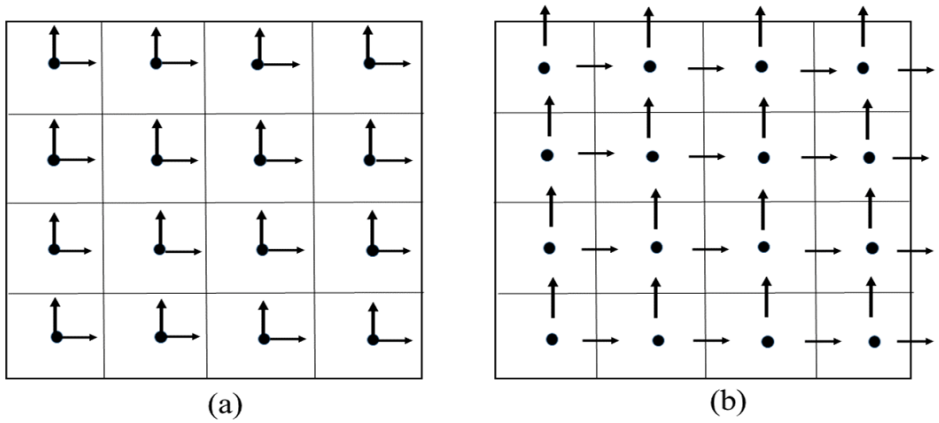

Figure 1.1: (a) Collocated arrangement of variables, and (b) Staggered grid arrangement of variables

to the storage of components at different locations, it requires more computational space which makes it difficult to handle different control volumes for different variables and to keep track of the metrics. Fig. 1.1(b) shows a portion of a two-dimensional grid. In Fig. 1.1(b), the positions of the two velocity components are represented by arrows in the direction of the components of the velocity. Other variables, including (pressure and temperature), are located at the grid points denoted by the dots. A significance of this type of arrangement is that the normal velocity components are directly available at the faces of the control-volume, where they are needed for determining mass flow rates. In addition, the pressure difference between two adjacent cells can be used to derive the velocity component located between them. The staggering for the third velocity component in a three-dimensional situation is performed in a similar fashion.

1.8.2 Solution Algorithm

The governing equations of fluid flow contains an additional time variable t for the case of unsteady flow. These equations must be discretized in time, in order to see the transient effect. The numerical solution of the time-dependent problem can be achieved using the following approaches:

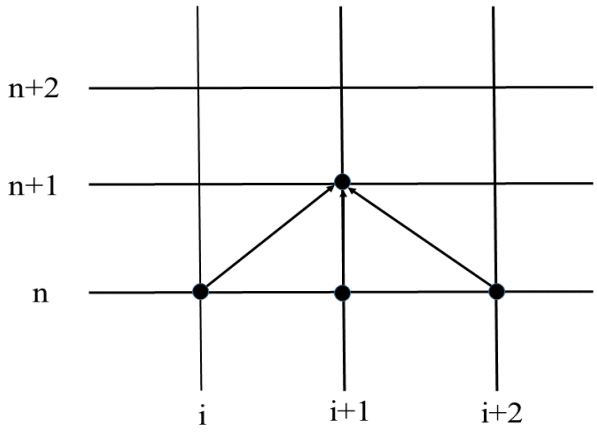

Figure 1.2: Explicit Method

(a) **Explicit Method**

This method involves the calculation of the variables at a current state of time from the values at the previous time step (Fig. 1.2). In this algorithm, variables are updated from one time level to the next time level node by node in a straight forward manner. That is, value at time t^{n+1} computed from values at time t^n. These schemes are easier to implement since there is no coupling of nodes at new time level. However, explicit schemes have a tendency to be unstable and hence, require very small time steps $\triangle t$.

(b) **Implicit Method**

This method computes the values at time t^{n+1} from the unknown values at time t^{n+1}. Unlike explicit schemes, there is full coupling of nodes at new time level. This schemes leads to a system of equations which can be solved using direct or iterative solvers and hence require more number of operations. However, these schemes have clear advantage over explicit ones for not being restricted by stability criteria. Therefore, larger time steps is possible, which naturally expedites the solution procedure. Boundary information is transmitted to the interior in less computation time compared to explicit method.

(c) **Semi-Implicit Method**

In semi-implicit methods, some variables are treated explicitly while other are treated

implicitly. In time-dependent approach, the velocity components are updated to the new time level in an explicit manner while pressure may be calculated implicitly by solving Poisson equation of pressure using Successive over relaxation technique.

In order to achieve accuracy for solving partial differential equation numerically, the grid size must be fine enough to represent the expected spatial variation in all dependent variables. For stability of numerical solution of the differential equations Courant-Friedrichs-Lewy (CFL) condition is necessary. It arises in the numerical solution of explicit time integration schemes. According to CFL condition the particle should not travel more than one grid size $\triangle x$ in one time step $\triangle t$ because the equation assumes fluxes only between the near face cell. According to Courant et al. [20], the increment must satisfy the inequality

$$\triangle t < min\left\{\frac{\triangle x}{|u|}, \frac{\triangle y}{|v|}\right\}, \tag{1.18}$$

where u, v and $\triangle x$, $\triangle y$ are the velocity components and increment in grid size in x and y direction respectively. Implicit methods are usually less sensitive to numerical instability. Therefore, larger time step may be used.

1.8.3 Discretization

Discretization is the process of converting the continuum fluid flow problem into discretized numerical data which are then solved by the digital computers. After selection of an appropriate mathematical model, one has to choose a suitable method for replacing the partial differential system by a set of algebraic equations for the variables stored at discrete locations in space and time. Some of the discretization methods being used are:

(a) **Finite Difference Method**

Finite difference method (FDM) is introduced by Euler in 18^{th} century. It is the oldest and easiest method for performing numerical simulation. In FDM, the partial differential equations are approximated by means of series expansion usually a Taylor series expansion. Usually, the series is truncated after first or second terms. The addition of more terms lead to more accuracy.

(b) **Finite Element Method**

In finite element method (FEM), the computational domain is divided into a set of discrete elements. Within each element, an approximation of the solution is made by a linear shape function that guarantees continuity of the solution across element boundaries. Then, the approximated solution is substituted into a weighted integral of the conservation law. The equation are solved for derivatives of the integral with respect to each nodal values to be zero. The FEM has not extensively used in CFD. It has been found that FEM requires greater computational resources and computer processing power and therefore, its popularity is limited.

(c) **Finite Volume Method**

In finite volume method (FVM), the calculation domain is divided into small number of cells known as control volumes. Then the equations governing the fluid flow are integrated and solved iteratively based on the principles of conservation on each control volume. A set of algebraic equations are obtained by the discretization process within each control volumes that resolve the variables at a specified finite number of points using an integration method. The flow around the domain can be fully modelled through the integration on the control volumes. This method is used for the structured as well as unstructured meshes. This method is more efficient and easier to program as it involves direct integration. Hence, FVM is more common in recent CFD applications in comparison to FEM and FDM.

The standard form of the transport equation for a scalar property ϕ is

$$\frac{\partial \rho\phi}{\partial t} + \bigtriangledown \cdot (\rho \overrightarrow{U} \phi) = \bigtriangledown \cdot (\Gamma \bigtriangledown \phi) + S_\phi(\phi), \tag{1.19}$$

where ρ is the density, U is the velocity, Γ is the diffusivity and $S_\phi(\phi)$ represents the source term. The terms in the standard transport equation represent the rate of change per unit volume (time derivative), the convection per unit volume (convection term), the rate of transport due to diffusion (diffusion term) and the rate of production/destruction per unit volume (source term).

A finite volume discretization of the above equation is formulated by integrating over the control volume V

$$\int_V \frac{\partial \rho\phi}{\partial t} dV + \int_V \bigtriangledown \cdot (\rho \overrightarrow{U} \phi) dV = \int_V \bigtriangledown \cdot (\Gamma \bigtriangledown \phi) dV + \int_V S_\phi(\phi) dV. \tag{1.20}$$

By applying the divergence theorem to convection and diffusion terms, the above equation can be written as:

$$\int_V \frac{\partial \rho\phi}{\partial t} dV + \int_S \rho\phi \overrightarrow{U} \cdot \overrightarrow{n} dS = \int_S \Gamma \bigtriangledown \phi \cdot \overrightarrow{n} dS + \int_V S_\phi(\phi) dV, \tag{1.21}$$

where dS is the outward pointing differential of the surface area vector.

An expression for the time evolution of a variable ϕ appear in the equation (1.21) can be written as

$$\frac{\partial \phi}{\partial t} = F(\phi) \qquad (say). \tag{1.22}$$

If the time derivative is discretized using backward difference, the first order temporal discretization is given as

$$F(\phi) = \frac{\phi^{n+1} - \phi^n}{\triangle t}. \tag{1.23}$$

and for the uniform step size, the second order discretization is given by

$$F(\phi) = \frac{3\phi^{n+1} - 4\phi^n + \phi^{n-1}}{2\triangle t}, \tag{1.24}$$

where, ϕ = a scalar quantity,

n = value at the current time level t,

$n-1$ = value at the previous time level $t - \triangle t$ and,

$n+1$ = value at the next time level, $t + \triangle t$.

Similar expression for forward difference can be obtained.

The discretization of the diffusive terms by three-point central differencing formula for solving Navier-Stokes equations does not pose any problem. However, the convective part may pose some problem, especially for higher Reynolds number flows, if central

differencing is used for its discretization. The use of central differencing formula for convection terms leads to a solution with severe non-physical oscillations. To circumvent this problem, generally upwind schemes are used. The difference formula used in the original MAC (Marker and Cell) formula are central difference expressions. Attempts have been made to stabilize the flow solution by discretising the convective terms with two points upwind difference expressions or a weighted average of central and upwind difference expressions (Hirt et al. [21]). However, solutions are inaccurate particularly if the local velocity vector is oblique to the local grid and the local velocity gradients are large. More accurate solutions are obtained if the convective terms are represented by higher-order upwind schemes, such as the four-point upwind schemes.

One of the most commonly used higher-order scheme is the QUICK (Quadratic Up-

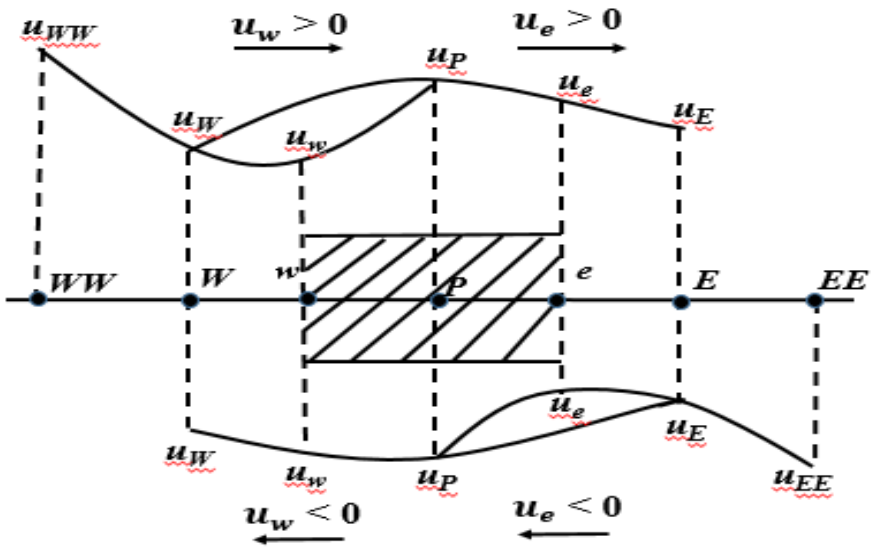

Figure 1.3: Schematics of quadratic upstream-based interpolation for u.

wind Interpolation for Convective Kinematics) scheme due to Leonard [22]. This scheme has been used frequently to combine the accuracy of the central differencing (with stability inherent in upwinding) by using in each direction separately. The QUICK can be interpreted as the pure upwind scheme augmented by gradient and curvature-type correction terms. This scheme has been widely used (Han et al. [23] ; Pollard and Siu [24]; Raithby et al. [25]; Shyy et al. [26] ; Hayase et al. [27]).

QUICK is a third order accurate scheme that considers upto second order derivative term and ignores the derivative of third order. It uses a three point upstream weighted quadratic interpolation for finding cell face values. In order to determine the cell face value a quadratic function is fitted using two surrounding nodes and one node at the upstream side. Convection-diffusion equations are solved by this scheme with second order central difference for the diffusion term and third order accurate in space and first order in time for convection term.

For one-dimensional domain as shown in Fig. 1.3, the ϕ value at a control volume face is approximated using three points quadratic function passing through the two surrounding nodes and one node on the upstream side. For calculating value of the property at the face, we should have two surrounding nodes and one upstream node depending on the flow direction. As shown in Fig. 1.3, the interface values ϕ_w and ϕ_e based on a uniform grid nodal points distribution can be evaluated as : if $u_w > 0$ and $u_e > 0$, then

$$\begin{aligned} \phi_w &= -\frac{1}{8}\phi_{WW} + \frac{3}{4}\phi_W + \frac{3}{8}\phi_P, \\ \phi_e &= -\frac{1}{8}\phi_W + \frac{3}{4}\phi_P + \frac{3}{8}\phi_E. \end{aligned} \tag{1.25}$$

However, if $u_w < 0$ and $u_e < 0$, then

$$\begin{aligned} \phi_w &= -\frac{1}{8}\phi_E + \frac{3}{4}\phi_P + \frac{3}{8}\phi_W, \\ \phi_e &= -\frac{1}{8}\phi_{EE} + \frac{3}{4}\phi_E + \frac{3}{8}\phi_P. \end{aligned} \tag{1.26}$$

Terms in the general transport equation which can not be treated as convective or diffusive terms are included as source terms.

1.8.4 Implementation of Boundary Condition

The grid is arranged so that boundaries pass through velocity points but not pressure points. All boundary conditions are imposed by suitably defining flow variables in the fictitious boundary cells. The fictitious cells are used to rest boundary conditions so that the same difference equations used in the interior of the mesh can also be used at the

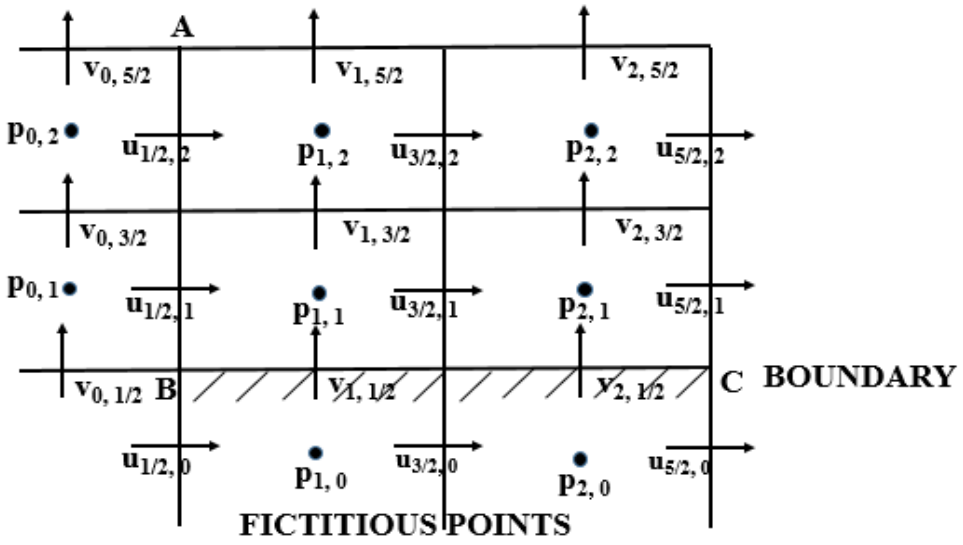

Figure 1.4: The staggered grid near a boundary.

boundaries. For example, consider the corner of a computational domain for which BC is a solid wall and AB is an inflow boundary (see Fig. 1.4):

1. For a rigid, free-slip wall :

$v_{i,1/2} = 0,\ u_{i+1/2,0} = u_{i+1/2,1}, i = 0, 1, \ldots$

2. For a rigid, no-slip wall :

$v_{i,1/2} = 0, u_{i+1/2,0} = -u_{i+1/2,1}.$

On AB, u and v are given say, α and β.

Thus, $u_{1/2,j} = \alpha$, and $v_{0,j+1/2} = 2\beta - v_{1,j+1/2}, \quad j = 0, 1, 2, \ldots$

The evaluation of the Poisson equation for the pressure requires values of the pressure outside of the domain. Along the boundary, pressure can be obtained from the following relation

$$\frac{\partial p}{\partial y} = \frac{1}{Re}\frac{\partial^2 v}{\partial y^2}. \tag{1.27}$$

In SIMPLE method, pressure corrections are obtained from the similar type of Poisson equation for pressure correction. The value of pressure correction at the boundary with no normal flow will be zero.

1.8.5 SIMPLE Algorithm

Patankar and Spalding [28] in 1972 has introduced a method for solving the Navier Stokes equations. They developed the algorithm SIMPLE (Semi-Implicit Method for Pressure-Linked Equations) to solve the Navier Stokes equations iteratively based on finite volume discretization. The Navier Stokes equations are difficult to solve due to the presence of unknown pressure field in these equations. These equations can be solved only when the pressure field is known or is estimated. For this, the pressure field is indirectly linked with the continuity equation. This is achieved by obtaining a whole set of discretized continuity and momentum equations and the obtained discretized equations is solved by a direct solution. The idea behind the SIMPLE algorithm is to establish a discrete equation for pressure and solve the discrete continuity equation in segregate manner. It couples the pressure and velocity terms after solving the discretized equations separately by an iterative approach.

The use of the SIMPLE algorithm is beneficial since it is based on iterative approach. The solutions obtained through iterative approach is commonly used to solve a complete set of discretized equations so that they may be applied to one single dependent variable or even to a single point. It is more difficult to solve the entire sets of velocity and pressure components using a direct solution.

SIMPLE algorithm can be applied to solve incompressible flow problems. For the compressible flow problems (Zaiyong et al. [29]), the pressure may be determined from the temperature and density by using the equation of state where the density is regarded as a dependent variable of the continuity equation as discussed by Versteeg and Malalasekera [30]. The density is constant for the incompressible flow and hence, is not linked to the pressure. For this case, a strong coupling between the velocity and pressure exists that establish a constant on the flow field solution. The resulting velocity field satisfies the continuity equation only when the correct pressure field is applied in the momentum equations. A brief discussion of the methodology of the SIMPLE algorithm can be found here (Barton and Kirby [31]), and in more detail by Patankar [32]. This method has been

successfully employed for flow computations in two-dimensional problems (Kobayashi and Pereira [33]; Ferziger and Peric [34]).

Two-dimensional laminar flow is governed by the set of partial differential equations. Conservation equations can be written in many different forms, depending on the coordinate system and basis vectors used. Assuming that the flow is incompressible, the following continuity, momentum and energy equations in their primitive dimensional form can be used to describe the nanofluid flow.

The continuity equation : (**conservation of mass**)

$$\frac{\partial u^*}{\partial x^*} + \frac{\partial v^*}{\partial y^*} = 0. \tag{1.28}$$

Navier-Stokes Equations : (**conservation of momentum**)
The conservation of momentum in the x and y direction are given by the u-momentum and v-momentum equation, respectively.

u-momentum equation,

$$\frac{\partial u^*}{\partial t^*} + \frac{\partial}{\partial x^*}\left(u^{*2} + \frac{p^*}{\rho_{nf}}\right) + \frac{\partial}{\partial y^*}(u^* v^*) = \nu_{nf}\left(\frac{\partial^2 u^*}{\partial x^{*2}} + \frac{\partial^2 u^*}{\partial y^{*2}}\right). \tag{1.29}$$

v-momentum equation

$$\frac{\partial v^*}{\partial t^*} + \frac{\partial}{\partial x^*}(u^* v^*) + \frac{\partial}{\partial y^*}\left(v^{*2} + \frac{p^*}{\rho_{nf}}\right) = \nu_{nf}\left(\frac{\partial^2 v^*}{\partial x^{*2}} + \frac{\partial^2 v^*}{\partial y^{*2}}\right). \tag{1.30}$$

Energy Equation : (**conservation of energy**)

$$\frac{\partial T}{\partial t^*} + u^*\frac{\partial T}{\partial x^*} + v^*\frac{\partial T}{\partial y^*} = \alpha_{nf}\left(\frac{\partial^2 T}{\partial x^{*2}} + \frac{\partial^2 T}{\partial y^{*2}}\right). \tag{1.31}$$

The variables in the above equations (1.29 - 1.31) are nondimensionalized as follows,

$$t = \frac{t^* U}{A^*}, \quad x = \frac{x^*}{A^*}, \quad y = \frac{y^*}{A^*}, \quad u = \frac{u^*}{U}, \quad v = \frac{v^*}{U}, \quad p = \frac{p^*}{\rho U^2}, \quad \theta = \frac{T - T_0}{T_w - T_0}. \tag{1.32}$$

where A^* is a characteristic length, and ρ, U and T_0 are the reference density, velocity and temperature respectively.

The nondimensional, conservative form of equations (1.29 - 1.31) can be written as :

$$\frac{\partial u}{\partial x} + \frac{\partial v}{\partial y} = 0, \tag{1.33}$$

$$\frac{\partial u}{\partial t} + \frac{\partial u^2}{\partial x} + \frac{\partial uv}{\partial y} = -\frac{\partial p}{\partial x} + \frac{1}{Re}\left(\frac{\partial^2 u}{\partial x^2} + \frac{\partial^2 u}{\partial y^2}\right), \tag{1.34}$$

$$\frac{\partial v}{\partial t} + \frac{\partial uv}{\partial x} + \frac{\partial v^2}{\partial y} = -\frac{\partial p}{\partial y} + \frac{1}{Re}\left(\frac{\partial^2 v}{\partial x^2} + \frac{\partial^2 v}{\partial y^2}\right), \tag{1.35}$$

$$\frac{\partial \theta}{\partial t} + \frac{\partial u\theta}{\partial x} + \frac{\partial v\theta}{\partial y} = \frac{1}{RePr}\left(\frac{\partial^2 \theta}{\partial x^2} + \frac{\partial^2 \theta}{\partial y^2}\right). \tag{1.36}$$

The nondimensional parameter Reynolds number (Re) is defined as

$$Re = \frac{\mathbf{U}A^*}{\nu} = \frac{\rho \mathbf{U}^2 A^{*2}}{\mu \frac{\mathbf{U}}{A^*} A^{*2}} = \frac{\text{Inertial force}}{\text{Viscous force}} \tag{1.37}$$

where ν is kinematic viscosity and μ is dynamic viscosity of the fluid. Two fluid motions are said to be dynamically similar if, with similar geometrical boundaries, the velocity fields are geometrically similar, i.e., if they have geometrically similar streamlines. For two flows about similar geometrical bodies with different fluids, different velocities and different linear dimensions to be dynamically similar, the following condition must be fulfilled: at all geometrically similar points the forces acting on a fluid particle must bear a fixed ratio at every instant of time. If Re is small then we can ignore the inertia force, whereas if Re is large then we can neglect the effect of the viscous force and consequently the fluid may be treated as non-viscous fluid. When the viscous-force is the predominant force, Reynolds number must be the same for dynamic similarity of two flows.

In order to solve numerically the velocity and pressure fields that obey the discretized momentum and continuity equations, the finite volume method was applied. This method

involves integrating the continuity and momentum equations over a two-dimensional control volume on a staggered grid shown in Fig. 1.1(b). The staggered grid evaluates the scalar variables, in this case only pressure, which are stored at the center of the cell. The u-velocity components are stored at the east and west cell faces of the scalar control volume and are indicated by the horizontal arrows ($\rightarrow$) and v-velocity components are stored at the north and south cell faces of the scalar control volume and are indicated by the vertical arrows($\uparrow$). The uniform grids are forward staggered since the u-velocity on the east and west faces are at a distance of $1/2\delta x$ from the center of scalar control volume and v-velocity on the north and south faces are at a distance of $1/2\delta y$ from the center of scalar control volume.

Integration of the x-momentum equation (1.34) at the $(n+1)^{th}$ time step over the $(j,k)^{th}$ control volume for u (see figure-1.5) gives

$$\begin{aligned}\frac{3u_{j,k}^{n+1}-4u_{j,k}^{n}+u_{j,k}^{n-1}}{2\triangle t}\triangle x_j^{+}\triangle y_k + F_e u_e - F_w u_w + F_n u_n - F_s u_s \\ -\left[\frac{1}{Re}\left(\frac{u_{j+1,k}^{n+1}-u_{j,k}^{n+1}}{\triangle x_{j+1}}\right)-\frac{1}{Re}\left(\frac{u_{j,k}^{n+1}-u_{j-1,k}^{n+1}}{\triangle x_j}\right)\right]\triangle y_k \\ -\left[\frac{1}{Re}\left(\frac{u_{j,k+1}^{n+1}-u_{j,k}^{n+1}}{\triangle y_k^{+}}\right)-\frac{1}{Re}\left(\frac{u_{j,k}^{n+1}-u_{j,k-1}^{n+1}}{\triangle y_k^{-}}\right)\right]\triangle x_j^{+} \\ = \triangle y_k(p_{j,k}^{n+1}-p_{j+1,k}^{n+1}),\end{aligned} \tag{1.38}$$

where,

$$\begin{aligned}F_e u_e = \Bigg[\frac{1}{4}\frac{(\triangle x_j+0.5\triangle x_{j+1})}{\triangle x_j^{+}}u_{j+1,k}^{n+1}+\frac{1}{2}\frac{(\triangle x_j+0.5\triangle x_{j+1})}{\triangle x_j}u_{j,k}^{n+1} \\ -\frac{1}{8}\frac{(\triangle x_{j+1}^2)}{(\triangle x_j)(\triangle x_j^{+})}u_{j-1,k}^{n+1}\Bigg][|F_e,0|]-\Bigg[\frac{1}{4}\frac{(\triangle x_{j+2}+0.5\triangle x_{j+1})}{\triangle x_j^{++}}u_{j,k}^{n+1} \\ +\frac{1}{2}\frac{(\triangle x_{j+2}+0.5\triangle x_{j+1})}{\triangle x_{j+2}}u_{j+1,k}^{n+1}-\frac{1}{8}\frac{(\triangle x_{j+1}^2)}{(\triangle x_{j+2})(\triangle x_j^{++})}u_{j+2,k}^{n+1}\Bigg][|-F_e,0|],\end{aligned}$$

where the symbol $[|a,b|]$ represents the maximum of two operands a and b. Similar expressions for $F_w u_w$, $F_n u_n$ and $F_s u_s$ can be obtained at the control volume face w, n and

s, respectively.

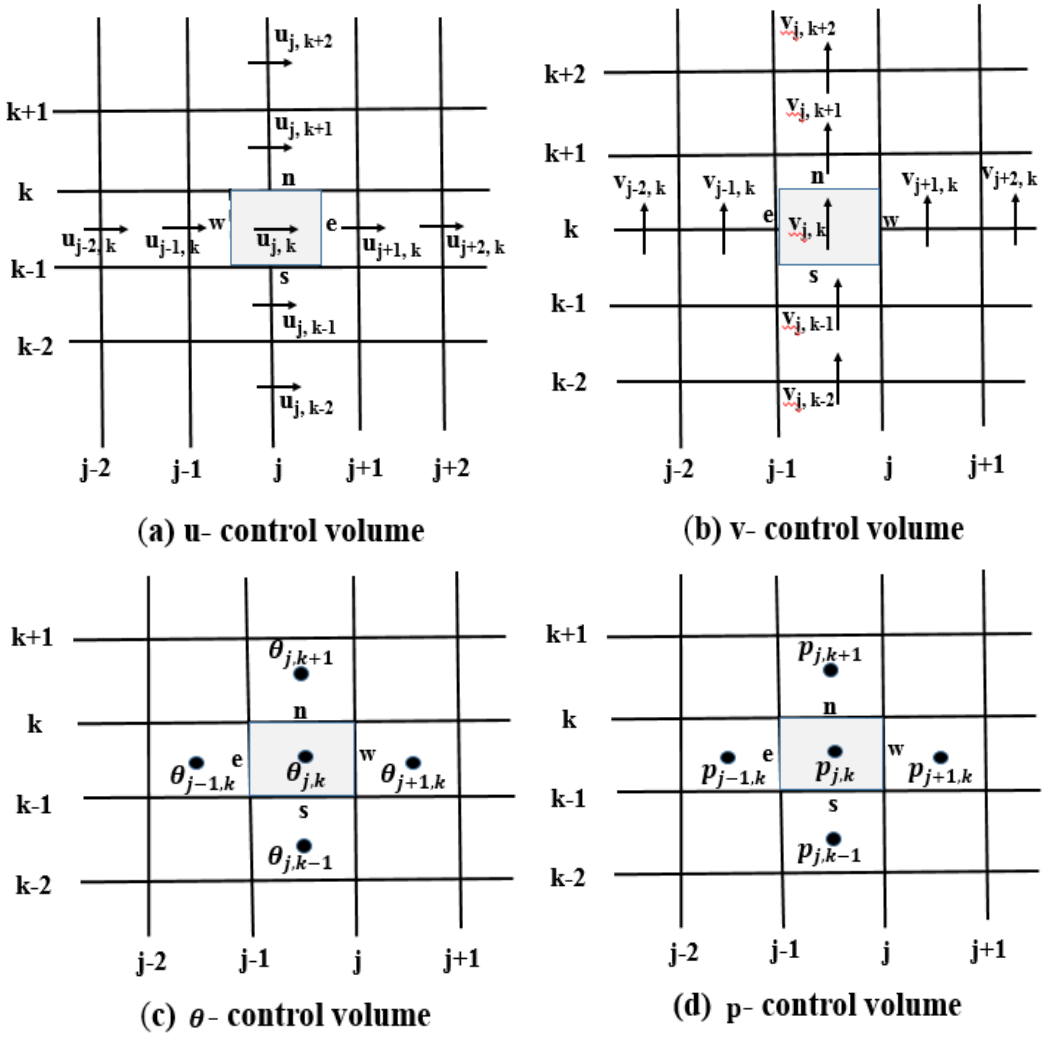

Figure 1.5: Control volumes

Rearranging the equation (1.38) the discretized equation for the x-momentum equation using the third-order upwind scheme is given by

$$a_j^u u_{j-1,k}^{n+1} + b_j^u u_{j,k}^{n+1} + c_j^u u_{j+1,k}^{n+1} = d_j^u - \triangle y_k (p_{j+1,k}^{n+1} - p_{j,k}^{n+1}), \tag{1.39}$$

$j = 2, 3, ..., N + 1$ and $k = 2, 3, ..., M + 1$. where,

$$a_j^u = -\frac{1}{Re}\left(\frac{\triangle y_k}{\triangle x_j}\right) - \frac{1}{8}\frac{(dx_{j+1}^2)}{(dx_j)\frac{(dx_j+dx_{j+1})}{2}}[|0.5(u_{j+1,k}^n + u_{j,k}^n)dy_k, 0|]$$
$$-\frac{1}{2}\frac{(0.5dx_j + dx_{j-1})}{dx_{j-1}}[|0.5(u_{j,k}^n + u_{j-1,k}^n)dy_k, 0|]$$
$$+\frac{1}{4}\frac{(0.5dx_j + dx_{j+1})}{\frac{(dx_j+dx_{j+1})}{2}}[|-0.5(u_{j,k}^n + u_{j-1,k}^n)dy_k, 0|],$$

$$b_j^u = \frac{3}{2}\left(\frac{\triangle x_j^+ \triangle y_k}{\triangle t}\right) + \frac{1}{Re}\left[\frac{\triangle x_j^+}{\triangle y_k^+} + \frac{\triangle x_j^+}{\triangle y_k^-} + \frac{\triangle y_k}{\triangle x_{j+1}} + \frac{\triangle y_k}{\triangle x_j}\right]$$
$$+\frac{1}{2}\frac{(dx_j + 0.5dx_{j+1})}{dx_j}[|0.5(u_{j+1,k}^n + u_{j,k}^n)dy_k, 0|]$$
$$-\frac{1}{4}\frac{(dx_{j+2} + 0.5dx_{j+1})}{\frac{(dx_{j+1}+dx_{j+2})}{2}}[|-0.5(u_{j+1,k}^n + u_{j,k}^n)dy_k, 0|]$$
$$-\frac{1}{4}\frac{(dx_{j-1} + 0.5dx_j)}{\frac{(dx_j+dx_{j-1})}{2}}[|0.5(u_{j,k}^n + u_{j-1,k}^n)dy_k, 0|]$$
$$+\frac{1}{2}\frac{(dx_{j+1} + 0.5dx_j)}{dx_{j+1}}[|-0.5(u_{j,k}^n + u_{j-1,k}^n)dy_k, 0|]$$
$$+\frac{1}{2}\frac{(dy_k + 0.5dy_{k-1})(dy_{k+1})}{(\frac{dy_k+dy_{k-1}}{2})(\frac{dy_k+dy_{k+1}}{2})}[|0.5(v_{j,k}^n dx_{j+1} + v_{j+1,k}^n dx_j), 0|]$$
$$-\frac{1}{2}\frac{(dy_{k+1} + 0.5dy_{k+2})(dy_{k+1})}{\frac{(dy_k+dy_{k+1})}{2}(0.5dy_k + dy_{k+1} + 0.5dy_{k+2})}$$
$$[|-0.5(v_{j,k}^n dx_{j+1} + v_{j+1,k}^n dx_j), 0|]$$
$$-\frac{1}{2}\frac{(dy_{k-1} + 0.5dy_{k-2})(dy_{k-1})}{\frac{(dy_k+dy_{k-1})}{2}(0.5dy_k + dy_{k-1} + 0.5dy_{k-2})}$$
$$[|0.5(v_{j,k-1}^n dx_{j+1} + v_{j+1,k-1}^n dx_j), 0|]$$
$$+\frac{1}{2}\frac{(dy_k + 0.5dy_{k+1})(dy_{k-1})}{\frac{(dy_k+dy_{k-1})}{2}\frac{(dy_k+dy_{k+1})}{2}}$$
$$[|-0.5(v_{j,k-1}^n dx_{j+1} + v_{j+1,k-1}^n dx_j), 0|],$$

$$c_j^u = -\frac{1}{Re}\left(\frac{\triangle y_k}{\triangle x_{j+1}}\right) + \frac{1}{4}\frac{(dx_j + 0.5dx_{j+1})}{\frac{(dx_j+dx_{j+1})}{2}}[|0.5(u_{j+1,k}^n + u_{j,k}^n)dy_k, 0|]$$
$$-\frac{1}{2}\frac{(dx_{j+2} + 0.5dx_{j+1})}{(dx_{j+2})}[|-0.5(u_{j+1,k}^n + u_{j,k}^n)dy_k, 0|]$$
$$-\frac{1}{8}\frac{(dx_j^2)}{\frac{(dx_j+dx_{j+1})}{2}(dx_{j+1})}[|-0.5(u_{j,k}^n + u_{j-1,k}^n)dy_k, 0|],$$

$$d_j^u = 2\left(\frac{\triangle x_j^+ \triangle y_k}{\triangle t}\right)u_{j,k}^n - \frac{1}{2}\left(\frac{\triangle x_j^+ \triangle y_k}{\triangle t}\right)u_{j,k}^{n-1} + \frac{1}{Re}\left(\frac{\triangle x_j^+}{\triangle y_k^+}\right)(u_{j,k+1}^n + u_{j,k-1}^n)$$
$$-\frac{1}{8}\frac{(dx_{j+1}^2)}{\frac{(dx_{j+1}+dx_{j+2})}{2}(dx_{j+2})}u_{j+2,k}^{n+1}[|-0.5(u_{j+1,k}^n + u_{j,k}^n)dy_k, 0|]$$
$$-\frac{1}{8}\frac{(dx_j^2)}{(dx_{j-1})(\frac{dx_j+dx_{j-1}}{2})}u_{j-2,k}^{n+1}[|0.5(u_{j,k}^n + u_{j-1,k}^n)dy_k, 0|]$$
$$-\left[\frac{1}{2}\frac{(dy_k)(dy_k + 0.5dy_{k-1})}{(0.5dy_{k+1} + dy_k + 0.5dy_{k-1})\frac{(dy_k+dy_{k+1})}{2}}u_{j,k+1}^{n+1}\right.$$
$$\left.-\frac{1}{4}\frac{(dy_k)(dy_{k+1})}{\frac{(dy_k+dy_{k-1})}{2}(0.5dy_{k-1} + dy_k + 0.5dy_{k+1})}u_{k-1,j}^{n+1}\right]\left[|0.5(v_{j,k}^n dx_{j+1} + v_{j+1,k}^n dx_j), 0|\right]$$
$$+\left[\frac{1}{2}\frac{(dy_k)(dy_{k+1} + 0.5dy_{k+2})}{(\frac{dy_k+dy_{k+1}}{2})(\frac{dy_{k+1}+dy_{k+2}}{2})}u_{j,k+1}^{n+1}\right.$$
$$\left.-\frac{1}{4}\frac{(dy_k)(dy_{k+1})}{(0.5dy_{k+2} + dy_{k+1} + 0.5dy_k)\frac{(dy_{k+1}+dy_{k+2})}{2}}u_{j,k+2}^{n+1}\right][|-0.5(v_{j,k}^n dx_{j+1} + v_{j+1,k}^n dx_j), 0|]$$
$$+\left[\frac{1}{2}\frac{(dy_k)(dy_{k-1} + 0.5dy_{k-2})}{\frac{(dy_k+dy_{k-1})}{2}\frac{(dy_{k-1}+dy_{k-2})}{2}}u_{j,k-1}^{n+1}\right.$$
$$\left.-\frac{1}{4}\frac{(dy_k)(dy_{k-1})}{(0.5dy_{k-2} + dy_{k-1} + 0.5dy_k)\frac{(dy_{k-1}+dy_{k-2})}{2}}u_{j,k-2}^{n+1}\right][|0.5(v_{j,k-1}^n dx_{j+1} + v_{j+1,k-1}^n dx_j), 0|]$$
$$-\left[\frac{1}{2}\frac{(dy_k)(dy_k + 0.5dy_{k+1})}{\frac{(dy_k+dy_{k-1})}{2}(0.5dy_{k-1} + dy_k + 0.5dy_{k+1})}u_{j,k-1}^{n+1}\right.$$
$$\left.-\frac{1}{4}\frac{(dy_k)(dy_{k-1})}{(0.5dy_{k+1} + dy_k + 0.5dy_{k-1})\frac{(dy_k+dy_{k+1})}{2}}u_{j,k+1}^{n+1}\right][|-0.5(v_{j,k-1}^n dx_{j+1} + v_{j+1,k-1}^n dx_j), 0|]. \tag{1.40}$$

Similarly integration of the y-momentum equation at the $(n+1)^{th}$ time step over the

$(j,k)^{th}$ control volume for v yields

$$a_j^v v_{j-1,k}^{n+1} + b_j^v v_{j,k}^{n+1} + c_j^v v_{j+1,k}^{n+1} = d_j^v - \triangle x_j (p_{j,k+1}^{n+1} - p_{j,k}^{n+1}), \tag{1.41}$$

$j = 2, 3, ..., N+1$ and $k = 2, 3, ..., M+1$. where,

$$\begin{aligned}
a_j^v = &-\frac{1}{Re}\left(\frac{\triangle y_k^+}{\triangle x_j^-}\right) - \frac{1}{4}\frac{(dx_j)(dx_{j+1})}{\frac{(dx_j+dx_{j-1})}{2}(0.5dx_{j-1}+dx_j+0.5dx_{j+1})}[|0.5(u_{j,k}^n dy_{k+1} + u_{j,k+1}^n dy_k), 0|] \\
&-\frac{1}{2}\frac{(dx_j)(dx_{j-1}+0.5dx_{j-2})}{\frac{(dx_j+dx_{j-1})}{2}\frac{(dx_{j-1}+dx_{j-2})}{2}}[|0.5(u_{j-1,k}^n dy_{k+1} + u_{j-1,k+1}^n dy_k), 0|] \\
&+\frac{1}{2}\frac{(dx_j)(dx_j+0.5dx_{j+1})}{\frac{(dx_j+dx_{j-1})}{2}(0.5dx_{j-1}+dx_j+0.5dx_{j+1})}[|-0.5(u_{j-1,k}^n dy_{k+1} + u_{j-1,k+1}^n dy_k), 0|],
\end{aligned}$$

$$\begin{aligned}
b_j^v = &\frac{3}{2}\left(\frac{\triangle x_j \triangle y_k^+}{\triangle t}\right) + \frac{1}{Re}\left[\frac{\triangle y_k^+}{\triangle x_j^+} + \frac{\triangle y_k^+}{\triangle x_j^-} + \frac{\triangle x_j}{\triangle y_{k+1}} + \frac{\triangle x_j}{\triangle y_k}\right] \\
&+\frac{1}{2}\frac{(dx_{j+1})(dx_j+0.5dx_{j-1})}{\frac{(dx_j+dx_{j+1})}{2}\frac{(dx_j+dx_{j-1})}{2}}[|0.5(u_{j,k}^n dy_{k+1} + u_{j,k+1}^n dy_k), 0|] \\
&-\frac{1}{2}\frac{(dx_{j+1})(dx_{j+1}+dx_{j+2})}{\frac{(dx_j+dx_{j+1})}{2}(0.5dx_j+dx_{j+1}+0.5dx_{j+2})}[|-0.5(u_{j,k}^n dy_{k+1} + u_{j,k+1}^n dy_k), 0|] \\
&-\frac{1}{2}\frac{(dx_{j-1})(dx_{j-1}+0.5dx_{j-2})}{\frac{(dx_j+dx_{j-1})}{2}(0.5dx_{j-2}+dx_{j-1}+0.5dx_j)}[|0.5(u_{j-1,k}^n dy_{k+1} + u_{j-1,k+1}^n dy_k), 0|] \\
&+\frac{1}{2}\frac{(dx_{j-1})(dx_j+0.5dx_{j+1})}{\frac{(dx_j+dx_{j-1})}{2}\frac{(dx_j+dx_{j+1})}{2}}[|-0.5(u_{j-1,k}^n dy_{k+1} + u_{j-1,k+1}^n dy_k), 0|] \\
&+\frac{1}{2}\frac{(dy_k+0.5dy_{k+1})}{dy_k}[|0.5(v_{j,k}^n + v_{j,k+1}^n)dx_j, 0|] \\
&-\frac{1}{4}\frac{(dy_{k+2}+0.5dy_{k+1})}{\frac{(dy_{k+1}+dy_{k+2})}{2}}[|-0.5(v_{j,k}^n + v_{j,k+1}^n)dx_j, 0|] \\
&-\frac{1}{4}\frac{(dy_{k-1}+0.5dy_k)}{\frac{(dy_k+dy_{k-1})}{2}}[|0.5(v_{j,k}^n + v_{j,k-1}^n)dx_j, 0|] \\
&+\frac{1}{2}\frac{(dy_{k+1}+0.5dy_k)}{dy_{k+1}}[|-0.5(v_{j,k}^n + v_{j,k-1}^n)dx_j, 0|],
\end{aligned} \tag{1.42}$$

$$
\begin{aligned}
c_j^v = & -\frac{1}{Re}\left(\frac{\triangle y_k^+}{\triangle x_j^+}\right) \\
& +\frac{1}{2}\frac{(dx_j)(dx_j+0.5dx_{j-1})}{\frac{(dx_j+dx_{j+1})}{2}(0.5dx_{j+1}+dx_j+0.5dx_{j-1})}[|0.5(u_{j,k}^n dy_{k+1}+u_{j,k+1}^n dy_k),0|] \\
& -\frac{1}{2}\frac{(dx_j)(dx_{j+1}+0.5dx_{j+2})}{\frac{(dx_j+dx_{j+1})}{2}\frac{(dx_{j+1}+dx_{j+2})}{2}}[|-0.5(u_{j,k}^n dy_{k+1}+u_{j,k+1}^n dy_k),0|] \\
& -\frac{1}{4}\frac{(dx_j)(dx_{j-1})}{(0.5dx_{j-1}+dx_j+0.5dx_{j+1})\frac{(dx_j+dx_{j+1})}{2}}[|-0.5(u_{j-1,k}^n dy_{k+1}+u_{j-1,k+1}^n dy_k),0|],
\end{aligned}
\tag{1.43}
$$

$$
\begin{aligned}
d_j^v = & 2\left(\frac{\triangle x_j \triangle y_k^+}{\triangle t}\right)v_{j,k}^n - \frac{1}{2}\left(\frac{\triangle x_j \triangle y_k^+}{\triangle t}\right)v_{j,k}^{n-1} + \frac{1}{Re}\left(\frac{\triangle x_j}{\triangle y_{k+1}}v_{j,k+1}^{n+1} + \frac{\triangle x_j}{\triangle y_k}v_{j,k-1}^{n+1}\right) \\
& -\frac{1}{4}\frac{(dx_j)(dx_{j+1})}{(0.5dx_j+dx_{j+1}+0.5dx_{j+2})\frac{(dx_{j+1}+dx_{j+2})}{2}}v_{j+2,k}^{n+1}[|-0.5(u_{j,k}^n dy_{k+1}+u_{j,k+1}^n dy_k),0|] \\
& -\frac{1}{4}\frac{(dx_j)(dx_{j-1})}{\frac{(dx_{j-1}+dx_{j-2})}{2}(0.5dx_{j-2}+dx_{j-1}+0.5dx_j)}v_{j-2,k}^{n+1}[|0.5(u_{j-1,k}^n dy_{k+1}+u_{j-1,k+1}^n dy_k),0|] \\
& -\left[\frac{1}{4}\frac{(dy_k+0.5dy_{k+1})}{\frac{(dy_k+dy_{k+1})}{2}}v_{j,k+1}^{n+1} - \frac{1}{8}\frac{dy_{k+1}^2}{\frac{(dy_k+dy_{k+1})}{2}(dy_k)}v_{j,k-1}^{n+1}\right][|0.5(v_{j,k}^n+v_{j,k+1}^n)dx_j,0|] \\
& +\left[\frac{1}{2}\frac{(dy_{k+2}+0.5dy_{k+1})}{dy_{k+2}}v_{j,k+1}^{n+1} - \frac{1}{8}\frac{dy_{k+1}^2}{(dy_{k+2})\frac{(dy_{k+1}+dy_{k+2})}{2}}v_{j,k+2}^{n+1}\right][|-0.5(v_{j,k}^n+v_{j,k+1}^n)dx_j,0|] \\
& +\left[\frac{1}{2}\frac{(dy_{k-1}+0.5dy_k)}{dy_{k-1}}v_{j,k-1}^{n+1} - \frac{1}{8}\frac{dy_k^2}{\frac{(dy_k+dy_{k-1})}{2}(dy_{k-1})}v_{j,k-2}^{n+1}\right][|0.5(v_{j,k}^n+v_{j,k-1}^n)dx_j,0|] \\
& -\left[\frac{1}{4}\frac{(dy_{k+1}+0.5dy_k)}{\frac{(dy_k+dy_{k+1})}{2}}v_{j,k-1}^{n+1} - \frac{1}{8}\frac{dy_k^2}{(dy_{k+1})\frac{(dy_k+dy_{k+1})}{2}}v_{j,k+1}^{n+1}\right][|-0.5(v_{j,k}^n+v_{j,k-1}^n)dx_j,0|],
\end{aligned}
\tag{1.44}
$$

with

$$
\begin{aligned}
\triangle x_j^+ &= \frac{\triangle x_j + \triangle x_{j+1}}{2}, \\
\triangle x_j^- &= \frac{\triangle x_{j-1} + \triangle x_j}{2}, \\
\triangle y_k^+ &= \frac{\triangle y_k + \triangle y_{k+1}}{2}, \\
\triangle y_k^- &= \frac{\triangle y_{k-1} + \triangle y_k}{2},
\end{aligned}
$$

$$\triangle x_j^{++} = \frac{\triangle x_{j+1} + \triangle x_{j+2}}{2}.$$

For fixed k, the system of equations (1.39) and (1.41) together can be written in matrix notation as

$$A_j X_{j-1}^{n+1} + B_j X_j^{n+1} + C_j X_{j+1}^{n+1} = D_j, \tag{1.45}$$

$j = 2, 3, .., N+1$, where the co-efficient matrices A_j, B_j, C_j and D_j are given by

$$A_j = \begin{pmatrix} a_j^u & 0 \\ 0 & a_j^v \end{pmatrix},$$

$$B_j = \begin{pmatrix} b_j^u & 0 \\ 0 & b_j^v \end{pmatrix},$$

$$C_j = \begin{pmatrix} c_j^u & 0 \\ 0 & c_j^v \end{pmatrix},$$

$$D_j = \begin{pmatrix} d_j^u - \triangle y_k (p_{j+1,k}^{n+1} - p_{j,k}^{n+1}) \\ d_j^v - \triangle x_j (p_{j,k+1}^{n+1} - p_{j,k}^{n+1}) \end{pmatrix},$$

and variable matrix is given by

$$X_j^{n+1} = \begin{pmatrix} u_{j,k}^{n+1} \\ v_{j,k}^{n+1}) \end{pmatrix}.$$

The system of equations (1.45) can be written as a block tri-diagonal form as

$$\overline{A}\overline{w} = \overline{D} \tag{1.46}$$

where,

$$\overline{A} = \begin{pmatrix} B_2 & C_2 & 0 & . & . & . & 0 \\ A_3 & B_3 & C_3 & 0 & . & . & . \\ 0 & . & . & . & . & . & . \\ . & . & A_j & B_j & C_j. & . & \\ . & & & . & . & . & 0 \\ . & . & . & 0 & A_N & B_N & C_N \\ 0 & . & . & . & . & A_{N+1} & B_{N+1} \end{pmatrix},$$

is a block tridiagonal matrix, each element being a square matrix of order two,

$$\overline{w} = \begin{pmatrix} X_2^{n+1} \\ X_3^{n+1} \\ . \\ . \\ X_{N+1}^{n+1} \end{pmatrix},$$

being the vector of unknowns and

$$\overline{D} = \begin{pmatrix} D_2 \\ D_3 \\ . \\ . \\ D_{N+1} \end{pmatrix},$$

is the vector of knowns.

The matrix equation (1.46) is solved by using block elimination Varga's Algorithm, to obtain the solution u', v' at each iteration.

Integrating the continuity equation at the $(n+1)^{th}$ time step over the $(j,k)^{th}$ control volume for pressure, one gets

$$(u_{j,k}^{n+1} - u_{j-1,k}^{n+1})\triangle y_k + (v_{j,k}^{n+1} - v_{j,k-1}^{n+1})\triangle x_j = 0. \tag{1.47}$$

To deduce the Poisson equation for pressure correction in non-uniform grid, we calculate the velocity field ($u'_{j,k}$, $v'_{j,k}$) from the matrix equation (1.46) using the guessed pressure field $p'_{j,k}$ (which is equal to the previous time step solution $p^n_{j,k}$) at the start of the iteration. Hence $u'_{j,k}$ and $v'_{j,k}$ satisfy the equations (1.39) and (1.41). We get,

$$a^u_j u'_{j-1,k} + b^u_j u'_{j,k} + c^u_j u'_{j+1,k} = d^u_j - \triangle y_k (p'_{j+1,k} - p'_{j,k}), \tag{1.48}$$

$$a^v_j v'_{j-1,k} + b^v_j v'_{j,k} + c^v_j v'_{j+1,k} = d^v_j - \triangle x_j (p'_{j,k+1} - p'_{j,k}). \tag{1.49}$$

But these $u'_{j,k}$ and $v'_{j,k}$ may not satisfy the continuity equation (1.47).

A pressure correction $p'_{j,k}$ is sought at each cell (j, k) as

$$p^{n+1}_{j,k} = p'_{j,k} + p^c_{j,k}, \tag{1.50}$$

and velocity corrections $u^c_{j,k}$ and $v^c_{j,k}$ as

$$u^{n+1}_{j,k} = u'_{j,k} + u^c_{j,k}, \tag{1.51}$$

$$v^{n+1}_{j,k} = v'_{j,k} + v^c_{j,k}, \tag{1.52}$$

where $u^{n+1}_{j,k}$ and $v^{n+1}_{j,k}$ satisfy the continuity equation (1.47).

Subtracting equation (1.48) from (1.39) and equation (1.49) from (1.41), we get respectively

$$a^u_j u^c_{j-1,k} + b^u_j u^c_{j,k} + c^u_j u^c_{j+1,k} = -\triangle y_k (p^c_{j+1,k} - p^c_{j,k}), \tag{1.53}$$

and

$$a^v_j v^c_{j-1,k} + b^v_j v^c_{j,k} + c^v_j v^c_{j+1,k} = -\triangle x_j (p^c_{j,k+1} - p^c_{j,k}). \tag{1.54}$$

Ignoring the neighbouring small correction terms $a^u_j u^c_{j-1,k}$, $c^u_j u^c_{j+1,k}$ and $a^v_j v^c_{j-1,k}$, $c^v_j v^c_{j+1,k}$ and approximating b^u_j and b^v_j by $\dfrac{\triangle x^+_j \triangle y_k}{\triangle t}$ and $\dfrac{\triangle x_j \triangle y^+_k}{\triangle t}$, respectively, the above equa-

tions give the velocity correction as:

$$u^c_{j,k} = -\left(\frac{\triangle t}{\triangle x^+_j}\right)(p^c_{j+1,k} - p^c_{j,k}), \tag{1.55}$$

$$v^c_{j,k} = -\left(\frac{\triangle t}{\triangle y^+_k}\right)(p^c_{j,k+1} - p^c_{j,k}). \tag{1.56}$$

The pressure field $p'_{j,k}$ is under-relaxed as

$$p^{n+1}_{j,k} = p'_{j,k} + \alpha_p.p^c_{j,k}, \tag{1.57}$$

where α_p is the under-relaxation factor. Similarly the velocity fields $u^{n+1}_{j,k}$ and $v^{n+1}_{j,k}$ are under-relaxed in following manner:

$$u^{n+1}_{j,k} = u'_{j,k} - \alpha_u.(p^c_{j+1,k} - p^c_{j,k}).\left(\frac{\triangle t}{\triangle x^+_j}\right), \tag{1.58}$$

$$v^{n+1}_{j,k} = v'_{j,k} - \alpha_v.(p^c_{j,k+1} - p^c_{j,k}).\left(\frac{\triangle t}{\triangle y^+_k}\right). \tag{1.59}$$

Substituting the corrected velocity fields from the equations (1.58)-(1.59) into the discretized continuity equation (1.47) yields the Poisson equation for pressure correction in discretized form as

$$\left[\alpha_u(\triangle t\triangle y_k)\left(\frac{1}{\triangle x^+_j} + \frac{1}{\triangle x^-_j}\right) + \alpha_v(\triangle t\triangle x_j)\left(\frac{1}{\triangle y^+_k} + \frac{1}{\triangle y^-_k}\right)\right]p^c_{j,k} = -div^* + \alpha_u(\triangle t\triangle y_k)\left(\frac{p^c_{j+1,k}}{\triangle x^+_j} + \frac{p^c_{j-1,k}}{\triangle x^-_j}\right) + \alpha_v(\triangle t\triangle x_j)\left(\frac{p^c_{j,k+1}}{\triangle y^+_k} + \frac{p^c_{j,k-1}}{\triangle y^-_k}\right), \tag{1.60}$$

where

$$div^* = (u'_{j,k} - u'_{j-1,k})\triangle y_k + (v'_{j,k} - v'_{j,k-1})\triangle x_j.$$

The equation (1.60) can be considered as the discretized form of a Poisson equation in non-uniform grid, which is referred to as Pressure Poisson equation. We have solved

the equation (1.60) through a Gauss-Seidel iteration method. In this problem a rapid convergence is found, empirically, for the under-relaxation parameters as $\alpha_p = 0.975$ and $\alpha_u = \alpha_v = \frac{2}{3}$.

Thus at any time step the single iteration in this algorithm consists of the following sequential steps:

1. The matrix equation (1.46) is solved by using block elimination Varga's Algorithm to obtain (u', v') using guessed pressure field (p').

2. The Poisson equation (1.60) for pressure correction (p^c) is solved using the successive under relaxation method.

3. The pressure field (p) and velocity field (u, v) from equation (1.57) and equation (1.58)-(1.59), respectively at each cell are updated using the pressure correction (p^c).

Iteration is continued at each time until the divergence-free velocity field is obtained. However for this purpose the divergence in each cell is towed below a preassigned small quantity (ε). In the present case, ε is 0.5×10^{-4}.

A time-dependent numerical solution is obtained by advancing the flow field variables through a sequence of short time steps of duration δt. At the initial stage of motion the time step δt is taken to be 0.001 which has been subsequently increased to 0.005 after the transient state. To facilitate the convergence of the solution for a given Reynolds number, the converged solution of a case with smaller Reynolds number was used as the initial guess.

1.9 Hydrodynamic and Heat Transfer Characteristics

The forces acting on a body immersed in a flowstream are produced by the tangential and normal stresses over its surface. On integration, these stresses give rise to the resultant force components, which are expressed in non-dimensional form by means of

the coefficients of the drag (C_D) and lift (C_L) defined as follows:

$$C_D = C_{DP} + C_{DSh} = \frac{F_D}{0.5\rho U_0^2 A},$$

$$C_L = C_{LP} + C_{LSh} = \frac{F_L}{0.5\rho U_0^2 A},$$

where C_{DP} and C_{DSh} represent the drag coefficient due to pressure and viscous forces, respectively; similarly, C_{LP} and C_{LSh} represent the lift coefficient due to pressure and viscous forces, respectively. F_D and F_L are the integrated drag and lift forces, respectively, acting on the surface of the body.

The nusselt number is defined as the ratio of convective heat transfer to the conductive heat transfer. This tell us about how much the heat transfer is enhanced due to fluid motion. The local Nusselt number (Nu), face-wise average Nusselt number (Nu_{avg}) and mean Nusselt number (Nu_M) along the surface of the body are defined as $Nu = \frac{hA}{k}$, $Nu_{avg} = \frac{1}{A}\int_0^{A^*}(Nu)dl$ and $Nu_M = \frac{1}{4}\sum_{AB} Nu_{avg}$, respectively, where h, A and k are convective heat transfer coefficient, characteristic length and thermal conductivity of fluid, respectively.

1.10 Least Square Method

The least squares method is an approach to find the best fitted line for the set of data points. This method provides a relationship between an unknown dependent and known independent variable that finds the line of best fit for a set of data points. The equation with minimum residual sum of squares (RSS) and maximum coefficient of determination (R^2) gives the best fitted line determines from the least square method. A RSS value close to 0 and R^2 value close to 1 implies the relation is best predictable.

1.11 Literature Review

Studies on the fluid flow past heated bluff bodies in the recent past has drawn considerable importance due to its wide applications in many areas of science and technology

such as cooling of microchips, electronic equipments, designing of compact heat exchangers, automobile sector etc. Several investigations are carried out on the problem of hydrodynamic and heat transfer characteristics past single heated objects. In general, fluid flow past two dimensional bluff bodies involves separation of flow, which produces wake in the downstream of the obhect and in turn generates Vortex Street. Bluff bodies of different cross-sections influences both location and time-dependent behavior of vortices. Bluff bodies with circular cross section have highest degree of symmetry, which has been studied by lot of researchers numerically and experimentally. Reynolds number plays an important role for circular cylinder because of the variation of separation location due to its rounded and continuous shape. This does not happen in the flow around a rectangular cylinder, as Reynolds number does not completely influence location of the separation because in the case of sharp-edged bodies, the point of separation is fixed at the sharp edges.

Flow and heat transfer characteristics of a rectangular cylinder exposed to a uniform flow with ground effect has been studied by Shuja et al. [35]. Yang and Fu [36] studied the unsteady heat transfer of a flow past a heated electronic component. Wang and Jaluria [37] found that the heat transfer rate from heated block increased with height for fixed width, and decreased with width keeping height fixed. Etminan et al. [4] numerically studied the unconfined flow characteristics around the tandem square cylinders in both steady and unsteady laminar flow regimes at fixed spacing (S = 5). Sharma and Eswaran [3] investigated the unconfined/confined flow and heat transfer past a square cylinder in two dimensional laminar regime for uniform heat flux and constant cylinder temperature boundary conditions at different Reynolds number. Bhattacharya et al. [38] have carried out a detailed study on flow and heat transfer past a heated cylinder of square cross section mounted horizontally above a plane wall. Lankadasu and Vengadesan [39] researched the flow of incompressible fluid past a pair of square cylinders in inline tandem arrangement and observed that the down-stream cylinder has experienced negative drag at some shear rates. Bhattacharya and Dhinakaran [40] carried out a study, on the two square cylinders placed near a wall at a fixed height of 0.5 times the cylinder height

and found that the vortex shedding starts for Re beyond 125 for all values of S.

In recent years, there is an alternative means to enhance the heat transfer rate by introducing nanoscale particle ($<$ 100nm) suspensions in base fluids such as water, ethylene glycol or oil (nanofluids) as compared to the conventional heat transfer medium. Choi [41] used nanoscale particle suspensions (nanofluids) as an alternative heat transfer medium due to its superior thermal properties, improved stability, and homogeneity. The very small size of the nanoparticles ($1 - 100nm$) imparts some unique physical and chemical properties to these nanofluids, as mentioned in the study of Lee et al. [42] and Eastman et al. [43]). Hwang et al. [44] in his study reported that the solution (water-based Al_2O_3 nanofluids) is more stable than the base fluid. There are several effective parameters on the thermal conductivity of nanofluids, such as nanofluid temperature, materials and particle volume concentration ϕ . The effect of volume fraction of nanoparticles on heat transfer was presented by various scholars. Heris et al. [45] have carried out experiment with water-Al_2O_3 and water- CuO nanofluids for volume fraction up to 3% and have shown that up to this limit the nanofluid behaves like Newtonian fluid. Ebrahimnia-Bajestan et al. [12] numerically concluded that increasing ϕ enhances the heat transfer. Based on water based nanofluids (using Cu, Al_2O_3 and TiO_2), Cho et al. [46] have shown that the mean Nusselt number (Nu_M) increases with an increasing ϕ and the Cu-water nanofluid yields the best heat transfer performance of the three nanofluids. Heidary and Kermani [47] showed that the heat transfer in channels can enhance up to 60% due to the presence of nanoparticles and the blocks in channels. Vakili et al. [48] experimentally concluded that the enhancement of the convective heat transfer coefficient for the mixture consisting of 60% ethylene glycol and 40% distilled water with TiO_2 is more than the nanofluid of distilled water. For unconfined flow of nano-fluids over a square cylinder, Etminan-Farooji et al. [4] resulted that there is an optimum value ϕ that results in the highest heat transfer coefficient. Apart from these literature survey, each chapter contains detail discussion on the previous studies related to flow past bluff bodies and nanofluid flow.

1.12 Gaps in Existing Research

Many researchers have studied the heat transfer characteristics of the flow past the bluff bodies which are commonly cylindrical in shape, not much focus has been stressed upon square geometry. Based on the previous studies, it is observed that introducing the promoter at the upstream side of an object can generate unsteadiness in the flow, and that depends on the shape and size of the promoter and other parameters such as angles and speed of incoming flow and the position of the promoter with respect to the wall and object. From the above literature review, the consideration of rectangular shape of the promoter would be interesting in generating the vortices (passively) to dominate the state of the wake of a downstream square cylinder. Additionally, there is no reported work on the forced convection heat transfer of nano fluids over tandem cylinders near a wall as frequently encountered in various chemical engineering applications. There has been several numerical studies of laminar convective heat transfer of nanofluid but not much attention has been given on several parameters such as nanoparticle concentration, base fluid type and nanoparticle material to improve the heat transfer characteristics from a heated object, which leads to difficulties in finding the suitable nanofluid for optimum operation.

1.13 Organisation of the Thesis

The thesis has been devoted to the study of some fluid flow past heated square cylinder utilizing nanofluids. The effect of loading of nanoparticles of different size and concentration in base fluid and also the presence of eddy promoter at the upstream have been studied numerically. The thesis consists of seven chapters. The first chapter is introductory. It includes brief discussion on certain relevant topics regarding use of nanofluids in heat transfer applications, basic equations governing the nanofluid flow and the numerical techniques used to solve these equations numerically.

In Chapter 2, we have studied the hydrodynamic and heat transfer nanofluid flow past heated square cylinder in the vicinity of a plane wall under the couette flow. Two types

of nanoparticles (Al_2O_3 and CuO) with base fluid as water is considered. Finite volume method is used to obtain numerical solution of the governing Navier stokes equations along with energy equation. It is found that heat transfer increases/decreases with the increase in ϕ / d_{np}.

In Chapter 3 , we have studied the performance of four type of nanofluids with varying particle size and concentration at two different temperatures. It is observed that Nu_M is reported high at lower fluid temperature but the presence of nanomaterials are more effective in the base fluid at higher temperature.

In Chapter 4 we have studied the heat transfer performance of nanofluids under the incident of Couette-Poiseuille flow. Also two types of thermal boundary conditions are considered on square cylinder. It is found that the flow becomes unsteady with the increase in non-linearity in the flow and consequently, increases the heat transfer at higher pressure gradient. Further, for the heat flux case, heat transfer enhancement is more as compared to the constant temperature condition.

In Chapter-5, heat transfer enhancement from the above square cylinder is investigated due to flow instability by employing an adiabatic upstream cylinder of rectangular shape of op- timum size (by varying height and width) placed at suitable distance (with respect to the downstream cylinder) by varying the spacing between the cylinders under the incident of Couette Poiseuille flow using $W - Al_2O_3$ nanofluid.

In Chapter-6, the effect of offsetting of upstream cylinder from/towards the plane wall on heat transfer characteristics of heated square cylinder is investigated. A comparison is made for the case of offset arrangement with that for the case of inline arrangement highlighting some of the major issues : vortex generation by the upstream cylinder, the appearance of multiple peaks in the spectra and the deviation of the hydrodynamic and heat transfer characteristics of the downstream cylinder from that of the isolated square cylinder.

Chapter 2

Heat Transfer Enhancement from a Heated Square Cylinder in the Vicinity of a Plane Wall Utilizing Nanofluids

2.1 Introduction

The study of the flow past bluff bodies has been imperative for a long time, because of the intrinsic complexities and importance of the flow in many practical applications such as nuclear reactor fuel rods, drying of different materials, cooling of industrial devices, plastics and glass, and chemical reactors. As such, heat transfer characteristics of the flow over bluff bodies have been examined in the literature. The flow field and various transport coefficients strongly depend on the shape and configuration of various bluff bodies including flat plates, circular cylinders, and other blunt cross-sections. Recently, square cylinders have received renewed attention because of their relevance to enhance the cooling from electronic devices. Yang and Fu [36] studied the unsteady heat transfer from a heated electronic component subjected to a flow. It is more difficult to understand when these bluff bodies are placed in the proximity of a wall. Apart from these applications, this issue is classical in advanced fluid mechanics and heat transfer.

The challenges in enhancing the heat transfer rate in the above applications have at-

tracted the attention of the fluid dynamics community. Nanoscale particle (< 100 nm) suspensions in base fluids such as water, ethylene glycol or oil (Nanofluids) have often been used as an alternative heat transfer medium due to superior thermal properties (Choi [41]). These fluids can constitute very interesting alternatives for electronic liquid cooling applications (Nguyen et al. [49]), automotive sector, nuclear reactors, computers and X-rays (Azmi et al. [50], Kakac and Pramuanjaroenkij [51]). Several effective parameters on the thermal conductivity of nanofluids have been presented, such as nanofluid temperature, concentration ϕ (Murshed et al. [52]) and materials (Murshed et al. [52]). Furthermore, some researchers believe that the Brownian motion of nanoparticles inside the fluid is a key mechanism of heat transfer in nanofluids (Ebrahimnia-Bajestan et al. [12]).

Sharma and Eswaran [3] focused on the heat transfer characteristic around a square cylinder for uniform heat flux and constant cylinder temperature. The flow and heat transfer past a heated cylinder mounted horizontally above a plane wall was studied by Bhattacharyya et al. [38]. Dhinakaran [53] performed a numerical simulation for the heat transfer from a square cylinder near a moving wall.

Heris et al. [45] indicated that the $W - Al_2O_3$ causes a greater enhancement in heat transfer coefficient compared with $W - CuO$. Valipour et al. [54] investigated the fluid flow and forced convective heat transfer around a square obstacle utilizing $W - Al_2O_3$ nanofluid at low Reynolds numbers. Ebrahimnia-Bajestan et al. [12] concluded that increasing ϕ enhances the heat transfer. Bovand et al. [55] showed that time average Nusselt number increases by using nanoparticles and increases ϕ . The heat transfer increases by considering the Brownian effects compared with that without Brownian motion. A numerical study on MHD natural convection for alumina-water nanofluid within the circular cylindrical enclosure with an inner triangular was performed by Sheikholeslami et al. [56]. Salimpour and Dehshiri [57] experimentally investigated the laminar forced convective heat transfer of TiO_2 /water nanofluids through conduits with different cross sections.

Heidary and Kermani [47] showed that the heat transfer in channels can be enhanced

up to 60% due to the presence of nanoparticles and the blocks in channels. Azimi and Riazi [58] analyzed the heat transfer and nanofluid flow between two non-parallel walls for both converging/diverging cases. Etminan-Farooji et al. [4] showed that for any given d_{np} there is an optimum value of ϕ that results in the highest heat transfer coefficient. Sarkar and Ganguly [59] demonstrated entropy generation due to laminar mixed convection of nanofluid past a square cylinder in vertically upward flow with the range of ϕ : 0-20 %.

For cavity flow, Alloui et al. [60] studied natural convection of nanofluids and various models for calculating the effective viscosity and thermal conductivity of nanofluids. Noghrehabadi et al. [61] showed an improvement in heat transfer rate for the whole range of Rayleigh numbers when Brownian and thermophoresis effects are considered. Malik and Nayak [62] numerically studied mixed convection flows of nanofluid in a lid-driven cavity.

2.2 Objectives

From the above literature discussion, it is observed that the presence of nanoparticles in the flowing base fluid would enhance the heat transfer from the heated object. An asymmetry in the two separated shear layers issuing from lower and upper faces of the cylinder can be produced by the existence of shear and wall confinement in the flow. To the best of our knowledge, there is no literature on the nanofluid flow and heat transfer around a heated square cylinder near a wall. The main objective of this study are:

1. To investigate the dependencies of hydrodynamic and heat transfer characteristics of the cylinder on non-dimensional parameters governing the fluid flow: Peclet number (Pe) and gap height ratio (L), and governing the nanofluids: Particle materials (Al_2O_3/CuO), concentration (ϕ) and diameter (d_{np}) of materials.

2. To compare the heat transfer enhancement ($\overline{Nu}_M$) of the cylinder and its drag coefficient's ($\overline{C}_D$) increment/reduction by presenting their ratio $\overline{Nu}_M/\overline{C}_D$.

3. To propose an explicit forms of $\overline{Nu}_M = \overline{Nu}_M(Pe)$ and $\overline{Nu}_M = \overline{Nu}_M(L)$ using

least square method.

2.3 Methodology

2.3.1 Problem Formulation

A long square cylinder (with height A^*) maintained at a constant temperature (T_w) is placed parallel to the wall lying along the x^*- axis at a gap height L^* (See Fig. 2.1). The ambient stream has a uniform temperatue T_0 ($< T_w$). The inlet flow is taken as the couette flow based linear velocity profile, which is in accord with the boundary layer theory (Maiti [63]). The incident velocity profile at the surface multiplied by A^* leaving $U_1 = \lambda A^*$ is taken as the velocity scale. The height of the cylinder A^* and temperature difference $\Delta T = T_w - T_0$ are considered as the characteristic length and temperature scales, respectively.

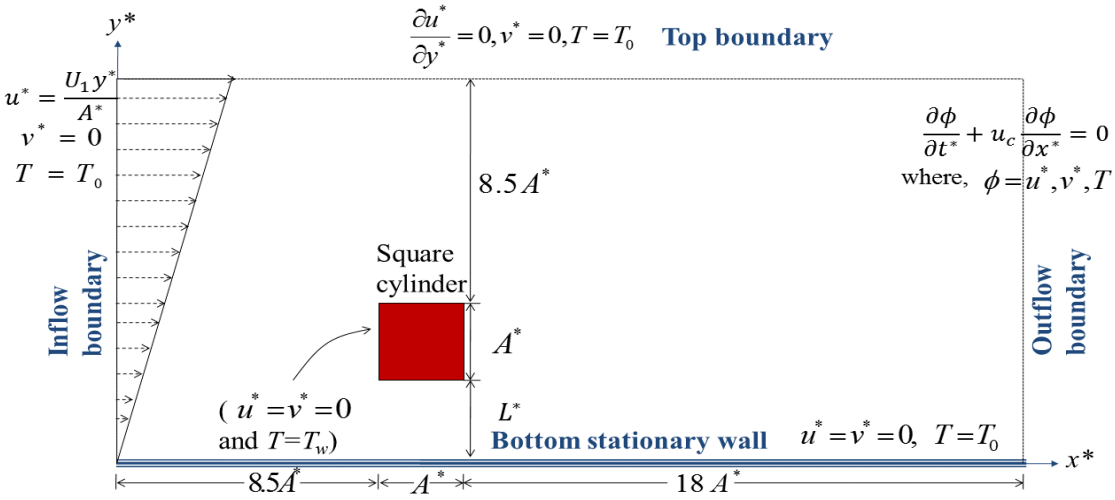

Figure 2.1: Schematics of flow configuration

2.3.2 Governing Equations with Initial and Boundary Conditions

The flow is considered to be two-dimensional and laminar. The fluid is considered as nanofluid. To derive the governing equations for numerical simulation of nanofluid flow problem, one needs to choose a suitable model (either single-phase or two-phase). Under

the single-phase model, both the fluid phase and the solid particles are in thermal equilibrium state and move with the same local velocity. While the two-phase model takes into account the fluid and solid phase role in the heat transfer process. Akbari et al. [64] reported that single- and two-phase models predict almost identical hydrodynamic fields but the two-phase models give closer predictions of the convective heat transfer coefficient to the experimental data; nevertheless, the two-phase model overpredicts the enhancement of heat transfer. Corcione et al. [65] and Vanaki et al. [66] observed that nanofluids behave more like single-phase fluids rather than like conventional solid–liquid mixtures. Vanaki et al. [66] confirmed that two-phase modeling has higher heat transfer magnitude in comparison to the homogeneous modeling, but because of contradictory results among the recently conducted numerical works, it is still controversial whether two-phase approach gives more credible results. To the best of the authors' knowledge, almost all the available studies on nanofluid flow over circular/triangular/square type bodies are based on a single-phase modeling approach, and therefore it is adopted here. The dimensional Navier-Stokes equations along with the energy equation governing the nanofluid flow are given by:

$$\nabla.\mathbf{V}^* = 0, \tag{2.1}$$

$$\frac{\partial \mathbf{V}^*}{\partial t^*} + (\mathbf{V}^*.\nabla)\mathbf{V}^* = -\frac{1}{\rho_{nf}}\nabla p^* + \nu_{nf}\nabla^2\mathbf{V}^*, \tag{2.2}$$

$$\frac{\partial T}{\partial t^*} + (\mathbf{V}^*.\nabla)T = \alpha_{nf}\nabla^2 T. \tag{2.3}$$

Here $\mathbf{V}^*$, p^*, T and t^* denote the dimensional velocity vector, pressure, temperature and time respectively, while ρ_{nf}, ν_{nf} and α_{nf} denote density, kinematic viscosity and thermal diffusivity of the nanofluid, respectively.

The nanofluid flow field is characterized by the non-dimensional parameters: Gap height L, Prandtl number Pr, Reynolds number Re, and Peclet number Pe which are defined, respectively by

$$L = \frac{L^*}{A^*}, \quad Pr = \frac{\nu_{nf}}{\alpha_{nf}}, \quad Re = \frac{U_1 A^*}{\nu_{nf}}, \quad Pe = Re \times Pr. \tag{2.4}$$

Here, Re and Pr are defined based on nanofluids. Therefore, the governing equations in dimensionless form can be written as:

$$\nabla.\mathbf{V} = 0, \tag{2.5}$$

$$\frac{\partial \mathbf{V}}{\partial t} + (\mathbf{V}.\nabla)\mathbf{V} = -\nabla p + \frac{1}{Re}\nabla^2\mathbf{V}, \tag{2.6}$$

$$\frac{\partial \theta}{\partial t} + (\mathbf{V}.\nabla)\theta = \frac{1}{RePr}\nabla^2\theta. \tag{2.7}$$

At the plane wall and cylinder surface, no-slip boundary condition is applied. At the far upstream, Couette flow based linear velocity profile $u^* = \frac{U_1 y^*}{A^*}$ is considered. A symmetry boundary condition for longitudinal velocity component along with zero value for the transverse velocity component is prescribed on the top lateral boundary. The Sommerfield radiation condition is applied at the outlet boundary (Maiti [63]). The mathematical form of the boundary conditions used in this study to solve the above equations is shown in the computational domain, presented in Fig. 2.1.

The flow is assumed to start impulsively at a particular value of Re . The converging solution (after the transient state) computed at this Re is considered as an initial solution for the case of other values (lower/higher) of Re. A time-independent stable numerical solution is achieved by advancing the flow field variables through a sequence of short time steps of duration Δt.

2.3.3 Nanofluid Modeling

Water (W) is considered as the base fluid. The nanoparticles are assumed to be uniform in shape and size. In addition, nanofluids are assumed to be homogeneous throughout the simulation. The thermophysical properties of the nanofluids are assumed constant. The material of the nanoparticles is selected as Al_2O_3 and CuO. Thermophysical properties are calculated as follows:

- **Density**: The density of nanofluids is calculated from proposed equation of Pak and Cho [6].

- **Specific heat**: The specific heat of nanofluids is determined using the equation given by Xuan and Roetzel [7] that assumes thermal equilibrium between the base fluid and the nanoparticles.

- **Thermal conductivity**: The thermal conductivity is calculated by the relation proposed by Koo and Kleinstreuer [9], which was later modified by Vajjha and Das [10] as a two terms function (which takes into account the effect of d_{np}, ϕ, temperature T and the properties of the base fluid).

- **Viscosity**: The effective viscosity of nanofluids is predicted by the theoretical model proposed by Masoumi et al. [17]. This model takes care of Brownian motion, temperature of base fluid, the mean nanoparticle diameter, the nanoparticle volume fraction, the nanoparticle density and the base fluid physical properties.

The detailed discussion of the thermophysical properties of nanofluids is made in Chapter–1. (ref. section–1.4). Thermophysical properties of water (ρ_{bf}, $C_{np,bf}$, k_{bf} and μ_{bf}) are calculated at base fluid temperature 300K from the temperature dependent relations given in Etminan-Farooji et al. [4]. Physical properties of nanoparticles (ρ_{np}, $C_{p,np}$ and k_{np}) are taken from Etminan-Farooji et al. [4].

2.4 Numerical Methodology

The computational domain is divided into Cartesian cells. The pressure correction based iterative algorithm SIMPLE (Patanker [32]), based on finite volume method (FVM) with staggered grids, is applied here. A third order accurate QUICK (Quadratic Upstream Interpolation for Convective Kinematics, Leonard [67]) is employed to discretise the convective terms and central differencing for diffusion terms. A fully implicit first order scheme is incorporated to discretise the time derivatives. The pressure link between continuity and momentum is accomplished by transforming the continuity equation into a Poisson equation for pressure. The Poisson equation implements a pressure correction for a divergent velocity field. A detailed discussion of the numerical methodology (staggered

grid, FVM, QUICK and SIMPLE algorithms) used here has been made in the previous chapter (Chapter–1).

Table 2.1: Grid refinement study on Nu_M, C_D, and C_L for the case of $W-CuO$ nanofluid at Pe = 200 for different d_{np} and ϕ. The value within the bracket is the percentage deviation at a grid from that of the grid 550 $\times$ 475.

$d_{np}(\phi)$	Re	Pr	Grid	$\overline{Nu}_M$	C_L	C_D
30 nm (2%)	35.4	5.650	550 $\times$ 475	7.17	1.77	4.09
			800 $\times$ 600	7.24(0.98)	1.77(0.0)	4.1(0.24)
			196 $\times$ 140	6.81(4.91)	1.71(3.39)	3.94(3.67)
30 nm (4%)	33.3	6.001	550 $\times$ 475	7.55	1.83	4.17
			800 $\times$ 600	7.6(0.66)	1.84(0.55)	4.18(0.24)
			196 $\times$ 140	7.25(4)	1.78(2.73)	4.03(3.36)
100 nm (2%)	40.6	4.930	550 $\times$ 475	7.15	1.63	3.93
			800 $\times$ 600	7.2(0.70)	1.63(0.0)	3.94(0.25)
			196 $\times$ 140	6.68(3.9)	1.57(3.68)	3.77(4.07)
100 nm (4%)	46.0	4.348	550 $\times$ 475	7.7	1.51	3.79
			800 $\times$ 600	7.75(0.65)	1.51(0.0)	3.8(0.26)
			196 $\times$ 140	7.33(4.8)	1.46(3.31)	3.65(3.69)

2.4.1 Size of Computational Domain and Consideration of Grid

The distance of the inlet boundary from the front face of the cylinder is taken as $8.5A^*$ while the top lateral boundary lies at $10A^*$ from the upper face of the cylinder. The inlet boundary and height of the top lateral boundary are chosen in such a way so that the influence of the boundary conditions on the wall shear stress is very weak. At the outlet, the convective boundary condition is implemented, which drastically reduces the downstream length of the computational domain and makes the convergence process faster. The outflow boundary lies at a distance of $18A^*$ from the cylinder rear face (Fig. 2.1). Further changes on the boundary distances do not produce any significant changes in the results. The errors due to computational domain size and boundary conditions can be regarded as very small (within a few percent).

A non-uniform grid distribution is considered for distributing uniform grids along the surfaces of the cylinder with expansion factors for the far-fields (away from the surfaces) starting with δ, the first grid point away from the body. A non-uniform grid of size

550×475 with the first and the second number being the number of mesh points in the $x-$ and $y-$ directions, respectively, is considered in the computational domain. The finer grids of size $\delta = 0.004$ are taken near the surfaces of cylinders and the walls to better resolve the gradients near the solid surfaces. It was reported in the previous studies (Maiti [63], [68]) that the refinement on the total number of grids by a factor 4 changed St, C_D, C_L and C_{Lrms} by less than 6% (Table – 1 of Maiti [63]) for different Re and Table – 1 of Maiti [36] for different gap heights). In order to see the effect of grid sizes on the hydrodynamic and heat transfer characteristics due to variation of parameters governing the nanofluid, Table – 2.1 is prepared by varying the grid between 196×140 to 800×600 for $\phi = 2$ and 4%, $d_{np} = 30$ and $100nm$ at $Pe = 200$. The results of 550×475 are compared with those of 800×600 and 196×140, and accordingly the relative percentage error is calculated and written within bracket in Table – 2.1. It is observed from Table – 2.1 that the major differences of these hydrodynamic and heat transfer characteristics occur on the very coarse grid, while the differences of these characteristics are found minor by varying between 550×475 and 800×600. In other words, the error is tending to zero with the increase in number of grid. It may be noted that the computation based on finer grid takes much more time than that on medium grids. Therefore the medium grid 550×475 is considered as a reasonably fine for the calculation domain.

2.4.2 Validation of Numerical Code

The numerical code used in the previous studies (Bhattacharyya and Maiti [69] for single square cylinder and Maiti ([63], [68]) for a single rectangular cylinder) has been used here incorporating the temperature field in the computational domain. This code was validated for the case of (i) a square cylinder without the plane wall for different Re (Fig. 3, Bhattacharyya and Maiti [69]), (ii) a square cylinder confined in a channel (Fig. 4 of Bhattacharyya and Maiti [70]). Thus, the previously published results also show the validity of the used code for this work.

The numerical code for the present case of heat transfer has also been validated with Sharma and Eswaran [3] for the channel confined flow at different Re and blockage ratio

Table 2.2: Comparison of present $\overline{Nu}_M$ and St with that obtained by Sharma and Eswaran [3]. Here $S \rightarrow$ Sharma and Eswaran [3] results, $P \rightarrow$ Present results.

		constant temperature				uniform heat flux			
		B/H=20%		B/H=50%		B/H=10%		B/H=20%	
Re		P	S	P	S	P	S	P	S
50	St	-	-	-	-	0.18	0.18	-	-
	$\overline{Nu}_M$	3.49	3.57	4.84	4.93	3.81	3.82	3.93	3.94
100	St	0.24	0.25	0.51	0.53	0.22	0.22	0.246	0.24
	$\overline{Nu}_M$	4.57	4.67	6.4	6.44	5.04	5.03	5.03	5.05
150	St	0.21	0.21	0.51	0.53	0.2	0.19	0.2	0.19
	$\overline{Nu}_M$	5.5	5.53	7.41	7.47	5.89	5.89	5.82	5.81

B/H. The results obtained by Sharma and Eswaran [3] along with our results are presented in Table – 2.2 for the case of constant temperature and for the case of a cylinder with uniform heat flux. The Table shows an excellent match between the two results in $\overline{Nu}_M$ and St computations. Although, it is noted that the maximum deviation in St is found 4.7% for the case of constant temperature and 5.26% for uniform heat flux.

Table 2.3: Comparison of present heat transfer coefficient h_1 with that obtained by Etminan-Farooji et al. [4]. Here $EF \rightarrow$ Etminan-Farooji et al. [4] results, $P \rightarrow$ Present results, $RPE \rightarrow$ Relative Percentage Error, $E \rightarrow EG : W$, $W \rightarrow$ Water.

Nanofluid	Pe = 25			Pe = 50			Pe = 100			Pe = 200		
	EF	P	RPE	EF	P	RPE	EF	P	RPE	EF	P	RPE
$Al_2O_3, 2\%, 30nm^W$	1.59	1.56	1.89	2.1	2.05	2.38	2.8	2.7	3.57	3.85	3.72	3.7
$Al_2O_3, 4\%, 30nm^W$	1.67	1.67	0.00	2.2	2.17	1.36	2.92	2.86	2.05	4.1	3.92	4.4
$CuO, 2\%, 30nm^W$	1.6	1.57	1.90	2.17	2.07	4.61	2.75	2.71	1.45	3.8	3.7	2.63
$CuO, 4\%, 30nm^W$	1.68	1.73	2.98	2.27	2.25	0.88	3.0	2.97	1.00	4.01	3.9	2.74
$CuO, 2\%, 100nm^W$	1.57	1.53	2.55	2.05	1.99	2.93	2.71	2.64	2.58	3.7	3.57	3.51
$Al_2O_3, 2\%, 30nm^E$	0.89	0.9	1.12	1.13	1.11	1.77	1.49	1.43	4.03	1.9	1.86	2.10
$Al_2O_3, 4\%, 30nm^E$	0.93	0.94	1.08	1.19	1.18	0.84	1.56	1.52	2.56	2.01	1.97	1.99
$Al_2O_3, 2\%, 100nm^E$	0.85	0.83	2.35	1.09	1.04	4.59	1.4	1.36	2.86	1.82	1.77	2.75
$Al_2O_3, 4\%, 100nm^E$	0.89	0.92	3.37	1.15	1.17	1.74	1.52	1.49	1.97	2.02	1.95	3.47
$CuO, 2\%, 30nm^E$	0.89	0.9	1.12	1.12	1.11	0.89	1.41	1.42	0.71	1.97	1.9	3.55
$CuO, 4\%, 30nm^E$	0.94	0.96	2.13	1.21	1.22	0.83	1.58	1.56	1.27	2.14	2.05	4.21
$CuO, 2\%, 100nm^E$	0.85	0.82	3.53	1.1	1.06	4.55	1.4	1.37	2.14	1.82	1.78	2.20
$CuO, 4\%, 100nm^E$	0.9	0.92	2.22	1.17	1.19	1.71	1.55	1.52	1.29	2.01	2.0	0.50

The code is also validated for the case of nanofluid modelling. The computed heat transfer coefficient (h_1) is compared with that obtained by Etminan-Farooji et al. [4] for

different $\phi(= 0\% - 4\%)$, particle materials (Al_2O_3 and CuO) and base fluid type (water (W) and a 60% ethylene glycol with 40% water ($EG : W$) mixture by mass) and size of nanoparticles ($30nm$ and $100nm$) at different Pe, ranging from 25 to 200. The comparison is presented in Table – 2.3. As can be seen in Table – 2.3, the maximum percentage differences of h_1 of the present calculation from those of Etminan-Farooji et al. [4] is 4.59% (occurs at $EG : W - Al_2O_3$ at $2\%(100nm)$ for $Pe = 50$). Relative percentage error is around 1% in most of the cases. The results show the excellent agreement of the present result with those of previous results in heat transfer coefficient over the whole range of Pe.

2.5 Results and Discussion

The numerical simulations are made with the choice of following parameter value:

- **Diameter of the nanoparticle (d_{np})**: $30nm$, $50nm$ and $100nm$.

- **Concentration (ϕ)**: 2%, 4% and 6%. Masoumi et al. [17] mentioned that the equation (1.9) is valid for $\phi < -b/a$, where a and b are defined in equation (1.11). In the present calculation the values of d_{np} are taken as $30, 50$ and $100nm$, accordingly $-b/a$ value registers $6.276, 6.912$ and 7.415% respectively. Therefore, the value of ϕ can be considered up to 6%. The variations of k_{nf}/k_{bf} and μ_{nf}/μ_{bf} with ϕ for $d_{np} = 30, 50$ and $100nm$ are plotted in Fig. 2.2. As seen in Fig. 2.2, both thermal conductivity ratio and viscosity ratio increase with the increase of nanoparticle volume fraction (ϕ). An anomaly behaviour of μ_{nf} with ϕ while changing ϕ from 5 to 6% for the case of $d_{np} = 30nm$ may be noted here.

- **Peclet number (Pe)**: Pe = 25, 50, 100, 150, 200, 300 and 400.

- **Prandtl number (Pr)**: Here Pr is defined based on the nanofluid characteristics, different for different values of d_{np} and ϕ as well as materials. Pr is ranged in 4.414 - 19.86.

- **Reynolds number** (Re): For a particular fluid (fix Pr), Pe variation results in the variation of Re (= 13 - 96.6). Here the flow is steady for all the cases since the critical Re at which the cylinder placed at a gap height $0.5A^*$ sheds vortices is 125 (Bhattacharya and Maiti [21]).

- **Gap height** (L): 0.1, 0.25, 0.5, 1.0, 1.5, 2.0, 3.0 and 4.0.

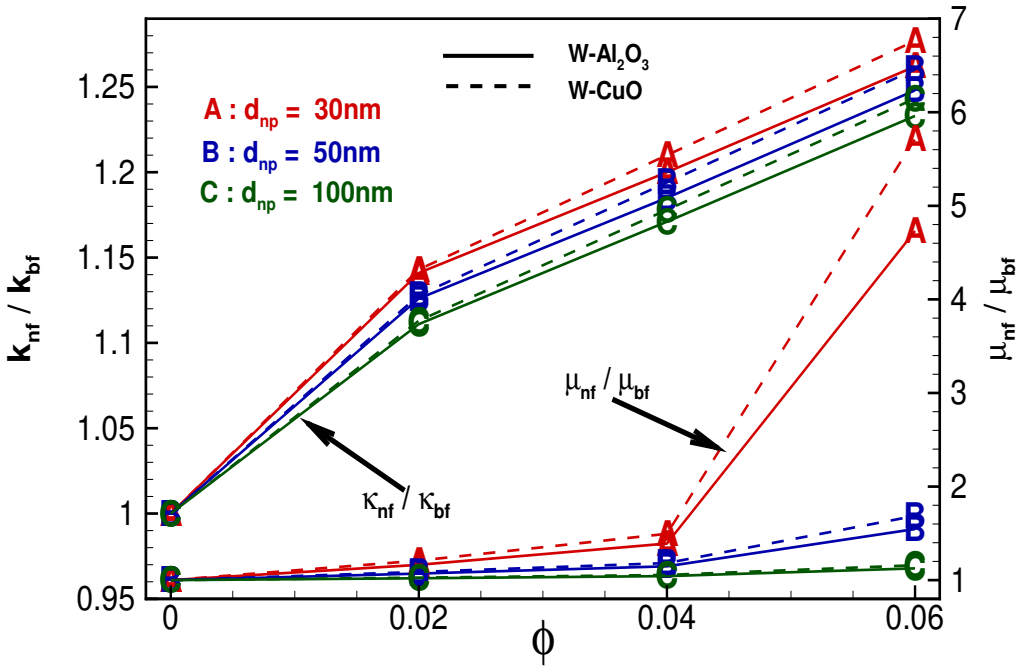

Figure 2.2: Ratio of thermal conductivity and viscosity of both the nanofluids ($W-CuO$ and $W-Al_2O_3$) at different d_{np} and ϕ.

2.5.1 Fluid Flow Analysis

The instantaneous flow fields are presented for $W-CuO$ nanofluid with d_{np} = $30nm$ and ϕ = 4% at Pe = 25 and 400. Numerical flow visualization in Figs. 2.3(a) and 2.3(b) suggests that there is no shedding of vortex/vortices from the cylinder, and the flow is found to be completely steady since the Re = 4.1 is much smaller than the critical Re = 125. Positive shear layer occupies the most of the surface of the cylinder and the negative shear layer lies only on top of the cylinder. With the increase of Pe (*i.e.*, increase of Re for fixed nanofluid) the lower shear layer is slightly detached from the rear face and the

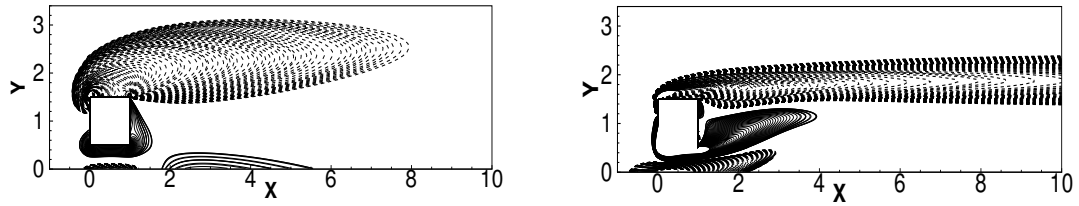

(a) Pe = 25 (b) Pe = 400

Figure 2.3: Vorticity contours of $W - CuO$ nanofluid with ϕ = 4% and d_{np} = 30 nm at different Pe. (a) Pe = 25 and, (b) Pe = 400.

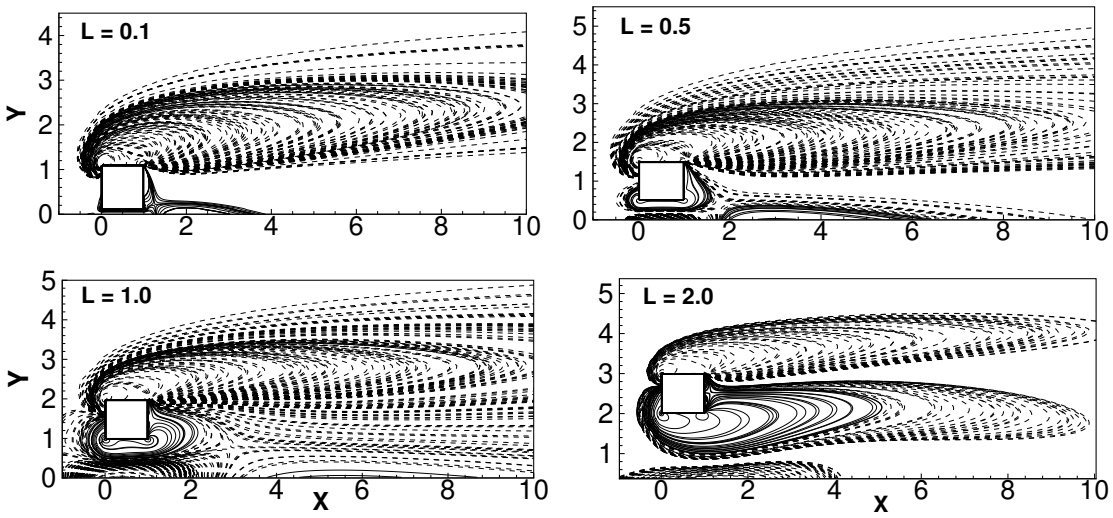

Figure 2.4: Vorticity contours of $W - CuO$ nanofluid with ϕ = 4 % and d_{np} =50 nm at Pe = 25 for different gap-heights.

upper shear layer is convected downstream without shedding. The layers of the cylinder are not interacting each other. Only a weak interaction between the wall negative shear layer and cylinder positive shear layer takes place at the cylinder's position.

The effect of gap height on the flow field is discussed based on the vorticity contour presented in Fig. 2.4 at Pe = 25 with d_{np} = 50 nm and ϕ = 4%. For a gap height larger than 0.5, the above interaction between the cylinder and wall diminishes and at L = 2.0, no more interaction is observed and the lower shear layer of the cylinder takes its proper form. However, at a lower L = 0.1, the lower shear layer of the cylinder is almost vanished due to a very negligible flow through the gap . Though the increment of the gap height is mechanically similar to that of Re, the flow is found to be steady even at L = 4.0.

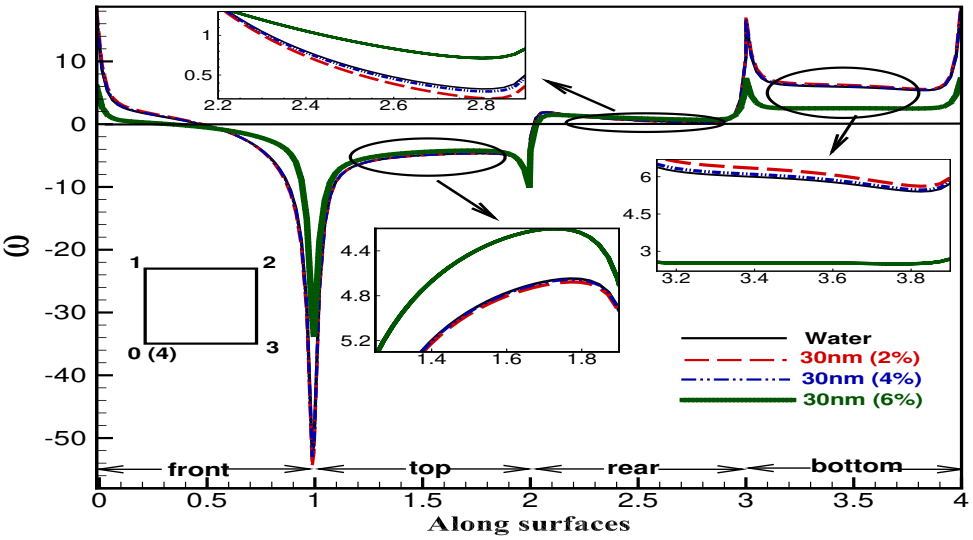

(a)

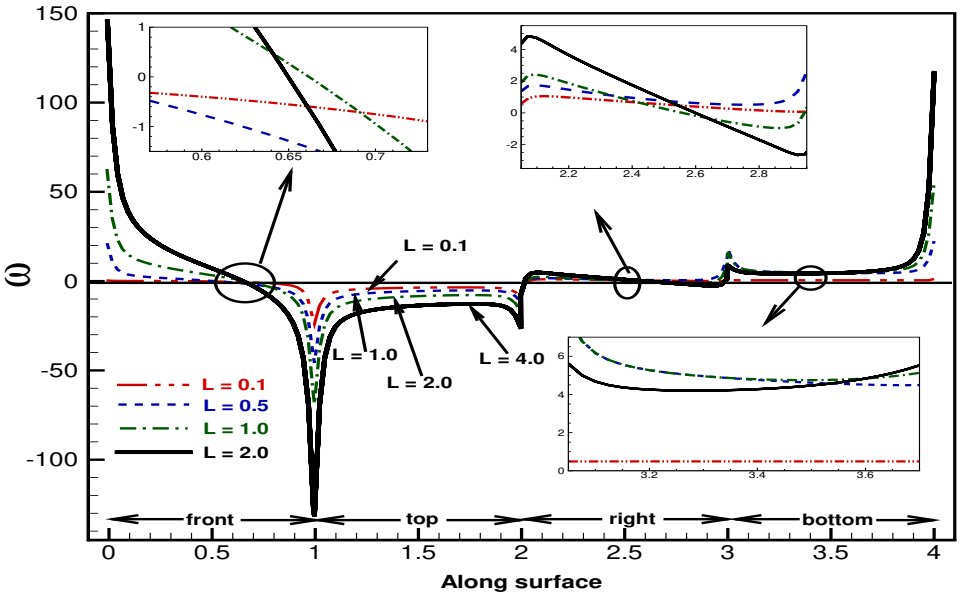

(b)

Figure 2.5: Wall vorticity (ω distribution around the cylinder for $W - CuO$ nanofluids for (a) different ϕ at d_{np} = 30 nm, Pe = 100 and L = 0.5; (b) different L with ϕ = 4 %, d_{np} = 50 nm and Pe = 25.

The effect of nanoparticle concentration (ϕ) on the vorticity generated at the cylinder surfaces is exemplified based on the wall vorticity distribution along the surfaces for different ϕ = $0, 2, 4$ and 6% at d_{np} = $30nm$ and Pe = 100 for $W - CuO$ (Fig. 2.5(a)) nanofluid. As seen the wall vorticity decreases sharply from the front-bottom corner

(point-0) and reaches to minimum value (first minima) at the point-1. Thereafter, it rapidly increases along the top face and remains almost steady in most part of the top face, followed by sudden decrease at the end of this face providing its second minima. Again it started increasing to reach a constant (close to zero-value) on the rear face, and then reaches to a second maxima (first maxima being at the point-0) at the point-3. Finally, after a sudden decrease, it maintains a constant positive value (depending on ϕ-value) and then reaches to a third maxima at the point-4. Overall, the sharpest variation in ω can be seen at the front-top corner, pointing to a large variation in the velocity. The global minimum and maximum of vorticity register at the point-1 and point-0, respectively. Moreover, sharing of positive and negative vorticity around the cylinder surfaces is almost $50 - 50$, but the strength of negative vorticity is more than that of positive vorticity, which may be due to the presence of wall on the side on which positive vorticity generated. From the variation of wall vorticity on the front face, it may be deduced that velocity variation along this face is less for ϕ = 6% than that for ϕ = $0 - 4\%$. Front stagnation is shifted very close to the bottom of the front face for the case of ϕ = 6%. From the closer view of top, rear and bottom faces, it can be noted that the effect of ϕ on the negativity/positivity in ω around the top/bottom face is negligible while changing ϕ from 0 to 4%, however the numerical value of ω on these faces decreases with increase in ϕ from 4 to 6%. These observations on the wall vorticity can be justified from the increased viscosity of the nanofluid. Though the value of ω on the rear face is small compared to other faces, the effect of ϕ on ω can be noticed here.

The effect of gap height (L) on ω can be seen in Fig. 2.5(b). As seen, the magnitude of ω is directly proportional to L since the increase of L is equivalent to expose the cylinder to higher velocity region under the present flow condition. A change of sign of ω on the rear face at a higher L may be noted here. The front stagnation point moves towards the bottom side as the cylinder moves close to the plane wall. A similar effort was made for $W - Al_2O_3$ nanofluid, not presented here, and the effect of nanoparticle material (Al_2O_3, CuO) on the vorticity around the cylinder surfaces is almost negligible.

As seen in Fig. 2.6, the gap flow (between the cylinder's lower face and the wall)

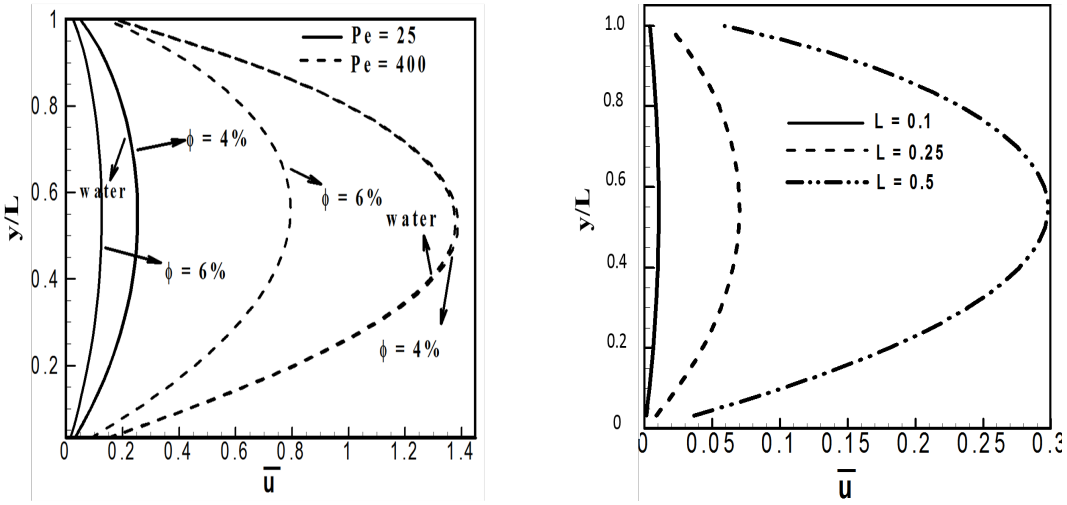

(a) (b)

Figure 2.6: Horizontal velocity profile along the vertical direction (y) at the exist position ($x^* = a$) of the gap between the cylinder's lower face and the wall for (a) different Pe and ϕ at d_{np} = 30 nm and L = 0.5; (b) different L with d_{np} = 50 nm, ϕ = 4% at Pe = 25.

becomes stronger with the increase of Pe and/or L and the velocity overshoots (jet action). Velocity profile takes its parabolic form in the gap flow. When the contour is very close to the wall (Fig. 2.6), the gap flow is found almost stagnant. Therefore, the heat transfer from the cylinder's lower face is expected to be more for the case of the presence of the wall, in comparison to that of the absence of the wall. It is evident from Fig. 2.6(a) that because of high viscosity at ϕ = 6 %, the flow becomes slower in comparison to the counterpart in ϕ = 0-4 %.

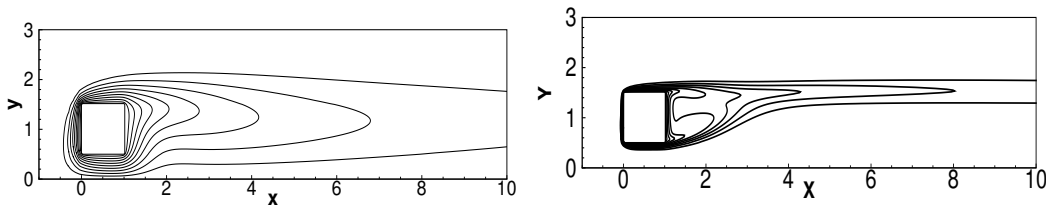

(a) (b)

Figure 2.7: Isotherms contours of $W - CuO$ nanofluid with ϕ = 4% and d_{np} = 30 nm at different Pe. (a) Pe = 25 and, (b) Pe = 400.

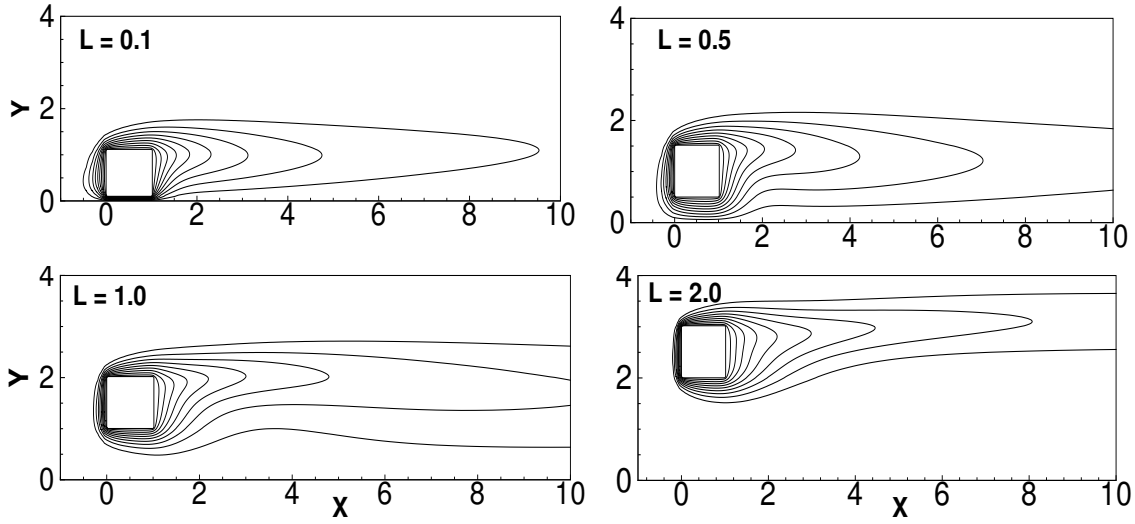

Figure 2.8: Isotherms of $W - CuO$ nanofluid with ϕ = 4 % and d_{np} =50 nm at Pe = 25 for different gap-height L.

2.5.2 Temperature Distribution

Isovorticity contour around the cylinder for $W - CuO$ is presented for different P in Fig. 2.7 and L in Fig. 2.8. As both vorticity and thermal energy are being transported by the flow in the wake, the contour lines of vorticity and temperature have similar features (Figs. 2.3 and 2.7; Figs. 2.4 and 2.8). Moreover, the equation of temperature is similar to that of vorticity. The temperature distributions show that the heat is distributed within the flow field as isolated warm blobs. These warm blobs are captured within the vortex structures and advected downstream without being influenced too much by mixing with their surroundings. The thermal boundary layer growth starts almost symmetrically from the front face of the cylinder and becomes thicker toward the rear. A higher induced temperature gradient in the vicinity of the cylinder surface is visible from the contours. Except for L = 0.1 in Fig. 2.8, the thermal boundary layer on the front surface is thinner and produces a higher heat transfer compared to the other surfaces. Temperature contours are clustered near the front top and bottom corners, indicating that convective cooling of the cylinder is maximum in these regions, while the convective cooling along the rear face is expected to be low. This is because of the circulation generated behind the cylinder, i.e., counter-rotating cell sweeps the heated fluid away from the wall at a lower rate.

Apparently, the thickness of thermal boundary is reduced at a higher Pe and L. At lower L = 0.1, the hot cylinder is very close to the cold wall, as a result conductive heat transfer through the wall is expected to occur, indicating higher heat transfer from the bottom of the cylinder.

2.5.3 Heat Transfer Characteristics

Fig. 2.9 plots the local Nusselt number ($\overline{Nu}$) distribution around the cylinder surfaces for $W - Al_2O_3$ nanofluid for different ϕ (Fig. 2.9(a) at d_{np} = 30 nm, Pe = 100 and L = 0.5) and L (Fig. 2.9(b) at d_{np} = 50 nm, ϕ = 4 % and Pe = 25). $\overline{Nu}$ attains local maxima at the four corners of the cylinder since the thermal boundary layer at these points is thinnest, having a higher thermal gradient. As seen in Fig. 2.9, the front face has a larger heat transfer rate compared to other faces as the incoming cold fluid directly impacts on it. The variation of $\overline{Nu}$ along the rear face is almost constant since the originating weak vortex rotates on this surface without being shed (Fig. 2.3). Apparently, the $\overline{Nu}$ distributions around the top (Faces 1-2) and bottom (Faces 4-3) faces are not in symmetry since the incident flow is not symmetric. The heat transfer from the cylinder is clearly enhanced due to the addition of nanoparticles in the base fluid (Water) and $\overline{Nu}$ increases with ϕ for ϕ = 2 % to 4 %. The addition of nanoparticles is more effective on the front and bottom faces of the cylinder. Surprisingly, heat transfer is found to decrease with the increase of ϕ from 4 % to 6 % and the $\overline{Nu}$-distribution at ϕ = 6 % is close to that without nanoparticles. The increase of ϕ in the base fluid enhances the μ_{nf} as well as k_{nf}. It is plausible that the role of thermal conductivity on the heat transfer is opposite to that of viscosity. As observed in Fig. 2.2, the viscosity at this d_{np} is highly sensitive to ϕ while changing ϕ from 4 % to 6 %.The rate of increment for thermal conductivity is around 1.05 for both cases: ϕ = 2% to 4% and 4% to 6%, while this rate for viscosity is 1.195 and 3.40 for ϕ = 2% to 4% and 4% to 6%, respectively (Fig. 2.2). Therefore, it shows that for the case of ϕ = 4 % to 6% at d_{np} = 30 nm, Nusselt number increases nominally due to the increase in κ_{nf} , while decreases marginally due to the μ_{nf} (by reducing the speed of incident velocity). It is observed from Fig. 2.9(b) that $\overline{Nu}$-distributions at different

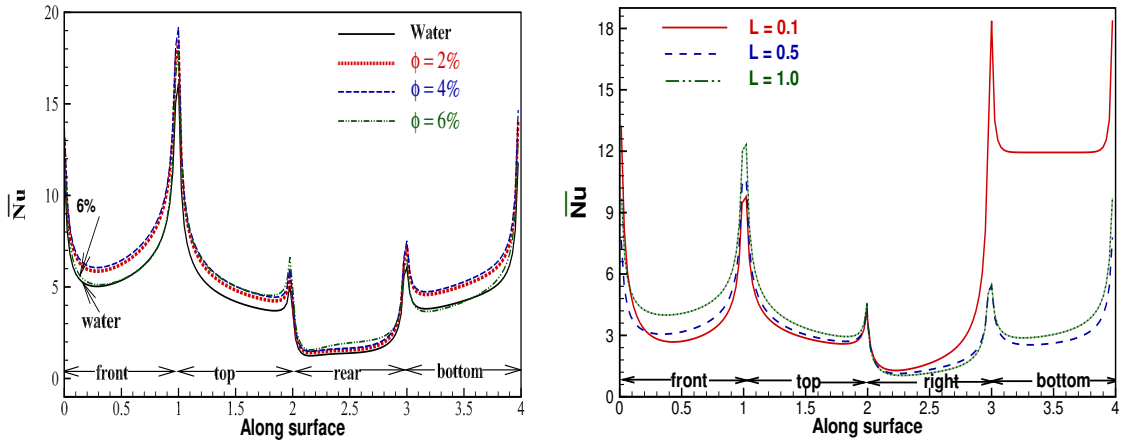

(a) (b)

Figure 2.9: Local Nusselt number ($\overline{Nu}$) distribution around the heated cylinder for $W - Al_2O_3$ nanofluids for (a) different ϕ at d_{np} = 30 nm and Pe = 100 and L = 0.5; (b) different L with ϕ = 4%, d_{np} = 50 nm and Pe = 25.

L are qualitatively similar to those at L = 0.5, but quantitatively different; that is, the bottom face produces maximum heat transfer at the lowest L = 0.1. In this bottom face, the Nusselt number is almost constant in the major portion since the gap flow is found minimum at L = 0.1 (Fig. 2.6(b)). Higher $\overline{Nu}$-value on this face is due to the fact that the bottom face is very close to the cold plane wall. As a result, the distance between T_w and T_0 becomes minimum, and the conductive heat transfer through the plane wall takes place. Moreover, at this L = 0.1, the maximum variation in $\overline{Nu}$-distribution is observed on the face (rear) where the $\overline{Nu}$-variation is minimum at other L. For L = 0.5, the $\overline{Nu}$ at each point on the surfaces increases with L, because of the higher incident velocity.

Face-averaged Nusselt numbers (front face: $Nu_{avg}-f$, rear face: $Nu_{avg}-r$, top face: $Nu_{avg}-t$ and bottom face: $Nu_{avg}-b$) as a functions of Pe, ϕ and d_{np} are presented in Fig. 2.10. As seen in Fig. 2.9 at any particular parameters value, front face shows maximum heat transfer while rear face dissipate minimum heat transfer, among all faces. Though the flow around the cylinder is asymmetric (due to incident shear flow and presence of the wall) heat transfers from bottom and top faces are almost equal for $Pe \geq 100$. At lower Pe (< 100), bottom face shows slightly lower heat transfer than that from the top face. As high as Pe, Re becomes higher which leads to accelerate the gap flow between the

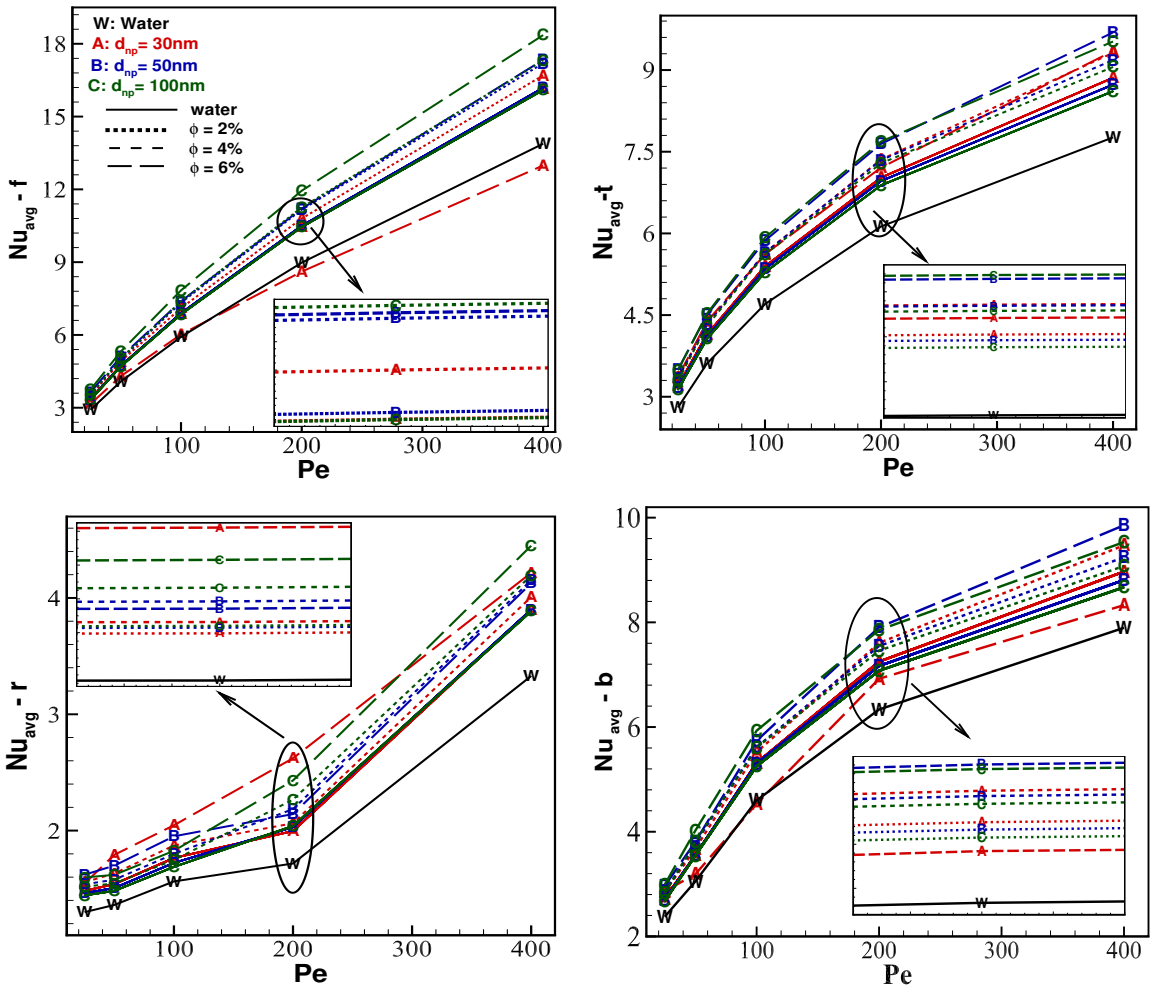

Figure 2.10: Face average Nusselt number (Nu_{avg}) along the surfaces of the cylinder as a function of Pe, ϕ and d_{np} for $W - Al_2O_3$ nanofluid. Here subscripts f, r, t and b stand for front, rear, top and bottom, respectively.

bottom face and the wall. $Nu_{avg} - f$ is almost linearly increasing with Pe, while effect of Pe on $Nu_{avg} - r$ is found more at higher Pe in comparison to lower Pe. Shape of all the curves along the top face is similar to their respective curves along the bottom face. It is interesting to note that addition of nanoparticles is not guaranteed to increase the heat transfer from all faces. Here, Nu from the front face for the case of d_{np} = $30nm$ and ϕ = 6% is found less than that for the pure water case. The speed of incident cold fluid on the front face is the major constituent of total heat transfer from this face. Here, for the case of d_{np} = $30nm$ and ϕ = 6% ($Re = 21.55$) the fluid velocity is lower than that of pure

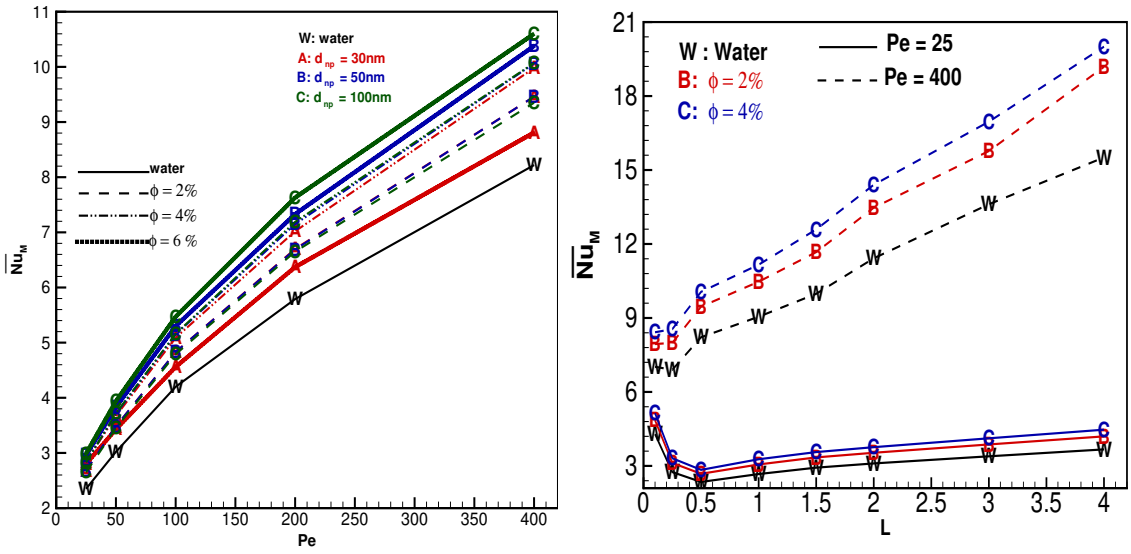

(a) (b)

Figure 2.11: Mean Nusselt number ($\overline{Nu}_M$) across the cylinder as a function of (a) Pe for different ϕ and d_{np} ; (b) L for Pe = 25, 400, ϕ = 0, 2, 4 % at d_{np} = 50 nm.

water ($Re = 65.15$) at Pe = 400. In fact the value of Re for the curve corresponding to d_{np} = 100nm with ϕ = 6% is 88.4. Nevertheless, overall heat transfer ($\overline{Nu}_M$) from the cylinder is found to be more for nanofluids (Fig. 2.11). Influences of ϕ and d_{np} on the $Nu_{avg} - f, Nu_{avg} - r, Nu_{avg} - t, Nu_{avg} - b$ is noticeable at higher Pe and the difference between the curve -W with other curves increases with the increase of Pe. The curves corresponding to highest nanoparticle concentration (ϕ) lie above the respective curves for the lower ϕ (Fig. 2.10).

The heat transfer across the surfaces of the heated cylinder is discussed based on the mean Nusselt number $\overline{Nu}_M$. Effects of ϕ , d_{np} and Pe on Nu_M are presented in Fig. 2.11(a), while Fig. 2.11(b) presents $\overline{Nu}_M$ as a function of L at Pe = 25 and 400 for $W - Al_2O_3$. As seen in 2.11(a), all the $\overline{Nu}_M$ curves are qualitatively similar, not crossing each other. For a particular combination of ϕ and d_{np} , i.e., for a fixed value of Pr, the $\overline{Nu}_M$ increases with Pe. Here, increase of Pe is due to the increase in Re for a particular curve. Therefore, the increment in $\overline{Nu}_M$ due to Pe is attributed to the increased intensity of the incident velocity. Effects of d_{np} and ϕ on the heat transfer rate are found to be more at a higher Pe (i.e), at a higher Re. The case with d_{np} = 100 nm

and ϕ = 6 % maximizes the heat transfer enhancement from the cylinder at all Pe since the value of Re is more at all Pe for this case compared to other cases. At higher Re, Brownian motion has an important role in heat transfer (Ebrahimnia-Bajestan et al. [12]). With the increase of ϕ , $\overline{Nu}_M$ increases at all Pe for d_{np} = 50 nm and 100 nm. As noted in Fig. 2.11(a), only for the case of d_{np} = 30 nm, $\overline{Nu}_M$ is found to decrease with increase of ϕ from 4 to 6%. Though there is a large increase in μ_{nf} than the increase in κ_{nf} at ϕ = 6% and d_{np} = 30 nm (Fig. 2.2), all nanofluids considered here can be used as coolants compared to the base fluid. The increment in Nu_M (from the value of its base fluid case) is about 6.57 % to 29.02% depending on the values of d_{np} , ϕ and Pe. Therefore, the increased number of nanoparticles in the base fluid where the κ_{nf} is more effective (than μ_{nf}) on heat transfer is responsible for the improved values of $\overline{Nu}_M$. Again at ϕ = 6% a reverse trend in $\overline{Nu}_M$ with d_{np} is observed since Pr decreases with the increase of d_{np} at much faster rate compared to ϕ =2% and 4% cases. Note that the present results (based on variations of Pe, ϕ and d_{np}) are analogous to Ebrahimnia-Bajestan et al. [12]. To discuss the effect of nano-materials on the heat transfer, a similar effort was made for the case of $W - CuO$, not presented here. The $\overline{Nu}_M$ follows similar trends of its respective curve plotted in Fig. 2.11(a) as the Pe increases. However, the presence of the CuO nanoparticle in water is slightly more pronounced on the heat transfer from the cylinder compared to that of Al_2O_3 nanoparticle presence. For example, at Pe = 200, the increment in $\overline{Nu}_M$ of $W - CuO$ (from the value of base fluid water case) is about 7.18% to 21.24%, while this value for $\overline{Nu}_M$ of $W - Al_2O_3$ is about 6.57% to 20.20%. A similar effect on the $\overline{Nu}_M$ is also observed due to the variations of d_{np} and ϕ . As depicted in Fig. 2.11(b), the $\overline{Nu}_M$ variation is not uniform with L, that is, with the increase of L, the $\overline{Nu}_M$ starts to decline and becomes minimum at L = 0.5 and 0.25 for Pe = 25 and 400, respectively, and thereafter increases with L. However, for the case of Pe = 25, $\overline{Nu}_M$ could not reach the value as the lowest L = 0.1 even at a gap height L = 4.0, because at this lower Pe, the value of Re is so small (falls in (4,4.65)) that the change of the gap height would not give noticeable variation in the incident velocity. This variation of $\overline{Nu}_M$ with L can be observed at higher Pe (i.e., Re) and the heat transfer is remarkably enhanced at

higher L.

An explicit form of functional dependency of $\overline{Nu}_M$ on Pe and L is presented using the least square method based on the computed values in Table – 2.4 for $W - Al_2O_3$ nanofluid with d_{np} = 50 nm. Numerical values written in first bracket against each relation are the residual sum of squares (RSS) and coefficient of determination (R^2). An R^2 between 0 and 1 indicates the extent to which the dependent variable is predictable. An R^2 of 0.99 means that 99% is predictable. A small RSS indicates a tight fit of the model to the data. Among other possible functions, using this method the one which gives minimum RSS and maximum R^2 is chosen here. As seen in Table – 2.4, R^2 is very close to 1.0 while RSS is less, indicating that the proposed relations (especially $\overline{Nu}_M = \overline{Nu}_M(Pe)$) are the best fitted relations. It is reconfirmed in the equations $\overline{Nu}_M = \overline{Nu}_M(Pe)$ that the $\overline{Nu}_M$ increases with Pe, but the increasing/decreasing of $\overline{Nu}_M = \overline{Nu}_M(L)$ is dependent on Pe. When the equations as well as their coefficients are compared to each other, all the observations made so far on the dependency of $\overline{Nu}_M$ on Pe, ϕ and L (based on its graphical representation) are consistent with these explicit functional forms of $\overline{Nu}_M$.

Table 2.4: Explicit form of functional dependency of $\overline{Nu}_M$ on Pe and L for $W - Al_2O_3$ nanofluid with d_{np} = 50 nm. Residual sum of squares (RSS) and coefficient of determination (R^2) are written in first bracket against each relation.

$\phi \downarrow$	$\overline{Nu}_M = \overline{Nu}_M(Pe)$
2%	$\overline{Nu}_M = (1.153Pe + 1.579)^{1/2}$ (0.0047,0.9998)
4%	$\overline{Nu}_M = (1.239Pe + 1.734)^{1/2}$ (0.0027,0.9999)
6%	$\overline{Nu}_M = (1.571Pe + 1.924)^{1/2}$ (0.009,0.9997)
$Pe \downarrow$	$\overline{Nu}_M = \overline{Nu}_M(L)$
25	$\overline{Nu}_M = 3.599L^{-0.0141/L}$ (2.274, 0.4089)
400	$\overline{Nu}_M = 2.966L + 8.189$ (0.4010,0.9966)

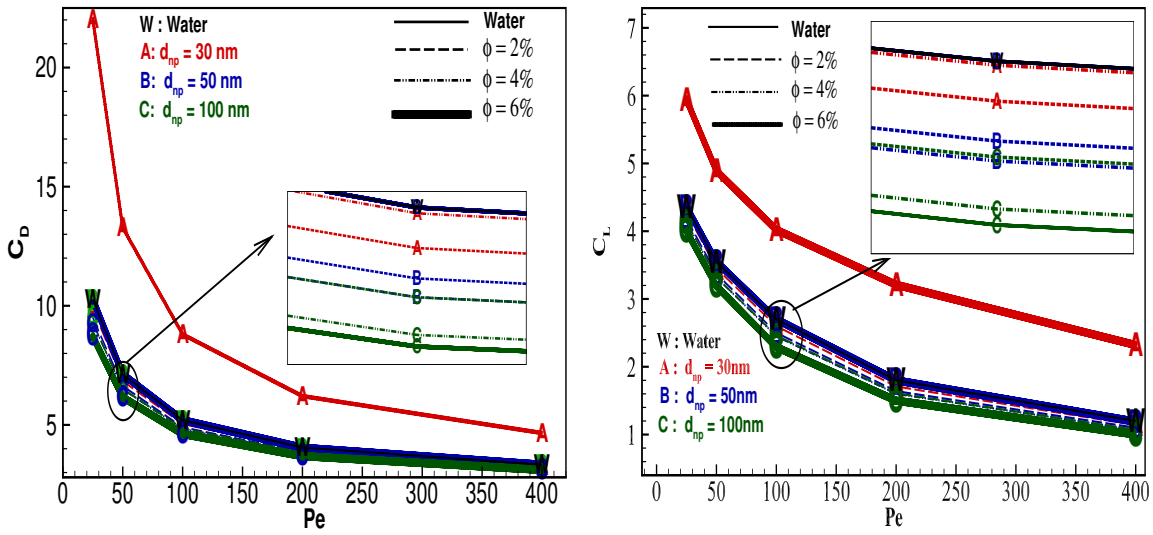

(a) (b)

Figure 2.12: Variation of (a) C_D ; (b) C_L with Pe for $W - Al_2O_3$ nanofluid at different d_{np} and ϕ.

2.5.4 Hydrodynamic Characteristics

The dependence of the hydrodynamic coefficients (Drag coefficient C_D and lift coefficient C_L) on Pe, d_{np} and ϕ is analyzed with the help of Fig. 2.12(a) (for C_D) and Fig. 2.12(b) (for C_L). The C_D at different d_{np} and ϕ shows qualitatively similar behavior with a change in Pe, monotonically decreasing with the increase of Pe. The C_D dependence on Pe becomes weaker at a higher range of Pe. Maiti [63] reported that C_D decreases with the increase of Re at a lower range of Re ($\leq$ 200). Here the maximum value of Re among all the cases is around 100. Note that ϕ have some effect on C_D only at the lower range of Pe. Also, the curve corresponding to ϕ = 6% with d_{np} = 30 nm shows much more higher value of C_D to the cylinder at all Pe. As in this case Pr = 18.85, the Re registers much lower value where viscous effect becomes more significant. All C_L curves show qualitatively similar behavior with changing Pe. Like C_D , C_L also decreases with the increase of Pe, but the variation is found continuous over the whole range of Pe. Moreover, the effects of ϕ and d_{np} on C_L are pronounced over the whole range of Pe. Essentially the curve corresponding to d_{np} = 30 nm (6%) in Fig. 2.12(b)

also distinctly appears among all other curves and lift coefficient of the cylinder becomes much more for the case of ϕ = 6% with d_{np} = 30 nm. For fixed nanofluid (for given material, ϕ and d_{np}), the present observation on effect of Re (Due to variation of Pe) on C_L is analogous to that of Maiti [63]. Apparently, hydrodynamic forces for $W - CuO$ nanofluid are found comparable to the respective force for $W - Al_2O_3$ nanofluid at each value of d_{np} and ϕ , therefore not presented here. Also, the variations of hydrodynamic forces with the gap height for the present case of nanofluid are qualitatively similar to those (C_D increases uniformly with L while C_L is not uniform with L) for the case of without nanofluid reported in the previous study (Maiti [68]), consequently it is avoided here.

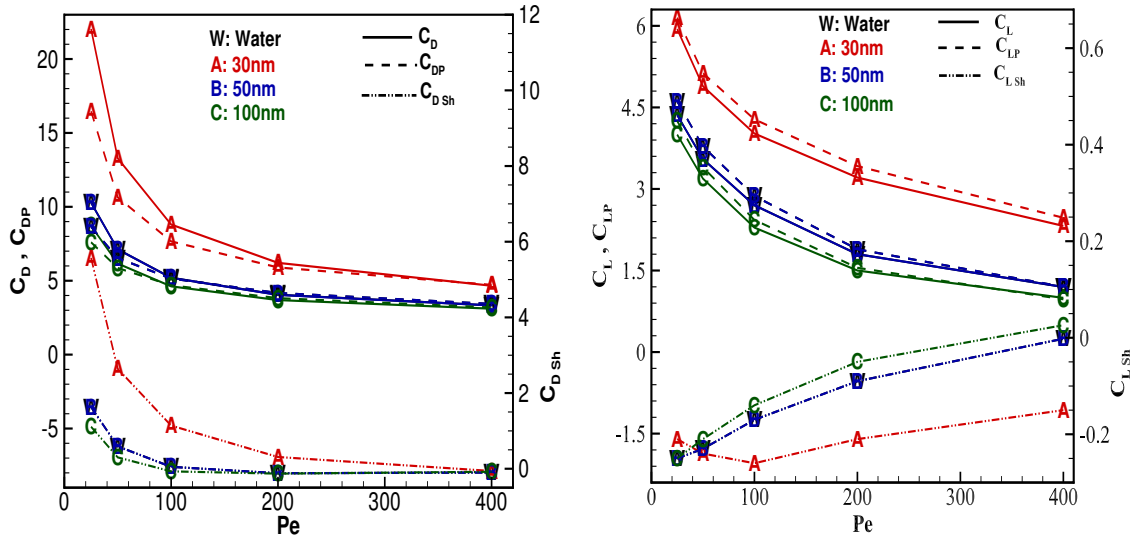

(a) (b)

Figure 2.13: (a) Comparison of drag coefficients (C_D) with their counterpart due to pressure (C_{DP}) and due to shear (C_{DSh}); (b) comparison of lift coefficient (C_L) with their counterpart due to pressure (C_{LP}) and due to shear (C_LSh) at different Pe for $W - Al_2O_3$ nanofluid with ϕ = 6 %.

The role of viscosity on the hydrodynamic forces at ϕ = 6% is discussed by presenting the drag and lift coefficients due to pressure and shear (Figs. 2.13(a) and 2.13(b)) for the case of $W - Al_2O_3$ and d_{np} = 30, 50 and 100 nm. Values for the base fluid are also presented. As seen in Figs. 2.13(a) and 2.13(b), the solid curve appears close to the

respective dashed curve, indicating that the pressure force is the major constituent of the overall hydrodynamic forces. Curves corresponding to d_{np} = 30 nm appear distinctly, and it is immediately evident that viscous forces for both lift and drag coefficients have an appreciable contribution to the total hydrodynamics forces at lower Pe, remarkably for d_{np} = 30 nm. To assess the heat transfer enhancement of the heated cylinder together

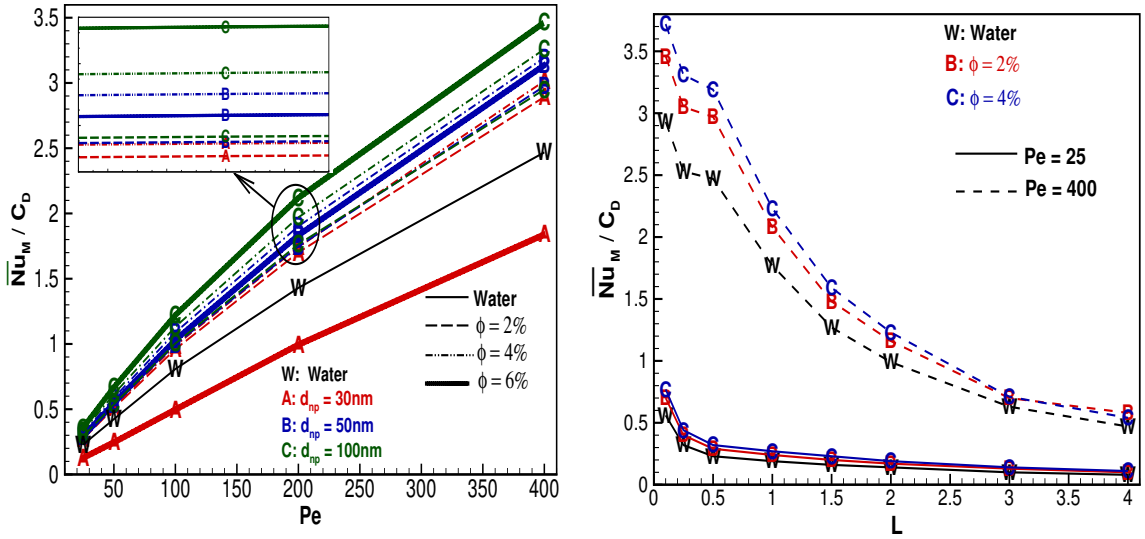

(a) (b)

Figure 2.14: Ratio of Nusselt number to drag coefficient (Nu_M/C_D) of the cylinder for different values of (a) Pe, ϕ and d_{np} , for L = 0.5; (b) L with Pe = 25 and 400; ϕ = 0, 2, 4 %.

with its drag coefficient reduction/increment due to the variation of Pe and L in nanofluid flow, Fig. 2.14 is presented for $\overline{Nu}_M/C_D$ against Pe (Fig. 2.14(a)) and L (Fig. 2.14(b)). Eventually, the ratio increases with Pe in Fig. 2.14(a) since $\overline{Nu}_M$ increases while C_D decreases with the increase of Pe. As seen in Fig. 2.14(a), the curve for d_{np} = 100 nm with ϕ = 6% appears at the top of all curves, while the curve for d_{np} = 30 nm with ϕ = 6% appears at the bottom, even below the curve-W. Unlike Fig. 2.14(a), the ratio decreases with L at both Pe, and at a lower Pe the variation becomes negligible at higher L (> 1.5). These results indicate that the rate at which the heat transfer enhancement occurs with L is less than that of drag coefficient increment. It also suggests that placing the cylinder sufficiently close to the plane wall is beneficial in terms of the heat transfer enhancement

along with minimum drag coefficient. It may be noted that the ratio is more for nanofluids case in comparison to clear fluid case at both Pe.

2.6 Conclusion

This numerical study provides qualitative insight of the nanofluid ($W - Al_2O_3/CuO$) flow over a heated square cylinder placed in the vicinity of a cold wall under the incident of Couette flow at the inlet. The flow field and heat transfer characteristics are analysed for various values of Pe (nanofluid based), concentration(ϕ), diameter (d_{np}) of nanoparticles and gap height (L) of the heated cylinder from the plane wall. The major observations of the present study can be highlighted as follows:

1. The front stagnation point shifts very close to the bottom of the front face of the square cylinder for the case of ϕ = 6 % with d_{np} = 30 nm and moves towards the bottom side as L increases.

2. In-spite of asymmetry in the flow around the cylinder (due to incident shear flow and presence of the wall), heat transfers from the bottom and top faces are reported almost equal for Pe = 100 at L = 0.5. The addition of nanoparticles did not necessarily increase the heat transfer from all faces. At lower Pe = 25, the maximum heat transfer was from the bottom face (among all faces) at the lowest L = 0.1.

3. Nusselt number ($\overline{Nu}_M$) increased with the increase of Pe. Except for d_{np} = 30nm (and ϕ = 6 %), $\overline{Nu}_M$ increased (and decreased) with an increase of ϕ (and d_{np}) at all Pe. Surprisingly only for the case of d_{np} = 30 nm, $\overline{Nu}_M$ was found to decrease with an increase in ϕ from 4-6 % due to a sudden jump in Pr from Pr = 6.086 to 18.85 with ϕ changing from 4-6 %.

4. The heat transfer enhancement from the cylinder was slightly more for CuO compared to Al_2O_3 . Effects of diameter and concentration of nanoparticles on the heat transfer were observed more at a higher Pe. At a lower Pe = 25, the maximum $\overline{Nu}_M$ was found at the lowest L examined, while at a higher Pe = 400, $\overline{Nu}_M$

increased with L.

5. Observations based on the graphical representation of dependencies of $\overline{Nu}_M$ on Pe (at L = 0.5) and L (at Pe = 25 and 400) were reconfirmed by presenting their explicit functional form $\overline{Nu}_M = \overline{Nu}_M(Pe)$ and $\overline{Nu}_M = \overline{Nu}_M(L)$.

6. C_D and C_L both decreased with the increase of Pe. Essentially, C_L and C_D curves corresponding to ϕ = 6% with d_{np} = 30 nm distinctly appeared from all other curves, and C_D and C_L both registered much higher values.

7. The ratio $\dfrac{\overline{Nu}_M}{C_D}$ increased with Pe, while decreased with L increased, and was more at each L for the nanofluid case in comparison to clear fluid case at both Pe.

Chapter 3

Effectiveness of Temperature of Base Fluid on Heat Transfer Augmentation around a Heated Square Cylinder under the Incident of Couette Flow

3.1 Introduction

In recent years, cooling of devices has become the most important challenge in various sectors including automobiles, telecommunications, industrials, microprocessors etc. One of the method for dissipation of excess heat is to increase the area available for exchanging heat with an effective working fluid. Due to the poor thermal conductivity of the traditional base fluids, the concept of nanofluids has been introduced by Choi [41] by the suspension of nanoparticles in the base fluid. Nguyen et al. [71] experimentally showed the heat transfer performance by using the $W - Al_2O_3$ nanofluid for a liquid system that is utilized for cooling of electronic components. In cold regions of the world, such as Alaska, Canada, Northern Europe and Russia, it is a common practice to use ethylene glycol and water mixture ($EG : W$, $60 : 40$ by weight) as a heat transfer fluid in building heating systems, automobiles and heat exchangers.

There are several effective parameters on the thermal conductivity of nanofluids, such as nanofluid temperature, materials and particle volume concentration ϕ. Using copper-water nanofluid around a circular cylinder, Valipour et al. [72] indicated that at a given Re, local and average Nusselt number are enhanced by adding nanoparticles to base fluid. The effect of nanoparticle concentration and Reynolds number of the nanofluids on the heat transfer characteristics of $W - CuO$ nanofluids jet on a hot surface is studied by Modak et al. [73]. Bovand et al. [55] studied the forced convective heat transfer of $W - Al_2O_3$ nanofluid over an equilateral triangular obstacle and reported that the maximum effect of nanoparticles on heat transfer rate augmentation is for the side facing flow and the minimum is related to the vertex facing flow. Yoon et al. [74] numerically investigated the heat transfer enhancement in channel flow by using an inclined vortex generator. Forced convective heat transfer of nanofluids around a circular bluff body with the effects of slip velocity using a multi-phase mixture model has been conducted by Selvakumar and Dhinakaran [75]. They reported that the highest mean Nusselt number is observed at $\phi = 5\%$ at any Reynolds number. In the previous chapter (Chapter-2) we studied the nanofluid ($W - Al_2O_3/CuO$) flow over a heated square cylinder placed near a wall under Couette flow. It is reported that addition of nanoparticles is not guaranteed to increase the heat transfer from all faces of the cylinder due to large increase in viscosity than that in thermal conductivity.

Also, temperature has an important role on the k_{nf} and μ_{nf} of nanofluid, and hence on heat transfer enhancement rate. Das et al. [76] were the first, who experimentally proved that a dramatic enhancement in thermal conductivity takes place with temperature for $W - Al_2O_3$ and $W - CuO$ nanofluids. Sundar and Sharma [77] reported a twofold to fourfold increase in thermal conductivity enhancement of nanofluids for $W - Al_2O_3$ and water-CuO nanofluids. While measuring the thermal conductivity of alumina nanoparticles dispersed in water, EG, and water-$EG : W$ mixture nanofluids over a temperature range from $296K$ to $420K$, Beck et al. [78] made a conclusion that the temperature dependence of the effective thermal conductivity of nanofluids is due mostly to that of the base fluid. Parametric study of overall heat transfer coefficient of $W - CuO$ nanofluids in

a car radiator is made by Naraki et al. [79] and there they reported that increasing the inlet liquid temperature decreases the overall heat transfer coefficient. Vajjha and Das [80] observed that addition of nanoparticles to a liquid increases the viscosity significantly and the thermal conductivity moderately, however the specific heat and density change modestly. It is also reported that the thermal diffusivity of nanofluid increases with an increase in particle concentration and temperature.

3.2 Objectives

It is plausible that due to the large increase in viscosity than that in thermal conductivity, nanofluids would be poorer coolants as compared to base fluids. Most of the previous studies have considered their model at a room temperature without attention to that the temperature has an important role on the heat transfer enhancement rate. This study is numerically performed for four types of nanofluids flowing past square heated cylinder in the vicinity of a plane wall. The following are the objectives of the present study:

1. The role of base fluid temperature, and parameters governing the nanofluids (particle concentration (ϕ), particle materials (Al_2O_3 and CuO), and base fluids (water and $EG:W$) on the heat transfer from the cylinder.

2. A critical dissertation on efficiency of the aforementioned parameters on the heat transfer enhancement rate.

3. A comparison between the heat transfer enhancement of the cylinder and its drag coefficient reduction/increment due to addition of nanomaterials (of different d_{np} and ϕ) in both base fluids at two different temperature under Couette flow.

4. To propose the classical fluid dynamics relationship among $\overline{Nu}_M$, Reynolds number (Re) and Prandtl number (Pr) through Colburn $j-$factor, and a correlation between $j-$factor and Re.

3.3 Modeling

3.3.1 Problem Formulation

The geometrical configuration for the present study consists of a wall lying along the x^*-axis and a long square cylinder (with height A^*) maintained at constant temperature T_w is placed parallel to the wall at a fixed gap height $0.5A^*$ from the wall. The ambient stream is considered at a uniform temperature T_0. The upstream flow field is taken as Couette-flow based linear velocity profile $u^* = \dfrac{U_1 y^*}{A^*}$ where U_1 is the velocity at height A^* from the wall.

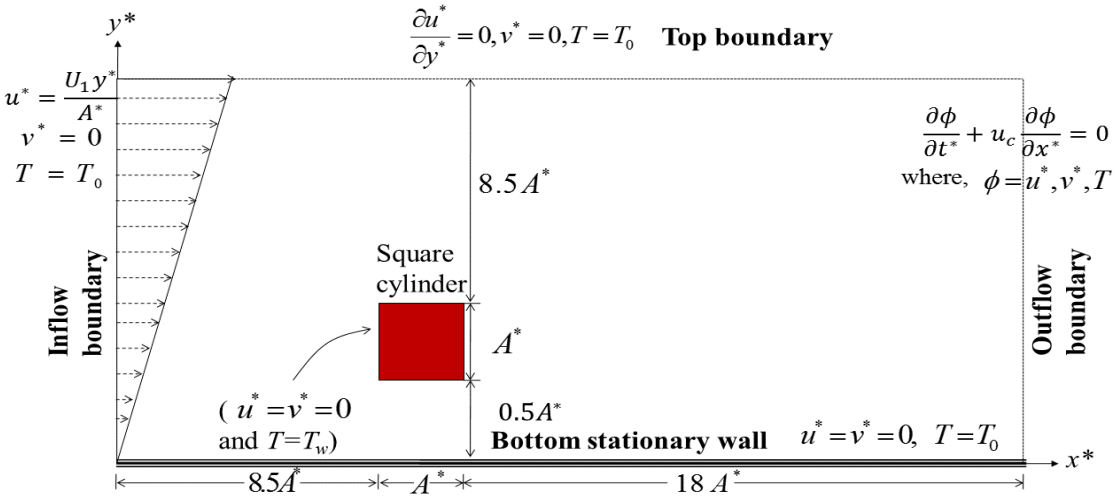

Figure 3.1: Schematics of flow configuration.

3.3.2 Governing Equations with Initial and Boundary Conditions

The flow is considered to be two-dimensional and laminar and fluid is taken as nanofluid. Single phase modeling approach is considered here. The detailed discussion of single and two-phase approach has been discussed in Chapter-2. The non dimensional Navier-Stokes equations along with the energy equation governing the nanofluid flow and heat transfer characteristics are given by:

$$\frac{\partial u}{\partial x} + \frac{\partial v}{\partial y} = 0. \tag{3.1}$$

$$\frac{\partial u}{\partial t}+\frac{\partial u^2}{\partial x}+\frac{\partial uv}{\partial y}=-\frac{\partial p}{\partial x}+\frac{1}{Re}*\frac{\nu_{nf}}{\nu_f}(\frac{\partial^2 u}{\partial x^2}+\frac{\partial^2 u}{\partial y^2}). \tag{3.2}$$

$$\frac{\partial v}{\partial t}+\frac{\partial uv}{\partial x}+\frac{\partial v^2}{\partial y}=-\frac{\partial p}{\partial y}+\frac{1}{Re}*\frac{\nu_{nf}}{\nu_f}(\frac{\partial^2 v}{\partial x^2}+\frac{\partial^2 v}{\partial y^2}). \tag{3.3}$$

$$\frac{\partial \theta}{\partial t}+\frac{\partial u\theta}{\partial x}+\frac{\partial v\theta}{\partial y}=\frac{\alpha_{nf}}{\alpha_f}*\frac{1}{RePr}(\frac{\partial^2 \theta}{\partial x^2}+\frac{\partial^2 \theta}{\partial y^2}). \tag{3.4}$$

The equations (3.1) - (3.4) are non-dimensionalized using the non-dimensional variables defined by

$$t=\frac{t^*U_1}{A}, x=\frac{x^*}{A}, y=\frac{y^*}{A}, u=\frac{u^*}{U_1}, v=\frac{v^*}{U_1}, p=\frac{p^*}{\rho_{nf}{U_1}^2}, \theta=\frac{T-T_0}{T_w-T_0}. \tag{3.5}$$

The non dimensional variables u, v, p, t and θ denote the velocity along x-direction, y-direction, pressure, time and temperature respectively, while ν and α denote kinematic viscosity and thermal diffusivity, respectively. The subscript $'nf'$ and $'f'$ denote the nanofluid and base fluid respectively. The variables with $'*'$ denote dimensional variables. The flow field is characterized by the parameters:

(i) Reynolds number

$$Re=\frac{U_1A^*}{\nu_f}, and$$

(ii) Prandtl number

$$Pr=\frac{\nu_f}{\alpha_f}.$$

The boundary conditions used to solve the governing equations (3.1) - (3.4) are same as used in Chapter-2. The flow is assumed to start impulsively at a particular value of Re. A time-independent stable numerical solution is achieved by advancing the flow field variables through a sequence of short time steps of duration Δt.

3.3.3 Nanofluid Modelling

The conventional fluids (also base fluids) is chosen to be water (W) and a 60% ethylene glycol and 40% water mixture by mass ($EG : W$). This kind of heat transfer fluid is common in cold regions of the world because of its low freezing point. The material of the nanoparticles are selected as Al_2O_3 and CuO. Here, the nanofluid is considered as single phase flow. The base fluid and nanoparticle are in thermal equilibrium and move with the same local velocity. The thermophysical properties of nanofluids are the function of both base fluids and nanoparticles. A detailed discussion for calculating these properties are made in chapter - 2.

The thermophysical properties equations summarised in the previous chapter require the values of the properties of the base fluid as well as nanoparticles. The thermophysical properties of W and $EG : W$ are obtained as a function of the temperature with the relation given in Etminan et al. [4]

3.4 Numerical Method

The pressure correction based iterative algorithm SIMPLE based on Finite volume method (FVM) with staggered grids, is applied here. A third-order accurate QUICK (Quadratic upstream interpolation for convective kinematics) is employed to discretize the convective terms and central differencing for diffusion terms. The numerical methodology (Staggered grid, FVM, QUICK and SIMPLE algorithms) used here has been discussed in Chapter-1.

3.4.1 Size of Computational Domain and Consideration of Grid

The cylinder is placed at a distance of $8.5A^*$ from the inlet while the top lateral boundary lies at $10A^*$ from the top face of the cylinder. In this study, the convective boundary condition at the outlet is implemented, which drastically reduces the downstream length of the computational domain and hence the convergence process becomes faster. The distance of the outflow boundary from the cylinder rear face is taken as $18A^*$ (Fig. 3.1).

Further changes on the boundary distances do not produce any significant changes in the results. The errors due to computational domain size and boundary conditions can be regarded as very small (within a few percent). The grid independency test is conducted for the case of water-CuO with $\phi = 2$ and 4 %, d_{np} = 30 and 100nm at Peclet number $Pe = 200$ by varying the grid between 196×140 to 800×600 and presented in Table-1 of chapter-2. Based on the grid independent results, it was concluded that the medium grid 550×475 can be considered as a reasonably fine for the calculation domain and this grid is also considered here since the computational domain is same for both studies.

3.4.2 Validation of numerical code

In order to assure the accuracy of our numerical code, the results are validated with Sharma and Eswaran [3], are presented in Table-2.2 of Chapter-2 for the cases of the uniformly heated cylinder and cylinder with constant heat flux. The table shows an excellent match between the two results in $\overline{Nu}_M$ and St computations. The code was also validated for the case of nanofluid modelling. The computed heat transfer coefficient (h) was compared with that obtained by Etminan-Farooji et al. [4]. The comparison is presented in Table-2.3 of Chapter-2. As can be seen, the maximum percentage difference of h of the present calculation from those of Etminan-Farooji et al. [4] is 4.59%. Relative percentage error was around 1% in most of the cases. The results show the excellent agreement of the present result over the whole range of Pe.

3.5 Results and Discussion

Here the operational nanofluids parameters are particle concentrations ϕ, particle diameter d_{np}, type of base fluid ($water(W)$ and $EG : W$) and particle materials (Al_2O_3 and CuO). The operational dimensionless parameters are Re and base fluid based Pr. In addition, the temperature of base fluid (T) is varied with $T = 300K$ and $T = 340K$. Therefore the values of Pr for $water$ become 6.14 and 2.86 at $T = 300K$ and $T = 340K$, respectively, while for $EG : W$ become 40.23 and 11.80 at $T = 300K$ and $T = 340K$, respectively. This study is done at Re = 50.

Table 3.1: Percentage of enhancement of $\frac{k_{nf}}{k_f}$ due to temperature increase from $T = 300K$ to $T = 340K$, defined by $\left(\frac{\frac{k_{nf}}{k_f}|_{T=340K}}{\frac{k_{nf}}{k_f}|_{T=300K}} - 1\right) \times 100$ where $a : W - CuO$; $b : W - Al_2O_3$; $c : EG : W - CuO$ and $d : EG : W - Al_2O_3$.

$d_{np} \rightarrow$ $\phi \downarrow$	30nm				50nm				100nm			
	a	b	c	d	a	b	c	d	a	b	c	d
1%	9.24	9.9	13.01	13.94	7.18	7.77	10.31	10.96	5.13	5.56	7.36	7.97
2%	8.51	8.41	12.94	12.72	6.36	6.31	9.96	10.86	4.13	4.05	6.92	6.78
3%	10.42	9.88	14.69	13.88	8.17	7.75	11.66	10.91	5.93	5.54	8.36	7.86
4%	9.59	8.59	14.33	13	7.2	6.5	11.12	11.05	4.67	4.18	7.74	6.88
5%	11.41	10.07	15.99	14.21	8.89	7.9	12.59	11.14	6.37	5.67	9.04	8.02

Table 3.2: Percentage of enhancement of $\frac{\mu_{nf}}{\mu_f}$ due to temperature increase from $T = 300K$ to $T = 340K$, defined by $\left(\frac{\frac{\mu_{nf}}{\mu_f}|_{T=340K}}{\frac{\mu_{nf}}{\mu_f}|_{T=300K}} - 1\right) \times 100$ where $a : W - CuO$; $b : W - Al_2O_3$; $c : EG : W - CuO$ and $d : EG : W - Al_2O_3$.

$d_{np} \rightarrow$ $\phi \downarrow$	30nm				50nm				100nm			
	a	b	c	d	a	b	c	d	a	b	c	d
1%	0.79	0.63	0.7	0.63	0.38	0.29	0.38	0.29	0.2	0.1	0.1	0.2
2%	1.37	1.2	3.6	0.86	0.57	0.37	0.55	0.37	0.43	0.39	0.19	0.1
3%	1.52	1.36	1.52	1.2	0.71	0.64	0.71	0.64	0.19	0.19	0.29	0.19
4%	2.39	2.08	2.07	1.79	1.38	0.78	1.01	0.78	0.54	0.48	0.38	0.29
5%	3.16	2.79	3.16	2.79	1.45	1.29	1.45	1.29	0.55	0.47	0.46	0.47

3.5.1 Temperature Distribution

Before analysing the computed (output) results, it is essential to see the behaviour of physical properties (inlet) of the nanofluids (especially viscosity and thermal conductivity) due to the variation in nanofluid parameters. The percentage of enhancement of $\frac{k_{nf}}{k_f}$ due to temperature increase from $T = 300K$ to $340K$, defined by $(\frac{\frac{k_{nf}}{k_f}|_{T=340K}}{\frac{k_{nf}}{k_b}|_{T=300K}} - 1) \times 100$ is tabulated in Table-3.1 for all four nanofluids ($W - CuO$, $W - Al_2O_3$, $EG : W - CuO$ and $EG : W - Al_2O_3$) at different d_{np} and ϕ. As seen in Table-3.1, the thermal conductivity of a nanofluid is increased due to increase in fluid temperature. The percentage of enhancement increases/decreases with the increase of concentration/diameter of nanoparticles for all four nanofluids. Thermal conductivity of the base fluid $EG : W$ is found to be more, in comparison to water, for both nanomaterials. It is also to be noted that thermal conductivity of CuO is slightly more than that of Al_2O_3 in both base fluids. Overall, the maximum enhancement is observed for $EG : W - CuO$ nanofluid with smaller nanoparticles diameter d_{np} = $30nm$ at all ϕ. A similar effort is made for $\frac{\mu_{nf}}{\mu_f}$ and is presented in Table-3.2. As can be seen in Table-3.2, the percentage of enhancement of $\frac{\mu_{nf}}{\mu_f}$ is also increasing function of ϕ while decreasing function of d_{np} in all four nanofluids. The percentage of enhancement is much more for d_{np} = $30nm$ case, remarkably high when ϕ increases from 4 to 5 $\%$. Observation of Table - 3.1 and Table-3.2 discloses the fact that the percentage of enhancement due to temperature increase is found more for thermal conductivity ratio than viscosity ratio.

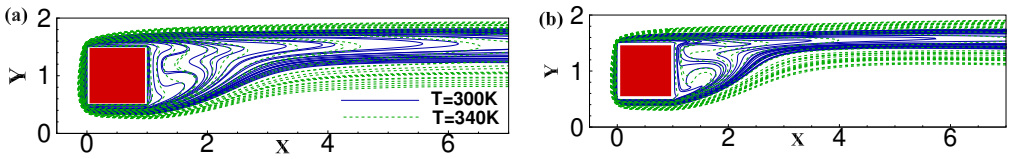

Figure 3.2: Isotherms across the heated square cylinder at $Re = 50$ for (a) $W - Al_2O_3$ and (b) $EG : W - Al_2O_3$ at $T = 300K$ (Solid lines) and $T = 340K$ (Dotted lines).

Isothermal lines for both fluid temperatures, are combinely plotted in Fig. 3.2(a) for $W - Al_2O_3$ and Fig. 3.2(b) for $EG : W - Al_2O_3$ nanofluids (Solid lines: $T = 300K$ and dotted lines: $T = 340K$). It may be noted that the flow around the cylinder is

found steady at all parameters values considered in this subsection. As seen the heat is distributed within the flow field and advected downstream without being influenced too much by mixing with their surroundings. Because of temperature difference between the cylinder and ambient fluid, the heat transfer takes place around the cylinder surface and trying to achieve equilibrium temperature between T_w and T_0. It may be noted that at the surface only the conductive heat transfer takes place since no penetration ($v = 0$) is applied on the surfaces. Thermal boundary layer growth starts almost symmetrically from the front face and then becomes thicker towards the rear. Basically the thermal boundary layer may be defined as an insulation layer, laying between the cylinder surfaces (with temperature T_w) and ambient fluid (with temperature T_0). As more as thermal boundary layer is, the convection heat transfer coefficient is less. Therefore, Fig.3.2 suggests that the convective heat transfer is found to be more on the front surface in comparison to other surfaces. Isothermal lines are cluster near the front, top and bottom corners, indicating that the convective cooling of the cylinder is maximum in these regions while the convective cooling along the rear surface is expected to be low. At this face the distance between T_w and T_0 is found to be maximum. It is worthy to note from Fig. 3.2 that the thermal boundary layer for the case of higher fluid temperature is thicker than that of lower temperature, indicating lower heat transfer rate at higher fluid temperature. While comparing the effect of base fluid on thermal energy distribution around the cylinder, it is clearly seen that the thermal boundary layers for $EG : W$ are much thinner than that their counterpart for water, implying higher heat transfer for the case of $EG : W$ base fluid. In other words, the temperature field around the cylinder is decayed while changing the base fluid from water to $EG : W$. The crowding of isotherms near the rear face in the recirculation regions is increased for the $EG : W$ base fluid case, suggesting greater heat transfer from this face.

3.5.2 Heat Transfer Characteristics

The heat transfer across the surfaces of the heated cylinder is discussed based on the time-averaged mean Nusselt number ($\overline{Nu}_M$), presented in Fig. 3.3 at two temperatures

($T = 300K$ and $T = 340K$) of both base fluids (Water $\rightarrow$ left side and $EG : W \rightarrow$ right side) for d_{np} = $30, 50$ and $100nm$ and ϕ = $0 - 5\%$. Apparently as seen in Fig. 3.3 that the value of $\overline{Nu}_M$ is found more at lower fluid temperature in comparison to higher temperature for both base fluids at all ϕ and d_{np}. This is physically realistic because the heat transfer from a heated object is proportional to the temperature difference between

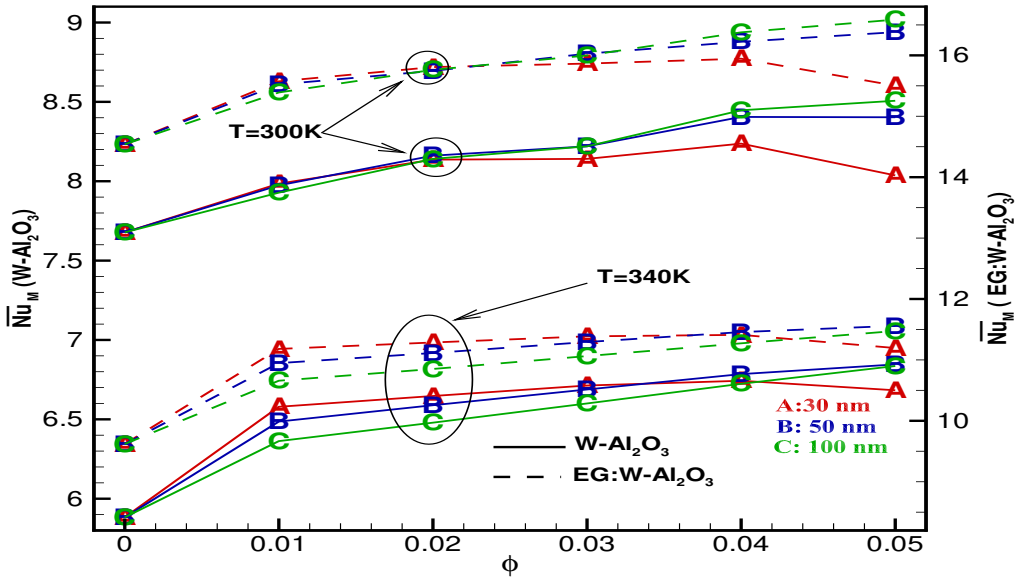

Figure 3.3: Time-averaged mean Nusselt number ($\overline{Nu}_M$) across the heated square cylinder as a function of ϕ for different d_{np}, T and both base fluids with Al_2O_3 nanoparticles at $Re = 50$.

the heated object and the ambient stream, and this difference becomes more at lower fluid temperature. Moreover, as the temperature of base fluid increases the value of Pr reduces, which in turns lowers the heat transfer from the object. It is clear from the Fig. 3.3 that the rate of increase in $\overline{Nu}_M$ due to increase in ϕ is slightly more at higher fluid temperature. The effect of d_{np} on $\overline{Nu}_M$ is negligible only at lower values of ϕ for the case of lower fluid temperature for both base fluids. While comparing the role of base fluid on heat transfer, it is seen that $EG : W$ produces much higher Nusselt number. This is due to the fact that the value of Pr (and of thermal conductivity) of $EG : W$ at a particular fluid temperature is much higher than that of water (ref. Table-3.1). For the case of d_{np} = $30nm$, an anomaly behaviour of $\overline{Nu}_M$ with ϕ while changing ϕ from 4 to 5% is observed

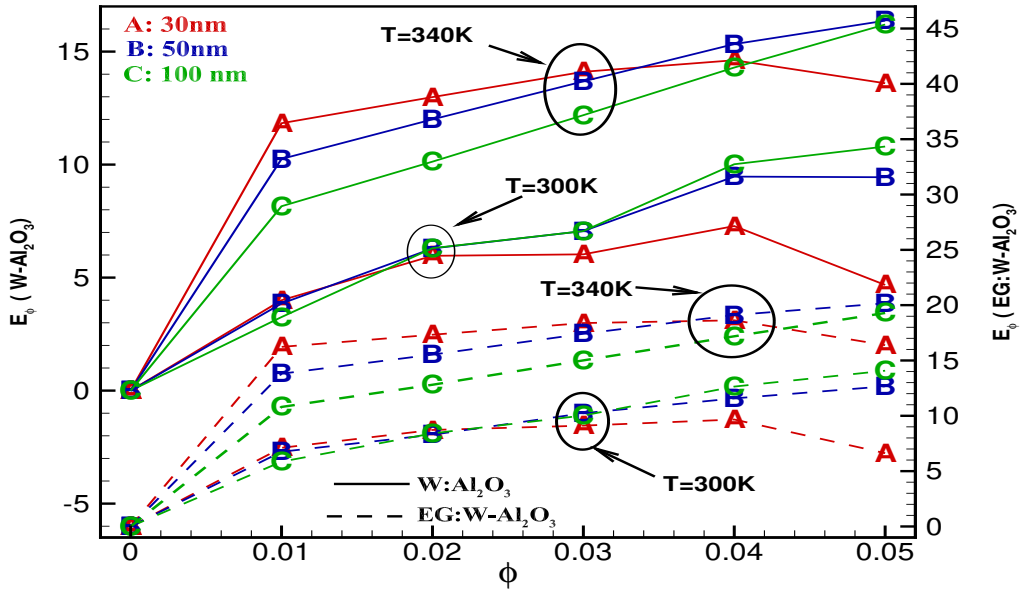

Figure 3.4: Effectiveness of loading of nanoparticles (Al_2O_3) in both base fluids with fluid temperature $T = 300K$ and $T = 340K$ for different ϕ and d_{np} at $Re = 50$.

in both base fluids at both temperatures. The increase of particle concentration in the base fluid enhances the viscosity as well as the thermal conductivity of the nanofluid (Tables-3.1 and 3.2). It is plausible that the role of thermal conductivity on the heat transfer is opposite to that of viscosity. At this d_{np} = $30nm$, there is a large increase in viscosity than that in thermal conductivity resulting to a situation where Nusselt number increases nominally (due to thermal conductivity increase) while decreases marginally (due to viscosity increase).

Effectiveness of loading of nanoparticles (Al_2O_3) in both base fluids (W and EG : W) on the heat transfer is discussed by presenting the effectiveness parameter, defined by $E_\phi = (\frac{\overline{Nu}_{M|_\phi}}{\overline{Nu}_{M|_{\phi=0}}} - 1) * 100$, graphically in Fig. 3.4 for ϕ = $0 - 5\%$ and d_{np} = 30, 50 and $100nm$ at both temperatures $T = 300K$ and $T = 340K$. It is evident from Fig. 3.4 that the variation of E_ϕ with ϕ for different d_{np} is noticeable, remarkably at the very beginning from ϕ = 0 to 1% at both fluid temperatures. For example, in Fig. 3.4 for $W - Al_2O_3$ with d_{np} = $50nm$, the percentage of enhancement in heat transfer is around 10% for $T = 340K$ and 4% for $T = 300K$ while changing ϕ from 0 to 1%. Though the heat transfer from cylinder is reported higher in Fig. 3.3 at lower temperature than higher

temperature in both base fluids, it is interesting to note that the heat transfer enhancement at higher temperature is more effective than that at lower temperature in both base fluids. This is not surprising, because as observed in Table-3.1 and 3.2, the increase of thermal conductivity due to temperature increase is more than that of viscosity. Therefore, it can be deduced that nanofluids can be made more attractive as cooling fluid for devices with high energy density where the cooling fluid is likely to work at a temperature higher than that of room temperature. The nanofluid with smallest nanoparticle diameter dissipate maximum heat from the heated object for the case of higher fluid temperature, while at the lower base fluid temperature the largest one ($d_{np} = 100nm$) gives slightly more heat transfer enhancement rate especially at higher ϕ, in comparison to other d_{np}, as is evident in Fig. 3.3. At a particular temperature, both nanomaterials are more efficient in the $EG : W$ base fluid in comparison to the water. E_ϕ for CuO materials is not presented here for sake of brief. Both nanofluids with d_{np} = $30nm$ and ϕ = 5% at both temperature behave as poorer coolent as compared to other non-zero values of d_{np} and ϕ, nevertheless, these nanofluids are better (in terms of heat transfer enhancement) than their respective base fluids.

The functional relationship between the Reynolds number, Prandtl number and Nusselt number through the use of Colburn j-factor defined by

$$j = \frac{\overline{Nu}_M}{RePr^{1/3}}, \tag{3.6}$$

is discussed with the help of Fig. 3.5(a) for both base fluids (with Al_2O_3) and temperatures. It is evident from Fig. 3.5(a) that results for four Pr values almost coincide with a single curve where j-factor vary inversely proportional to Re. In other words, the present results obey the classical fluid dynamics relationship among Re, Pr and $\overline{Nu}_M$. At any particular Re, j-factor is nearly independent of flowing fluid for the variation of Pr ranging from 2.86 to 40.23. The following correlation between j-factor and Re is established based on the present results for $5 \leq Re \leq 125$ and $2.86 \leq Pr \leq 40.23$ using a least

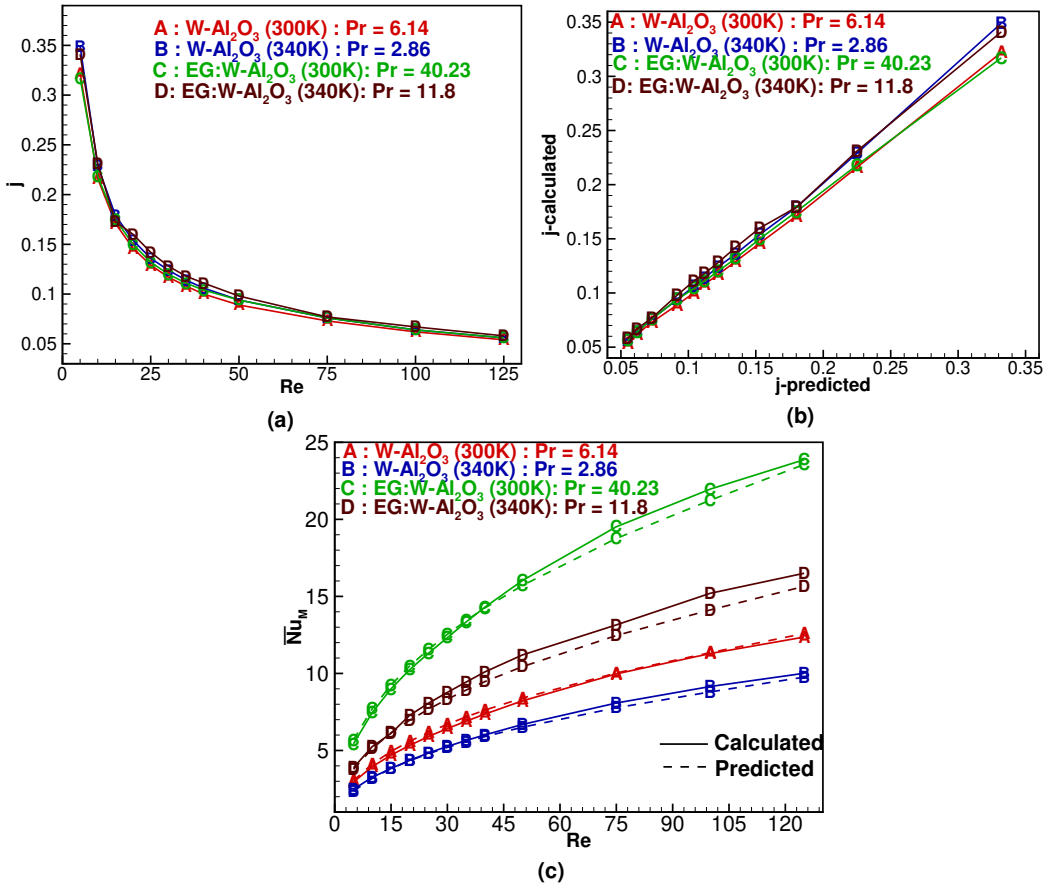

Figure 3.5: (a) Colburn j-factor as a function of Reynolds number Re, (b) Comparison of j-factor between computed (using equation (3.6)) and predicted (using equation (3.7)) values, and (c) Comparison of time-averaged mean Nusselt number ($\overline{Nu}_M$) between computed and predicted (through equation (3.7) for both base fluids and temperatures.

square method

$$j = 0.815 Re^{-0.5584}, \tag{3.7}$$

with maximum deviation as 5.63% and average deviation as 1.67%. This proposed relation is analogous to that of Bharti et al. [81]. Fig. 3.5(b) shows the comparison of j-factor between the calculated values (using equation (3.6)) and predicted (using equation (3.7)) values. As seen the values are lying close to the line $j - calculated = j - predicted$. As per the engineering utility of the proposed relation (3.7), one can find j-value at a Re, ranged in $[5, 125]$, and then with the help of relation (3.6) Nusselt number can be predicted at any Pr ranged in $[2.86, 40.23]$. In fact, the predicted values of $\overline{Nu}_M$ are plotted against

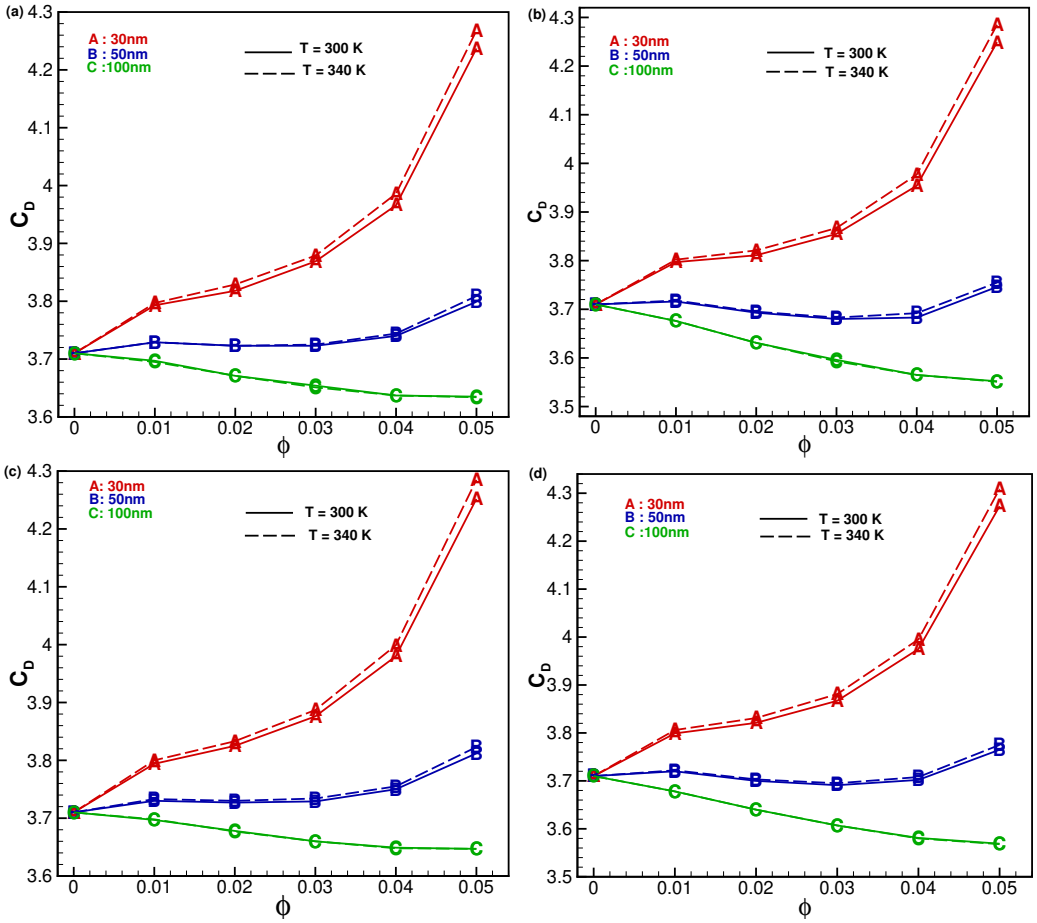

Figure 3.6: Variation of C_D with ϕ for different d_{np} and T at $Re = 50$. (a) $W - Al_2O_3$, (b) $W - CuO$, (C) $EG : W - Al_2O_3$, and (d) $EG : W - CuO$.

Re in Fig. 3.5(c) at four Pr values and compared with those of computed values (using present numerical simulation). Except at some Re for the case of $Pr = 11.80$, all the predicted values agree well with those of computed values. In particular, the maximum deviations for the cases of $Pr = 6.14, 2.86, 40.23$ and 11.8 are observed as 5.0% (falls at $Re = 20$), 4.8% (falls at $Re = 5$), 4.7% (falls at $Re = 5$) and 7.1% (falls at $Re = 100$), respectively. As can be seen in Fig. 3.5(c), $\overline{Nu}_M$ increases with Re and effect of Re on $\overline{Nu}_M$ is more pronounced on $EG : W$ (than water) base fluid, especially at $T = 300K$.

3.5.3 Hydrodynamic Characteristics

Fig. 3.6 shows the dependency of hydrodynamic force, drag coefficient C_D, on fluid temperature, type of base fluid, nanomaterials and its diameter along with concentration.

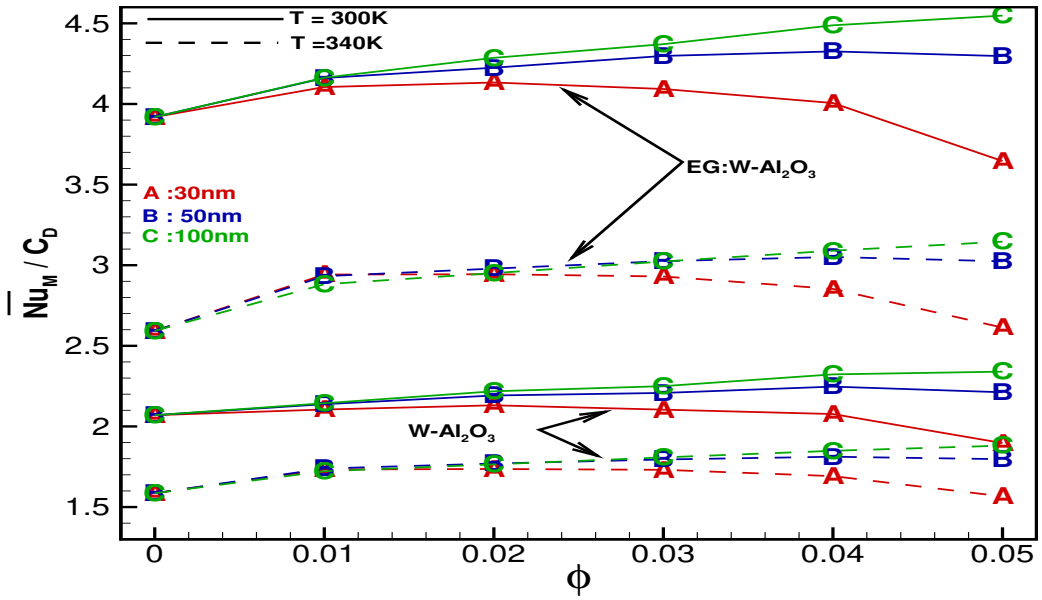

Figure 3.7: Ratio of time-averaged mean Nusselt number to drag coeffcient ($\overline{Nu}_M/C_D$) due to loading of nanoparticles (Al_2O_3) in both base fluids with fluid temperature $T = 300K$ and $T = 340K$ for different ϕ and d_{np} at $Re = 50$.

As seen in Fig. 3.6, depending upon diameter, $C_D(\phi)$-curves follow all three patterns: increasing (for smallest d_{np}), almost constant (for moderate d_{np}) and decreasing (for largest d_{np}) with the increase of ϕ. For a particular base fluid at a fixed Reynolds number, the variation of coefficient of diffusion term of momentum equations occurs due to change in μ_{nf}/ρ_{nf}. As per the nanofluid modelling, ρ_{nf} increases with ϕ, but is independent on d_{np}, while μ_{nf} also increases with ϕ and the increment rate is more at smaller d_{np}. Therefore, at a particular ϕ, the increase of drag coefficient is due to increase in the viscosity of nanofluid at smaller d_{np}. On the other hand, the change of μ_{nf}/ρ_{nf} due to ϕ is dependent on d_{np}. For example, at $d_{np} = 30nm$, percentage of enhancement of μ_{nf}/ρ_{nf} at $\phi = 3\%$ (with respect to $\phi = 1\%$) and $\phi = 5\%$ (with respect to $\phi = 3\%$) are 6.6% and 33%, respectively; while these values for $d_{np} = 100nm$ are -3.9% and -17.5%, respectively. It is seen that the temperature of base fluid has negligible effect on the drag coefficient. At the same time nanomaterials and base fluids have not much effect on the drag coefficient.

In order to assess the heat transfer enhancement from the heated cylinder together with its drag coefficient reduction/increment due to addition of nanaparticles (of different

diameter and concentration) in both base fluids at two different temperatures, Fig. 3.7 is presented the ratio of time-average mean Nusselt number to drag coefficient ($\overline{Nu}_M/C_D$). Except the curve - A, all curves are qualitatively similar, i.e., increasing with ϕ. As seen in Figs. 3.3 and 3.6, for the smallest $d_{np} = 30nm$, $\overline{Nu}_M$ increases with ϕ upto 4%, while C_D increases throughout the whole range of ϕ. As per Fig. 3.7, the maximum value of their ratio corresponding to this $d_{np} = 30nm$ is found at $\phi = 2\%$. This implies that the enhancement rate of $\overline{Nu}_M$ is more than that of C_D upto $\phi = 2\%$ but beyond this ϕ value, C_D increment gains dominance over the $\overline{Nu}_M$ enhancement. The pattern of curve-B in Fig. 3.7 suggests that increment rate of $\overline{Nu}_M$ is more than that of C_D in the whole range of ϕ. The pattern of curve-C is obvious in Fig. 3.7 because $\overline{Nu}_M$ increases , at the same time, C_D decreases with the increase of ϕ in Fig. 3.3 and Fig. 3.6. While comparing the role of both base fluids on $\overline{Nu}_M/C_D$, it is confirmed from Fig. 3.7 that the $EG : W$ base fluid behaves better coolant at both fluid temperatures since both base fluids generate the same drag coefficient from the cylinder. Having different C_D at two temperatures, it is also evident from Fig. 3.7 that the ratio $\overline{Nu}_M/C_D$ is more at lower temperature. Overall it may be deduced from the ongoing discussion that the $EG : W - Al_2O_3$ nanofluid with largest diameter of nanomaterials is the best nanofluid working at lower temperature in terms of heat transfer enhancement and drag coefficient reduction at all ϕ. In this condition, the heat transfer can be enhanced upto 12.64%, while the drag coefficient can be reduced upto 2.05%.

3.6 Conclusion

A numerical study is conducted on the enhancement of heat transfer $\overline{Nu}_M$ from a square heated cylinder placed near a wall under the incident of Couette flow using nanofluids, suspensions of nanomaterials (Al_2O_3 and CuO) of different concentration ϕ and diameter d_{np} in base fluids: water and ethylene glycol-water mixture). The role of temperature of base fluids on the $\overline{Nu}_M$ enhancement is analysed under the Couette flow situation. The major observations (against the main issues motivating the present study)

are:

1. Thermal boundary layer around the cylinder at higher fluid temperature is found thicker than that lower fluid temperature. The temperature field around the cylinder is decayed and crowding of isotherms in rear face is increased while changing the base fluid from W to $EG : W$.

2. Though $\overline{Nu}_M$ is reported high at lower fluid temperature, nanomaterials are more effective in the base fluid at higher temperature.

3. Under Couette flow, $EG : W - Al_2O_3$ nanofluid with largest d_{np} is found the worthy fluid, which works efficiently at lower temperature at which the heat transfer is enhanced upto 12.64% and drag coefficient is reduced upto 2.05%.

4. It is shown that $\overline{Nu}_M$ can be predicted using the proposed correlation between j-factor and Re for $5 \leq Re \leq 125$ and ($2.86 \leq Pr \leq 40.23$).

Chapter 4

Heat Transfer Augmentation from a Square Cylinder (Uniformly Heated or Heat Flux) due to Nanofluids and Non-Linearity of Incident Velocity

4.1 Introduction

Researchers for a long time have been fascinated to study the flow past bluff bodies, because of the intrinsic complexities and importance of these flows in many practical applications such as drying of different materials, cooling of glass, plastics and industrial devices, chemical reactors and so forth. Various studies have been carried out numerically as well as experimentally related to heat transfer characteristics of flow past bluff bodies. In the recent past, much attention has been given to enhance the heat transfer rate by introducing nanoscale particle ($< 100nm$) suspensions in base fluid such as water, ethylene glycol, ethylene glycol and water mixture or oil. Choi [41] used nanoscale particle suspensions (nanofluids) as an alternative heat transfer medium due to its superior thermal

properties, improved stability, and homogeneity. The fundamental studies on convective transport of nanofluids are increasing rapidly for engineering applications such as automotive sector, nuclear reactors, cooling of electronics and X-rays (Azmi et al. [50], Escher et al. [82], Ahmed et al. [83], Nguyen et al. [71]). Because of fast improvement of computer performance, the CPU chips become small and a huge heat is generated in the chips, which needs to dissipate using such effective working fluid as nanofluids.

The effect of volume fraction of nanoparticles on heat transfer was presented by various scholars. Haddad et al. [84] found that higher heat transfer is formed when Brownian and thermophoresis effects are considered. Rashidi et al. [85] highlighted that the effects of Brownian force on heat transfer are stronger than thermophoretic. Vakili et al. [48] experimentally concluded that the enhancement of the convective heat transfer coefficient for the mixture consisting of 60% ethylene glycol and 40% distilled water ($EG : W$) with TiO_2 is more than the nanofluid of distilled water. Umavathi et al. [86] performed numerical study on natural convective flow and heat transfer of nanofluids in a vertical rectangular duct filled with porous matrix and they reported that the heat transfer is enhanced with the use of a nanofluid. Azmi et al. [50] introduced the historical background about the development of water based, ethylene glycol (EG) based and $EG : W$ mixture nanofluids for the past 20 years. For unconfined flow of nanofluids over a square cylinder, Etminan-Farooji et al. [4] resulted that there is an optimum value of ϕ that results in the highest heat transfer coefficient.

Maiti and Bhatt [87] made a conclusion that increasing the pressure gradient (P) at the inlet under the same characteristic velocity causes the steady flow of a single cylinder to convert to a proper periodic flow and the shedding of weak to stronger positive vortex from the lower side of the cylinder. Sharma and Eswaran [88] focused on the unconfined/confined flow and heat transfer characteristic around a square cylinder in the $2D$ laminar regime for uniform heat flux and constant cylinder temperature boundary conditions. The flow and heat transfer past a heated cylinder of square cross section mounted horizontally above a plane wall is studied by Bhattacharyya et al. [38]. The laminar mixed convection flow across the porous square cylinder with the heated cylinder bottom at the

axis in the channel is studied numerically by Wu and Wang [89]. Malik and Nayak [62] studied mixed convection flows of copper-water nanofluid in a lid driven cavity with heat source mounted on hot and cold vertical wall alternatively. The effect is that thermal conductivity increases with increase in Rayleigh (Ra) number and Nusselt (Nu) number increases with increase in Ra, Re and ϕ.

4.2 Objectives

It is clear from the study of Maiti and Bhatt [87] that the Couette-Poiseuille flow based nonuniform linear/nonlinear velocity profile over a cylinder can generate the developing boundary layers, swirl and flow destabilization, and that depends on the non-dimensional pressure gradient (P). Wall proximity with non-uniform incident flow over a cylinder using nanofluids has not been addressed previously, to the best of authors knowledge. Studies on forced convection heat transfer using $EG : W$ mixture as base fluid are limited in the literature of nanofluid fluid flow over bluff body/eis. Couette flow based non-uniform but linear velocity profile at the inlet has been considered in the previous chapter (Chapter - 2 and 3). Couette-Poiseuille flow based non-linear velocity profile $u^*(y^*)$ would be interesting to perform additional calculations as a sequel to the previous chapters in order to explore the dependency of the vortex shedding and heat transfer performance of the nanofluids from the cylinder (for both the thermal conditions) under different pressure gradients P at the inlet. This chapter's specific objectives are:

1. The effect of pressure gradient P on the hydrodynamic and heat transfer characteristics of the cylinder is studied for both the thermal conditions: either dissipating constant heat flux (q_w) or maintaining at a constant temperature (T_w) at the cylinder surfaces.

2. The effect of type of thermal boundary conditions at the cylinder surfaces on the flow and heat transfer characteristics is studied for each of nanofluids and certain values of ϕ and P.

3. In order to reconfirm the observation on heat transfer based on its graphical representations, an effort is made to propose functional forms of $\overline{Nu}_M = \overline{Nu}_M(P)$, $\overline{Nu}_M = \overline{Nu}_M(\phi)$, and hence $\overline{Nu}_M = \overline{Nu}_M(P, \phi)$ using least square method.

4. The quantitative difference of hydrodynamic and heat transfer characteristics of cylinder between two base fluids (water (W) and ethylene glycol - water ($EG : W$)) are explored.

4.3 Modeling

4.3.1 Problem Formulation

The geometrical configuration consists of a long square cylinder with side A^* is placed parallel to the wall (lying along x^*-axis) at a gap-height of $0.5A^*$ from the wall. (Fig. 4.1). The cylinder is either dissipating constant heat flux q_w or maintained at a constant temperature T_w. The wall is considered to be at T_0 with $T_0 < T_w$ The ambient stream is considered at a uniform temperature T_0. The inlet flow field is considered as Couette-Poiseuille flow based nonuniform linear/nonlinear velocity profile $u^*(y^*)$.

$$u^*(y^*) = \frac{y^*}{H^*}U_2 + PU_2\frac{y^*}{H^*}(1 - \frac{y^*}{H^*}), \tag{4.1}$$

where,

$$P = \frac{H^{*2}}{2\mu_f U_2}(-\frac{dp^*}{dx^*}) = \frac{1}{2}H^2 Re_{U_2}\frac{\rho_{nf}}{\rho_f}(-\frac{dp}{dx}). \tag{4.2}$$

The equation 4.2 represents the non-dimensional pressure gradient, U_2 is the velocity at a distance $H^* = 10A^*$ from the wall and $Re_{U_2} = (U_2A^*/\nu_f)$. Different forms of the non-dimensional velocity profiles corresponding to different values of P (≥ 0) with fixed height $H^* = 10A^*$ is presented in Fig. 4.2.

4.3.2 Governing Equations with Initial and Boundary Conditions

The flow is considered to be two-dimensional and laminar. A single phase modelling approach is adopted to derive equations governing the nanofluid flow. A detailed discussion

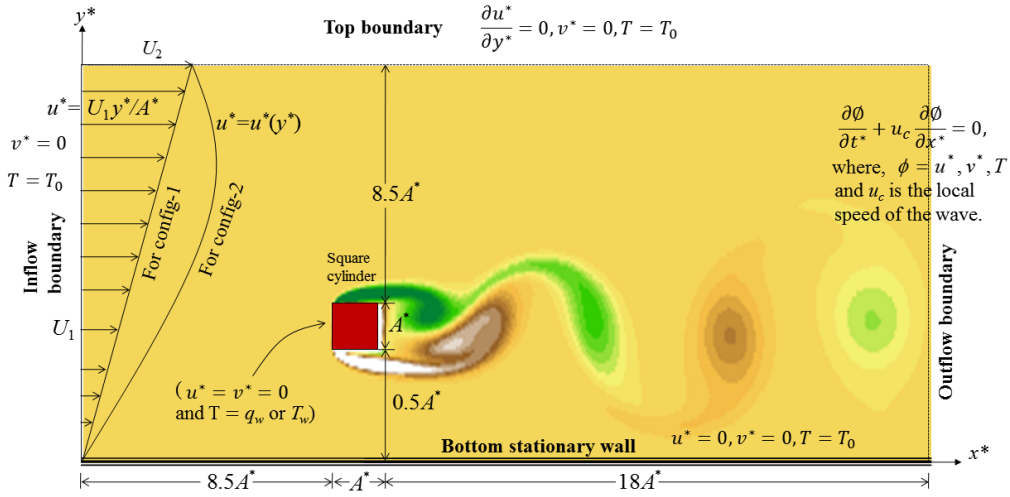

Figure 4.1: Schematics of the flow configuration.

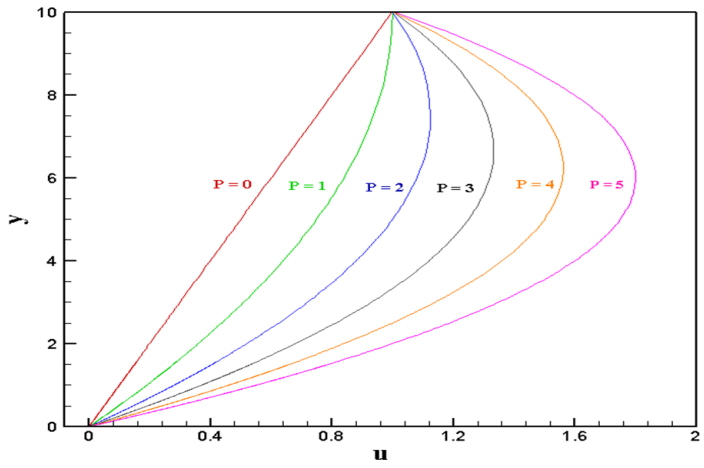

Figure 4.2: Non dimensional velocity profiles for different P.

on adopting this model has already been discussed in previous chapter (Chapter - 2). The nondimensional Navier–Stokes equations along with the energy equation governing the nanofluid flow and heat transfer characteristics are given by

$$\nabla.\mathbf{V} = 0, \tag{4.3}$$

$$\frac{\partial \mathbf{V}}{\partial t} + (\mathbf{V}.\nabla)\mathbf{V} = -\nabla p + \frac{1}{Re} * \frac{\nu_{nf}}{\nu_f}\nabla^2\mathbf{V}, \tag{4.4}$$

$$\frac{\partial \theta}{\partial t} + (\mathbf{V}.\nabla)\theta = \frac{1}{RePr} * \frac{\alpha_{nf}}{\alpha_f}\nabla^2\theta. \tag{4.5}$$

In the above equations, the dimensionless variables are defined by

$$t = \frac{t^* U_2}{A^*}, x = \frac{x^*}{A^*}, y = \frac{y^*}{A^*}, u = \frac{u^*}{U_2}, v = \frac{v^*}{U_2}, p = \frac{p^*}{\rho_{nf}(U_2)^2}, Pr = \frac{\mu_f C_{p,f}}{k_f},$$

$$\theta = \frac{T - T_0}{q_w A^*/k_f} \text{ (for } q_w\text{) and } \theta = \frac{T - T_0}{T_w - T_0} \text{ (for } T_w\text{).}$$

The boundary conditions in mathematical form is as follows:

$u = v = 0$ and $T = T_0$ on the lower wall $y = 0$.

$u = v = 0$ and $T = q_W/T_w$ on the cylinder's surface.

At the top lateral boundary, symmetry boundary condition is taken.

$v = \dfrac{\partial u}{\partial y} = 0$ and $T = T_0$.

The convective boundary condition is taken at the outlet boundary.

$\dfrac{\partial \phi}{\partial t} + u_c \dfrac{\partial \phi}{\partial x} = 0.$ where, $\phi = u, v$ and θ.

The flow is assumed to start impulsively at a particular value of Re_{U_2} . A time-independent stable numerical solution is achieved by advancing the flow field variables through a sequence of short time steps of duration Δt.

4.3.3 Nanofluid Modelling

The conventional fluids (also base fluids) is taken as water (W) and ethylene glycol-water mixture ($EG : W$, $60 : 40$ by weight). The material of the nanoparticles are selected as Al_2O_3 and CuO. The thermophysical properties of water and $EG : W$ as a

function of the temperature is taken from ASHRAE Handbook [90] and are calculated at base fluid temperature $T = 300K$. Nanofluid models which take care of Brownian motion, diameter and concentration of nanomaterials, temperature of base fluid and base fluid physical properties are considered here. The detailed discussion on calculation of the thermophysical properties of nanofluids (density, specific heat, thermal conductivity and viscosity) is available in chapter - 2 .

4.4 Numerical Methodology

In order to solve the governing equations numerically, the pressure correction based iterative SIMPLE algorithm is used. The computational domain is divided into small control volumes. Staggered grid arrangement is taken to store the variables. The equations are then discretized over each control volume using finite volume method (FVM). A third order accurate QUICK (Quadratic Upstream Interpolation for Convective Kinematics) is employed to discretise the convective terms and central differencing for diffusion terms. A fully implicit third order scheme is incorporated to discretise the time derivatives. A detailed discussion of the numerical methodology (staggered grid, FVM, QUICK and SIMPLE algorithms) is made in Chapter-1.

4.4.1 Size of Computational Domain and Consideration of Grid

The inflow, outflow and top lateral boundary distances are shown in Fig. 4.1 for both configurations. A non-uniform grid is considered by distributing the uniform grids along the surfaces of the cylinder and expanding the grid size for the far-fields starting with δ_1 = 0.004, the first grid size away from the surface. The grid independency test is conducted for the case of water-CuO with $\phi = 2$ and 4 %, d_{np} = 30 and 100nm at Peclet number $Pe = 200$ by varying the grid between 196×140 to 800×600 and presented in Table-1 of chapter-2. Based on the grid independent results, it was concluded that the medium grid 550×475 can be considered as a reasonably fine for the calculation domain and this grid is also considered here since the computational domain is same for both studies.

4.4.2 Validation of Numerical Code

The numerical code for the present case of heat transfer has also been validated with Sharma and Eswaran [3] for the cases of T_w and q_w in the channel and presented in Table-2.2 of Chapter-2. An excellent match between the two results in Nu and St computations has been reported there. Furthermore the code is validated for the case of nanofluid modelling with Etminan-Farooji et al. [4] for different $\phi(= 0\% - 4\%)$, particle materials (Al_2O_3 and CuO) and base fluid type (water (W) and ethylene glycol and water mixture ($EG : W$, $60 : 40$ by weight)) and d_{np} ($30nm$ and $100nm$) at different Pe, ranging from 25 to 200. The comparison has been presented in Table-2.3 of Chapter-2. It has been reported there that the relative percentage error is around 1% in most of the cases.

4.5 Results and Discussion

Couette flow based non-uniform but linear velocity profile at the inlet has been considered in the previous chapter (Chapter-3). There are, however, a number of practical cases in which not only the flow approaching a body is non-uniform but also the inlet velocity profile is a non-linear function. Couette-Poiseuille flow based non-linear velocity profile $u^*(y^*)$ would be interesting to perform additional calculations as a sequel to the previous study in order to explore the dependency of heat transfer performance of the nanofluids from the cylinder (for both thermal conditions: uniformly heated (T_w) and heat flux (q_w)) under different pressure gradients P at the inlet. For a fixed value of H, e.g., $H^* = 10A^*$, $Re_{U_2} = 10Re$ for $P = 0$ (Maiti and Bhatt [87]). Therefore, in this chapter the numerical results are computed at a $Re_{U_2} = 500$, which is mechanically equivalent to $Re = 50$ (chapter-3). The diameter of the nanoparticle is fixed at d_{np} = $50nm$ and the fluid temperature is kept at $T = 300K$, implying Pr = 6.14 and 40.23 for W and $EG : W$, respectively. The operational nanofluids parameters are particle concentrations ϕ, type of base fluid (water (W) and ethylene glycol and water mixture ($EG : W$, $60 : 40$ by weight)) and particle materials (Al_2O_3 and CuO).

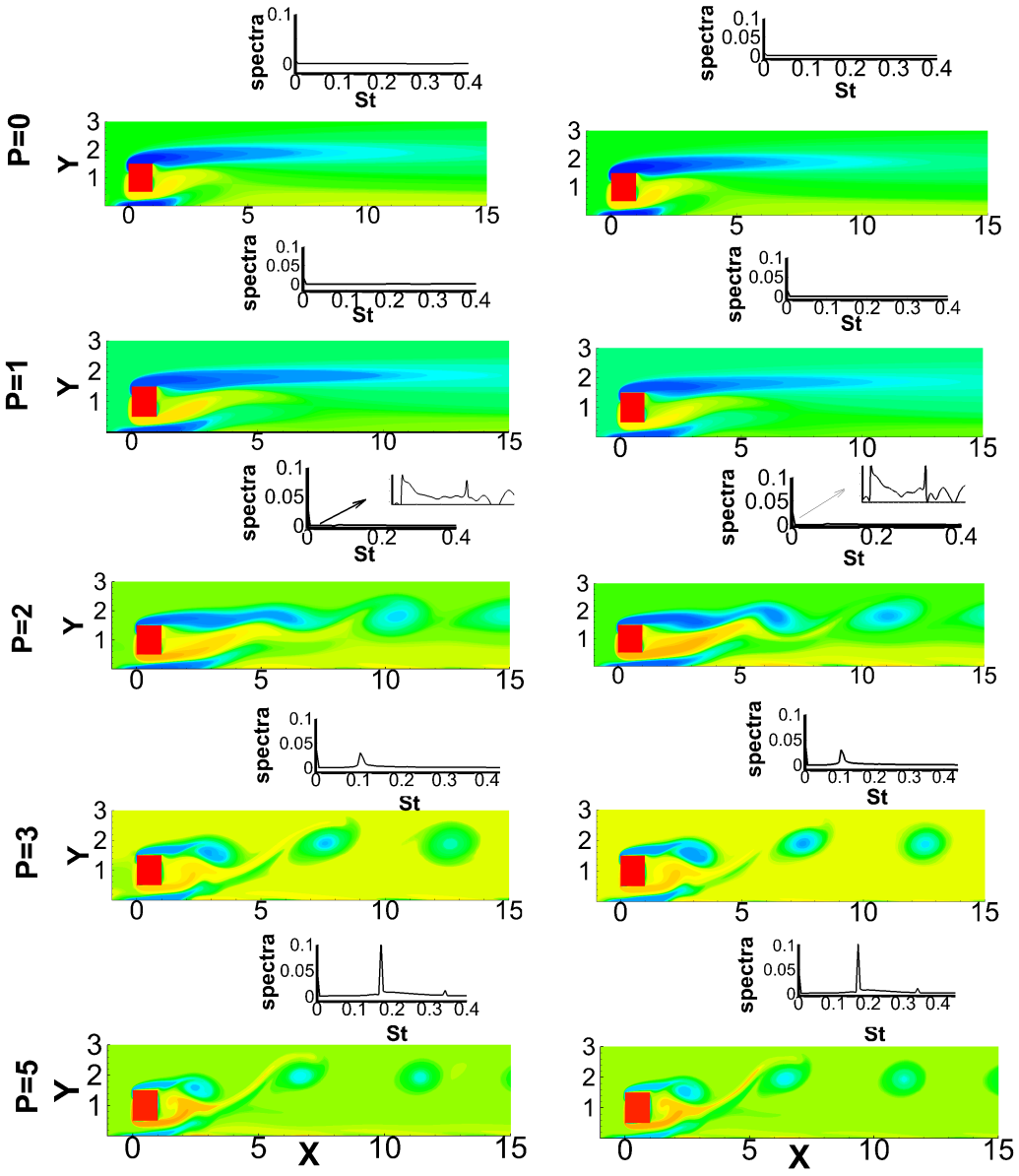

Figure 4.3: Instantaneous vorticity contour and spectra of lift coefficient for $W-CuO$ nanofluid with $\phi = 3\%$ at different P and $Re_{U_2} = 500$. (a) Uniformly heated cylinder (left side) and (b) Uniform heat flux (right side). Here, St is the Strouhal number.

4.5.1 Fluid Flow Analysis

Fig. 4.3 presents the instantaneous isovorticity lines along with the spectra of fluctuating lift coefficient of the cylinder for $W-CuO$ nanofluid with $\phi = 3\%$ for both thermal boundary conditions. It is clear from Fig. 4.3 that the nanofluid flow over the cylinder (of

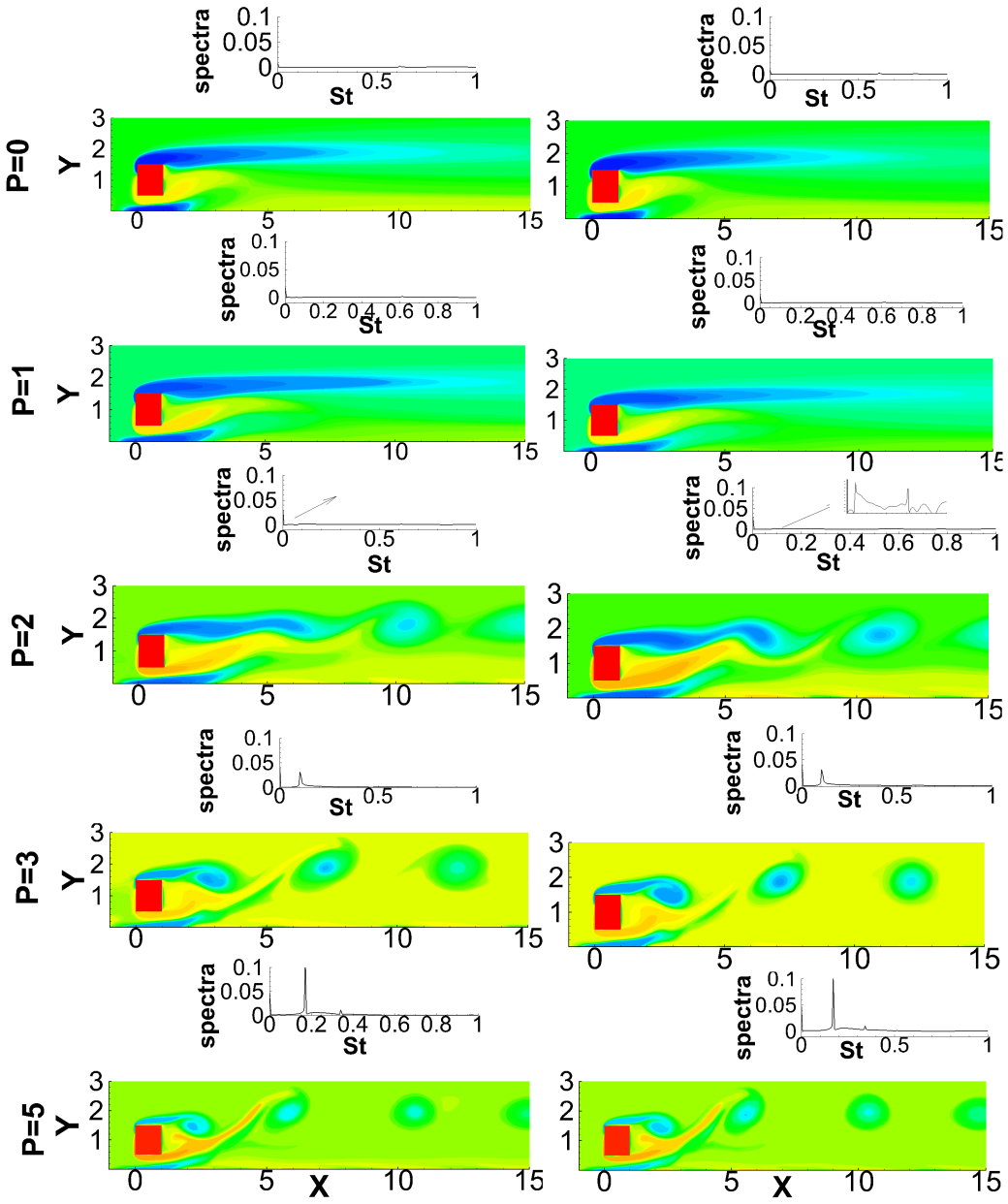

Figure 4.4: Instantaneous vorticity contour and spectra of lift coefficient for $EG : W - CuO$ nanofluid with $\phi = 3\%$ at different P and $Re_{U_2} = 500$. (a) Uniform heated cylinder (left side) and (b) Uniform heat flux (right side).

uniformly heated and uniform heat flux) is completely steady upto $P = 1$, while a clear unsteadiness is observed for $P = 3$ and 5. The steady/unsteadiness can be confirmed from the peak of spectra presented in Fig. 4.3 since the peak value is zero for $P = 0$

and 1, owing to the situation of no-oscillation in the flow. The upper shear layer issuing from top surface of the cylinder emerges almost horizontally in the streamwise direction and the lower shear layer reattaches the rear surface of the cylinder. While increasing the pressure gradient to $P = 2$ under the same inlet characteristic velocity ($Re_{U_2} = 500$) an unsteadiness is developed in the far field and propagating towards the cylinder, and the flow becomes quasi-steady in nature [Maiti [68] for more details]. Further increase in P at 3, the quasi-steady flow at $P = 2$ is converted to a proper periodic flow with a single sharp peak in the spectra of lift coefficient (Fig. 4.3 for $P = 3$). With further increase in P, the peak becomes more sharper, indicating that the vortex shedding becomes more regular and stronger for both thermal boundary conditions. Not much differences is observed in the flow between the cylinder with uniformly heated and the one with uniform heat flux.

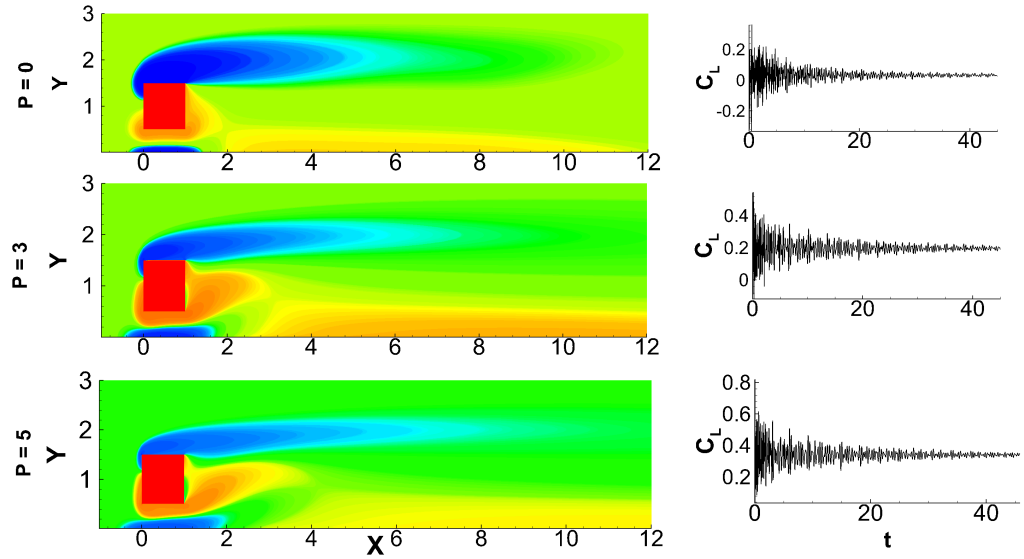

Figure 4.5: Equivorticity line along with the time histories of lift coefficient of the cylinder for $EG : W - CuO$ nanofluid for uniformly heated cylinder with $\phi = 3\%$ and $Re_{U_2} = 101.43$.

A similar attempt is made to see the flow characteristics for $EG : W - CuO$ nanofluid by presenting the isovorticity contour and spectra in Fig. 4.4. Apparently, flow features and spectra are observed exactly same for both base fluids for a particular thermal boundary conditions at a fixed P. Because these two cases (of base fluids) are exactly mechanically similar (same geometry, governing momentum equations and boundary conditions)

at this same $Re_{U_2} = 500$. In other words, the characteristic velocity U_2 at the inlet for $EG : W$ base fluid has to be more than that for water base fluid in order to have the same Re_{U_2} for both cases, because the kinematic viscosity of $EG : W$ is more than that of water. In order to show the differences in flow characteristics for these two cases by taking the same inlet velocity U_2, the equivorticity lines along with the time histories of lift coefficient of the cylinder of same characteristic length A^* are presented in Fig. 4.5 for $EG : W - CuO$ nanofluid ($\phi = 3\%$). Here the ratio of kinematic viscosity of $EG : W$ to water is 4.9295. Therefore, the Reynolds number becomes 101.43. In comparison to Fig. 4.3 for water base fluid, the flow here in Fig. 4.5 for $EG : W$ base fluid becomes completely steady even at $P = 5$, because of high viscosity. In other way around, while comparing with Fig. 4.4, here the flow becomes steady because of lower Reynolds number. After a transient time (at which the flow becomes stable: steady/unsteady), the flow at all P becomes stable (steady state). However, the transition time increases with P (assuming the flow starts impulsively at all P), suggesting that the flow may be unsteady for further increase in P.

In order to validate ongoing discussion, Fig. 4.6 is presented for time-average surface pressure distribution ($\overline{C_P}$) along the cylinder's bottom face and the plane wall (see plot-a) and time-average horizontal velocity ($\overline{u}$) profile along the vertical direction (y) at the exit position of the gap flow between the cylinder's bottom face and the plane wall (see plot-b). Fig.4.6(a) shows that the pressure distribution difference between the bottom face and the plane wall is almost zero in the core of the gap region for $Re_{U_2} = 101.43$ (at both P = 0 and 5) and $Re_{U_2} = 500$ (at $P = 0$). As a result, the gap flow becomes unidirectional, and the core flow looks like a channel flow, owing to a fact that the interaction between shear layers of the cylinder gets lost. Therefore, the vortex shedding is completely suppressed for the above parameters values. On the other hand, when $Re_{U_2} = 500$ and $P = 5$ as seen in Fig. 4.6(a), the bottom face pressure is less than that along the wall. In this situation, the interaction of shear layers of the cylinder takes place in the rear of the cylinder, consequently the vortex shedding occurs behind the cylinder, as observed in Fig. 4.3. It is evident from Fig. 4.6(b) that the velocity profiles overshoot and the gap

flow (which plays a major role in the shedding of vortex behind the cylinder near a wall) becomes stronger with the increase of either P or Re_{U_2}. Lee et al. [91] reported that in the cases where the vortex shedding occurs , the value of maximum velocity is greater than in the cases without vortex shedding. Also, the position at which the maximum velocity occurs is closer to the bottom face of the cylinder. The results in Fig. 4.6(b) provide some insight into the validity of the ongoing argument.

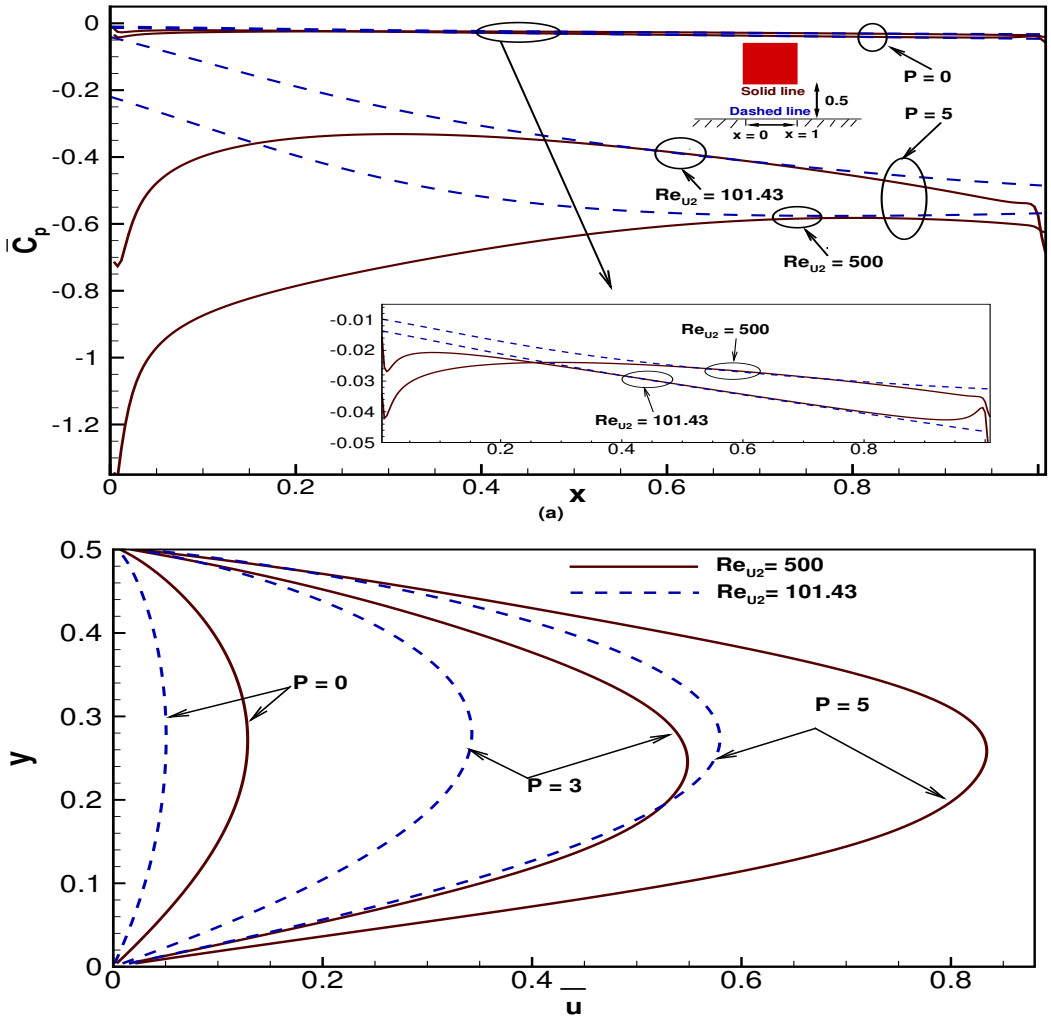

Figure 4.6: (a) Surface pressure distribution ($\overline{C_P}$) along lower face of cylinder(solid lines) and along plane wall (dashed lines), and (b) Mean horizontal velocity distribution along $y-$ direction at the exit of gap flow between the cylinder's lower face and the plane wall (at $x = 1$, as Fig.(a)) for $EG : W - CuO$ nanofluid for $Re_{U_2} = 500$ and $Re_{U_2} = 101.43$ at $\phi = 3\%$.

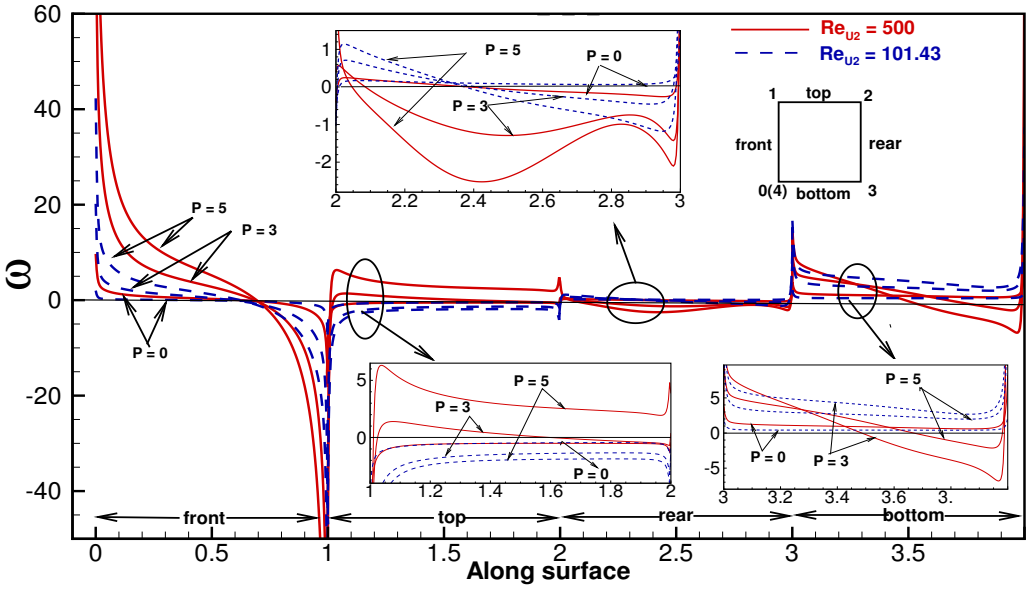

Figure 4.7: Wall Vorticity (ω) distribution around the cylinder surfaces for $EG : W - CuO$ nanofluid for $Re_{U_2} = 500$ and $Re_{U_2} = 101.43$ at $\phi = 3\%$ for uniform heat flux case.

The steady/unsteadiness of the flow of two base fluids $EG : W$ at $Re_{U_2} = 101.43$ and water at $Re_{U_2} = 500$ is exemplified based on the wall vorticity distribution around the cylinder surfaces for different P = 0,3 and 5 presented in Fig. 4.7 for uniform heat flux case. A zero line (a line with $\omega = 0$) is drawn in the figure. It is evident from Fig. 4.7 that variation of wall vorticity of all six lines on each face can be classified into two subgroups: one group consists of four lines (three dashed lines at $Re_{U_2} = 101.43$ for all three values of P and one solid line at $Re_{U_2} = 500$ for $P = 0$) and the other one consists of two lines (both are solid at $Re_{U_2} = 500$ for $P = 3$ and 5). Hence it is quite clear from the ongoing discussion (based on Figs. 4.3 - 4.6) that the former group belongs to the steady flow while the later one is a member of the unsteady flow. One may discuss the wall vorticity variation face-wise as follows: front face (the front stagnation point of the steady case is slightly towards the bottom side, due to viscous effect, in comparison to unsteady case), top face (wall vorticity of the steady case lies below the zero-line giving negative vorticity while positive vorticity is observed for the unsteady case, because of oscillatory behaviour of both shear layers of the cylinder during the vortex shedding process, ref. Fig. 4.3), rear face (vorticity variation is slightly more

for the unsteady case, in comparison to the steady case), and bottom face (apparently positive vorticity for the steady case but negative vorticity is also observed at some part of the bottom face for the unsteady case, because of interaction of two shear layers of the cylinder). As depicted in Fig. 4.7 the numerical value of wall vorticity is proportional to the pressure gradient as well as Reynolds number.

4.5.2 Temperature Distribution

Isotherms around the cylinder are presented in Fig. 4.8 for $W - Al_2O_3$ (left side) and $EG : W - Al_2O_3$(right side) nanofluids for different P at $Re_{U_2} = 500$. Effect of the thermal boundary conditions on the isothermal lines is discussed by presenting both in same figure (solid lines : constant temperature and dashed lines : uniform heat flux). As both vorticity and thermal energy are being transported by the flow in the wake, contour lines of temperature are equivalent to those of vorticity for a particular base fluid. As can be seen in Fig. 4.8, insulation layer (thermal boundary layer) around the surfaces, especially at the front, lower and upper surfaces, decreases with the increase of pressure gradient. This is due to the fact that the incident velocity on the cylinder becomes stronger at higher P. It is worthy to note that the crowding of isotherms near the rear face in the recirculation region increases with pressure gradient with a noticeable change in the shape of isotherms for both base fluids as well as thermal boundary conditions. Therefore, by generating unsteadiness in the flow by increasing P, the heat transfer from the rear face is expected to improve. In other words, the rear hot face is washed out by the recirculating colder water or $EG : W$ vortex periodically in the process of vortex shedding. Though vorticity fields for both base fluids are reported exactly same at a same Re_{U_2}, the thermal boundary layer of $EG : W$ base fluid is found thinner than the water base fluid. Because vorticity equations for both base fluids are same at a particular Re_{U_2} but the energy equations are differ by constant coefficient involving Pr. Dashed lines are more crowder around the cylinder's surfaces than the solid lines at all P, indicating higher Nusselt number for q_w case than that for T_w case. Among all, the thinnest thermal boundary layer is observed for the heat flux case with $EG : W$ base fluid.

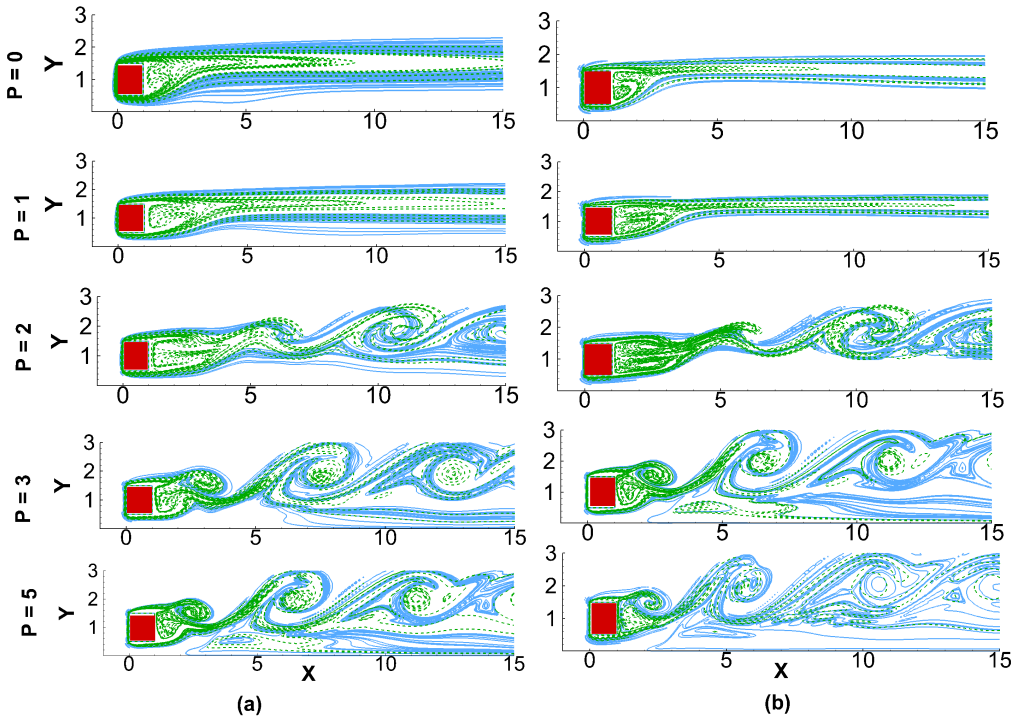

Figure 4.8: Instantaneous isotherms for C-P flow of (a) $W - Al_2O_3$ (left side) and (b) $EG : W - Al_2O_3$ (right side) for different P at $Re_{U_2} = 500$. Solid line (blue color) for constant temperature and dotted (green color) for uniform heat flux.

4.5.3 Heat Transfer Characteristics

Fig. 4.9 plots the time-averaged Nusselt number ($\overline{Nu}$) distribution around the cylinder surfaces for $W : CuO$ and $EG : W - CuO$ nanofluids and both thermal boundary conditions (T_w and q_w) when the pressure gradient is varied from P = 0 to 5 at a fix ϕ = 3%. As seen from Fig. 4.9, Nusselt number attains its local maximum at all the four corners having global maximum at the front top corner (point-1 in Fig. 4.9), because of steepest temperature gradient. Pattern of the $\overline{Nu}$-distribution along the front and top faces are qualitatively similar for all P, while along other two faces pattern can be classified into two categories (depending on values of P): steady case (for P = 0 and 1, similar to each other) and unsteady case (for P = 3 and 5, different for different P). The front face (0-1 in Fig. 4.9) shows higher heat transfer among all other faces since the incoming cold fluid first contacts the outgoing hot fluid surround the hot cylinder. Having maximum at point - 1, $\overline{Nu}$ decreases along the top face as we move downstream because fluid velocity

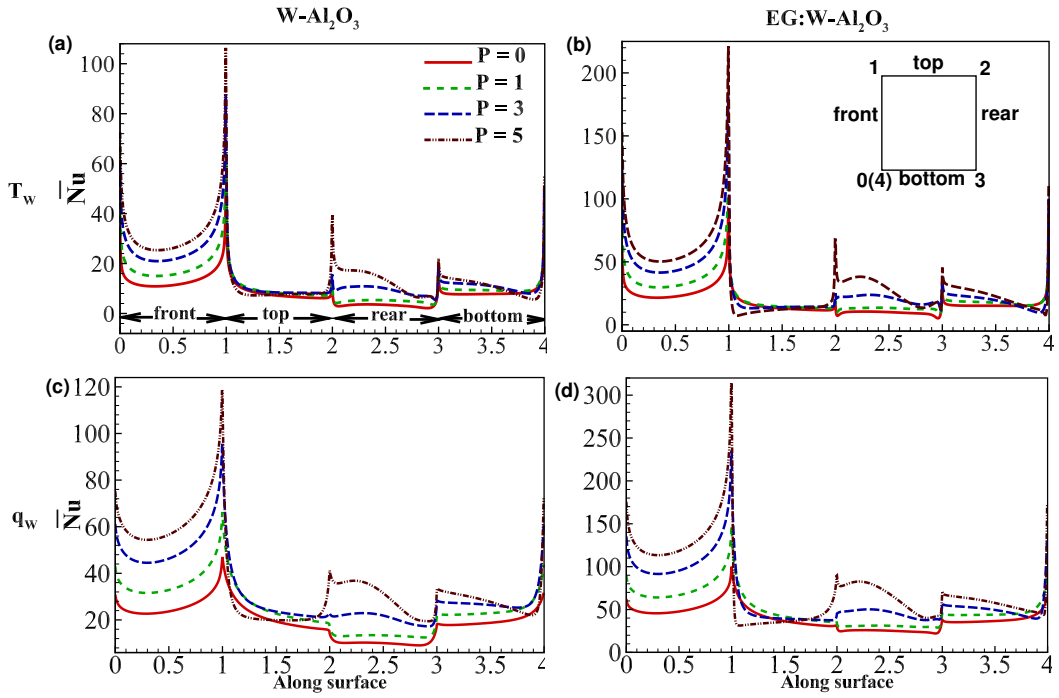

Figure 4.9: Time-averaged Nusselt number ($\overline{Nu}$) distribution around the cylinder for uniform temperature (1st row: (a)-(b)) and constant heat flux (2nd row: (c)-(d)), and $W - Al_2O_3$ (1st column: (a),(c)) and $EG : W - Al_2O_3$ (2nd column: (b), (d)) nanofluids for different P at $Re_{U_2} = 500$.

is much more at the point - 1. On the rear face, $\overline{Nu}$ variation for the steady case is almost negligible since the originating vortex is rotating on this face without being shed (ref. Fig. 4.3 and Fig. 4.8 for P = 0 and 1). On the other hand, an exchange of hot fluid adjacent to this face with ambient cold fluid is occurred due to shedding of vortices from the cylinder (ref. Fig. 4.3 and Fig. 4.8 for P = 3 and 5). In other words, the cavity formed by merging the upper and lower shear layers (originating from top and bottom faces, respectively) on the downstream side of the cylinder is forced to open during the vortex shedding process. As a result, cold fluid enters the cavity and hot fluid from the rear face could find a space to leave the hot face. At the bottom face, oscillation (unsteady case) and non-oscillation (steady case) of the positive shear of the cylinder make the difference in the $\overline{Nu}$ - distribution. While looking at the role of the non-linearity of incident velocity, it is clearly evident from the Fig. 4.9 that the total heat transfer from the cylinder is expected to be more as long as P is high. The Nusselt number value at each point on the surfaces

is found more for the heat flux case in comparison to the uniformly heated case for both nanofluids, and for $EG : W - Al_2O_3$ in comparison to $W - Al_2O_3$ nanofluid for both thermal conditions. These observations are consistent with what is observed in Figs - 4.3 and 4.8.

The dependencies of time-averaged-mean Nusselt number ($\overline{Nu}_M$) on pressure gradient (P) and concentration (ϕ) are discussed by presenting the contour lines $\overline{Nu}_M(P, \phi)$ = *constant* in Fig. 4.10 for all four nanofluids: 1st row: water, 2nd row: $EG : W$, 1st column : Al_2O_3 and 2nd column: CuO. A comparison between both thermal conditions is made by presenting contour lines of both cases in one frame here (solid line for constant temperature (T_w) and dashed lines for uniform heat flux (q_w)). As can be seen in Fig. 4.10 that all lines of T_w case are qualitatively similar to that of q_w case. $\overline{Nu}_M$ is an increasing function of both P and ϕ for both thermal conditions. But the effect of non-linearity of incident velocity (due to P) is more pronounced on $\overline{Nu}_M$ than that of concentration (ϕ). A critical dissertation on efficiency of pressure gradient (P) and concentration (ϕ) for heat transfer enhancement is made in Table - 4.4 and 4.5. One can easily see that for a particular contour value, the dashed line lies below the solid line, indicating that for a particular combination of P with ϕ, $\overline{Nu}_M$ registers higher value for q_w case in comparison to that for T_w case. Apparently, $\overline{Nu}_M$ is found more for $EG : W$ base fluid. Contour lines of both thermal conditions seems to be linear with concentration in this range of ϕ, especially for $EG : W - Al_2O_3$ nanofluid. The slope of lines is slightly more for $EG : W$ base fluid because nanoparticles are more effective in $EG : W$ than water base fluid (ref. Table - 3.1), and sensitivity of $\overline{Nu}_M$ on ϕ is found maximum in $EG : W - CuO$ nanofluid among all four nanofluids. Also, among all four nanofluids, $EG : W - CuO$ produces highest $\overline{Nu}_M$. These observations on $\overline{Nu}_M$ are consistent with what is predicted in Fig. 4.8 and 4.9. The difference between solid and dashed lines at lower P is less in $EG : W$ compared to water base fluid. Finally, it may be deduced that time-averaged-mean Nusselt number ($\overline{Nu}_M$) has strong dependency on angle of incident flow velocity (P) and base fluid, moderate dependency on concentration (ϕ) and type of thermal boundary condition, and a weak dependency on nanomaterials.

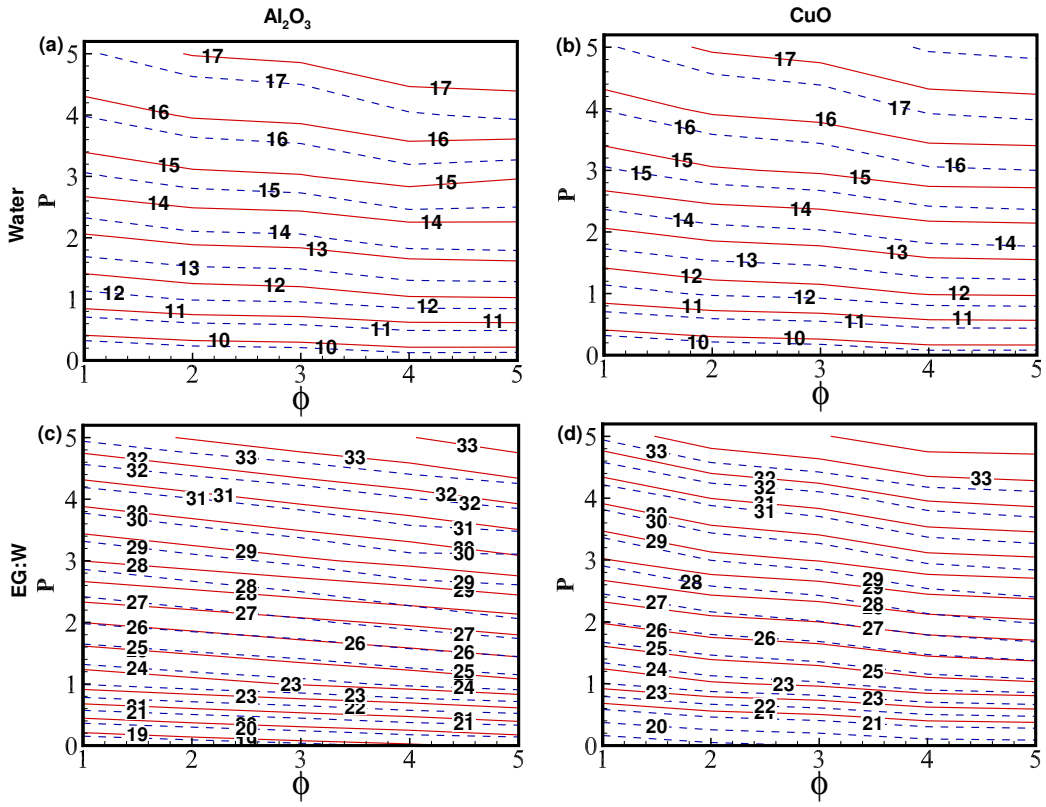

Figure 4.10: Contour plot for time-averaged-mean Nusselt number ($\overline{Nu}_M$) of cylinder as a function of ϕ and P for water (1st row: (a)-(b)) and $EG : W$ (2nd row : (c)-(d)) base fluids, and Al_2O_3 (1st column: (a), (c)) and CuO (2nd column: (b), (d)) nanomaterials at $Re_{U_2} = 500$. Solid lines for constant temperature (T_w) and dashed lines for constant heat flux (q_w).

The dependency of time-averaged mean Nusselt number ($\overline{Nu}_M$) on the main parameters (pressure gradient (P) and concentration (ϕ)) in the functional form for both base fluids and temperature conditions are discussed based on proposed relations written in Table - 4.1 for $\overline{Nu}_M = \overline{Nu}_M(P)$ at three $\phi = 0, 0.03$ and 0.05, and Table - 4.2 for $\overline{Nu}_M = \overline{Nu}_M(\phi)$ at three $P = 0, 3$ and 5). These relations are fitted using the least-square curve fitting method based on the computed values. Numerical values written in first bracket against each relation are the residual sum of squares (RSS) and coefficient of determination (R^2). An R^2 between 0 and 1 indicates the extent to which the dependent variable is predictable. An R^2 of 0.99 means that 99% is predictable. A small RSS indicates a tight fit of the model to the data. Among other possible functions, using this

Table 4.1: Propose dependency of time-average mean Nusselt number ($\overline{Nu}_M$) on pressure gradient (P) in the functional form $\overline{Nu}_M = \overline{Nu}_M(P)$ for fixed value of $\phi = 0\%, 3\%$ and 5% for both base fluids and thermal conditions.

$\phi\downarrow$		$Water$	$EG:W$
0%	T_w	$\overline{Nu}_M = 7.289ln(P+2.901)$ $(0.0406, 0.9989)$	$\overline{Nu}_M = \sqrt{(119.0P+234.9)}$ $(0.1625, 0.9987)$
	q_w	$\overline{Nu}_M = 7.822ln(P+3.160)$ $(0.0933, 0.9977)$	$\overline{Nu}_M = 14.61ln(P+3.272)$ $(0.7265, 0.9944)$
3%	T_w	$\overline{Nu}_M = 7.837ln(P+2.879)$ $(0.0398, 0.9990)$	$\overline{Nu}_M = \sqrt{(143.1P+284.6)}$ $(0.2395, 0.9984)$
	q_w	$\overline{Nu}_M = 8.429ln(P+3.129)$ $(0.1239, 0.9972)$	$\overline{Nu}_M = 15.99ln(P+3.294)$ $(0.5513, 0.9964)$
5%	T_w	$\overline{Nu}_M = 8.039ln(P+2.864)$ $(0.0566, 0.9987)$	$\overline{Nu}_M = \sqrt{(152.9P+304.2)}$ $(0.2658, 0.9983)$
	q_w	$\overline{Nu}_M = 8.705ln(P+3.089)$ $(0.1756, 0.9964)$	$\overline{Nu}_M = 16.36ln(P+3.329)$ $(0.9601, 0.9939)$

method the one which gives minimum RSS and maximum R^2 is chosen here. As seen in

Table 4.2: Propose dependency of time-average mean Nusselt number ($\overline{Nu}_M$) on concentration (ϕ) in the functional form $\overline{Nu}_M = \overline{Nu}_M(\phi)$ for fixed value of $P = 1, 3$ and 5 for both base fluids and thermal conditions.

$P\downarrow$		$Water$	$EG:W$
1	T_w	$\overline{Nu}_M = 0.3259\sqrt{\phi}+7.756$ $(0.0067, 0.9809)$	$\overline{Nu}_M = 0.8787\sqrt{\phi}+15.17$ $(0.0124, 0.9952)$
	q_w	$\overline{Nu}_M = 0.3714\sqrt{\phi}+8.831$ $(0.0103, 0.9778)$	$\overline{Nu}_M = 0.9199\sqrt{\phi}+17.25$ $(0.0154, 0.9945)$
3	T_w	$\overline{Nu}_M = 0.5354\sqrt{\phi}+13.04$ $(0.0692, 0.9317)$	$\overline{Nu}_M = 1.458\sqrt{\phi}+24.42$ $(0.0442, 0.9937)$
	q_w	$\overline{Nu}_M = 0.6226\sqrt{\phi}+14.35$ $(0.0589, 0.9559)$	$\overline{Nu}_M = 1.468\sqrt{\phi}+26.64$ $(0.1228, 0.9830)$
5	T_w	$\overline{Nu}_M = 0.7203\sqrt{\phi}+14.99$ $(0.0269, 0.9845)$	$\overline{Nu}_M = 1.607\sqrt{\phi}+28.86$ $(0.0626, 0.9927)$
	q_w	$\overline{Nu}_M = 0.8019\sqrt{\phi}+16.21$ $(0.0355, 0.9835)$	$\overline{Nu}_M = 0.1507\sqrt{\phi}+31.49$ $(0.0616, 0.9918)$

Tables - 4.1–4.3, R^2 value lies in $(0.98, 0.999)$ in all cases, implying that the considered relations are the best predicted. In order to validate these proposed relations, the relations $\overline{Nu}_M = \overline{Nu}_M(P)$ and $\overline{Nu} = \overline{Nu}_M(\phi)$ are plotted in Fig. 4.11 and Fig. 4.12, respec-

tively, and compared with the original (computed) data. It is evident that, except in Fig. 4.12$(a)-(c),(e)$ when ϕ is ranged only in $[0.04, 0.05]$, all the fitted curves correlate the original computed data/curves adequately. In this range of ϕ, the maximum deviation is 1.27% at $\phi = 5\%$. It may be noted that the nanofluid model for viscosity calculation used here is not well behaved with ϕ in this range of ϕ. The use of other nanofluid model for viscosity calculation where the viscosity increases continuously with ϕ would have given much more better approximation to the propose relations in the aforementioned range of ϕ also.

Mainly two types of functions are observed in Table- 4.1 and 4.2. Logarithmic function for $\overline{Nu}_M = \overline{Nu}_M(P)$ exists for water base fluid at both thermal conditions and all ϕ, and $EG : W$ base fluid at q_w condition and all ϕ; while radial or square root function for $\overline{Nu}_M = \overline{Nu}_M(P)$ exists for $EG : W$ basefluid at T_w conditions and all ϕ, and for $\overline{Nu}_M = \overline{Nu}_M(\phi)$ for both base fluids and thermal conditions at all P. Here the domain for $\overline{Nu}_M(\phi)$ starts at $\phi = 0$, but for $\overline{Nu}_M(P)$ starts around $P = -3$ or $P = -2$. The negative P is physically exists in Couette-Poiseuille flow, however, the present physical problem with given boundary condition (mainly at downstream) may not accept this negative P value. It is reconfirmed that all the functions ($\overline{Nu}_M(P)$ and $\overline{Nu}_M(\phi)$) are increasing functions (in P and ϕ, respectively) in both base fluids and both thermal conditions. It is observed that the slope of curves of $\overline{Nu}_M = \overline{Nu}_M(P)$ is more for q_w than T_w (for both base fluids at all ϕ), $EG : W$ than water (for both thermal conditions at all ϕ), and higher ϕ than lower ϕ (for both base fluids and thermal conditions). These can physically be interpreted as $\overline{Nu}_M(P)$ increases more rapidly with P for q_w (than T_w), $EG : W$(than water) and higher ϕ (than lower ϕ). A similar behaviour in $\overline{Nu}_M(\phi)$ with ϕ is also observed. In comparison to non-linear behaviour of $\overline{Nu}_M = \overline{Nu}_M(P)$, $\overline{Nu}_M = \overline{Nu}_M(\phi)$ behaves close to linearly within the considered range of ϕ in both base fluids and thermal conditions, which is consistent with what is recommended in Fig. 4.10.

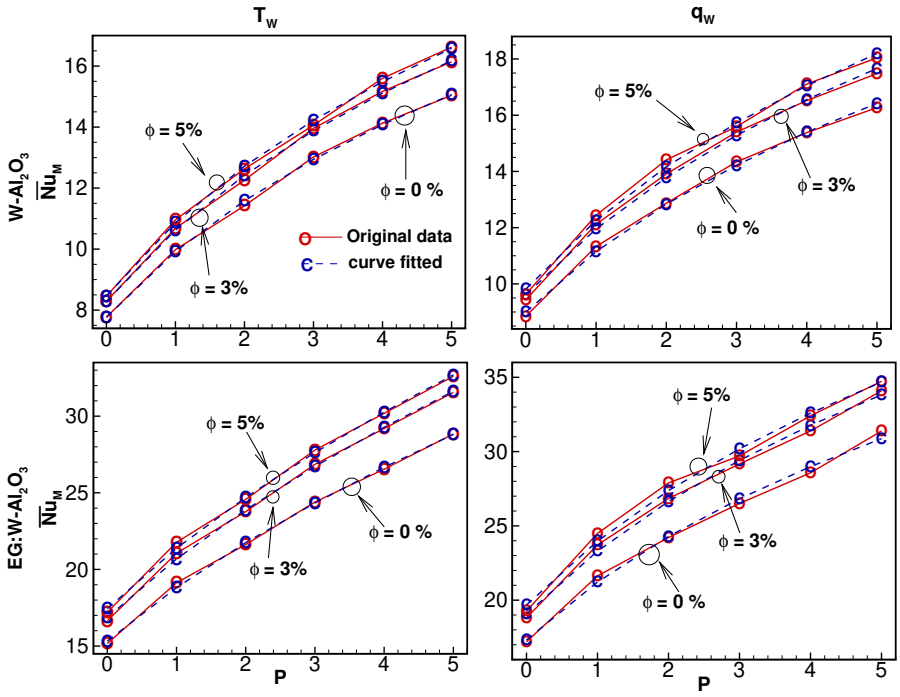

Figure 4.11: Validation of proposed relations for $\overline{Nu}_M = \overline{Nu}_M(P)$ (as noted in Table 4.1) with that of original computed data/curves for both base fluids and thermal conditions at $\phi = 0\%, 3\%$ and 5% and $Re_{U_2} = 500$.

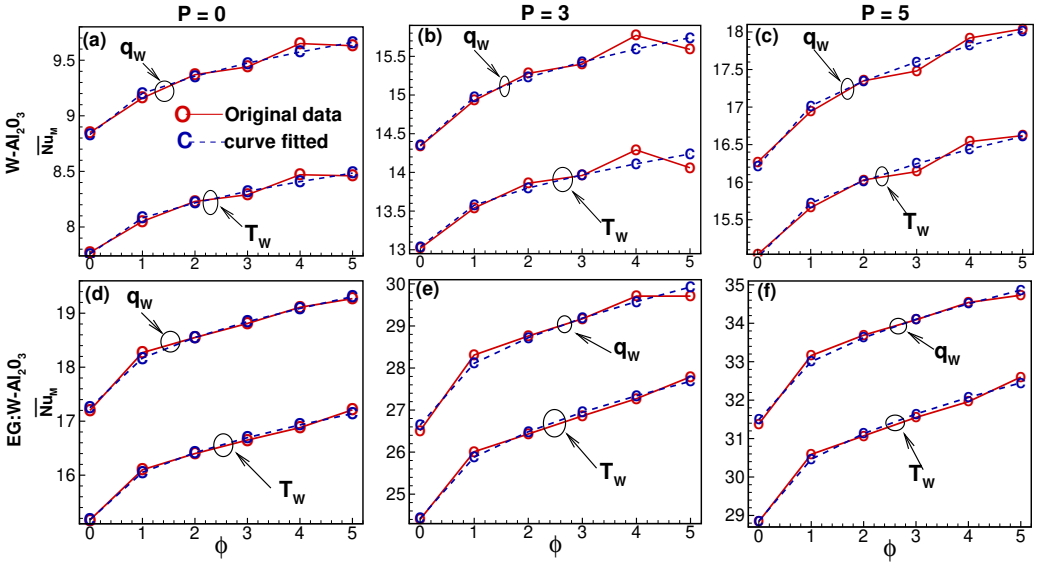

Figure 4.12: Validation of proposed relations for $\overline{Nu}_M = \overline{Nu}_M(\phi)$ (as noted in Table-4.2) with that of original computed data/curves for both base fluids and thermal conditions at $P = 0, 3$ and 5 and $Re_{U_2} = 500$.

Table 4.3: Propose dependency of time-average mean Nusselt number ($\overline{Nu}_M$) on concentration (ϕ) and pressure gradient(P) in the functional form $\overline{Nu}_M = \overline{Nu}_M(\phi, P)$ for both base fluids and thermal conditions.

Nanofluid	T_w	q_w
$W - Al_2O_3$	$\overline{Nu}_M$=0.1763ϕ+1.561P+8.345 (4.742, 0.9784)	$\overline{Nu}_M$=0.2077ϕ+1.577P+9.627 (8.552, 0.9626)
$W - CuO$	$\overline{Nu}_M$=0.2222ϕ+1.566P+8.291 (4.996, 0.9776)	$\overline{Nu}_M$=0.2495ϕ+1.583P+9.564 (8.147, 0.9648)
$EG : W - Al_2O_3$	$\overline{Nu}_M$=0.4013ϕ+2.915P+16.35 (10.29, 0.9865)	$\overline{Nu}_M$=0.3893ϕ+2.898P+18.94 (19.47, 0.9745)
$EG : W - CuO$	$\overline{Nu}_M$=0.4508ϕ+2.941P+16.36 (10.78, 0.9862)	$\overline{Nu}_M$=0.4948ϕ+2.960P+18.74 (17.93, 0.9776)

Further attempt is made to propose a functional form of dependency of $\overline{Nu}_M$ on both P and ϕ, and relations are listed in Table - 4.3 for all the four nanofluids at both thermal conditions. As seen in Table - 4.3, $\overline{Nu}_M$ is linearly related to both P and ϕ for all cases. While comparing the equations and their coefficients, all the observations made so far on the dependency of $\overline{Nu}_M$ on base fluids, pressure gradient, concentration, thermal conditions and materials can be reconfirmed from these explicit functional form of $\overline{Nu}_M$.

The effectiveness of pressure gradient (P) on the heat transfer ($\overline{Nu}_M$) at each ϕ is analysed based on effective parameter $E_P = \left(\frac{\overline{Nu}_{M|_P}}{\overline{Nu}_{M|_{P=0}}} - 1 \right) * 100$ presented in Table - 4.4 (values written in normal font for T_w and bold for q_w) for all four nanofluids and ϕ. The values of E_P are presented in tabular form because it was very difficult to access the change in E_P due to ϕ variation in the graphical representation of $E_P(P, \phi)$ = *constant*. As seen in Table - 4.4, change in $\overline{Nu}_M$ due to ϕ occurs at third digit only. That is, the ratio $\frac{\overline{Nu}_{M|_P}}{\overline{Nu}_{M|_{P=0}}}$ is almost same while varying ϕ because $\overline{Nu}_M$ at a particular P is normalised by the respective value at $P = 0$, not by at $\phi = 0$. Notwithstanding the percentage of enhancement of the heat transfer due to increased pressure gradient in the non-linear incident velocity (with respect to its value at linear velocity) is very noticeable at both the thermal conditions, and for all the nanofluids and ϕ. The maximum jump (around 28%

Table 4.4: Effectiveness of pressure gradient (P) on time-averaged-mean-Nusselt number ($\overline{Nu}_M$), defined as $E_P = (\frac{\overline{Nu}_{M|_P}}{\overline{Nu}_{M|_{P=0}}} - 1) \times 100$, for all four nanofluids and both thermal conditions at all ϕ. Values written in normal font for constant temperature (T_w) and bold for uniform heat flux (q_w).

$\phi \rightarrow$ / $P \downarrow$		1%		2%		3%		4%		5%	
		Al_2O_3	CuO	Al_2O_3	CuO	Al_2O_3	CuO	Al_2O_3	CuO	Al_2O_3	CuO
1	W	28.70	28.54	28.80	28.47	28.83	28.40	29.04	28.52	29.55	28.99
		28.39	**28.24**	**28.50**	**28.10**	**28.39**	**28.02**	**28.60**	**28.12**	**29.18**	**28.76**
	$EG:W$	26.58	26.26	26.34	26.12	26.49	26.01	26.66	26.16	26.50	26.88
		26.11	**26**	**26.15**	**25.85**	**26.10**	**25.71**	**26.43**	**25.95**	**27.09**	**26.61**
2	W	47.83	47.64	48	47.53	47.89	47.49	48.29	47.73	49.29	48.43
		47.93	**46.78**	**47.81**	**46.45**	**47.35**	**46.38**	**48.60**	**46.52**	**47.64**	**47.70**
	$EG:W$	42.92	43.20	42.5	42.94	42.76	42.86	43.07	43.08	42.77	44.21
		42.64	**42.62**	**42.64**	**41.84**	**42.69**	**41.80**	**43.22**	**42.19**	**44.73**	**43.71**
3	W	68.20	67.99	68.41	68.03	68.40	68.14	68.71	68.34	66.19	68.68
		62.99	**62.81**	**63.07**	**62.67**	**63.14**	**62.75**	**63.42**	**62.88**	**61.89**	**63.77**
	$EG:W$	61.55	61.02	61.16	61.04	61.32	61.01	61.55	61.16	61.48	61.53
		54.95	**54.74**	**55.04**	**54.64**	**55.08**	**54.47**	**55.47**	**54.88**	**54.18**	**55.42**
4	W	82.73	82.38	82.99	82.27	82.99	82.10	83.35	82.54	84.40	83.47
		74.89	**74.81**	**75.13**	**74.66**	**75**	**74.50**	**75.65**	**74.74**	**77.67**	**76.25**
	$EG:W$	75.59	75.05	75.12	74.97	75.32	74.94	75.53	75.06	75.36	75.78
		66.89	**66.76**	**66.90**	**66.68**	**66.88**	**66.56**	**67.19**	**66.80**	**68.19**	**67.45**
5	W	94.53	94.17	94.78	93.97	94.69	93.91	95.28	94.18	96.45	95.34
		84.94	**84.73**	**85.17**	**84.62**	**85.17**	**84.58**	**85.7**	**84.76**	**87.33**	**86.08**
	$EG:W$	90.0	89.63	89.45	89.87	89.49	90.0	89.34	89.71	89.42	89.28
		81.50	**81.90**	**81.62**	**82.68**	**81.23**	**82.97**	**80.74**	**82.43**	**80.23**	**80.45**

for water and 26% for $EG:W$) is reported while changing the pattern of incident velocity from linear ($P = 0$) to its first non-linear ($P = 1$) profile. In particular, the enhancement rate is more for T_w case in comparison to q_w case, and the difference in E_P between two thermal boundary conditions increases with P for both base fluids and nanomaterials at all ϕ. Though the values of $\overline{Nu}_M$ were reported more for $EG:W$ (than water) base fluid and CuO (than Al_2O_3) material in Fig. 4.10, an opposite behaviour of E_P with base fluid and

Table 4.5: Effectiveness of concentration (ϕ) on time-averaged-mean-Nusselt number ($\overline{Nu}_M$), defined as $E_\phi = \left(\frac{\overline{Nu}_{M|_\phi}}{\overline{Nu}_{M|_{\phi=0}}} - 1\right) \times 100$, for all four nanofluids and both thermal conditions at all P. Values written in normal font for constant temperature (T_w) and bold for uniform heat flux (q_w).

$\phi \rightarrow$ $P \downarrow$		1%		2%		3%		4%		5%	
		Al_2O_3	CuO	Al_2O_3	CuO	Al_2O_3	CuO	Al_2O_3	CuO	Al_2O_3	CuO
0	W	3.604 **3.512**	3.73 **3.63**	5.92 **5.89**	6.69 **6.57**	6.692 **6.68**	7.85 **7.70**	9.009 **9.052**	10.55 **10.52**	8.88 **8.826**	10.55 **10.41**
	$EG:W$	6.13 **6.22**	6.196 **5.99**	8.11 **7.85**	9.29 **9.07**	9.756 **9.36**	10.74 **10.58**	11.27 **11.10**	13.38 **13.14**	13.45 **12.03**	13.78 **13.60**
1	W	3.808 **3.80**	3.81 **3.80**	6.212 **6.27**	6.71 **6.620**	7.014 **6.973**	7.82 **7.679**	9.52 **9.532**	10.62 **10.59**	9.82 **9.797**	11.02 **11.03**
	$EG:W$	6.53 **6.519**	6.325 **6.195**	8.31 **8.18**	9.304 **9.154**	10.09 **9.66**	10.66 **10.54**	11.76 **11.70**	13.43 **13.31**	13.80 **13.22**	14.48 **14.38**
2	W	4.203 **5.284**	4.203 **4.584**	6.65 **7.615**	7.09 **7.304**	7.356 **8.081**	8.23 **8.392**	9.982 **11.42**	11.12 **11.34**	10.60 **11.97**	11.65 **12.12**
	$EG:W$	6.429 **7.64**	6.707 **7.39**	8.09 **9.293**	9.62 **9.91**	9.94 **10.86**	11.01 **11.40**	11.70 **13.05**	13.83 **14.29**	13.64 **15.20**	15.12 **15.99**
3	W	3.993 **4.114**	3.99 **4.114**	6.452 **6.56**	6.99 **6.97**	7.22 **7.392**	8.22 **8.16**	9.75 **9.972**	11.06 **11.09**	7.99 **8.717**	11.29 **11.58**
	$EG:W$	6.598 **6.79**	6.31 **6.413**	8.320 **8.49**	9.43 **9.43**	10.08 **10.03**	10.86 **10.83**	11.76 **12.05**	13.61 **13.69**	13.89 **12.07**	14.26 **14.56**
4	W	4.104 **4.161**	4.03 **4.23**	6.582 **6.697**	6.94 **7.087**	7.36 **7.412**	7.997 **8.127**	9.908 **10.21**	10.97 **11.12**	10.40 **11.25**	11.54 **11.96**
	$EG:W$	6.518 **6.72**	6.25 **6.41**	8.214 **8.37**	9.307 **9.45**	9.984 **9.87**	10.74 **10.89**	11.64 **11.83**	13.45 **13.62**	13.72 **13.44**	14.32 **14.53**
5	W	4.122 **4.118**	4.056 **4.118**	6.582 **6.64**	6.914 **7.007**	7.314 **7.44**	8.05 **8.113**	9.973 **10.14**	10.90 **11.06**	10.51 **10.88**	11.57 **11.74**
	$EG:W$	6.07 **5.67**	7.419 **5.67**	7.73 **7.36**	9.15 **9.21**	9.397 **8.64**	10.68 **10.90**	10.82 **10.07**	13.14 **13.13**	13.04 **10.68**	13.28 **12.36**

material is observed in Table - 4.4. Overall, the maximum enhancement of heat transfer from the cylinder registers in $W - Al_2O_3$ nanofluid at $P = 5$ for T_w, where the value of $\overline{Nu}_M$ reaches almost double the value at $P = 0$. The effectiveness of nanofluid on the heat transfer at each P is deliberated based on the parameter $E_\phi = \left(\frac{\overline{Nu}_{M|_\phi}}{\overline{Nu}_{M|_{\phi=0}}} - 1\right) * 100$ noted in Table - 4.5 (values written in normal font for T_w case and bold font for q_w) for both the thermal conditions. From the table, one can find a noticeable change in E_ϕ due to ϕ at each value of P for both T_w and q_w and all four nanofluids. However, the rate of percentage enhancement of heat transfer is not uniform with ϕ for water base fluid at

both thermal conditions. The maximum enhancement is observed while changing ϕ from $0-1\%$, followed by from $3-4\%$, $1-2\%$, $2-3\%$ and $4-5\%$ at all P considered here for both T_w and q_w. For the $EG:W$ base fluid, the maximum enhancement is also found at $\phi = 0-1\%$, but the rate at which E_ϕ increases is almost uniform during $\phi = 1-4\%$. Contrary to the lowest enhancement rate of E_ϕ in $\phi = 4-5\%$ for water base fluid, here at $EG:W$ base fluid the aforementioned rate is found highest in this range of ϕ in comparison to other non-zero ϕ at both thermal conditions and nanomaterials. While comparing the efficiency of nanomaterials, it is observed that the CuO material is slightly more effective in the base fluid for heat transfer than the Al_2O_3 material. For linear shear flow ($P = 0$), E_ϕ is found more for T_w than that for q_w for all four nanofluids, consistent with what is observed in Couette flow (Chapter-3). However, an opposite situation (E_ϕ for T_w is less than that for q_w) is noticed in Table - 4.5 while changing velocity profile from linear to non-linear.

4.5.4 Hydrodynamic Characteristics

Dependencies of time-averaged drag coefficient ($\overline{C_D}$) on P, ϕ, nano-materials, base fluid and thermal boundary condition are discussed based on the contour plot of $\overline{C_D}(P, \phi)$ = *constant* presented in Fig. 4.13. It is clearly seen from Fig. 4.13 that $\overline{C_D}$ increases with P, but almost insensitive to ϕ, increases very nominally with ϕ. It may be noted that the increase of Reynolds number is mechanically similar to the increase of P since $-(\frac{dp}{dx}) = 2P(1/h)^2(1/Re_{U_2})$. Therefore the change in P will have much effect on the flow field, consequently on the hydrodynamic characteristics. It is worthwhile noting that at a particular P, $\overline{C_D}$ value is almost same for all four nano fluids, this reconfirm the observation of the same flow features (i.e., pressure and velocity, constitutive components for hydrodynamic forces) for both base fluids at same Re_{U_2} discussed in Figs. 4.3 - 4.4. Moreover, the coefficient $\frac{\nu_{nf}}{\nu_f}$ of the diffusion term of the momentum equations at $Re_{U_2} = 500$ is found almost same (change occurs at third/fourth decimal places) for all four fluids for a particular P. Different $\overline{C_D}$ is expected in the situation when the incident velocity is same (for Fig. 4.3 and 4.5). One can see that though there is some difference

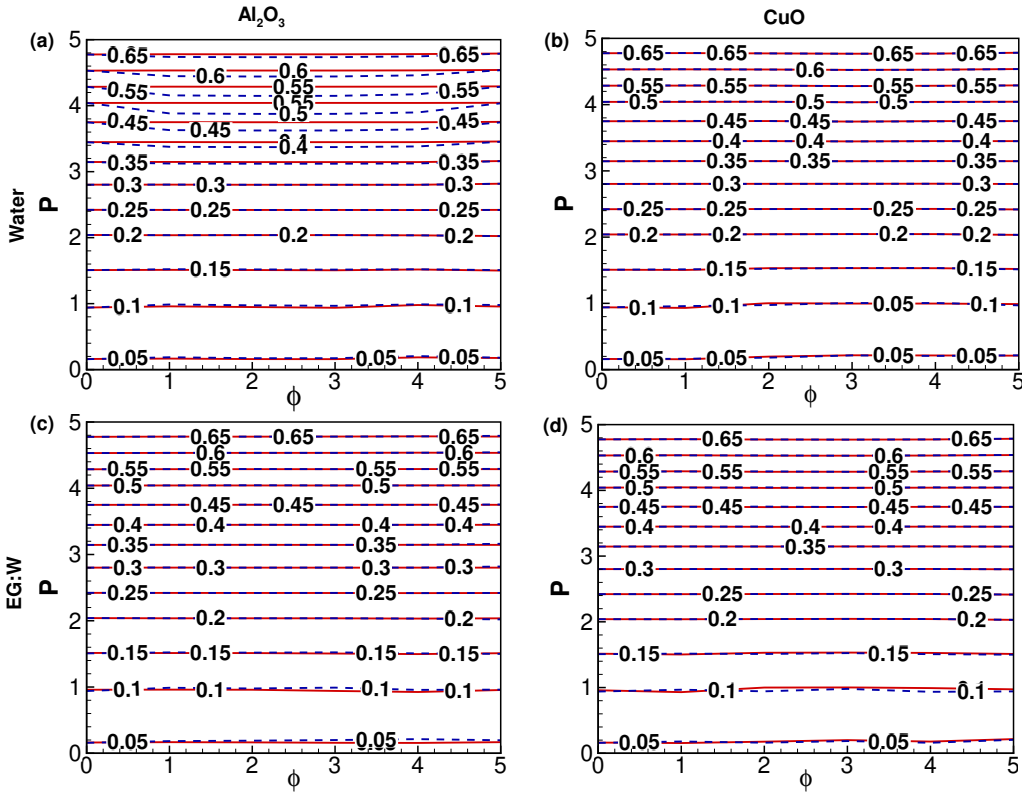

Figure 4.13: Contour plot for time-averaged drag coefficient ($\overline{C_D}$) for different ϕ and P for water (1st row: (a)-(b)) and $EG : W$ (2nd row : (c)-(d)) base fluids, and Al_2O_3 (1st column: (a), (c)) and CuO (2nd column: (b), (d)) nanomaterials at $Re_{U_2} = 500$. Solid lines for constant temperature (T_w) and dashed lines for constant heat flux (q_w).

in $\overline{C_D}$ between T_w and q_w cases at larger $P(> 3)$, but at lower P, $\overline{C_D}$ is almost insensitive to the thermal boundary condition also.

4.6 Conclusion

A numerical study is conducted on a physical problem of heat transfer from a square cylinder (either uniformly heated T_w or uniform heat flux q_w) placed near a wall under the incident of Couette-Poiseuille flow using nanofluids. An effort is made to enhance the heat transfer from the cylinder due to variation in pressure gradient at the inlet (P) and concentration (ϕ) of nanomaterials (Al_2O_3 and CuO) in both base fluids for both thermal conditions. The major observations (against the main issues motivating the present study) are:

1. The flow around the cylinder (of both thermal conditions) is reported unsteady for $P > 2$ in all four nanofluids at $Re_{U_2} = 500$.

2. At a fixed P, hydrodynamic characteristics (vorticity, spectra and forces) are found exactly same for both base fluids at a Re_{U_2} due to mechanical similarity, on the contrary, the heat transfer characteristics (isotherms and Nusselt number) are eventually different for two base fluids due to difference in Prandtl number.

3. It is also shown that $EG : W$ based nanofluids flow over the cylinder can be made steady at all considered P ($0 \leq P \leq 5$) by taking the characteristic velocity same as water at $Re_{U_2} = 500$. The crowding of isotherms near the rear face in the recirculation region increases with P.

4. $\overline{Nu}_M$ has strong dependency on P (increases with P) and base fluid ($EG : W$ produces more), moderate dependency on ϕ (increases with ϕ) and type of thermal boundary conditions (q_w produces more), and weak dependency on nanomaterials (more for CuO). These observations are reconfirmed based on functional form of $\overline{Nu}_M = \overline{Nu}_M(P)$, $\overline{Nu}_M = \overline{Nu}_M(\phi)$, and hence $\overline{Nu}_M = \overline{Nu}_M(P, \phi)$ proposed by the least-square curve fitting method.

5. Though $\overline{Nu}_M$ is reported more for q_w (than T_w) condition , $EG : W$ (than water) base fluid and CuO (than Al_2O_3) material, an opposite behaviour in the enhancement rate of $\overline{Nu}_M$ with the thermal condition, base fluids and materials is observed. The maximum enhancement of $\overline{Nu}_M$ attains in $W - Al_2O_3$ nanofluid at $P = 5$ for T_w condition, where $\overline{Nu}_M$ registers a value double the value at $P = 0$. Efficiency of concentration (ϕ) on enhancement of $\overline{Nu}_M$ is found more for T_w than that for q_w at linear incident velocity, however, this behaviour of efficiency with the thermal condition becomes opposite upon changing the velocity profile from linear to its non-linear.

Chapter 5

Influence of Position of Upstream Cylinder of Different Size on Heat Transfer around Heated Square Cylinder

5.1 Introduction

The study of fluid flow and heat transfer around multiple bluff bodies has become a subject of considerable importance in recent years (e.g. Alam et al. [92]; Kim et al. [93]; Maiti [94]; Zafar and Alam [95]) because of its extensive applications in various industrial fields, such as cooling of glass, electronic equipment, drying of different materials and so on. It is important to understand the flow and its control over bluff bodies so that engineering design and public comfort can be improved continuously (e.g. Alam et al. [96], [97], [98], [99]; Kim et al. [100]). Various studies have been carried out numerically as well as experimentally related to heat transfer characteristics of flow past bluff bodies. When the flow passes over multiple cylinders, a complex flow structure originates as a

consequence of the mutual interactions among them. The wake structure forming behind the obstacles strongly depends on the shape and arrangement of the bodies and on the incoming flow. The flow becomes even more complicated when the wakes are further influenced by heat transfer and/or loading of nanoparticles in the base fluid.

Flow and heat transfer characteristics of a rectangular cylinder exposed to a uniform flow with ground effect have been studied by Shuja et al. [35]. Yang and Fu [36] studied the unsteady heat transfer from a heated electronic component subjected to a flow. Wang and Jaluria [37] found that the heat transfer rate from a heated block increases with the height for fixed width, and decreases with increasing the width when the height is fixed. Maiti and Bhatt [87] investigated the effect of pressure gradient at the inlet and observed that the steady flow converts to a periodic flow with the increase in pressure gradient .

Devarakonda [101] did an extensive study of the unsteady flow past a pair of square cylinders in tandem arrangement through an experimental-numerical approach. He concluded that the presence of the eddy promoter enhances the heat transfer from the downstream cylinder. A similar study was done by Tatsutani et al. [102] for cylinder diameter ratio 2 (based on the upstream cylinder diameter) in which the smaller cylinder was placed at an optimal location, upstream of the large heated cylinder, which resulted in a maximum heat transfer from the downstream cylinder. Sohankar and Etminan [2] numerically studied the heat transfer from tandem square cylinders and observed that the Nusselt number is larger for the upstream cylinder. Etminan et al. [103] numerically studied the unconfined flow characteristics around the tandem square cylinders in both steady and unsteady laminar flow regimes at a fixed spacing, i.e. S = 5. Chatterjee and Mondal [1] reported the effect of spacing between the cylinders on heat transfer enhancement at different Reynolds numbers.

It is equally important to note that the heat transfer can be enhanced by the loading of nanoparticles in the base fluid. Several numerical studies on convective laminar heat transfer using nanofluids as working fluid are reported in the literature. The fundamental studies on convective transport of nanofluids are rapidly increasing for engineering applications such as automotive sector, nuclear reactors, cooling of electronics and X-rays

(Nguyen et al. [49], Escher et al. [82], Ahmed et al. [83], and Sarkar et al. [104]).

Hwang et al. [44] reported that the solution (water- based Al_2O_3 nanofluids) is more stable than the base fluid. Sarkar et al. [105] presented the global stability of nanofluids in a mixed convective flow at the onset of vortex shedding. For the unconfined flow of nanofluids over a square cylinder, Etminan et al. [4] reported that there is an optimum value of ϕ that results in the highest heat transfer coefficient. Based on water-based nanofluids (using Cu and Al_2O_3), Sarkar et al. [106] studied heat transfer characteristics past a circular cylinder in cross flow and observed that the presence of nanoparticles imparts a counterbalancing force to that of buoyancy force. For the case of square cylinders, Sarkar et al. [107] observed that Cu-water and Al_2O_3 – water nanofluids show suppression of vortex shedding at Richardson number $Ri \geq 0.15$. Vortex shedding initiates and a completely new phenomenon comes into being when ϕ is increased.

Valipour et al. [72] indicated that, at a given Reynolds number Re, local time-mean Nusselt number $\overline{Nu}$ were enhanced by adding nanoparticles to the base fluid. Talebi et al. [108] found that for any given Re and Rayleigh number Ra, heat transfer in the enclosure, filled with Cu-water nanofluid with a moving top wall, increases with the volumetric fraction of the copper nanoparticles in the water. Rayleigh-Benard problem was examined by Haddad et al. [84] in which they observed that an enhancement in heat transfer is more pronounced at low volume fraction of nanoparticles under the effect of Brownian motion and thermophoresis for Cu-water nanofluid. Sarkar and Ganguly [59] demonstrated the entropy generation due to laminar mixed convection of water-based nanofluid (using Cu, Al_2O_3) past a square cylinder in vertically upward flow with the range of ϕ:0–20%. In the previous chapters, we have already seen the effect of concentration (ϕ), particle size (d_{np}), type of base fluids and nanoparticles on heat transfer from a long heated square cylinder placed near a cold wall under the incident of a Couette flow/ Couette Poiseuille flow and observe that the Nusselt number is an increasing function of ϕ and P while it decreases with the increase of d_{np} .

5.2 Objectives

From the above review, it is obvious that investigations on the heat transfer from a cylinder in the presence of another cylinder in a flow with nanofluids are scarce. To the best of our knowledge, not a single article is available based on the heat transfer around a square heated cylinder (DSC) in the presence of another upstream rectangular cylinder (UREP) near a wall under the incident of nonlinear velocity profile utilizing nanofluids. The main objective of this study is to enhance the heat transfer from the DSC due to
(i) the flow instability by employing the UREP of optimum size placed at suitable distance, and
(ii) by loading of nanoparticles in the base fluid.

Here the horizontal centerline of both the cylinders, bisecting the height of cylinders, is aligned. More specifically, objectives are classified as:

1. Yang and Fu [36] reported that the heat flux for the case of flow with vortex shedding was higher than that of the without vortex shedding. It is worthy to note from the previous studies that the unsteadiness in the steady flow of DSC is generated by employing a UREP of aspect ratio $r_1 < 1$. Therefore, the dependency of hydrodynamic and heat transfer characteristics of DSC on the parameters: r_2 , r_1 and S is studied.

2. The role of reduction of the height (and hence thinning) of the UREP on the total heat transfer from the DSC due to combined effect of the shedding frequency and perturbation amplitude is studied.

3. The role of the nondimensional pressure gradient P at the inlet and of the nanoparticle concentrations (ϕ) on the hydrodynamic and heat transfer characteristics of the heated cylinder (DSC) is investigated. An effort is made to examine the mechanism of improvement/reduction of drag coefficient of and heat transfer from the heated cylinder in the presence of the upstream cylinder (UREP).

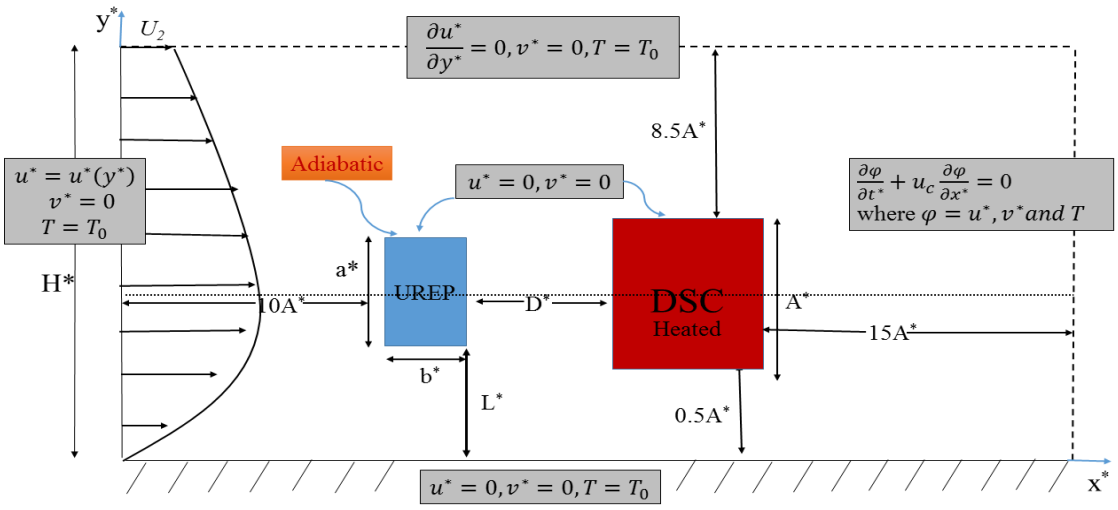

Figure 5.1: Schematics of flow configuration. DSC: Downstream square cylinder, UREP: Upstream rectangular eddy promoter.

5.3 Modelling

5.3.1 Problem Formulation

A square heated cylinder (hereafter, it will be referred as DSC) of height A^* is placed parallel to the wall (lying along x^* axis) at a fixed gap-height of $0.5A^*$ from the wall. Another cylinder of aspect ratio b^*/a^* with height a^* and width b^* (hereafter, it will be referred as UREP) is placed at a distance D^* at the upstream side of the square cylinder and parallel to the wall at a gap height of L^* from the wall. The upstream flow field is taken as Couette-Poiseuille flow based non-linear velocity profile. Detailed discussion on consideration of Couette-Poiseuille flow can be found in Chapter-4.

5.3.2 Governing Equations with Initial and Boundary Conditions

The flow is considered as two dimensional and laminar while the fluid is taken as nanofluid. To the best of authors' knowledge, almost all the available studies on nanofluid flow over circular/triangular/square type bodies are based on a single- phase modeling approach, and therefore it is adopted here. The non-dimensional Navier-Stokes equations along with the energy equation governing the nanofluid flow and heat transfer character-

istics are given by:

$$\frac{\partial u}{\partial x} + \frac{\partial v}{\partial y} = 0, \tag{5.1}$$

$$\frac{\partial u}{\partial t} + \frac{\partial u^2}{\partial x} + \frac{\partial uv}{\partial y} = -\frac{\partial p}{\partial x} + \frac{1}{Re} * \frac{\nu_{nf}}{\nu_f}(\frac{\partial^2 u}{\partial x^2} + \frac{\partial^2 u}{\partial y^2}), \tag{5.2}$$

$$\frac{\partial v}{\partial t} + \frac{\partial uv}{\partial x} + \frac{\partial v^2}{\partial y} = -\frac{\partial p}{\partial y} + \frac{1}{Re} * \frac{\nu_{nf}}{\nu_f}(\frac{\partial^2 v}{\partial x^2} + \frac{\partial^2 v}{\partial y^2}), \tag{5.3}$$

$$\frac{\partial \theta}{\partial t} + \frac{\partial u\theta}{\partial x} + \frac{\partial v\theta}{\partial y} = \frac{\alpha_{nf}}{\alpha_f} * \frac{1}{RePr}(\frac{\partial^2 \theta}{\partial x^2} + \frac{\partial^2 \theta}{\partial y^2}). \tag{5.4}$$

Here u and v denote the non-dimensional velocity components along the $x-$ and $y-$ direction, respectively, t is the time, and α is the thermal diffusivity. The governing equations are non-dimensionalised by A^*, U_2 and $\rho_{nf}{U_2}^2$. Here U_2 is the velocity of the top plane wall at the gap height H^* from the plane wall. Prandtl number (Pr) and non-dimensional temperature (θ) are respectively, defined as $Pr = \frac{\nu_f}{\alpha_f}$ and $\theta = \frac{T - T_0}{T_w - T_0}$.
The nanofluid flow is characterized by the following parameters:
(i) Non dimensional pressure gradient P at the inlet,
(ii) Reynolds number: $Re = \frac{U_2 A^*}{\nu_f}$,
(iii) Inter-cylinder spacing distance : $S = \frac{D^*}{A^*}$,
(iv) Aspect ratio of the UREP: $r_1 = \frac{b^*}{a^*}$, and
(v) Ratio of heights of cylinders: $r_2 = \frac{a^*}{A^*}$.
Following are the boundary conditions used in this study to solve equations (5.1) - (5.4):
$u = v = 0$ at the plane wall ($y = 0$) and on the surfaces of both the cylinders.
At the top lateral boundary: $\frac{\partial u}{\partial y} = 0$, $v = 0$ and $T = T_0$.
At the outlet boundary, sommerfield condition is taken.

$$\frac{\partial \phi}{\partial t} + u_c \frac{\partial \phi}{\partial x} = 0.$$

where, $\phi = u, v$ and θ.

The DSC is maintained at a constant temperature T_w , while the UREP is considered as an

adiabatic. The wall and ambient stream are considered to be at T_0 with $T_0 < T_w$. The flow is assumed to start impulsively at a particular value of Re_{U_2} . A time-independent stable numerical solution is achieved by advancing the flow field variables through a sequence of short time steps of duration Δt.

5.3.3 Nanofluid Modelling

Density, effective viscosity, Specific heat, and thermal conductivity of nanofluids are calculated from relations discussed in Chapter - 1. The detailed discussion on the calculation of the thermophysical properties of nanofluids, like density, specific heat, thermal conductivity and viscosity is available in Chapter - 2. Nanofluid is considered as $W - Al_2O_3$. Parameters governing the nanofluid is particle concentrations (ϕ). Diameter of the nanoparticle d_{np} is considered as 50nm. Thermophysical properties are calculated at room temperature 300K.

5.4 Numerical Methodology

The computational domain is divided into cartesian cells. The pressure correction based iterative algorithm SIMPLE, based on finite volume method (FVM) with staggered grids, is applied here. A third order accurate QUICK (Quadratic Upstream Interpolation for Convective Kinematics) is employed to discretise the convective terms and central differencing for diffusion terms. A fully implicit third order scheme is incorporated to discretise the time derivatives. The pressure link between continuity and momentum is accomplished by transforming the continuity equation into a Poisson equation for pressure. The Poisson equation implements a pressure correction for a divergent velocity field. A detailed discussion of the numerical methodology (staggered grid, FVM, QUICK and SIMPLE algorithms) used here is made in Chapter-1.

5.4.1 Size of Computational Domain and Consideration of Grid

The height of the top lateral boundary and inflow boundary is chosen large enough so that the influence of the boundary conditions on the wall shear stress is very weak. The inflow boundary is kept at a distance $10A^*$ from the front face of the UREP while

the top lateral boundary lies at $8.5A^*$ from the top face of the DSC. The distance of the outflow boundary from the DSC rear face is taken as $15A^*$ since convective boundary condition at the outlet is used here. A non-uniform grid distribution is considered in the computational domain distributing uniform grids along the surfaces of both the cylinders with expansion factors for the far-fields (away from the surfaces). A symmetry grid (along the x-dir. about the mid-line in spacing distance between the cylinders) is incorporated. The number of grids are varied between 475 $\times$ 250 and 850 $\times$ 600. The time step is considered as 10^{-4}.

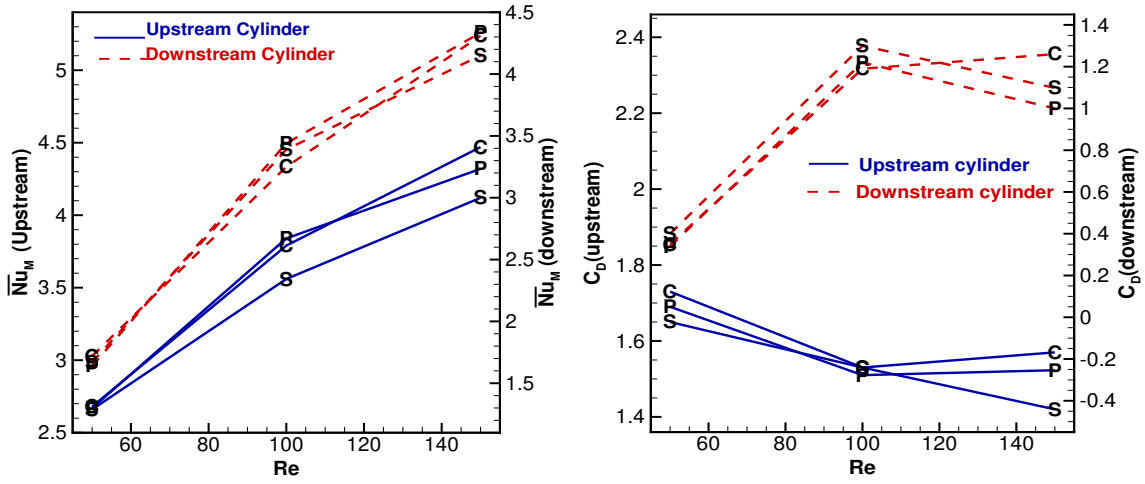

Figure 5.2: Validations of (a) present time- and surface-averaged Nusselt numbers and (b) time-mean drag coefficients with those of Chatterjee and Mondal [1] (C) and Sohankar et al. [2] (S) for S = 5. Here P: Present results.

5.4.2 Validation of Numerical Code

The numerical code is already validated for the case of nanofluid modeling and single cylinder with Etminan et al. [4] and presented in Table-2.3 in Chapter-2. The numerical code for the cases of heat transfer around two equal isothermal square cylinders placed in a tandem arrangement is validated with Chaterjee and Mondal [1] and Sohankar and Etminan. [2] for different values of Re and presented in Figs. 5.2(a) and 5.2(b). An excellent match between the two results in time- and surface-mean $\overline{Nu}_M$ as well as drag

coefficient (C_D) for both upstream and downstream cylinders are observed.

5.5 Results and Discussion

Numerical simulations are presently performed to examine the effects of particle concentration ϕ, pressure gradient P, spacing between cylinders S, aspect ratio r_1 and height ratio r_2 on hydrodynamic and heat transfer characteristics of the DSC. The Re is kept constant at 250, and the value of Pr is taken as 6.14 for $W - Al_2O_3$ nanofluid. It may be noted that, due to variation in ϕ, only physical properties of nanofluid (ν_{nf} and α_{nf}) are changed, which are reflected in Eqs. 5.2 - 5.4.

The consideration of the values of the parameters are as follows:

(i) r_2 = 1.0 and 0.5,

(ii) r_1 = 1.0, 0.5 and 0.1,

(iii) S = 0.5, 1, 2, 3, 4, 5, 7 and 10,

(iv) P = 0 – 5 in steps of 1.0, and

(v) ϕ = 0 – 5%.

5.5.1 Fluid Flow Analysis

The equivorticity lines at different spacing (S) are presented in Fig. 5.3(left side) with r_2 = 0.5 and r_1 = 1 under the incident of shear flow. It can be seen from the Fig. 5.3(left side) that no shedding of vortices takes place at all S and the flow around the cylinders is found to be completely steady. At sufficiently closed spacing (S = 0.5), the lower shear layers issuing from the UREP attached with the rear face of the DSC, while the upper shear layers issuing from the UREP merges with the shear layers generated from the DSC. With the increase in spacing, interaction between the upper shear layers issuing from both the cylinders is found diminished. The lower shear layers genearted from the cylinders occupt most of the surface of the cylinders.

To investigate the effect of height ratio (r_2) and aspect ratio (r_1) on flow field, Fig. 5.4(left side) presents equivorticity lines exposed to linear shear flow at P = 0 with sufficiently closed spacing S = 0.5. Here, the flow remains steady for all considered combina-

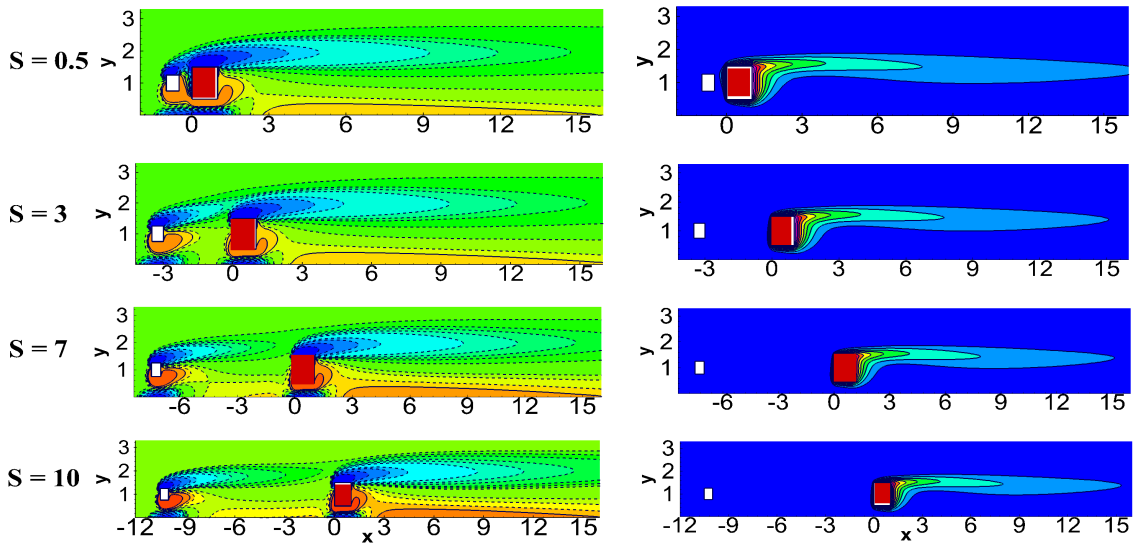

Figure 5.3: Vorticity contours (left side) along with corresponding isotherms (right side) at different spacing S for r_2 = 0.5 and r_1 = 1 with P = 0 and ϕ = 0% at Re = 250.

tions of r_2 and r_1. The flowing fluid separates from the sharp corners of the UREP, form a stagnant pair of vortices attached to the rear face of the DSC. Shortening of upper shear layers is observed with decrease in height and width of the UREP. No significant impact on flow field is observed by reducing the height and width of UREP under the incident of linear shear flow.

Fig. 5.5 (left side) presents the effect of nonlinearity of the inlet flow on the flow field for $W - Al_2O_3$ nanofluid with r_2 = 1 and r_1 = 0.5 at S = 3 and ϕ = 3%. As seen, the flow is is completely steady up to P = 4, and no vortex shedding takes place behind the cylinder. Up to P = 3, the upper shear layer issuing from the UREP merges with its DSC counterpart and emerges horizontally in the streamwise direction, while the lower shear layer of the UREP reattaches with the front face of the DSC. At P = 3 and 4, the steady gap reattachment of the shear layers is found. Unsteadiness is generated in the flow at P = 5. Clearly, the upstream cylinder sheds vortices alternatively, and the shed negative vortices (black color) roll over the top of the downstream cylinder while the positive vortices impinge on the front face of DSC and then pass through the gap between the wall and the bottom face of the DSC. Therefore, the nanofluid flow over the downstream

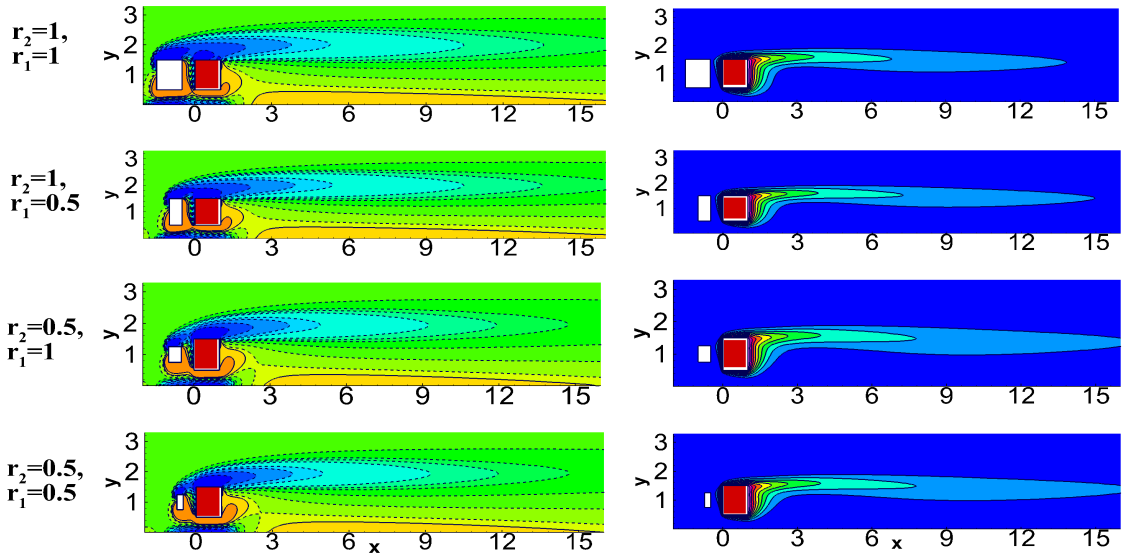

Figure 5.4: Vorticity contours (left side) along with corresponding isotherms (right side) for closed spacing S = 0.5 at different height ratio r_2 and aspect ratio r_1 with P = 0, ϕ = 0% at Re = 250.

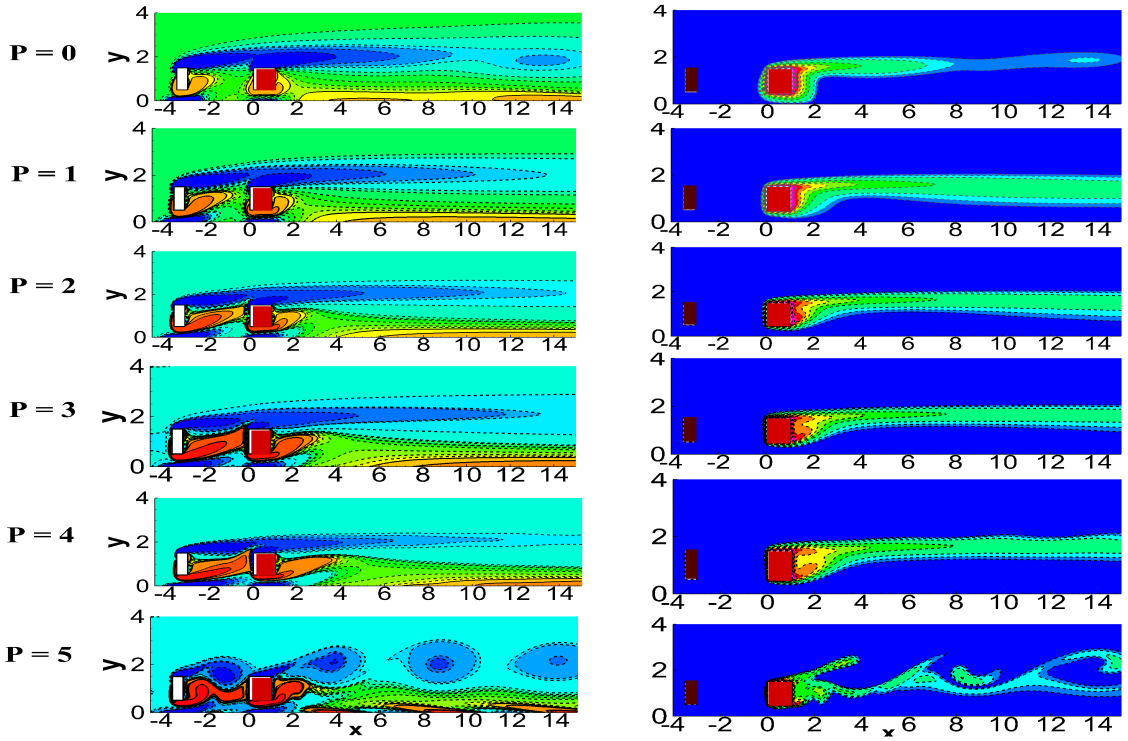

Figure 5.5: Vorticity contours (left side) along with corresponding isotherms (right side) at different pressure gradient P with S = 3, ϕ = 3% at Re = 250.

cylinder can be made unsteady by increasing P at a lower Re at which the isolated square cylinder flow was reported to be steady.

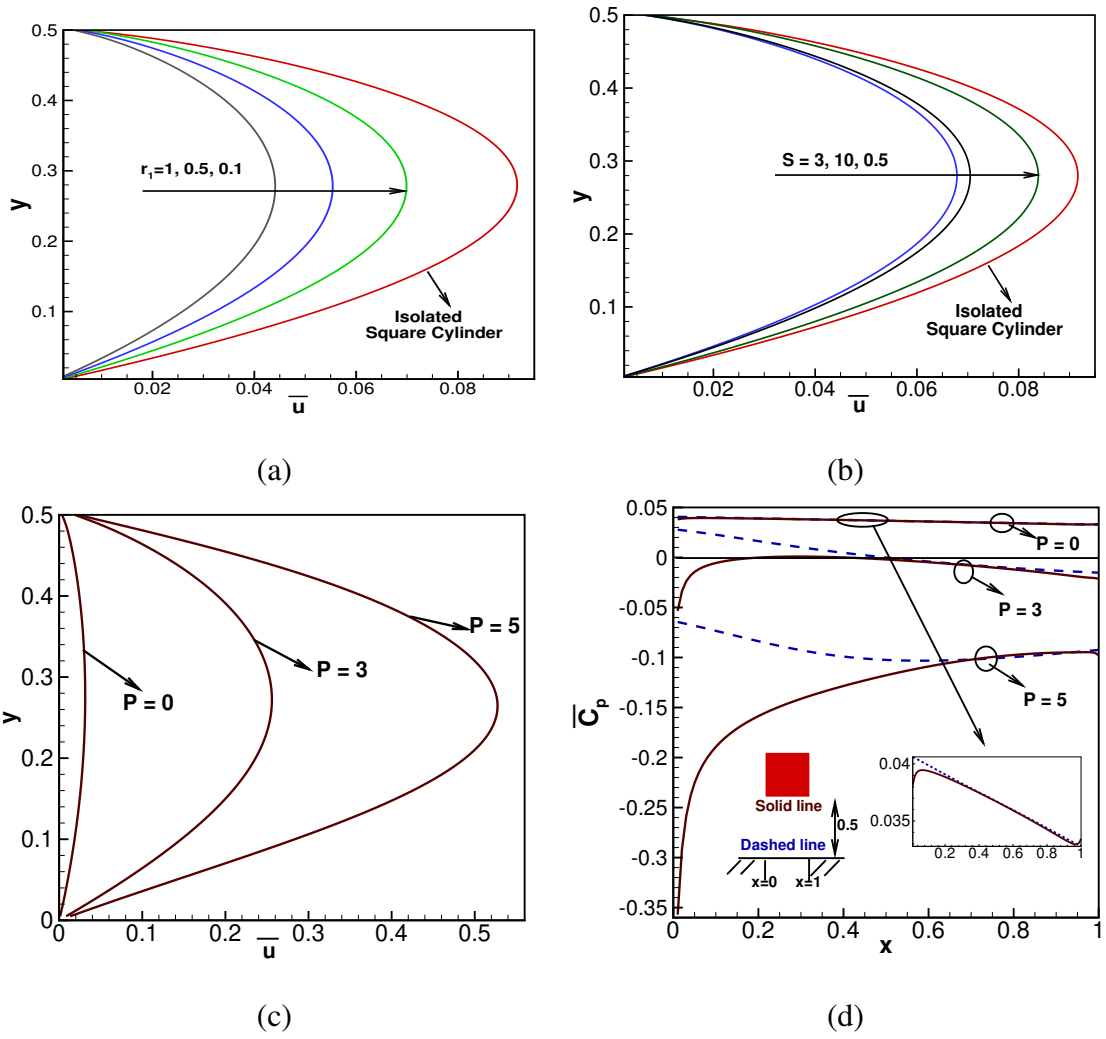

Figure 5.6: Time-mean streamwise velocity distributions along the $y-$ direction at x = 1 between the DSC lower face and the plane wall for (a) different r_1 = 1, 0.5 and 0.1 with r_2 = 1.0 at $P = 0$ and $\phi = 0\%$ (b) at different S with $P = 0$, r_2 = 1 and r_1 = 0.5 (c) at different P with S = 3 and ϕ = 3%, and (d) surface pressure distribution ($\overline{C_P}$) along the plane wall (dashed line) and along the lower face of the DSC (solid lines) at ϕ = 3%.

Fig. 5.6 shows the time-averaged streamwise velocity ($\overline{u}$) profile along y for different r_1, S and P at the exit position of the gap flow between the DSC's bottom face and the plane wall and time-averaged surface pressure $\overline{C_P}$ distributions along the DSC's bottom face and the plane wall at different P. It is quite clear from Fig. 5.6(a) that the gap flow

(which plays a major role in the shedding of vortex behind the cylinder near a wall) becomes weaker in presence, compared to absence, of the downstream cylinder. From Fig. 5.6(b), it is clear that the gap flow is stronger for closely spaced arrangement. Further, when the spacing is increased, the gap-flow becomes weaker and then stronger at S = 10 and the velocity profile approaches to that of an isolated cylinder case. As can be seen in Fig. 5.6(d), the pressure difference between the bottom face and the plane wall is almost zero at P = 0 and 3 in the core of the gap region. As a result, the gap flow becomes unidirectional, and the core flow looks like a channel flow, owing to the fact that the interaction between shear layers of the cylinder get lost. Therefore, the vortex shedding is completely suppressed at P = 0 and 3 (ref. Fig. 5.5). On the other hand, at P = 5, the pressure on the bottom face is less than that on the wall. As a result, the interaction of DSC shear layers takes place in the wake, leading to the vortex shedding (ref. Fig. 5.5). It is evident from the Fig. 5.6(c) that the velocity profiles overshoot, and the gap flow (which plays a major role in the vortex shedding behind the cylinder) becomes stronger with the increase of P. Also, the position at which the maximum velocity occurs shifts closer to the DSC'S bottom face at the highest value of P = 5, indicating the shedding of vortex from the DSC at P = 5 (ref. Fig. 5.5).

Unsteadiness in the wake of the DSC at P = 5 is reconfirmed with the help of phase diagram (u vs v at a point $3A^*$ distance from the rear face of the DSC) in Fig. 5.7(a). As seen in Fig. 5.7(a), a limit cycle exists at both ϕ = 0 and 5% with P = 5, indicating the existence of periodic flow with a single and sharp peak in the spectra of fluctuating lift coefficient of the DSC (Fig. 5.7(b)). It is clear that concentration ϕ has very negligible influence on the hydrodynamic characteristics in the considered range of ϕ here.

The effect of aspect ratio (r_1) with r_2 = 1 and nonlinearity (P) on the wall vorticity generated at surfaces of the DSC is exemplified in Fig. 5.9 for ϕ = 3%. All the curves are qualitatively similar to each other. Overall, the sharpest variation in the wall vorticity ω can be seen at the front-top corner, pointing to a large variation in the velocity. The global minimum and maximum of ω register at points 1 and 0, respectively. The front stagnation point is largely affected by the variation of P, compared to that of r_1. Moreover. P has

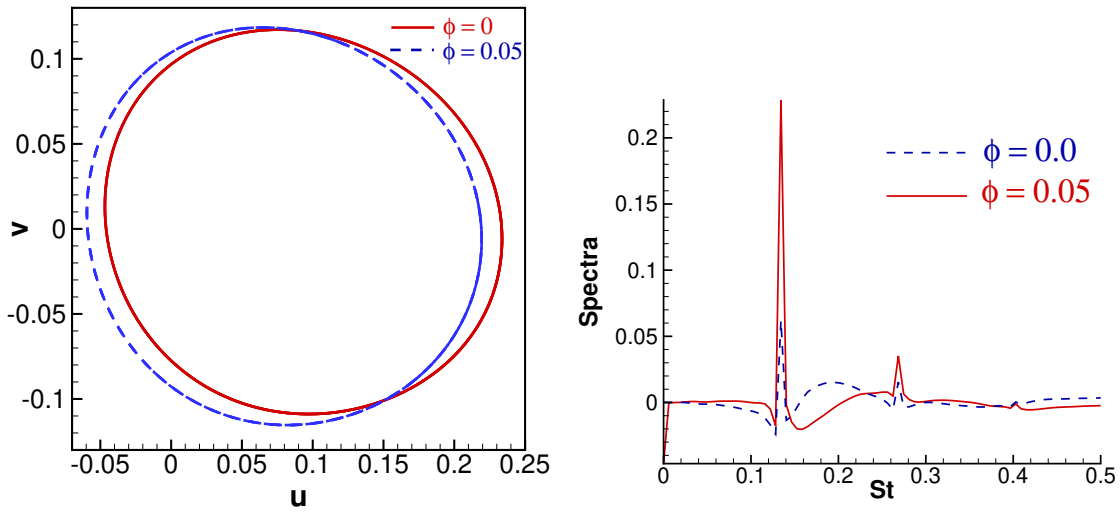

Figure 5.7: (a) Phase diagram (u against v at a location of $3A^*$ from the rear face of the DSC), and (b) spectra of fluctuating lift coefficient of the DSC for $\phi = 0$ and 5% at $P = 5$ with $r_2 = 1$ and $r_1 = 0.5$.

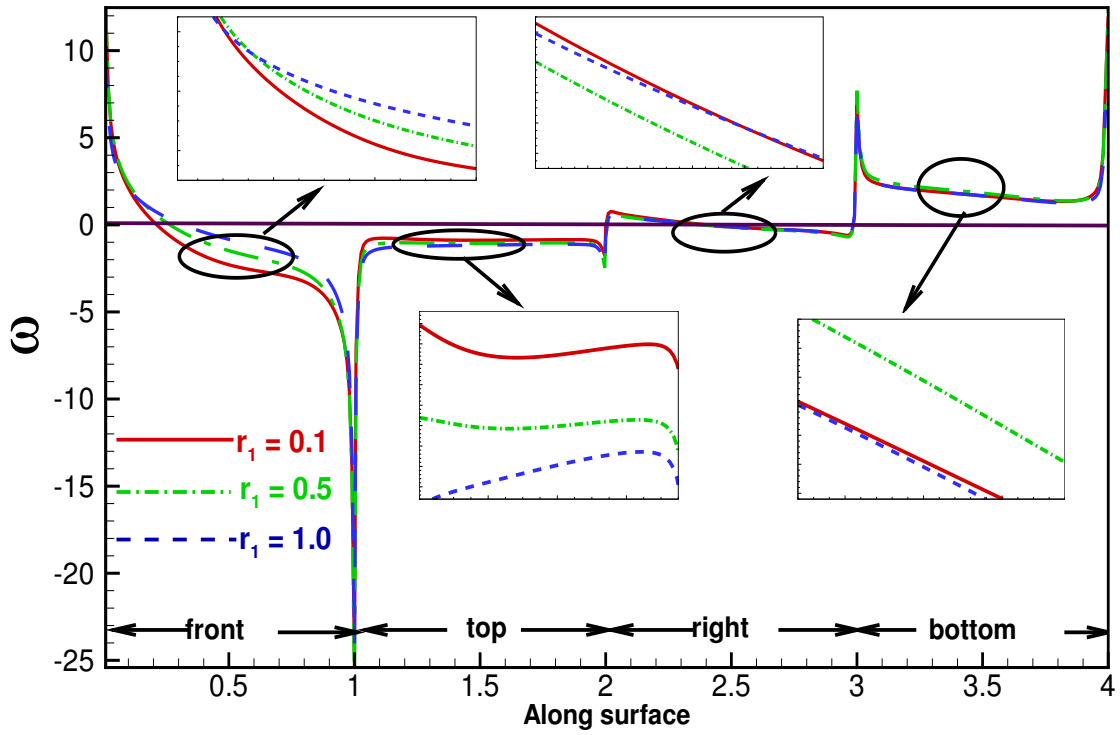

Figure 5.8: Wall vorticity around surfaces of the DSC at different $r_1 = 1$, 0.5 and 0.1 with $r_2 = 1$ for $S = 3$ and $\phi = 3\%$.

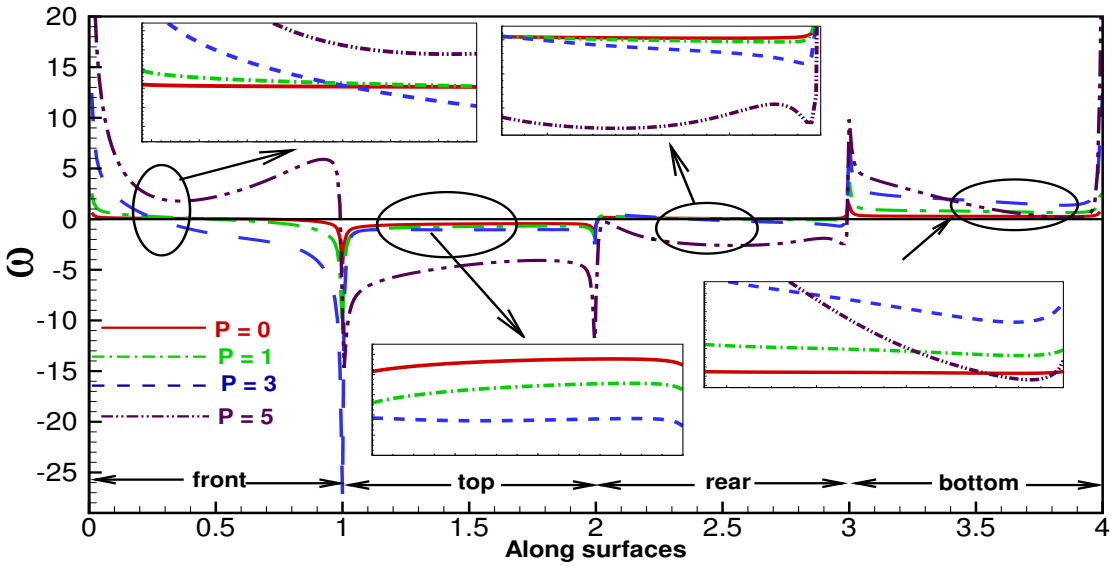

Figure 5.9: Wall vorticity around surfaces of the DSC at different P for S = 3 and ϕ = 3% with r_2 = 1 and r_1 = 0.5.

more effect on ω than r_1. The curve for P = 5 distinctly appears in the figure. As seen, the magnitude of ω is directly proportional to P since the increase of P is equivalent to increase the intensity of the incidence velocity under the present flow condition.

5.5.2 Temperature Distribution

Isotherms contours are presented at different S (Fig. 5.3 (right side)) with r_2 = 1 and r_1 = 0.5, for different r_2 and r_1 (Fig. 5.4 (right side)) with S = 0.5 and at different P (Fig. 5.5 (right side)) with S = 3, r_2 = 1 and r_1 = 0.5. As both vorticity and thermal energy are being transported by the flow in the wake, contours of temperature are equivalent to those of vorticity. As can be seen , the insulation layer (thermal boundary layer) around the cylinder surfaces, especially at the front, lower and upper surfaces, decreases with the increase of P and r_1 and decreases with S. This is due to the fact that the incident velocity on the cylinder becomes stronger at a higher P and r_1. It is worth noting that the crowding of isotherms in the recirculation region (behind the rear face) decreases with S, causing a noticeable change in the isotherm pattern. Therefore, by generating unsteadiness in the flow by increasing P and by placing an adiabatic thinner rectangular cylinder at the upstream side, the heat transfer from the rear face of DSC is expected to

improve.

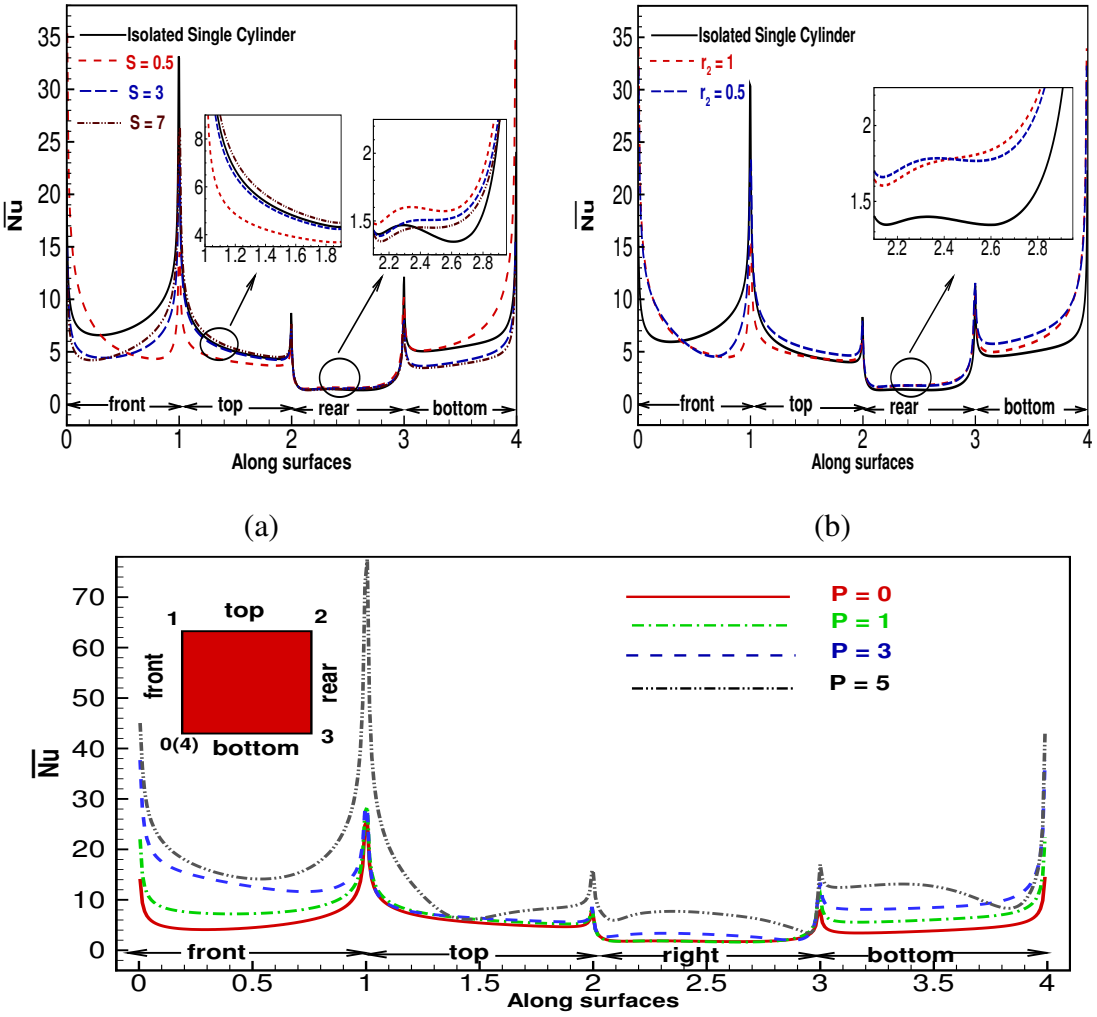

Figure 5.10: Nusselt distributions along the surfaces of the DSC (a) at different spacing S for r_2 = 0.5 and r_1 = 1.0 with P = 0, (b) at different ϕ and r_2 with r_1 = 1.0, (c) for different P with ϕ = 3%, r_2 = 1 and r_1 =0.5.

5.5.3 Heat Transfer Characteristics

Fig. 5.10 plots the time-averaged local Nusselt number ($\overline{Nu}$ distribution around the DSC surfaces) for different S (Fig. 5.10 (a)), r_2 and ϕ (Fig. 5.10 (b)) and, P = 0, 1, 3 and 5 at a fix ϕ = 3% (Fig. 5.10 (c)) . As seen from Fig. 5.10, $\overline{Nu}$ attains a local maximum at all of the four corners, having a global maximum at the front top corner (point 1 in Fig.

5.10), because of the steepest temperature gradient. As can be seen in Fig. 5.10 (a), $\overline{Nu}$ variation along the surfaces for different S can be divided into two groups: closed spaced (S = 0.5) and moderate spacing (S = 3 and 7). It is observed from Fig. 5.10 (a) that along the front face, $\overline{Nu}$ is more for isolated square cylinder than the tandem case at all S. This is not surprising since virtually no exchange of fluid occurs between the fluid in the inter cylinder gap and free stream. It is seen from Fig. 5.10 (b) that dashed lines (for r_2 = 0.5) are above the solid lines (for r_2 = 1), indicating the more heat transfer from the downstream cylinder for the case of upstream cylinder of smaller height. Apparently, $\overline{Nu}$ at each point on the surface of the downstream cylinder is proportional to P (Fig. 5.10 (c)). As a result, the total heat transfer from the cylinder is expected to be large as long as P is high. As seen in Fig. 5.10 the front face (0-1) shows higher heat transfer among all other faces since the incoming cold fluid first contacts the outgoing hot fluid surrounding the hot cylinder. On the right face, $\overline{Nu}$ variation for the steady case (P = 0 ,1 and 3) is almost negligible since the circulating vortex rotates on this face without being shed. On the other hand, an exchange of hot fluid adjacent to this face with ambient cold fluid occurs due to the vortex shedding from the cylinderS for P = 5. Among P, S and r_2, the effect of P is more pronounced on the local $\overline{Nu}$ distribution.

The effect of S and P on the time- and surface-averaged Nusselt number ($\overline{Nu}_M$) for different r_2, r_1 and ϕ is presented in Fig. 5.11. As can be observed in Fig. 5.11, $\overline{Nu}_M$ increases with increasing P and ϕ but with the increase in spacing, it first decreases and then increases gradually. Also, the effect of non-linearity of incident velocity P and height ratio r_2 is more pronounced than that of ϕ and aspect ratio r_1 . The concentration influence on heat transfer is slightly more prominent at higher P. It is evident from Fig. 5.11 that $\overline{Nu}_M$ of the DSC decreases at all P. This is physically realistic, because the $\overline{Nu}$ values at the front face that is the major contributing face to the total $\overline{Nu}_M$ is drastically reduced by the UREP (Fig. 5.10). At a lower P, the exchange of ambient cold fluid and hot fluid near to the front face of the DSC is found to be minimum, and with the increase of P, this exchange of fluids increases due to oscillatory behaviour of the shear layers of the UREP, indicating recovery of $\overline{Nu}$ from the front face (ref. Fig. 5.10). Consequently

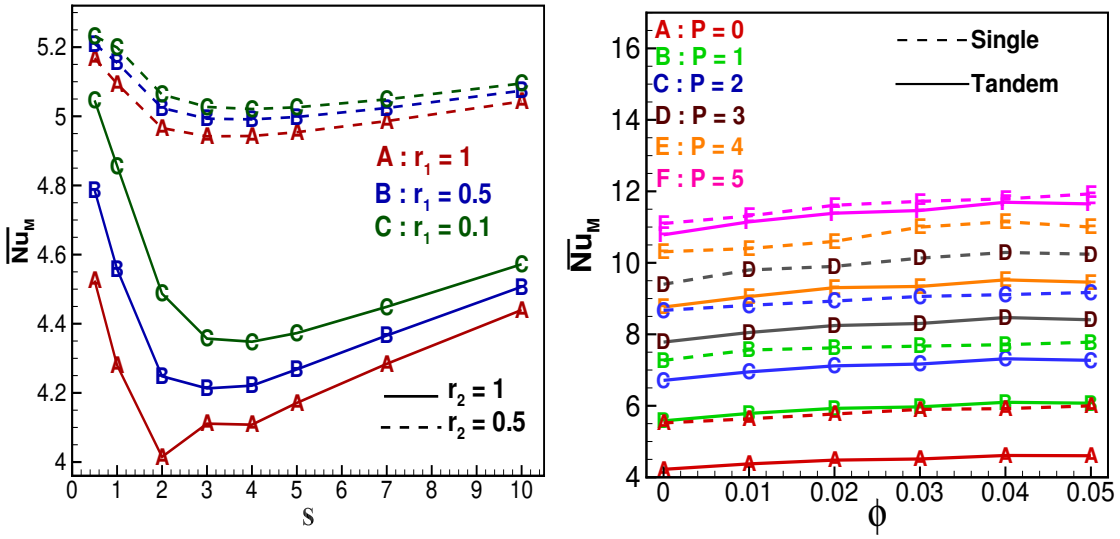

Figure 5.11: Time-averaged mean Nusselt number of the DSC (a) as a function of S for different r_2 and r_1 with P = 0 and, (b) as a function of ϕ at different P with S = 3 for r_2 = 1 and r_1 = 0.5.

the difference in $\overline{Nu}_M$ between the isolated and tandem cases decreases with the increase in P. Tables 5.1 and 5.2 show the proposed relationship of $\overline{Nu}_M$ on P and ϕ in the functional forms $\overline{Nu}_M = \overline{Nu}_M(P)$ and $\overline{Nu}_M = \overline{Nu}_M(\phi)$, respectively. These relations are fitted using the least square method based on the computed values for range of ϕ : 0 – 5% and P : 0 - 5 . Numerical values written in bracket against each relation are the residual sum of squares (RSS) and coefficient of determination (R^2). An R^2 of 0.99 means that it is 99% predictable. A small RSS indicates a tight fit of the model of the data. As can be seen from the table, all the values of R^2 lies in (0.9821, 0.9995) implies that the relations are best fitted. It is seen from Tables 5.1 and 5.2 that $\overline{Nu}_M$ is strongly dependent on P, but weakly on ϕ, which supports the observation reported in Fig. 5.11 (b). Function form $\overline{Nu}_M = \overline{Nu}_M(P)$ are similar for different ϕ (ref. Table - 5.1).

In order to validate these relations, Fig. 5.12 is presented to compare the original computed values with the values obtained by proposed relations. It is evident from the figure that all the fitted values are well correlated with the original computed values and hence, one can predict the $\overline{Nu}_M$ at different P and ϕ (within the considered range of P and ϕ) using these proposed relations.

Table 5.1: Propose dependency of $\overline{Nu}_M$ on ϕ in the functional form $\overline{Nu}_M = \overline{Nu}_M(P)$ with S = 3, r_2 = 1 and r_1 = 0.5.

ϕ	$\overline{Nu}_M = \overline{Nu}_M(P)$
0%	4.2 $e^{0.00925P^3-0.0807P^2+0.3606P}$ (0.01482, 0.9994)
3%	4.492 $e^{0.00924P^3-0.08086P^2+0.3605P}$ (0.01549, 0.9995)
5%	4.582 $e^{0.009414P^3-0.08143P^2+0.3581P}$ (0.01588, 0.9995)

Table 5.2: Propose dependency of $\overline{Nu}_M$ on P in the functional form $\overline{Nu}_M = \overline{Nu}_M(\phi)$ with S = 3, r_2 = 1 and r_1 = 0.5.

P	$\overline{Nu}_M = \overline{Nu}_M(\phi)$
0	-0.04504 $\phi^{3/2}$+0.1624ϕ+0.03635$\phi^{1/2}$+4.221 (0.001567, 0.9857)
3	$(-0.01181\phi^{3/2} - 0.413\phi^2 + 4.408\phi + 60.65)^{1/2}$ (0.005776, 0.9821)
5	-0.01283 $\phi^{3/2}$+0.4462ϕ+0.04072$\phi^{1/2}$+10.784 (0.009836, 0.9831)

5.5.4 Hydrodynamic Characteristics

The time-averaged drag coefficient ($\overline{C}_D$) of the DSC as a function of S at different r_2 and r_1 for P = 0 (Fig. 5.13(a)) and as a function of ϕ at different P is presented in Fig. 5.13(b). It can be easily noticeable that the time-mean drag coefficient $\overline{C}_D$ increases

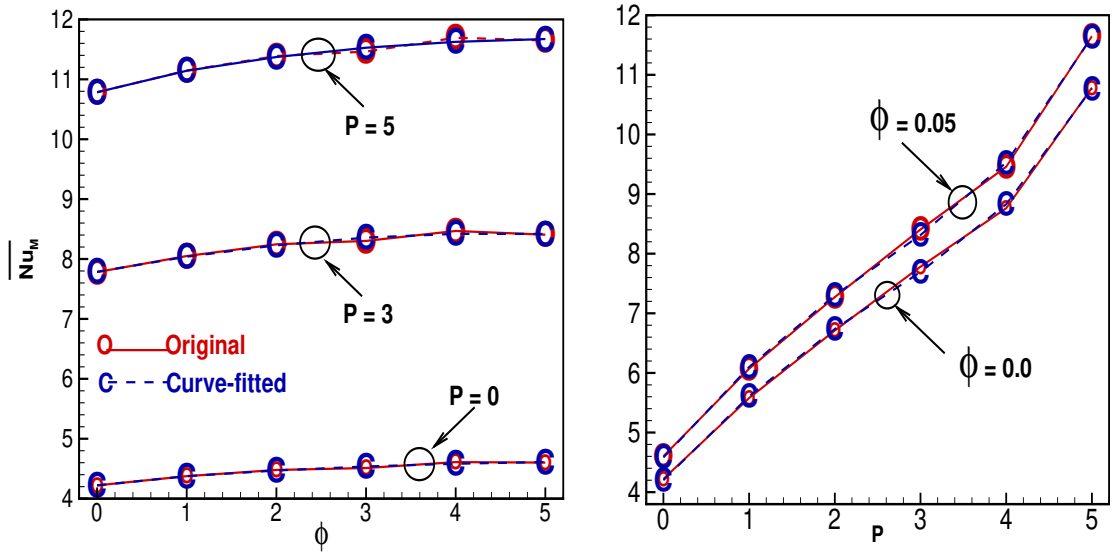

Figure 5.12: Validation of proposed relations for (a) $\overline{Nu}_M = \overline{Nu}_M(\phi)$ and (b) $\overline{Nu}_M = \overline{Nu}_M(P)$(as noted in Tables 5.1 and 5.2) with that of original computed data.

with increasing S and P but it is very weakly dependent on the nanoparticle concentration ϕ. As observed in Fig. 5.13(a), with the increase of spacing and depending on r_1 first increases and then gradually decreases and then finally approching to the isolated value of the DSC. It may be noted that the increase of Reynolds number is mechanically similar to the increase of P since $-\frac{dp}{dx} = 2P(\frac{1}{H^2})\frac{1}{Re}$. Therefore the change in P will have much effect on the flow field and consequently, on the hydrodynamic characteristics (Fig. 5.13(b)). Nominal increase in $\overline{C}_D$ due to ϕ is due to the fact that nanofluid viscosity increases with ϕ. Comparing the value of isolated square cylinder at respective P value, it is seen that the drag coefficient of the DSC declines due to sheltering effect by the UREP. The reduction is found more as long as P is high.

The ratio $\frac{\overline{Nu}_M}{C_D}$ is presented in Fig. 5.14 as a function of S for different r_2 and r_1 (Fig. 5.14 (a)) and as a function of ϕ at different P (in Fig. 5.14 (b)). It is observed from Figs. 5.11 and 5.13 that the heat transfer from the DSC is reduced by the UREP, while increasing with P, S and ϕ. Also, heat transfer is more for smaller UREP. At the same time, the drag coefficient of the DSC also reduces because of the sheltering effect by the UREP, while it increases with P, S and ϕ. Now, it is evident from Fig. 5.14 that their

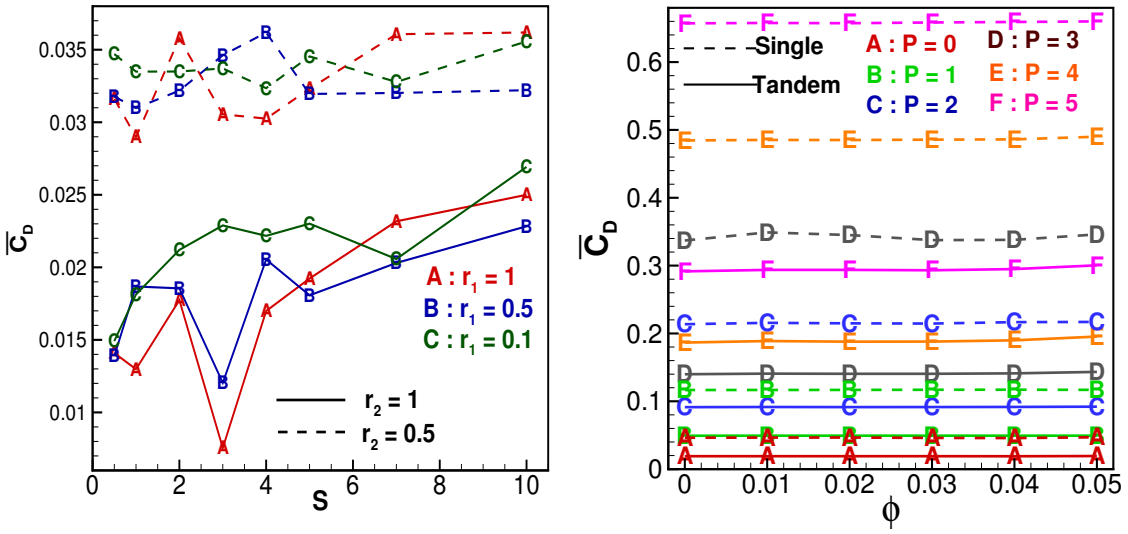

Figure 5.13: Variation of time-averaged drag coefficient ($\overline{C}_D$) of the DSC (a) as a function of S for different r_2 and r_1 with $P = 0$ and, (b) as a function of ϕ at different P with $S = 3$ for $r_2 = 1$ and $r_1 = 0.5$.

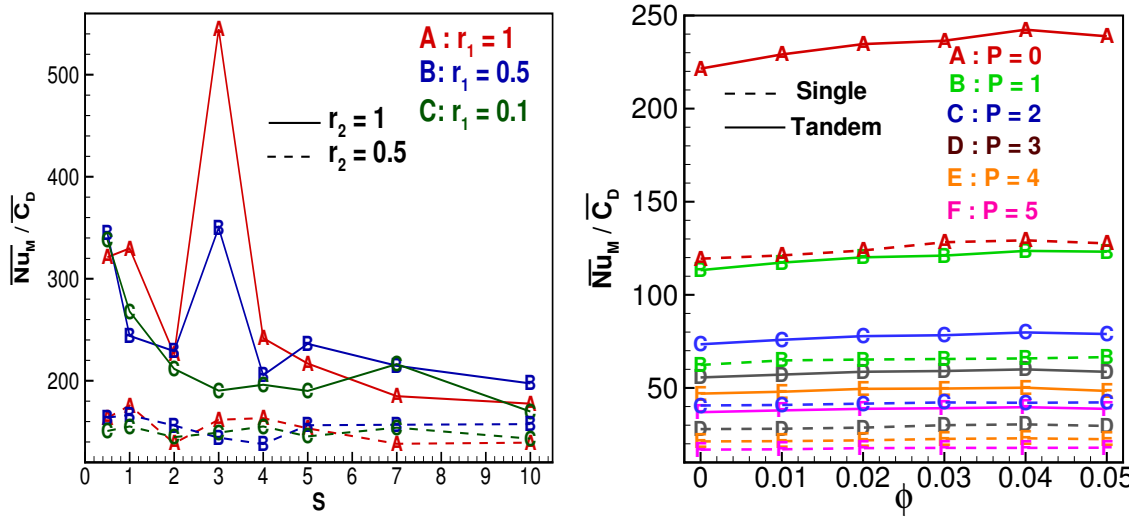

(a) (b)

Figure 5.14: Ratio of time-average mean Nusselt number to drag coefficient of the DSC (a) as a function of S for different r_2 and r_1 with $P = 0$ and, (b) as a function of ϕ at different P with $S = 3$ for $r_2 = 1$ and $r_1 = 0.5$.

ratio $\frac{\overline{Nu}_M}{C_D}$ increases nominally with ϕ , decreases with ϕ while for S, it first increases (reaches maximum at S = 3) and then gradually decreases. Since the ratio is maximum at S = 3, indicating that at this spacing it is beneficial with minimum drag and maximum heat transfer. Also, the curve for P = 0 distinctly appears at the top, indicating that consideration of linear velocity profile at the inlet is beneficial in terms of heat transfer enhancement together with minimum drag coefficient from the DSC in this inline tandem arrangement. It may be noted that the ratio is larger for the nanofluid than for the clear fluid at all P, remarkably at lower P. At a particular ϕ, a drastic jump in $\frac{\overline{Nu}_M}{C_D}$ is observed when the incident velocity is changed from linear to its first non-linear form. The $\frac{\overline{Nu}_M}{C_D}$ is greater for tandem case than that for the single cylinder, and the difference in $\frac{\overline{Nu}_M}{C_D}$ between the two cases is large at a lower P, remarkable at P = 0.

5.6 Conclusion

The present study deals with the numerical investigation of nanofluid flow around a heated square cylinder in the presence of an upstream rectangular cylinder placed at a gap height of $0.5A^*$ from the wall under the incidence of Couette- Poiseuille flow. The effects of pressure gradient P, spacing between the cylinders (S), height ratio between two cylinders (r_2), aspect ratio of the upstream cylinder (r_1) and nanoparticle concentration ϕ on the flow field and heat transfer characteristics of the DSC are investigated. The numerically simulated results lead to the following conclusions:

1. The shear layers issuing from the upstream cylinder merge with the shear layers of the downstream cylinder and form a steady closed circulation region between the cylinders at a lower P. At a higher P, the above recirculation region is opened and unsteadiness comes into being in the flow of the downstream cylinder at a lower Re at which isolated square cylinder reported to be steady.

2. The heat exchange between ambient cold fluid and hot fluid near to the front face of the heated cylinder enhances with increasing P, as does the crowding of isotherms near the rear face of the downstream cylinder.

3. The time- and surface-averaged heat transfer ($\overline{Nu}_M$) and drag coefficient ($\overline{C}_D$) of the downstream cylinder are suppressed from those of an isolated situation due to the tandem effect. They however increase with increasing P and ϕ. Their ratio $\frac{\overline{Nu}_M}{\overline{C}_D}$ increases nominally with ϕ, but decreases with the increase of P. A drastic jump in $\frac{\overline{Nu}_M}{\overline{C}_D}$ is observed when P is changed from 0 to 1. The value of $\frac{\overline{Nu}_M}{\overline{C}_D}$ is large for the tandem case than for the isolated case.

4. The functional forms of $\overline{Nu}_M = \overline{Nu}_M(P)$ and $\overline{Nu}_M = \overline{Nu}_M(\phi)$ are proposed by the least square curve fitting method.

Chapter 6

Forced Convective Heat Transfer Around Heated Square Cylinder due to Offsetting Rectangular Cylinder

6.1 Introduction

The study of the fluid flow and heat transfer past two-dimensional bluff bodies have attracted the community of fluid dynamics in recent years. These studies have many practical application including cooling of electronic equipments, tubes in compact heat exchangers, groups of chimney stacks, chemical reaction towers and so on. Flow over multiple bluff bodies involve different types of complex flow patterns behind the bluff body that are important to examine the hydrodynamic and heat transfer characteristics. A number of studies have been devoted for the flow over cylinders in tandem (Sharma et al. [109]; Alam et al. [110]). In tandem case, the mutual interaction of shear layers alter the physics of flow and the resultant vortex shedding involves more flow complexity as compared to single ones. Furthermore, offsetting the upstream one from/towards the plane wall and fixed downstream cylinder can display unsteady motion since both the cylinders will experience different centerline velocity. Hence, the effect of incoming flow will be different depending on whether the upstream cylinder is situated at a higher or

lower center-line velocity than the downstream cylinder.

Previous numerical studies have focused on the fluid flow past single square or circular cylinders. But, still it is required to conduct a systematic study of fluid flow past tandem cylinders. The geometry of the tandem arrangement of two cylinders is quite simple but the position of upstream cylinder with respect to downstream one can generate multiple flow structures such as recirculation, vortex shedding, separation of flow due to the existence of hydrodynamic interferences between the two cylinders. Singha and Sinhamahapatra [111] studied the flow and heat transfer characteristics in tandem arrangements. Zhu et al. [112] investigated the enhancement of heat transfer by the interaction of vortices generated by the vortex generator. The flow over two circular cylinders at different spacing and diameter ratios was studied by Baxendale et al. [113] and Sayers and Saban [114]. Valencia [115] numerically analysed the effect of spacing between cylinder separation on heat transfer from tandem rectangular cylinders in a channel over a range of Reynolds numbers ($100 \leq Re \leq 1000$). For $Re > 600$, eddy shedding phenomenon for the downstream cylinder and an enhancement of heat transfer was observed. Tatsutani et al. [102] studied the unsteady flow and heat transfer characteristics from square cylinders in a channel and shown that for small-large tandem pair, there exists an optimal location of upstream cylinder for which heat transfer can be enhanced at a fixed Re. Similar study was done by Rosales et al. [116] at $Re = 500$ with parabolic velocity profile at the inlet. They numerically observed an overall increase in heat transfer and decrease in drag experienced by the downstream cylinder in the presence of eddy promoter. Later, Rosales et al. [117] numerically observed that the movement of the eddy promoter towards the wall decreases the nusselt number from the downstream cylinder. Bahaidarah et al. [118] numerically studied the flow past cylinders of flat, circular, diamond and oval shapes at Re=25–350. They found that the influence of the geometric shape on heat transfer performance is more significant for $Re > 50$. In comparison to circular geometry, the oval and flat cylinders showed higher heat transfer rate, while the cylinder with diamond shape has the lowest heat transfer rate for $Re \leq 250$. Flow across two tandem rectangular cylinders in a channel for Re=1–40 and spacing between cylinders as 1–4 is studied by Agarwal

and Dhiman [119]. They observed that the flow converted to unsteady at Re = 30–40 and S = 4; the time averaged mean nusselt number increases with the increase in spacing. In the work of Farhadi et al. [120], the effect of spacing and blockage ratio B (ratio between cylinder width and channel height) from 12.5% to 50% is simulated for the fluid flow across tandem heated square cylinders at Re = 100–300. Their results indicated that the rate of heat transfer from the downstream cylinder increases with the spacing and decreases with B. In the higher B regime, heat transfer performance is not affected with spacing. A significant increase in nusselt number is observed for the downstream cylinder compared to upstream one at higher spacing distance. Kanna et al. [121] studied the forced convection heat transfer from two isothermal square cylinders placed in an offset arrangement using air as working fluid. They reported that the nusselt number for the downstream cylinder is higher than the upstream cylinder.

Apart from increasing the heat transfer by placing an obstacle/eddy promoter at the upstream side, various studies have been done to enhance heat transfer by improving the thermal conductivity of the working fluid. A suspension of nanoparticles in base fluid was started in 1995 to improve thermal conductivity of the conventional fluids like water, ethylene-glycol-water, engine oil etc. Convective heat transfer of $W - TiO_2$ and $W - Al_2O_3$ nanofluids in turbulent flow regime was studied by Pak and Cho [6]. Their observation showed an increase in Nusselt number with the increase in the particle volume concentration and the Reynolds number. Wen and Ding [122] experimentally investigated $W - Al_2O_3$ nanofluid flow through a copper tube in a laminar flow regime and observed a significant enhancement of convective heat transfer behaviour at the inlet. Ting and Hou [123] numerically studied an enhancement in heat transfer coefficient by 25.5% using 2.5 vol% of Al_2O_3 nanoparticles in water in forced convection case. Vajjha and Das [80] observed an enhancement in heat transfer with a low particle concentration of Al_2O_3 nanofluid at a low pumping power. Bouguerra et al. [124] reported an enhancement in thermal conductivity of water by 23% with the addition of 2% volume fraction of Al_2O_3 nanoparticles. Sidik et al. [125] numerically studied the heat transfer performance of nanofluid flow in a channel with five mounted objects using the lattice Boltzmann

method. Their results indicated an enhancement in heat transfer with the increase in the concentration of alumina nanoparticles and this is more prominent at higher Re. Esfe et al. [126] investigated the heat transfer performance of $W - Al_2O_3$ nanofluid in an adiabatic channel with two hot obstacles. They observed that the nusselt number increases by using nanofluids and decreases with the increase in obstacle dimensions. With increase in ϕ from 0 to 5%, the mean nusselt number over the obstacles increases by 10%. Foroutani and Rahbari [127] numerically studied forced convection heat transfer in a 2D rectangular channel using $W - Cu$ nanofluid with different block geometries. They observed that Nu increases as the copper nanoparticle volume fraction increases for different block geometries.

6.2 Objectives

It is anticipated that a staggered arrangement offers additional complicacy compared to an inline arrangement of the obstacles. Here, the upstream rectangular eddy promoter (UREP) is moved from/towards the wall (by offsetting the UREP about the horizontal centerline of downstream sqaure cylinder (DSC)) typically at $L = 0.25, 1.25$ and 2 since the wake oscillation of the DSC is almost independent on the presence of UREP beyond $L = 2$. It is to be noted that placing the UREP from the wall is equivalent to expose the front face of the DSC towards the approaching original incident flow of colder fluid. As a result, the time average mean nusselt number at front surface ($\overline{Nu}_{avg} - f$) of DSC would not be affected much by these arrangements. The objectives of the present study are to study:

1. The dependency of flow and heat transfer characteristics of the DSC on the presence (and shape) of the UREP at a fixed spacing $S = 3$ at different gap height L of UREP from the wall.
2. The effect of non-linearity on the heat transfer enhancement from DSC in the presence of UREP placed at different gap height L.
3. A comparison between the offset and inline tandem arrangement with the aid of

hydrodynamic and heat transfer characteristics.

4. Searching of an optimum location of UREP of optimum size for the enhancement of total heat transfer from the DSC.

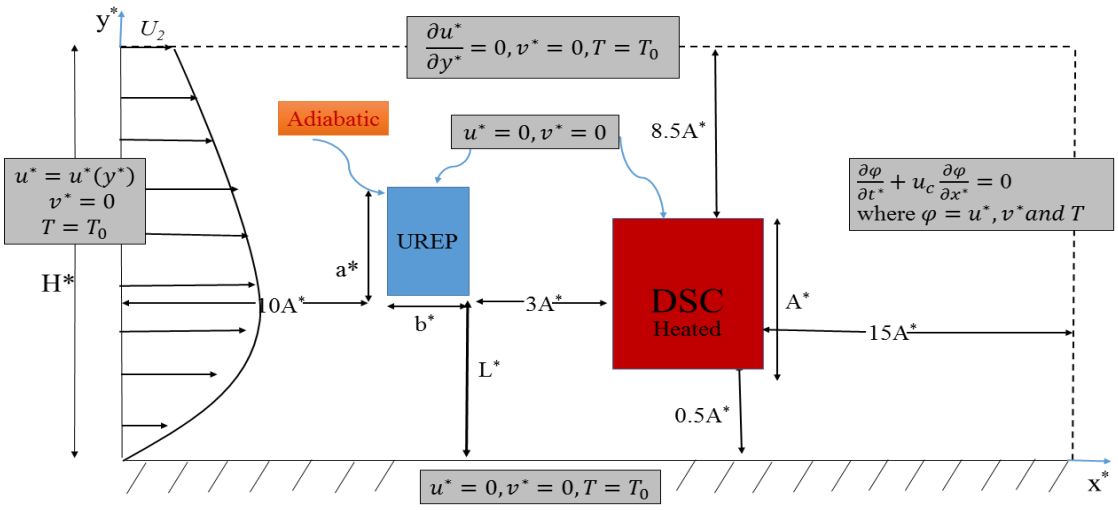

Figure 6.1: Schematics of flow configuration; UREP: Upstream rectangular eddy promoter, DSC: Downstream square cylinder.

6.3 Modeling

6.3.1 Problem Formulation

A plane wall lying along the x^*-axis and a long square cylinder (with height A^*) maintained at constant temperature T_w is placed parallel to the wall at a fixed gap height $0.5A^*$ from the wall. At the upstream side of the DSC, cylinder of rectangular cross-section of aspect ratio b^*/a^* with height a^* and width b^* is placed at a fixed distance $3A^*$ and parallel to the wall at different gap heights L^* from the wall (see Fig. 6.1). The upstream flow field is taken as Couette-Poiseuille flow based non-linear velocity profile $u^*(y^*)$. (A detailed discussion of this flow configuration is presented in Chapter - 4).

6.3.2 Governing Equations with Initial and Boundary Conditions

The flow is considered as two-dimensional, incompressible and laminar and the fluid is taken as nanofluid. Moreover, a single-phase modeling approach is adopted for the formulation of nanofluid flow. A detailed discussion of this approach is made available in Chapter-1. The non-dimensional Navier- Stokes equations along with energy equation governing the nanofluids can be expressed as:

The continuity equation:

$$\frac{\partial u}{\partial x} + \frac{\partial v}{\partial y} = 0. \tag{6.1}$$

The momentum equation in $x-$ direction:

$$\frac{\partial u}{\partial t} + \frac{\partial u^2}{\partial x} + \frac{\partial uv}{\partial y} = -\frac{\partial p}{\partial x} + \frac{1}{Re} * \frac{\nu_{nf}}{\nu_f}\left(\frac{\partial^2 u}{\partial x^2} + \frac{\partial^2 u}{\partial y^2}\right). \tag{6.2}$$

The momentum equation in $y-$ direction:

$$\frac{\partial v}{\partial t} + \frac{\partial uv}{\partial x} + \frac{\partial v^2}{\partial y} = -\frac{\partial p}{\partial y} + \frac{1}{Re} * \frac{\nu_{nf}}{\nu_f}\left(\frac{\partial^2 v}{\partial x^2} + \frac{\partial^2 v}{\partial y^2}\right). \tag{6.3}$$

The energy equation:

$$\frac{\partial \theta}{\partial t} + \frac{\partial u\theta}{\partial x} + \frac{\partial v\theta}{\partial y} = \frac{\alpha_{nf}}{\alpha_f} * \frac{1}{RePr}\left(\frac{\partial^2 \theta}{\partial x^2} + \frac{\partial^2 \theta}{\partial y^2}\right). \tag{6.4}$$

Here, $Re = \dfrac{U_2 A^*}{\nu_f}$ and $Pr = \left(\dfrac{\nu}{\alpha}\right)_f$ are considered based on base fluid. The non-dimensional quantities u, v, p, t and θ denote the velocity in x and y direction, pressure, time and temperature, respectively and are defined as:

$$u = \frac{u^*}{U_2},\ v = \frac{v^*}{U_2},\ p = \frac{p^*}{\rho_{nf}(U_2)^2},\ x = \frac{x^*}{A^*},\ y = \frac{y^*}{A^*},\ t = \frac{t^* U_2}{A^*},$$

and

$$\theta = \frac{T - T_0}{T_w - T_0}.$$

The following boundary conditions are applied to solve equations (6.1) - (6.4).

At the lower wall ($y = 0$): $u = v = 0$ and $T = T_0$.

On the surface of DSC: $u = v = 0$ and $T = T_w$.

On the surface of UREP: $u = v = 0$ and an adiabatic temperature condition is considered.

At the top lateral boundary: $\frac{\partial u}{\partial y} = 0$, $v = 0$ and $T = T_0$.

At the outlet boundary, sommerfield condition is taken.

$$\frac{\partial \phi}{\partial t} + u_c \frac{\partial \phi}{\partial x} = 0.$$

where, $\phi = u, v$ and θ.

The flow is assumed to start impulsively at a particular value of Re_{U_2} . A time-independent stable numerical solution is achieved by advancing the flow field variables through a sequence of short time steps of duration Δt.

6.3.3 Nanofluid Modeling

The thermophysical properties of nanofluids such as density, specific heat, thermal conductivity and viscosity is calculated based on the relationships available in the literature:

Density: The density of nanofluids is calculated from proposed equation of Pak and Cho [6].

Specific heat: The specific heat of nanofluids is determined using the equation given by Xuan and Roetzel [7] that assumes thermal equilibrium between the base fluid and the nanoparticles.

Thermal conductivity: The relation proposed by Koo and Kleinstreuer [9] and later modified by Vajjha and Das [10] for thermal conductivity as a two-term function, which takes into account the effect of particle size d_{np}, particle volumetric concentration ϕ, temperature T and the properties of the base fluid as well as the effect of the Brownian motion of nanoparticles, is considered here. Kim et al. [11] experimentally and Ebrahimnia-Bajestan et al. [12] numerically confirmed that this model predicts the thermal conduc-

tivity and hence predict the heat transfer coefficient of nanofluids more accurately as compared to the models based on the pure static conditions of the nanofluids.

Viscosity: Masoumi et al. [17] developed a theoretical model for the prediction of the effective viscosity of nanofluids based on Brownian motion and showed that their model could accurately predict the effective viscosity of different nanofluids. This model is taken here to calculate the effective viscosity.

The detailed discussion of the above mentioned models can be found in Chapter-1. These thermal properties are calculated at room temperature (i.e.) 300K.

6.4 Numerical Methodology

The calculation domain is divided into small control volumes. The variables (pressure, temperature and velocity field) are stored using staggered grid arrangement at each control volume. The pressure correction based SIMPLE algorithm, based on finite volume method (FVM), is applied here. A third order accurate QUICK (Quadratic Upstream Interpolation for Convective Kinematics) is employed to discretise the convective terms and central differencing for diffusion terms. A fully implicit first order scheme is incorporated to discretise the time derivatives. The pressure link between continuity and momentum is accomplished by transforming the continuity equation into a Poisson equation for pressure. The Poisson equation implements a pressure correction for a divergent velocity field. A detailed discussion of the numerical methodology (staggered grid, FVM, QUICK and SIMPLE algorithms) used here has been discussed in Chapter-1.

6.4.1 Size of Computational Domain and Consideration of Grid

The distance of the inflow boundary from the front face of the upstream cylinder and the height of the top lateral boundary are chosen large enough so that the effect of the boundary conditions on the wall shear stress is very weak. The inflow boundary is taken at a distance $10A^*$ from the front face of the UREP while the top lateral boundary lies at $8.5A^*$ from the top face of the DSC. The distance of the outflow boundary from the DSC rear face is taken as $15A^*$ since convective boundary condition at the outlet is used here.

A non-uniform grid distribution is considered in the computational domain distributing uniform grids along the surfaces of both the cylinders with expansion factors for the far-fields (away from the surfaces). A symmetry grid (along the x-dir. about the mid-line in spacing distance between the cylinders) is incorporated. A grid independency test is conducted by varing the number of grids between 475 $\times$ 250 and 850 $\times$ 600 as discussed in Chapter-2. The time step is considered as 10^{-4}.

6.4.2 Validation of Numerical Code

The numerical code is already validated for the case of nanofluid modeling and single cylinder with Etminan et al. [4] and presented in Table-2.3 in Chapter-2. The numerical code for the cases of heat transfer around two equal isothermal square cylinders placed in a tandem arrangement is validated with Chaterjee and Mondal [1] and Sohankar and Etminan [2] for different values of Re and presented in Figs. 5.2(a) and 5.2(b) of Chapter-5. An excellent match between the two results in time- and surface-mean $\overline{Nu}_M$ as well as drag coefficient (C_D) for both upstream and downstream cylinders are reported in chapter-5.

6.5 Results and Discussion

The numerical simulations are performed with the consideration of the following parameters:

- Nanoparticle concentration (ϕ): 0% and 5%.
- Pressure Gradient (P): 0, 3, 5.
- Reynolds number (Re): 250.
- Ratio of heights of the two cylinders (r_2): 1.0 and 0.5.
- Aspect ratio (r_1): 0.5.
- Spacing between the cylinders (S): 3.0.

- Gap height of upstream cylinder from the wall (L): 0.25, 0.5 (inline tandem case), 1.25 and 2.0.

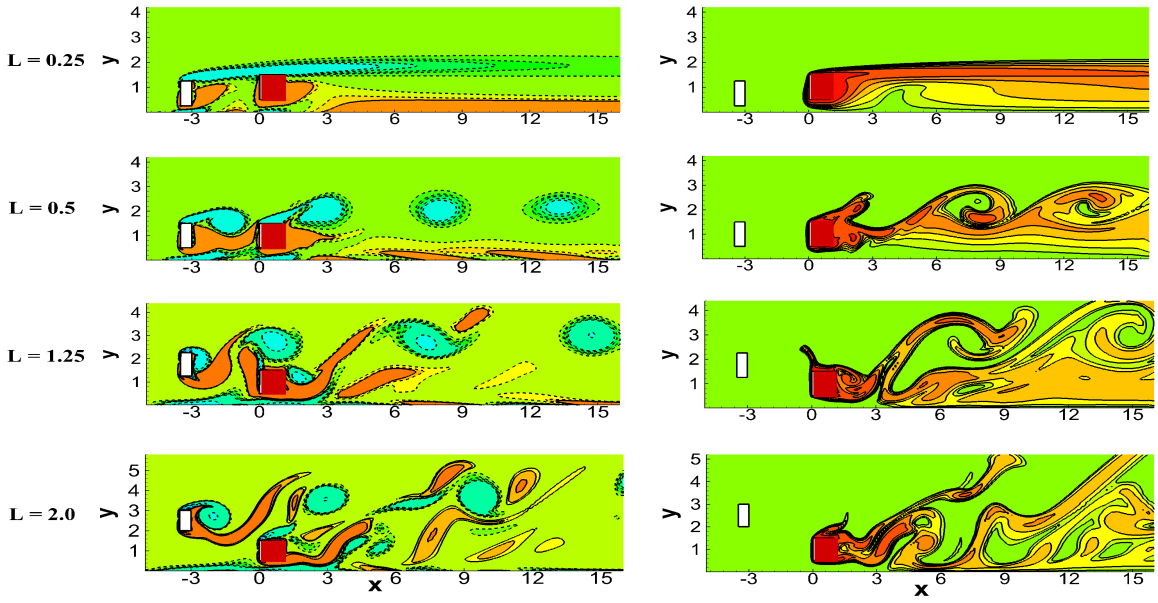

Figure 6.2: Vorticity contours (left side) along with corresponding isotherms (right side) at different gap heights L of UREP with P = 5, ϕ = 5% for height ratio r_2 = 1 and aspect ratio r_1 = 0.5 at Re = 250.

6.5.1 Fluid flow analysis

Fluid flow patterns at different gap height L of UREP are presented in Fig. 6.2(left side) for the case of r_2 = 1 and r_1 = 0.5 at $\phi = 5\%$ and P = 5. As can be seen from the Fig. 6.2(left side), the flow is completely suppressed for both the cylinders at L = 0.25. The upper shear layers lies only at the top of the cylinders while the lower shear layers occupies most of the surface of the cylinders. Moreover, the upper shear layers issuing from the UREP merges with its counterpart emerging from the DSC and hence, thicken the upper shear layers of the DSC. A weak interaction is seen between the plane wall shear layers and the shear layers emerging from the bottom face of the UREP as well as DSC. As the L increased to 0.5 (inline tandem case), the flow becomes unsteady and the vortex shedding takes place behind the cylinder. The upper shear layers from the UREP curl up in a periodic manner on the top of the DSC and the lower shear layers from the

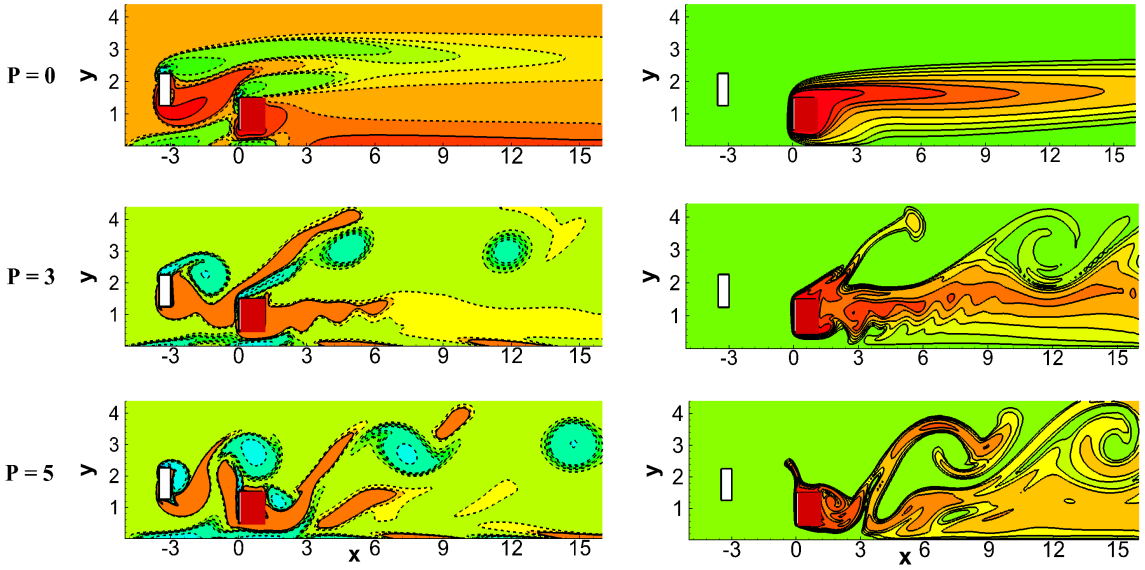

Figure 6.3: Vorticity contours (left side) along with corresponding isotherms (right side) at different pressure gradient P with L = 0.25, ϕ = 5% for height ratio r_2 = 1 and aspect ratio r_1 = 0.5 at Re = 250.

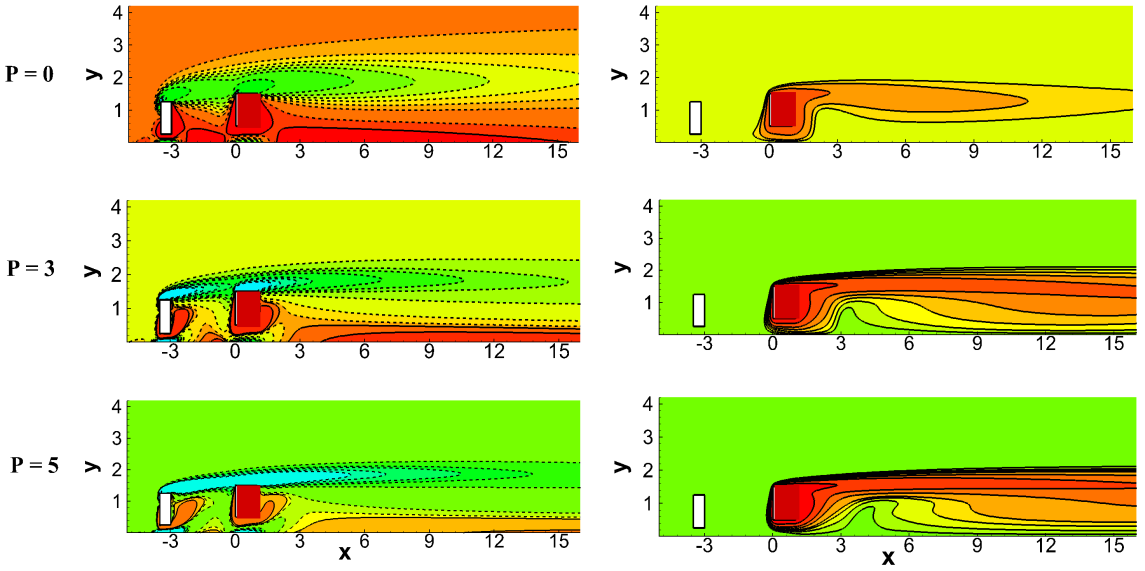

Figure 6.4: Vorticity contours (left side) along with corresponding isotherms (right side) at different pressure gradient P with L = 1.25, ϕ = 5% for height ratio r_2 = 1 and aspect ratio r_1 = 0.5 at Re = 250.

UREP reattaches with the front face of the DSC. With L = 1.25, the lower shear layers from the UREP deflects towards the upper face of the DSC. A single row of vortices induced by upper shear layers of UREP is observed with the small vortices generated by lower shear layers in the wake of the DSC. At the same time, the lower shear layers from the DSC starts to roll up, and splits into small vortices due to the plane wall shear layers. At L = 2.0, a combination of vortex shedding generated from both the cylinders is seen at the downstream side of the DSC. These generated vortices are sufficiently close to each other due to which interaction among them occurs and consequently, form a very complex wake.

The effect of pressure gradient P at L = 0.25 and L = 1.25 on fluid flow is presented in Figs. 6.3(left side) and 6.4(left side), respectively for the case of r_2 = 1 and r_1 = 0.5 at ϕ = 5%. There is no shedding of vortices takes place and the flow is found to be completely steady at L = 0.25 for all P (the upper shear layer issuing from top surface of the cylinders emerges almost horizontally in the streamwise direction and the lower shear layer reattaches the rear surface) (Fig. 6.3(left side)) while an unsteadiness in the flow is observed at L = 1.25 for $P \geq 3$. Also, it may be noted that the flow for the inline tandem case (i.e L = 0.5) is unsteady at P = 5 (Fig. 5.5(left side)). Therefore the nanofluid flow can be made unsteady by either increasing gap height L of UREP from the plane wall or with the increase of P.

In order to validate the ongoing discussion, Fig. 6.5 presents the mean horizontal velocity profile ($\overline{u}$) along the vertical direction (y) at the exit position (i.e. x = 1) at different P with $L = 1.25$ (Fig. 6.5(a)) and at different L for fixed $P = 5$ (Fig. 6.5(b)). Identification of gap flow is imperative to explore the shedding of vortices behind the cylinder. As can be seen in Fig. 6.5, the gap flow (between the DSC lower face and the wall) becomes stronger with the increase of P and/or L and the velocity profile overshoots (jet action) for all P and L. Velocity profile takes its parabolic form in the gap flow. Therefore, the heat transfer from the cylinder's rear face is expected to be more at large L and P.

The time-average surface pressure distribution $\overline{C_P}$ along the plane wall and bottom

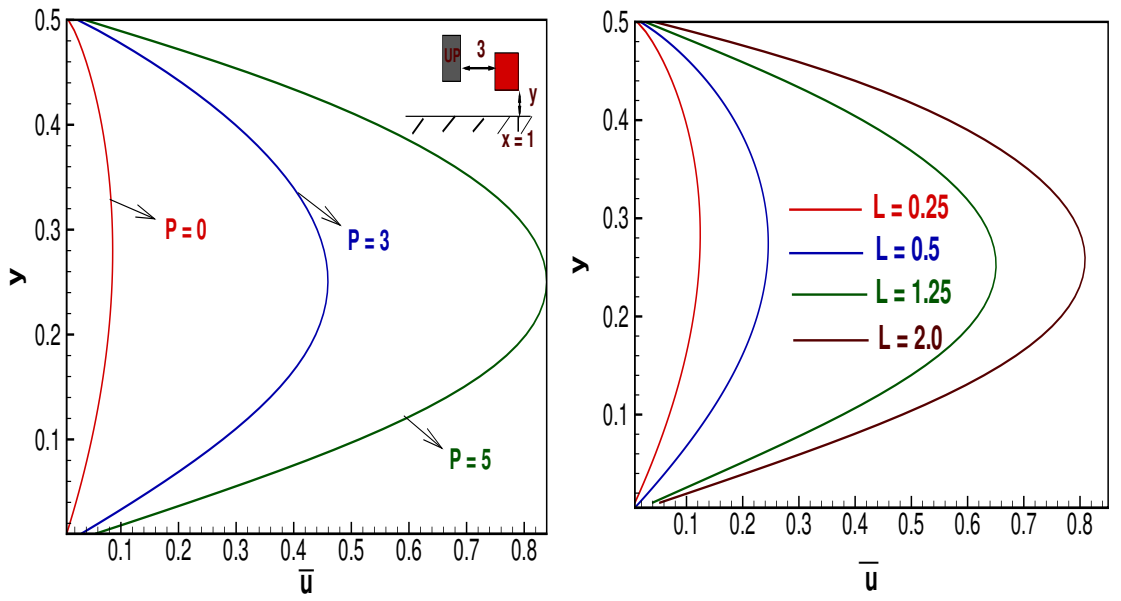

(a) (b)

Figure 6.5: Horizontal velocity profile along the vertical direction (y) at the exist position ($x = 1$) of the gap between the downstream cylinder's lower face and the wall for (a) different P and ϕ =5% ,L = 1.25 and, (b) different L with P = 5, ϕ = 5% for r_2 = 1.0 and r_1 = 0.5.

face of the DSC is exemplified in Fig. 6.6 at different P for $L = 1.25$ (Fig. 6.6(a)) and at different L for fixed $P = 5$ (Fig. 6.6(b)). As can be seen from Fig. 6.6(a), at P = 0, the difference in pressure between the DSC's bottom face and the plane wall is almost zero in the core of the gap region. Hence, the interaction between shear layers of the cylinder get lost. Therefore, the vortex shedding is completely suppressed at P = 0. On the other hand, at P = 3 and 5, the pressure on the plane wall is more than that on the bottom face of the DSC due to which interaction of DSC's shear layers takes place in the wake, leading to the shedding of vortices (ref. Fig. 6.4). While looking at the effect of gap height L at P = 5 in Fig. 6.6(b), it is observed that the pressure difference is almost zero at lower L = 0.25 due to which the flow is steady. With the increase in L from 0.5 to 2, the pressure difference between DSC bottom's face and the plane wall increases, which in turn initiates the process of vortex shedding along the surface of the DSC. This leads to the overall increase in heat transfer at higher value of L (ref. Fig. 6.2).

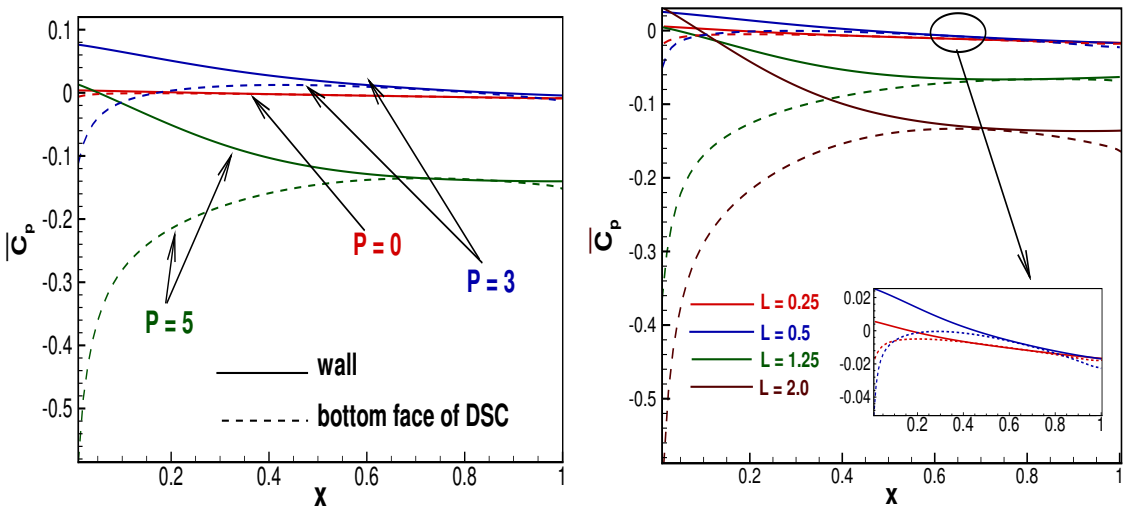

Figure 6.6: Surface pressure distribution along the lower face of downstream cylinder (dashed line) and along plane wall (solid line) for (a) different P and ϕ =5%, L = 1.25 and, (b) different L with P = 5, ϕ = 5% for r_2 = 1.0 and r_1 = 0.5.

6.5.2 Temperature Distribution

Isotherms contours are plotted in Fig. 6.2 (right side) at different gap height L of UREP from/towards the wall with P = 5 for r_2 = 1 and r_1 = 0.5. At lower L = 0.25, the thermal field exhibits steady behaviour and no clustering of isotherms is observed near the rear face of the DSC. With the increase in L, the intensity of isotherms becomes non uniform around the cylinder due to separation of flow. The crowding of isotherms can be seen at higher L especially at front, top and bottom face, which in turn, indicates the thinning of thermal boundary layer over these faces and consequently the heat transfer rate increases. While, looking at the role of pressure gradient P, contour lines of temperature are plotted at different P with L = 0.25 (Fig. 6.3 (right side)) and L = 1.25 (Fig. 6.4 (right side)) for r_2 = 1 and r_1 = 0.5. The temperature distributions show that the heat is distributed within the flow field as isolated warm blobs. These warm blobs are captured within the vortex structures and advected downstream without being influenced too much by mixing with their surroundings. As can be seen, insulation layer (thermal

boundary layer) around the surfaces, especially at the front, lower and upper surfaces, decreases with the increase of pressure gradient at both L. This is due to the fact that the incident velocity on the cylinder becomes stronger at higher P. It is worthy to note that the crowding of isotherms near the rear face in the recirculation region increases with pressure gradient with a noticeable change in the shape of isotherms. Therefore, by generating unsteadiness in the flow by increasing P or by increasing L, the heat transfer from the rear face is expected to improve.

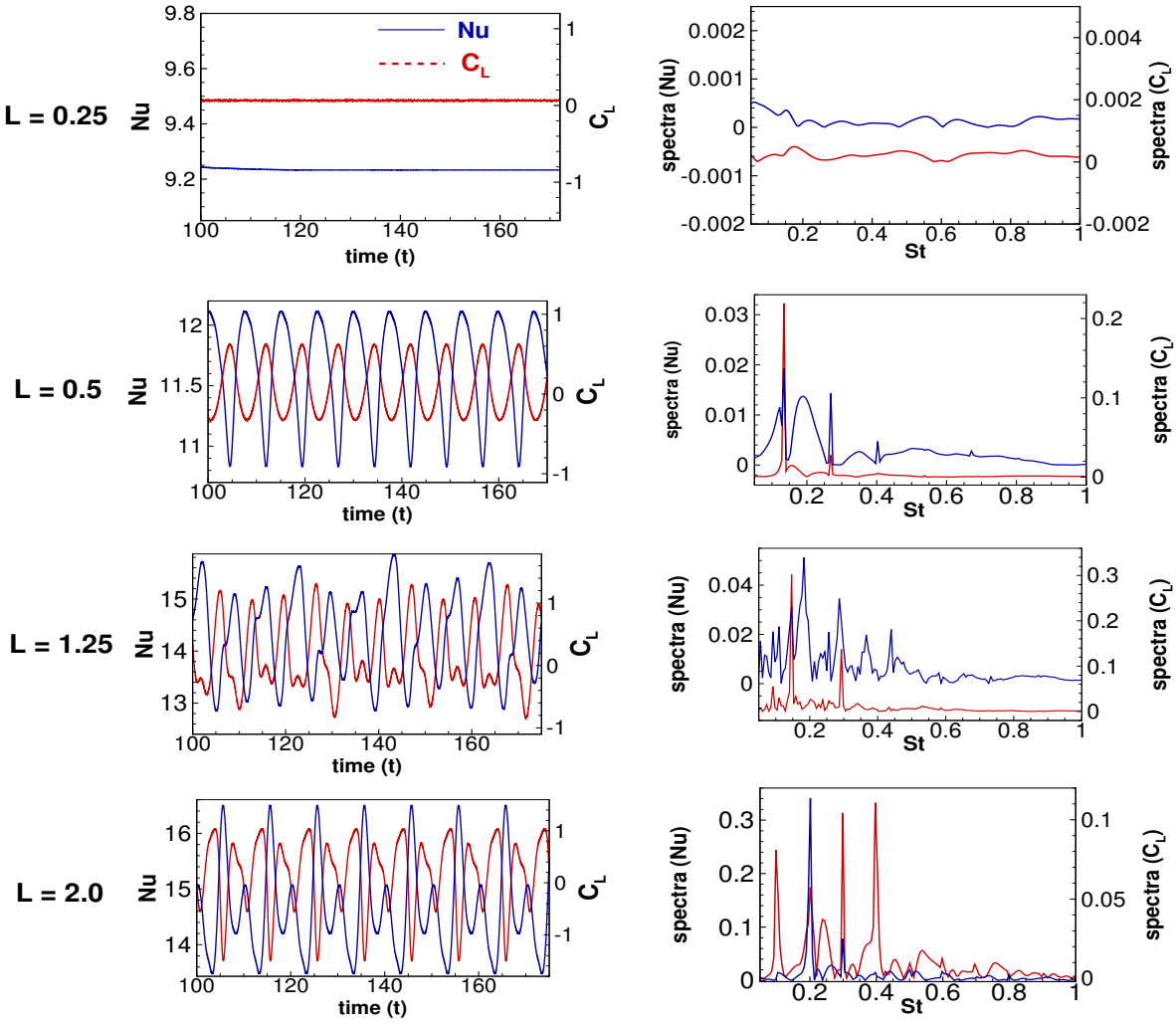

Figure 6.7: Time histories of Nusselt number Nu and lift force C_L along with corresponding spectra at different L and $P = 5$, $\phi = 0\%$ for $r_2 = 1$ and $r_1 = 0.5$.

6.5.3 Heat Transfer Characteristics

Fig. 6.7 (left side) shows the time histories of Nu and C_L along with spectra of Nu and C_L (Fig. 6.7 (right side) for different L at P = 5, r_2 = 1 and r_1 = 0.5. At L = 0.25, no fluctuation in the signals of Nu and C_L is observed due to steady flow behaviour at L = 0.25. The fluctuation of Nu and C_L is found periodic for L = 0.5, while it is quasi-periodic for L = 1.25 and 2.0, consisting of multiple frequencies. In order to explore heat transfer, identification of the frequencies in Nu is of vital importance. No sharp peak is observed for L = 0.25. (Fig. 6.7 (right side)). A sharp peak can be at L = 0.5 while for L = 1.25 and 2.0, a series of multiple peaks is shown. When L increases from 0.25 to 2, the frequency peaks heightens which has a significant influence on heat transfer and contributes to the fluctuation of Nu.

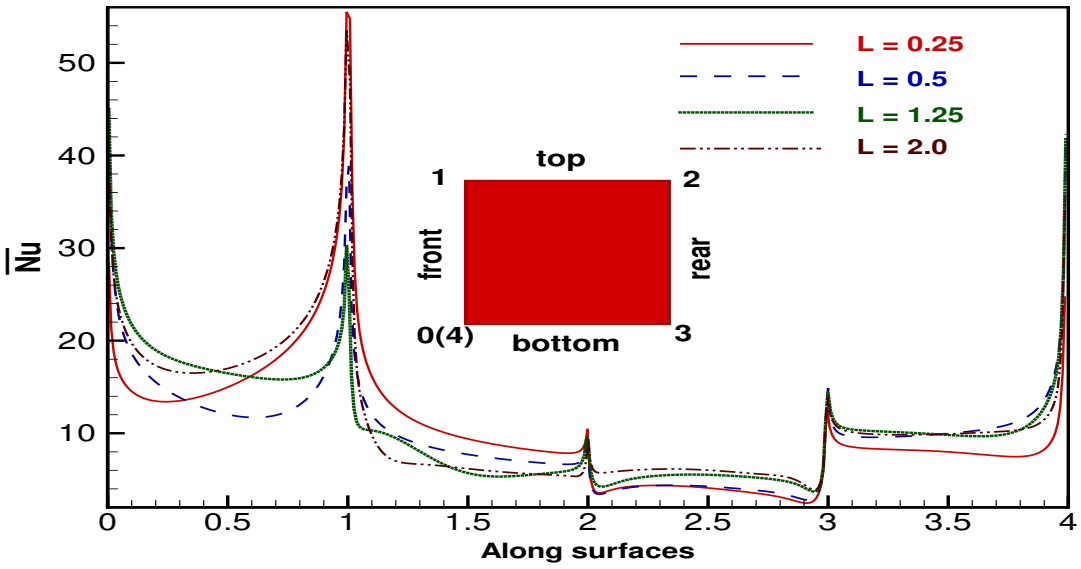

Figure 6.8: Nusselt number distribution along the surfaces of downstream cylinder (DSC) at different L with P = 5, ϕ = 5% for $r_2 = 1$ and r_1 = 0.5.

Fig. 6.8 shows $\overline{Nu}$ distributions on the downstream cylinder surface at different L. A few interesting observations can be made here. It is observed that the $\overline{Nu}$ reaches maximum along four corners of the cylinder because of steepest thermal gradient. The front face of the cylinder shows highest $\overline{Nu}$ among all faces at all L. It reaches maximum

at point-1 since the incoming cold flow directly impacts it. The presence of UREP at different L shows the variation in $\overline{Nu}$ along all surfaces. That is, the physics of the heat transfer around the DSC differs due to the presence of UREP at different heights. As we move downstream, along the top face of the cylinder the $\overline{Nu}$ decreases, due to the low fluid velocity for all L. On the rear face, $\overline{Nu}$ variation for the steady case ($L = 0.25$) is almost negligible since the originating vortex is rotating on this face without being shed. On the other hand, for the case of L = 0.5, 1.25 and 2.0, an exchange of hot fluid adjacent to this face with ambient cold fluid is expected to occur due to shedding of vortices from the DSC. At the bottom face, the difference in the $\overline{Nu}$ variation is found due to oscillation and non oscillation for unsteady and steady case respectively. This information may be very helpful in enhancing the heat transfer using the flow control techniques.

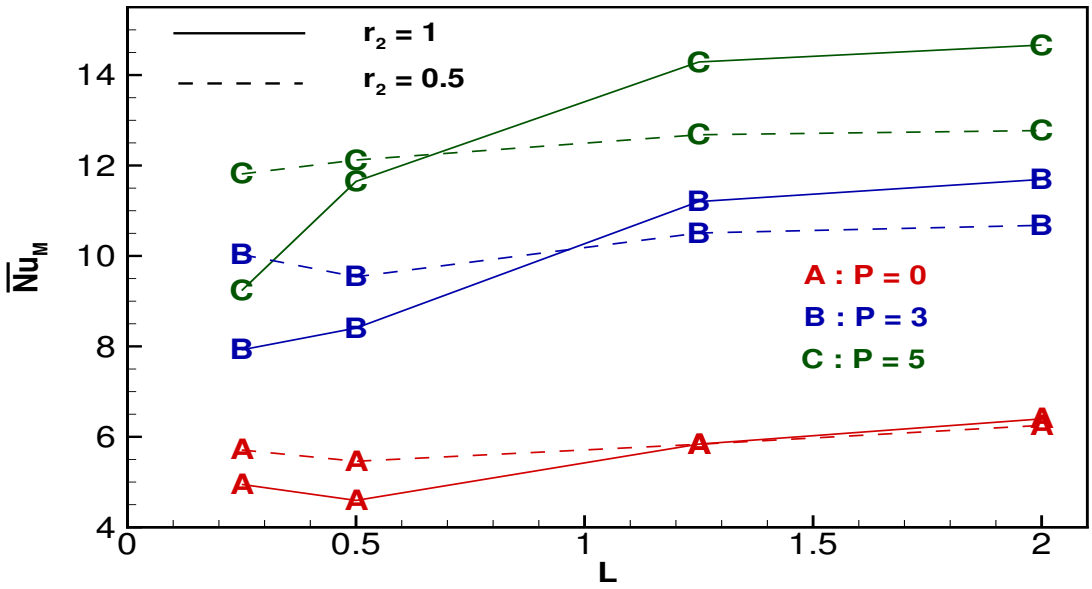

Figure 6.9: Time averaged mean Nusselt number ($\overline{Nu}_M$) as a function of L for different P and r_2 with r_1 = 0.5 and ϕ = 5%.

Fig. 6.9 shows the time averaged mean Nusselt number as a function of L at different P and r_2 with r_1 = 0.5 and ϕ = 5%. As can be seen, $\overline{Nu}_M$ is an increasing function of P and L but not uniform with r_2 variation. Here the effect of P is remarkable than that of L and r_2. At lower L, $\overline{Nu}_M$ is found more for r_2 = 0.5 than that of r_2 = 1, while a

reverse situation is observed at higher L. It is not surprising since the incoming cold fluid towards the heated DSC is obstructed by the UREP at lower gap-height. On the other hand, when the UREP is moved far from the wall, the front face of the DSC is exposed to the incoming cold fluid. At the same time, the UREP produces flow instability in front of the DSC. Now, in comparison to the inline case (L = 0.5), heat transfer from the downstream cylinder is found more here in off-setting case for these parameters values.

6.5.4 Hydrodynamic Characteristics

Variation of hydrodynamic coefficients as a function of L for different P and r_2 with r_1 = 0.5 is illuminated in Figs. 6.10(a) (for drag coefficient $\overline{C}_D$) and 6.10(b) (for lift coefficient $\overline{C}_L$). As seen, the drag coefficient increases with L as well as P. Dependency of $\overline{C}_D$ on L is dependent on P, that is, $\overline{C}_D$ variation is nominal with L at lower P, while substantial at higher P. At lower L, apparently drag coefficient of the DSC is found less for longer UREP, while an opposite situation is observed at higher L. However the lift coefficient is not uniform with L, while it is an increasing function of P. Moderately, lift coefficient is more for smaller UREP.

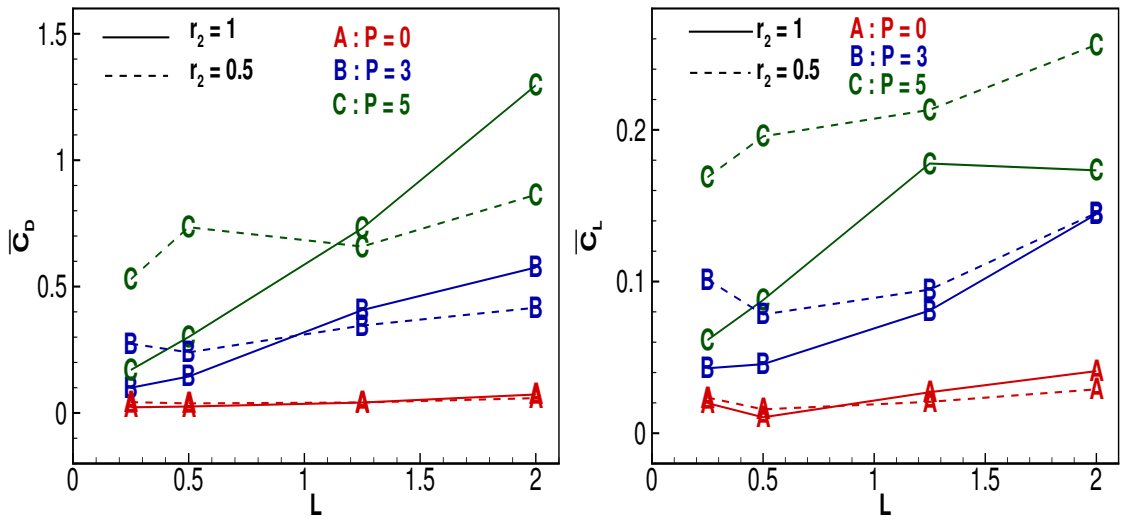

Figure 6.10: Variation of (a) time-averaged drag coefficient ($\overline{C}_D$) and, (b) time-averaged lift coefficient ($\overline{C}_L$) as a function of L for different P and r_2 with r_1 = 0.5 and ϕ = 5%.

The ratio of $\overline{Nu}_M/\overline{C}_D$ as a function of L at different P and r_2 with r_1 = 0.5 is exem-

Table 6.1: Propose dependency of $\overline{Nu}_M$ on L in the functional form $\overline{Nu}_M = \overline{Nu}_M(L)$ with r_1 = 0.5 and ϕ = 5%.

	$\overline{Nu}_M = \overline{Nu}_M(L)$	
P	r_2 = 1	r_2 = 0.5
0	$\overline{Nu}_M = -2.11L^3 + 7.302L^2 - 5.963L + 6.018$ (0, 1)	$\overline{Nu}_M = -0.835L^3 + 3.168L^2 - 3.01L + 6.277$ (0, 1)
3	$\overline{Nu}_M = -2.201L^3 + 6.204L^2 - 1.762L + 8.011$ (0, 1)	$\overline{Nu}_M = -2.263L^3 + 7.776L^2 - 6.803L + 11.280$ (0, 1)
5	$\overline{Nu}_M = 2.352L^3 - 10.835L^2 + 16.749L + 5.688$ (0, 1)	$\overline{Nu}_M = 0.4317L^3 - 0.5743L^2 + 1.644L + 11.438$ (0, 1)

plified in Fig. 6.11. Here $\overline{Nu}_M/\overline{C}_D$ is uniformly decreasing with the increase of L. It is interesting to note that maximum $\overline{Nu}_M/\overline{C}_D$ is found for linear shear flow case at each L. It is also to be noted that $\overline{Nu}_M/\overline{C}_D$ is found more for $r_2 = 1$ than that for $r_2 = 0.5$ at each L.

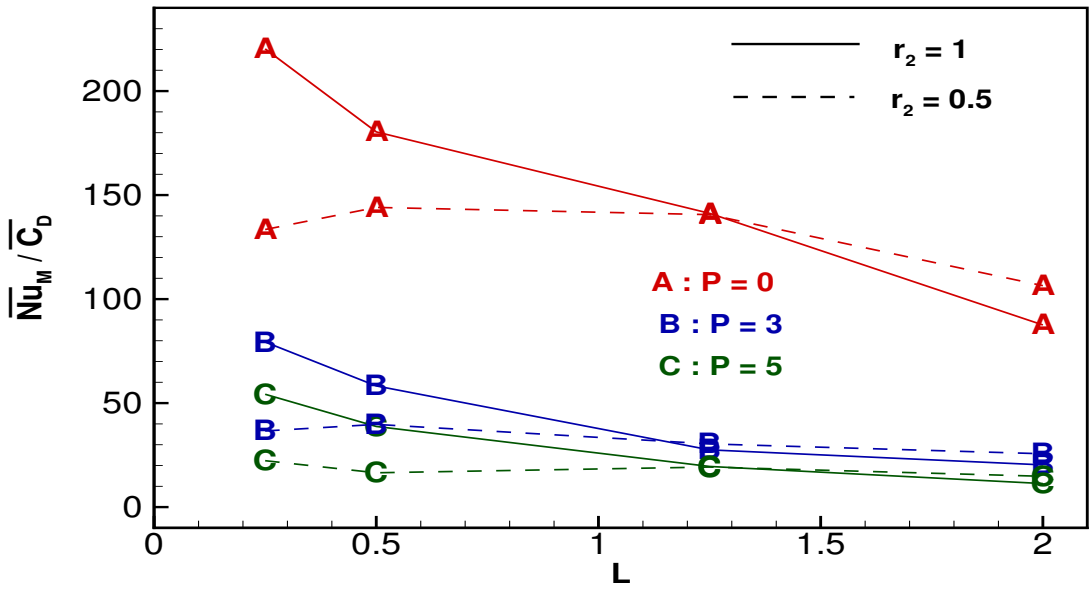

Figure 6.11: Ratio of time-averaged mean nusselt number to the drag coefficient ($\overline{Nu}_M/\overline{C}_D$) as a function of of L for different P and r_2 with r_1 = 0.5 and ϕ = 5%.

The dependency of time-averaged mean nusselt number ($\overline{Nu}_M$) of the downstream cylinder on gap height L at different P with r_1 = 0.5 and ϕ = 5% in the functional form is discussed based on proposed relations written in Table - 6.1. These relations are fitted

using the least-square curve fitting method based on the computed values. Numerical values written in bracket against each relation is the residual sum of squares (RSS) and coefficient of determination (R^2). These relations are polynomials of degree 3 with RSS value is 0 and R^2 is 1 which means that these relations are 100% predictable. One can predict $\overline{Nu}_M$ at different values of L using these propose relations.

6.6 Conclusion

This study presents the numerical investigation of flow around a square cylinder in the presence of an upstream rectangular cylinder of different heights in an offset tandem arrangement under the incience of Couette-Poiseuille flow based non-uniform/non-linear velocity profile. The effect of gap height L of the upstream cylinder from the wall, angle of attack (P), height ratio of the two cyliders (r_2) on the hydrodynamic and heat transfer characteristics of the square cylinder are investigated. The following observations are reported from this study:

1. The flow is found to be unsteady at large L and P. The unsteadiness in the incoming flow to the square cylinder can be generated at lower values of P in the offset arrangement (offsetting from the wall), in comparison to the inline tandem arrangement, since the upstream cylinder is exposed to a higher velocity zone in the offsetting case. At lower L = 0.25, $r_1 = 0.5$ and r_2 = 1.0, the upper negative shear layer of the downstream cylinder cancels part of lower positive shear layer of the upstream cylinder, as a results interaction between the layers of the upstream cylinder is lost.

2. The effect of non-linearity on the heat transfer from the DSC in presence of the UREP is found remarkable at higher gap height L.

3. Heat transfer characteristics ($\overline{Nu}_M$) and hydrodynamic characteristics ($\overline{C}_D$ and $\overline{C}_L$) are found to be more for the case of offsetting the UREP from the wall, in comparison to offsetting towards the wall and inline tandem arrangement. These

characteristics are found to be proportional to P.

4. Maximum heat transfer is found for the longer UREP placed at higher gap height L with higher pressure gradient (P). However, $\frac{\overline{Nu}_M}{\overline{C}_D}$ is reported at the lowest P (P = 0) and lowest L (L = 0.25).

Chapter 7

Conclusion and Future Work

7.1 Conclusion

This thesis focus on the enhancement of heat transfer by dissipating excess heat from the heated objects. This thesis studied the effect of nanofluids over base fluid and the effect of height, width and position of the upstream cylinder on the flow around heated square cylinder in the vicinity of a plane wall. The equations governing the nanofluid flow are solved numerically using finite volume method with staggered grid arrangement using QUICK scheme. The resulting equations are then solved iteratively using pressure correction-based SIMPLE algorithm. In this chapter , a concluding summary of the chapter is presented. Finally a discussion on the future scope of the present study is made. In this thesis, we have considered different geometrical arrangements based on single cylinder, and tandem arrangement. Tandem arrangement further divided into inline tandem arrangement and offset tandem arrangement. The major observations of the present study can be reported categorically

1. Single Cylinder:

   (a) The expression for thermal conductivity (which considers brownian motion and it is accurate) has an important role in enhancing the heat transfer, and

therefore it is considered in this study.

(b) It is interesting to note that addition of nanoparticles does not necessarily increase the heat transfer from all faces. At lower $Pe = 25$, the maximum heat transfer is reported from the bottom face (among all faces) at the lowest $L = 0.1$. Nusselt number ($\overline{Nu}_M$) increases with the increase of Pe. Except for $d_{np} = 30nm$ (and $\phi = 6\%$), $\overline{Nu}_M$ increases (and decreases) with an increase of ϕ (and d_{np}) at all Pe. Surprisingly only for the case of $d_{np} = 30nm$, $\overline{Nu}_M$ is found to decrease with an increase in ϕ from 4 to 6% due to a sudden jump in Pr from Pr = 6.086 to 18.85 with ϕ changing from $4to6\%$. Overall, though there is a large increase in viscosity than that in thermal conductivity at ϕ = 6% and $d_{np} = 30nm$, all nanofluids considered here can be used as coolants compared to the base fluid. The increment in $\overline{Nu}_M$ (from the value of its base fluid case) is about 6.57% to 29.02% depending on the values of d_{np}, ϕ and Pe at $L = 0.5$.

(c) Observations based on the graphical representation of dependencies of $\overline{Nu}_M$ on Pe (at $L = 0.5$) and L (at $Pe = 25$ and 400) are reconfirmed by presenting their explicit functional form $\overline{Nu}_M = \overline{Nu}_M(Pe)$ and $\overline{Nu}_M = \overline{Nu}_M(L)$.

(d) C_D and C_L both decrease with the increase of Pe. It is reported that the ratio $\overline{Nu}_M/C_D$ increases with Pe, while decreases with L increases, and is more at each L for the nanofluid case in comparison to clear fluid case at both Pe.

(e) Though $\overline{Nu}_M$ is reported high at lower fluid temperature, nanomaterials are more effective in the base fluid at higher temperature.

(f) Under Couette flow, $EG : W - Al_2O_3$ nanofluid with largest d_{np} is found the worthy fluid, which works efficiently at lower temperature at which the heat transfer is enhanced upto 12.64% and drag coefficient is reduced upto 2.05%. It is shown that $\overline{Nu}_M$ can be predicted using the proposed correlation between

j-factor and Re at a Re ($5 \leq Re \leq 125$) and any Pr ($2.86 \leq Pr \leq 40.23$).

(g) The flow around the cylinder is reported unsteady for $P > 2$ in all four nanofluids at $Re_{U_2} = 500$. The crowding of isotherms near the rear face in the recirculation region increases with P.

(h) $\overline{Nu}_M$ has strong dependency on P (increases with P) and base fluid ($EG : W$ produces more), moderate dependency on ϕ (increases with ϕ) and type of thermal boundary conditions (q_W produces more), and weak dependency on nanomaterials (more for CuO). These observations are reconfirmed based on functional form of $\overline{Nu}_M = \overline{Nu}_M(P)$, $\overline{Nu}_M = \overline{Nu}_M(\phi)$ and hence $\overline{Nu}_M = \overline{Nu}_M(P, \phi)$ proposed by the least-square curve fitting method.

(i) Though $\overline{Nu}_M$ is reported more for q_W (than T_W) condition , $EG : W$ (than water) base fluid and CuO (than Al_2O_3) material, an opposite tendency in the enhancement rate of $\overline{Nu}_M$ with the thermal condition, base fluids and materials is observed. The maximum enhancement of $\overline{Nu}_M$ is reported in $water - Al_2O_3$ nanofluid at $P = 5$ for T_W condition where $\overline{Nu}_M$ registers a value double the value at $P = 0$.

2. Inline Tandem Arrangement :

Here the horizontal centerline of both the cylinders, bisecting the height of cylinders lies at the same height from the plane wall. For different height ratios r_2 ,the effect of thinning of the rectangular upstream cylinder on the hydrodynamic and heat transfer characteristics are analyzed for different values of P and S. The numerically simulated results exhibit the following conclusions:

(a) The shear layers issuing from the UREP reattach with the shear layers of the DSC and form a steady closed circulation region between the cylinders at lower P. At higher P, the above recirculation region is opened and unsteadiness in the flow of DSC is generated at a lower Re at which isolated square

cylinder reported steady.

(b) The exchange of ambient cold fluid with hotter fluid near to the front face of the heated cylinder and crowding of isotherms near the rear face of the downstream cylinder increase with pressure gradient P.

(c) The heat transfer ($\overline{Nu}_M$) and drag coefficient (C_D) of the downstream cylinder are decreased, in comparison to the value of its isolated case due to tandem arrangement, however, they increase with P and ϕ. Their ratio increases nominally with ϕ, but decreases with the increase of P and a drastic jumb in the ratio is observed while changing the form of incident velocity from linear P = 0 to its first non-linear (P = 1). It is worthy to note that the ratio is reported more for tandem than that of isolated arrangement.

(d) It is observed that the UREP of rectangular shape ($r_1 < 1$), introducing at the upstream side of the DSC, can generate unsteadiness in the flow depending on the angle and speed of approaching flow, and the position with respect to the obstacle and wall, to dominate the state of the wake.

(e) The functional forms of $\overline{Nu}_M = \overline{Nu}_M(P)$ and $\overline{Nu}_M = \overline{Nu}_M(\phi)$ are proposed by the least square curve fitting method.

3. Offset Tandem Arrangement:

The value of L is varied by offsetting the upstream cylinder towards/away from the wall. The specific conclusions based on this arrangement are as follows:

(a) The effect of non-linearity on the heat transfer from the DSC in presence of the UREP is found remarkable at higher gap height L.

(b) Heat transfer characteristics ($\overline{Nu}_M$) and hydrodynamic characteristics ($\overline{C}_D$ and $\overline{C}_L$) are found to be more for the case of offsetting the UREP from the wall, in comparison to offsetting towards the wall and inline tandem arrange-

ment. These characteristics are found to be proportional to P.

(c) Maximum heat transfer is found for the longer UREP placed at higher gap height L with higher pressure gradient (P). However, $\frac{\overline{Nu}_M}{\overline{C}_D}$ is reported at the lowest P (P = 0) and lowest L (L = 0.25).

7.2 Future scope

In this section, some recommendations for further research on the work performed on this thesis are listed. Although useful information has been obtained from the simulation. However, some problems still remain unsolved, such as

1. All the computations in the present study are restricted to two dimensions. In many cases, the flow exhibit three-dimensional flow. Therefore, an extension of the present study in three dimensional numerical investigation for cylinders in diferent arrangements is also a topic of further research.

2. In the present study, Couette-Poiseuille flow based velocity profile at the inlet has been considered. As concerns the numerical study, further insight into the physics of two-dimensional wakes in ground effect might be obtained by testing for a group of cylinders in different Reynolds number regimes, or a cylinder with different cross-sectional shapes under different inlet velocity profiles.

Bibliography

[1] D. Chatterjee and B. Mondal, "Forced convection heat transfer from tandem square cylinders for various spacing ratios," *Numerical Heat Transfer, Part A: Applications*, vol. 61, no. 5, pp. 381–400, 2012.

[2] A. Sohankar and A. Etminan, "Forced-convection heat transfer from tandem square cylinders in cross flow at low reynolds numbers," *International Journal for Numerical Methods in Fluids*, vol. 60, no. 7, pp. 733–751, 2009.

[3] A. Sharma and V. Eswaran, "Heat and fluid flow across a square cylinder in the two-dimensional laminar flow regime," *Numerical Heat Transfer, Part A: Applications*, vol. 45, no. 3, pp. 247–269, 2004.

[4] V. Etminan-Farooji, E. Ebrahimnia-Bajestan, H. Niazmand, and S. Wongwises, "Unconfined laminar nanofluid flow and heat transfer around a square cylinder," *International Journal of Heat and Mass Transfer*, vol. 55, no. 5-6, pp. 1475–1485, 2012.

[5] V. D. Narasimhamurthy, "Wake dynamics of flow past tapered bluff bodies," 2008.

[6] B. C. Pak and Y. I. Cho, "Hydrodynamic and heat transfer study of dispersed fluids with submicron metallic oxide particles," *Experimental Heat Transfer an International Journal*, vol. 11, no. 2, pp. 151–170, 1998.

[7] Y. Xuan and W. Roetzel, "Conceptions for heat transfer correlation of nanofluids," *International Journal of heat and Mass transfer*, vol. 43, no. 19, pp. 3701–3707, 2000.

[8] J. C. Maxwell, *A treatise on electricity and magnetism*, vol. 1. Clarendon press, 1881.

[9] J. Koo and C. Kleinstreuer, "A new thermal conductivity model for nanofluids," *Journal of Nanoparticle Research*, vol. 6, no. 6, pp. 577–588, 2004.

[10] R. S. Vajjha and D. K. Das, "Experimental determination of thermal conductivity of three nanofluids and development of new correlations," *International Journal of Heat and Mass Transfer*, vol. 52, no. 21-22, pp. 4675–4682, 2009.

[11] J. Kim, Y. T. Kang, and C. K. Choi, "Analysis of convective instability and heat transfer characteristics of nanofluids," *Physics of fluids*, vol. 16, no. 7, pp. 2395–2401, 2004.

[12] E. Ebrahimnia-Bajestan, H. Niazmand, W. Duangthongsuk, and S. Wongwises, "Numerical investigation of effective parameters in convective heat transfer of nanofluids flowing under a laminar flow regime," *International Journal of Heat and Mass Transfer*, vol. 54, no. 19-20, pp. 4376–4388, 2011.

[13] S. Özerinç, S. Kakaç, and A. G. Yazıcıoğlu, "Enhanced thermal conductivity of nanofluids: a state-of-the-art review," *microfluidics and nanofluidics*, vol. 8, no. 2, pp. 145–170, 2010.

[14] A. Einstein, "Eine neue bestimmung der moleküldimensionen," *Annalen der Physik*, vol. 324, no. 2, pp. 289–306, 1906.

[15] H. Brinkman, "The viscosity of concentrated suspensions and solutions," *The Journal of Chemical Physics*, vol. 20, no. 4, pp. 571–571, 1952.

[16] G. Batchelor, "The effect of brownian motion on the bulk stress in a suspension of spherical particles," *Journal of fluid mechanics*, vol. 83, no. 1, pp. 97–117, 1977.

[17] N. Masoumi, N. Sohrabi, and A. Behzadmehr, "A new model for calculating the effective viscosity of nanofluids," *Journal of Physics D: Applied Physics*, vol. 42, no. 5, p. 055501, 2009.

[18] J. Buongiorno, "Convective transport in nanofluids," *Journal of heat transfer*, vol. 128, no. 3, pp. 240–250, 2006.

[19] F. H. Harlow and J. E. Welch, "Numerical calculation of time-dependent viscous incompressible flow of fluid with free surface," *The physics of fluids*, vol. 8, no. 12, pp. 2182–2189, 1965.

[20] R. Courant, K. Friedrichs, and H. Lewy, "On the partial difference equations op mathematical physics," *Mathematische Annalen*, vol. 100, no. 1, pp. 32–74, 1928.

[21] C. Hirt, B. Nichols, and N. Romero, "Sola: A numerical solution algorithm for transient fluid flows," tech. rep., Los Alamos Scientific Lab., N. Mex.(USA), 1975.

[22] B. P. Leonard, "A stable and accurate convective modelling procedure based on quadratic upstream interpolation," *Computer methods in applied mechanics and engineering*, vol. 19, no. 1, pp. 59–98, 1979.

[23] T. Han, J. Humphrey, and B. Launder, "A comparison of hybrid and quadratic-upstream differencing in high reynolds number elliptic flows," *Computer Methods in Applied Mechanics and Engineering*, vol. 29, no. 1, pp. 81–95, 1981.

[24] A. Pollard and A. L.-W. Siu, "The calculation of some laminar flows using various discretisation schemes," *Computer Methods in Applied Mechanics and Engineering*, vol. 35, no. 3, pp. 293–313, 1982.

[25] G. Raithby, P. Galpin, and J. Van Doormaal, "Prediction of heat and fluid flow in complex geometries using general orthogonal coordinates," *Numerical Heat Transfer, Part A: Applications*, vol. 9, no. 2, pp. 125–142, 1986.

[26] W. Shyy, S. Tong, and S. Correa, "Numerical recirculating flow calculation using a body-fitted coordinate system," *Numerical Heat Transfer*, vol. 8, no. 1, pp. 99–113, 1985.

[27] T. Hayase, J. Humphrey, and R. Greif, "A consistently formulated quick scheme for fast and stable convergence using finite-volume iterative calculation procedures," *Journal of Computational Physics*, vol. 98, no. 1, pp. 108–118, 1992.

[28] S. V. Patankar and D. B. Spalding, "A calculation procedure for heat, mass and momentum transfer in three-dimensional parabolic flows," in *Numerical Prediction of Flow, Heat Transfer, Turbulence and Combustion*, pp. 54–73, Elsevier, 1983.

[29] S. Z. H. H. C. Timin, "Solving viscous flow in nozzle using improved simple algorithm [j]," *Journal Of Propulsion Technology*, vol. 3, 1998.

[30] H. K. Versteeg and W. Malalasekera, *An introduction to computational fluid dynamics: the finite volume method*. Pearson education, 2007.

[31] I. Barton and R. Kirby, "Finite difference scheme for the solution of fluid flow problems on non-staggered grids," *International journal for numerical methods in fluids*, vol. 33, no. 7, pp. 939–959, 2000.

[32] S. Patankar, *Numerical heat transfer and fluid flow*. CRC press, 1980.

[33] M. Kobayashi and J. Pereira, "Numerical comparison of momentum interpolation methods and pressure—velocity algorithms using non-staggered grids," *Communications in Applied Numerical Methods*, vol. 7, no. 3, pp. 173–186, 1991.

[34] J. H. Ferziger and M. Peric, *Computational methods for fluid dynamics*. Springer Science & Business Media, 2012.

[35] S. Shuja, B. Yilbas, and M. Budair, "Vortex shedding over a rectangular cylinder with ground effect: flow and heat transfer characteristics," *International Journal of Numerical Methods for Heat & Fluid Flow*, vol. 12, no. 8, pp. 916–939, 2002.

[36] R.-J. Yang and L.-M. Fu, "Thermal and flow analysis of a heated electronic component," *International Journal of Heat and Mass Transfer*, vol. 44, no. 12, pp. 2261–2275, 2001.

[37] Q. Wang and Y. Jaluria, "Unsteady mixed convection in a horizontal channel with protruding heated blocks and a rectangular vortex promoter," *Physics of Fluids*, vol. 14, no. 7, pp. 2113–2127, 2002.

[38] S. Bhattacharyya, D. Maiti, and S. Dhinakaran, "Influence of buoyancy on vortex shedding and heat transfer from a square cylinder in proximity to a wall," *Numerical Heat Transfer, Part A: Applications*, vol. 50, no. 6, pp. 585–606, 2006.

[39] A. Lankadasu and S. Vengadesan, "Interference effect of two equal-sized square cylinders in tandem arrangement: With planar shear flow," *International journal for numerical methods in fluids*, vol. 57, no. 8, pp. 1005–1021, 2008.

[40] S. Bhattacharyya and S. Dhinakaran, "Vortex shedding in shear flow past tandem square cylinders in the vicinity of a plane wall," *Journal of Fluids and Structures*, vol. 24, no. 3, pp. 400–417, 2008.

[41] S. U. Choi and J. A. Eastman, "Enhancing thermal conductivity of fluids with nanoparticles," tech. rep., Argonne National Lab., IL (United States), 1995.

[42] S. Lee, S. Choi, S. Li, and J. Eastman, "Measuring thermal conductivity of fluids containing oxide nanoparticles," *Journal of Heat transfer*, vol. 121, no. 2, pp. 280–289, 1999.

[43] J. A. Eastman, S. Phillpot, S. Choi, and P. Keblinski, "Thermal transport in nanofluids," *Annu. Rev. Mater. Res.*, vol. 34, pp. 219–246, 2004.

[44] K. S. Hwang, J.-H. Lee, and S. P. Jang, "Buoyancy-driven heat transfer of water-based al2o3 nanofluids in a rectangular cavity," *International Journal of Heat and Mass Transfer*, vol. 50, no. 19-20, pp. 4003–4010, 2007.

[45] S. Z. Heris, S. G. Etemad, and M. N. Esfahany, "Experimental investigation of oxide nanofluids laminar flow convective heat transfer," *International Communications in Heat and Mass Transfer*, vol. 33, no. 4, pp. 529–535, 2006.

[46] C.-C. Cho, C.-L. Chen, *et al.*, "Mixed convection heat transfer performance of water-based nanofluids in lid-driven cavity with wavy surfaces," *International Journal of Thermal Sciences*, vol. 68, pp. 181–190, 2013.

[47] H. Heidary and M. Kermani, "Heat transfer enhancement in a channel with block (s) effect and utilizing nano-fluid," *International Journal of Thermal Sciences*, vol. 57, pp. 163–171, 2012.

[48] M. Vakili, A. Mohebbi, and H. Hashemipour, "Experimental study on convective heat transfer of tio 2 nanofluids," *Heat and Mass Transfer*, vol. 49, no. 8, pp. 1159–1165, 2013.

[49] C. T. Nguyen, G. Roy, C. Gauthier, and N. Galanis, "Heat transfer enhancement using al2o3–water nanofluid for an electronic liquid cooling system," *Applied Thermal Engineering*, vol. 27, no. 8-9, pp. 1501–1506, 2007.

[50] W. Azmi, K. A. Hamid, N. Usri, R. Mamat, and K. Sharma, "Heat transfer augmentation of ethylene glycol: water nanofluids and applications—a review," *International Communications in Heat and Mass Transfer*, vol. 75, pp. 13–23, 2016.

[51] S. Kakaç and A. Pramuanjaroenkij, "Review of convective heat transfer enhancement with nanofluids," *International Journal of Heat and Mass Transfer*, vol. 52, no. 13-14, pp. 3187–3196, 2009.

[52] S. Murshed, K. Leong, and C. Yang, "Investigations of thermal conductivity and viscosity of nanofluids," *International Journal of Thermal Sciences*, vol. 47, no. 5, pp. 560–568, 2008.

[53] S. Dhinakaran, "Heat transport from a bluff body near a moving wall at re= 100," *International Journal of Heat and Mass Transfer*, vol. 54, no. 25-26, pp. 5444–5458, 2011.

[54] M. S. Valipour, R. Masoodi, S. Rashidi, M. Bovand, and M. Mirhosseini, "A numerical study on convection around a square cylinder using al2o3-h2o nanofluid," *Thermal science*, vol. 18, no. 4, pp. 1305–1314, 2014.

[55] M. Bovand, S. Rashidi, and J. A. Esfahani, "Enhancement of heat transfer by nanofluids and orientations of the equilateral triangular obstacle," *Energy conversion and management*, vol. 97, pp. 212–223, 2015.

[56] M. Sheikholeslami, M. Gorji-Bandpy, and K. Vajravelu, "Lattice boltzmann simulation of magnetohydrodynamic natural convection heat transfer of al2o3–water nanofluid in a horizontal cylindrical enclosure with an inner triangular cylinder," *International Journal of Heat and Mass Transfer*, vol. 80, pp. 16–25, 2015.

[57] M. R. Salimpour and A. Dehshiri-Parizi, "Convective heat transfer of nanofluid flow through conduits with different cross-sectional shapes," *Journal of Mechanical Science and Technology*, vol. 29, no. 2, pp. 707–713, 2015.

[58] M. Azimi and R. Riazi, "Mhd copper-water nanofluid flow and heat transfer through convergent-divergent channel," *Journal of Mechanical Science and Technology*, vol. 30, no. 10, pp. 4679–4686, 2016.

[59] S. Sarkar, S. Ganguly, and A. Dalal, "Analysis of entropy generation during mixed convective heat transfer of nanofluids past a square cylinder in vertically upward flow," *Journal of Heat Transfer*, vol. 134, no. 12, p. 122501, 2012.

[60] Z. Alloui, J. Guiet, P. Vasseur, and M. Reggio, "Natural convection of nanofluids in a shallow rectangular enclosure heated from the side," *The Canadian Journal of Chemical Engineering*, vol. 90, no. 1, pp. 69–78, 2012.

[61] A. Noghrehabadi, A. Samimi Behbahan, and I. Pop, "Thermophoresis and brownian effects on natural convection of nanofluids in a square enclosure with two pairs of heat source/sink," *International Journal of Numerical Methods for Heat & Fluid Flow*, vol. 25, no. 5, pp. 1030–1046, 2015.

[62] S. Malik and A. Nayak, "Buoyancy driven heat transfer in nanofluids due to wall mounted heat source," *Alexandria Engineering Journal*, vol. 55, no. 2, pp. 797–810, 2016.

[63] D. K. Maiti, "Dependence of flow characteristics of rectangular cylinders near a wall on the incident velocity," *Acta mechanica*, vol. 222, no. 3-4, pp. 273–286, 2011.

[64] M. Akbari, N. Galanis, and A. Behzadmehr, "Comparative analysis of single and two-phase models for cfd studies of nanofluid heat transfer," *International Journal of Thermal Sciences*, vol. 50, no. 8, pp. 1343–1354, 2011.

[65] M. Corcione, M. Cianfrini, E. Habib, and A. Quintino, "Optimization of free convection heat transfer from vertical plates using nanofluids," *Journal of Heat Transfer*, vol. 134, no. 4, p. 042501, 2012.

[66] S. M. Vanaki, P. Ganesan, and H. Mohammed, "Numerical study of convective heat transfer of nanofluids: a review," *Renewable and Sustainable Energy Reviews*, vol. 54, pp. 1212–1239, 2016.

[67] B. Leonard, "Order of accuracy of quick and related convection-diffusion schemes," *Applied Mathematical Modelling*, vol. 19, no. 11, pp. 640–653, 1995.

[68] D. K. Maiti, "Numerical study on aerodynamic characteristics of rectangular cylinders near a wall," *Ocean Engineering*, vol. 54, pp. 251–260, 2012.

[69] S. Bhattacharyya and D. Maiti, "Vortex shedding from a square cylinder in presence of a moving wall," *International journal for numerical methods in fluids*, vol. 48, no. 9, pp. 985–1000, 2005.

[70] S. Bhattacharyya and D. Maiti, "Shear flow past a square cylinder near a wall," *International Journal of Engineering Science*, vol. 42, no. 19-20, pp. 2119–2134, 2004.

[71] T. N. Cong, G. Roy, C. Gauthier, and N. Galanis, "Heat transfer enhancement using al 2 o 3-water nanofluid for an electronic liquid cooling system," *Applied Thermal Engineering*, vol. 27, no. 8-9, pp. 1501–1506, 2007.

[72] M. S. Valipour and A. Z. Ghadi, "Numerical investigation of fluid flow and heat transfer around a solid circular cylinder utilizing nanofluid," *International communications in heat and mass transfer*, vol. 38, no. 9, pp. 1296–1304, 2011.

[73] M. Modak, S. S. Chougule, and S. K. Sahu, "An experimental investigation on heat transfer characteristics of hot surface by using cuo–water nanofluids in circular jet impingement cooling," *Journal of Heat Transfer*, vol. 140, no. 1, p. 012401, 2018.

[74] D.-H. Yoon, K.-S. Yang, and C.-B. Choi, "Heat transfer enhancement in channel flow using an inclined square cylinder," *Journal of Heat Transfer*, vol. 131, no. 7, p. 074503, 2009.

[75] R. D. Selvakumar and S. Dhinakaran, "Forced convective heat transfer of nanofluids around a circular bluff body with the effects of slip velocity using a multiphase mixture model," *International Journal of Heat and Mass Transfer*, vol. 106, pp. 816–828, 2017.

[76] S. K. Das, N. Putra, P. Thiesen, and W. Roetzel, "Temperature dependence of thermal conductivity enhancement for nanofluids," *Journal of heat transfer*, vol. 125, no. 4, pp. 567–574, 2003.

[77] L. S. Sundar and K. Sharma, "Thermal conductivity enhancement of nanoparticles in distilled water," *International Journal of Nanoparticles*, vol. 1, no. 1, pp. 66–77, 2008.

[78] M. P. Beck, Y. Yuan, P. Warrier, and A. S. Teja, "The thermal conductivity of alumina nanofluids in water, ethylene glycol, and ethylene glycol+ water mixtures," *Journal of Nanoparticle research*, vol. 12, no. 4, pp. 1469–1477, 2010.

[79] M. Naraki, S. Peyghambarzadeh, S. Hashemabadi, and Y. Vermahmoudi, "Parametric study of overall heat transfer coefficient of cuo/water nanofluids in a car radiator," *International Journal of Thermal Sciences*, vol. 66, pp. 82–90, 2013.

[80] R. S. Vajjha and D. K. Das, "A review and analysis on influence of temperature and concentration of nanofluids on thermophysical properties, heat transfer and pumping power," *International Journal of Heat and Mass Transfer*, vol. 55, no. 15-16, pp. 4063–4078, 2012.

[81] R. P. Bharti, R. Chhabra, and V. Eswaran, "Steady forced convection heat transfer from a heated circular cylinder to power-law fluids," *International Journal of Heat and Mass Transfer*, vol. 50, no. 5-6, pp. 977–990, 2007.

[82] W. Escher, T. Brunschwiler, N. Shalkevich, A. Shalkevich, T. Burgi, B. Michel, and D. Poulikakos, "On the cooling of electronics with nanofluids," *Journal of heat transfer*, vol. 133, no. 5, p. 051401, 2011.

[83] H. Ahmed, H. Mohammed, and M. Yusoff, "An overview on heat transfer augmentation using vortex generators and nanofluids: approaches and applications," *Renewable and Sustainable Energy Reviews*, vol. 16, no. 8, pp. 5951–5993, 2012.

[84] Z. Haddad, E. Abu-Nada, H. F. Oztop, and A. Mataoui, "Natural convection in nanofluids: are the thermophoresis and brownian motion effects significant in nanofluid heat transfer enhancement," *International Journal of Thermal Sciences*, vol. 57, pp. 152–162, 2012.

[85] S. Rashidi, M. Bovand, J. A. Esfahani, and G. Ahmadi, "Discrete particle model for convective al2o3–water nanofluid around a triangular obstacle," *Applied Thermal Engineering*, vol. 100, pp. 39–54, 2016.

[86] J. Umavathi, O. Ojjela, and K. Vajravelu, "Numerical analysis of natural convective flow and heat transfer of nanofluids in a vertical rectangular duct using darcy-forchheimer-brinkman model," *International Journal of Thermal Sciences*, vol. 11, pp. 511–524, 2017.

[87] D. K. Maiti and R. Bhatt, "Interactions of vortices of a square cylinder and a rectangular vortex generator under couette–poiseuille flow," *Journal of Fluids Engineering*, vol. 137, no. 5, p. 051203, 2015.

[88] A. Sharma and V. Eswaran, "Effect of channel-confinement and aiding/opposing buoyancy on the two-dimensional laminar flow and heat transfer across a square cylinder," *International journal of heat and mass transfer*, vol. 48, no. 25-26, pp. 5310–5322, 2005.

[89] H.-W. Wu and R.-H. Wang, "Mixed convective heat transfer past a heated square porous cylinder in a horizontal channel with varying channel height," *Journal of Heat Transfer*, vol. 133, no. 2, p. 022503, 2011.

[90] A. Handbook, "Fundamentals. 2009, atlanta, ga: American society of heating, refrigerating and air-conditioning engineers," 2005.

[91] S.-J. Lee, S.-I. Lee, and C.-W. Park, "Reducing the drag on a circular cylinder by upstream installation of a small control rod," *Fluid dynamics research*, vol. 34, no. 4, p. 233, 2004.

[92] M. M. Alam, M. Moriya, K. Takai, and H. Sakamoto, "Suppression of fluid forces acting on two square prisms in a tandem arrangement by passive control of flow," *Journal of Fluids and Structures*, vol. 16, no. 8, pp. 1073–1092, 2002.

[93] S. Kim, M. M. Alam, M. Russel, *et al.*, "Aerodynamics of a cylinder in the wake of a v-shaped object," *Wind and Structures*, vol. 23, no. 2, pp. 143–155, 2016.

[94] D. K. Maiti, R. Bhatt, and M. M. Alam, "Aerodynamic forces on square cylinder due to secondary flow by rectangular vortex generator in offset tandem: Comparison with inline," *Computers & Fluids*, vol. 134, pp. 157–176, 2016.

[95] F. Zafar and M. M. Alam, "A low reynolds number flow and heat transfer topology of a cylinder in a wake," *Physics of Fluids*, vol. 30, no. 8, p. 083603, 2018.

[96] M. M. Alam, H. Sakamoto, and M. Moriya, "Reduction of fluid forces acting on a single circular cylinder and two circular cylinders by using tripping rods," *Journal of fluids and structures*, vol. 18, no. 3-4, pp. 347–366, 2003.

[97] M. M. Alam, H. Sakamoto, and Y. Zhou, "Effect of a t-shaped plate on reduction in fluid forces on two tandem cylinders in a cross-flow," *Journal of Wind Engineering and Industrial Aerodynamics*, vol. 94, no. 7, pp. 525–551, 2006.

[98] M. M. Alam, Y. Zhou, J. Zhao, O. Flamand, and O. Boujard, "Classification of the tripped cylinder wake and bi-stable phenomenon," *International Journal of Heat and Fluid Flow*, vol. 31, no. 4, pp. 545–560, 2010.

[99] M. M. Alam, M. Elhimer, L. Wang, D. L. Jacono, and C. Wong, "Vortex shedding from tandem cylinders," *Experiments in Fluids*, vol. 59, no. 3, p. 60, 2018.

[100] S. Kim, M. M. Alam, and D. K. Maiti, "Wake and suppression of flow-induced vibration of a circular cylinder," *Ocean Engineering*, vol. 151, pp. 298–307, 2018.

[101] R. Devarakonda, *Interactive computational-experimental methodologies in cooling of electronic components*. 1992.

[102] K. Tatsutani, R. Devarakonda, and J. Humphrey, "Unsteady flow and heat transfer for cylinder pairs in a channel," *International Journal of Heat and Mass Transfer*, vol. 36, no. 13, pp. 3311–3328, 1993.

[103] A. Etminan, M. Moosavi, and N. Ghaedsharafi, "Determination of flow configurations and fluid forces acting on two tandem square cylinders in cross-flow and its wake patterns," *Int. Journal of Mechanics*, vol. 5, pp. 63–74, 2011.

[104] S. Sarkar, S. Ganguly, G. Biswas, and P. Saha, "Effect of cylinder rotation during mixed convective flow of nanofluids past a circular cylinder," *Computers & Fluids*, vol. 127, pp. 47–64, 2016.

[105] S. Sarkar, S. Ganguly, A. Dalal, P. Saha, and S. Chakraborty, "Mixed convective flow stability of nanofluids past a square cylinder by dynamic mode decomposition," *International Journal of Heat and Fluid Flow*, vol. 44, pp. 624–634, 2013.

[106] S. Sarkar, S. Ganguly, and G. Biswas, "Mixed convective heat transfer of nanofluids past a circular cylinder in cross flow in unsteady regime," *International Journal of Heat and Mass Transfer*, vol. 55, no. 17-18, pp. 4783–4799, 2012.

[107] S. Sarkar, S. Ganguly, and A. Dalal, "Buoyancy driven flow and heat transfer of nanofluids past a square cylinder in vertically upward flow," *International Journal of Heat and Mass Transfer*, vol. 59, pp. 433–450, 2013.

[108] F. Talebi, A. H. Mahmoudi, and M. Shahi, "Numerical study of mixed convection flows in a square lid-driven cavity utilizing nanofluid," *International Communications in Heat and Mass Transfer*, vol. 37, no. 1, pp. 79–90, 2010.

[109] B. Sharman, F.-S. Lien, L. Davidson, and C. Norberg, "Numerical predictions of low reynolds number flows over two tandem circular cylinders," *International Journal for Numerical Methods in Fluids*, vol. 47, no. 5, pp. 423–447, 2005.

[110] M. M. Alam, M. Moriya, K. Takai, and H. Sakamoto, "Fluctuating fluid forces acting on two circular cylinders in a tandem arrangement at a subcritical reynolds number," *Journal of Wind Engineering and Industrial Aerodynamics*, vol. 91, no. 1-2, pp. 139–154, 2003.

[111] S. Singha and K. Sinhamahapatra, "High-resolution numerical simulation of low reynolds number incompressible flow about two cylinders in tandem," *Journal of Fluids Engineering*, vol. 132, no. 1, p. 011101, 2010.

[112] J. Zhu, H. Chen, and X. Chen, "Large eddy simulation of vortex shedding and pressure fluctuation in aerostatic bearings," *Journal of Fluids and Structures*, vol. 40, pp. 42–51, 2013.

[113] A. Baxendale, I. Grant, and F. Barnes, "Vortex shedding from two cylinders of different diameters," *Journal of Wind Engineering and Industrial Aerodynamics*, vol. 23, pp. 427–435, 1986.

[114] A. Sayers and A. Saban, "Flow over two cylinders of different diameters: the lock-in effect," *Journal of Wind Engineering and Industrial Aerodynamics*, vol. 51, no. 1, pp. 43–54, 1994.

[115] A. Valencia, "Unsteady flow and heat transfer in a channel with a built-in tandem of rectangular cylinders," *Numerical Heat Transfer, Part A Applications*, vol. 29, no. 6, pp. 613–623, 1996.

[116] J. Rosales, A. Ortega, and J. Humphrey, "A numerical investigation of the convective heat transfer in unsteady laminar flow past a single and tandem pair of square cylinders in a channel," *Numerical Heat Transfer: Part A: Applications*, vol. 38, no. 5, pp. 443–465, 2000.

[117] J. Rosales, A. Ortega, and J. Humphrey, "A numerical simulation of the convective heat transfer in confined channel flow past square cylinders: comparison of inline and offset tandem pairs," *International Journal of Heat and Mass Transfer*, vol. 44, no. 3, pp. 587–603, 2001.

[118] H. M. Bahaidarah, M. Ijaz, and N. Anand, "Numerical study of fluid flow and heat transfer over a series of in-line noncircular tubes confined in a parallel-plate

channel," *Numerical Heat Transfer, Part B: Fundamentals*, vol. 50, no. 2, pp. 97–119, 2006.

[119] R. Agarwal and A. Dhiman, "Flow and heat transfer phenomena across two confined tandem heated triangular bluff bodies," *Numerical Heat Transfer, Part A: Applications*, vol. 66, no. 9, pp. 1020–1047, 2014.

[120] M. Farhadi, K. Sedighi, and M. M. Madani, "Convective cooling of tandem heated squares in a channel," *Proceedings of the Institution of Mechanical Engineers, Part C: Journal of Mechanical Engineering Science*, vol. 223, no. 4, pp. 965–978, 2009.

[121] P. R. Kanna, M. Sivasubramanian, P. M. Prabu, and M. Uthayakumar, "Three dimensional numerical investigation of forced convection heat transfer from offset square cylinders placed in a confined channel," *International Journal of Computer Aided Engineering and Technology*, vol. 10, no. 1-2, pp. 141–156, 2018.

[122] D. Wen and Y. Ding, "Experimental investigation into convective heat transfer of nanofluids at the entrance region under laminar flow conditions," *International journal of heat and mass transfer*, vol. 47, no. 24, pp. 5181–5188, 2004.

[123] H.-H. Ting and S.-S. Hou, "Investigation of laminar convective heat transfer for al2o3-water nanofluids flowing through a square cross-section duct with a constant heat flux," *Materials*, vol. 8, no. 8, pp. 5321–5335, 2015.

[124] N. Bouguerra, S. Poncet, and S. Elkoun, "Dispersion regimes in alumina/water-based nanofluids: Simultaneous measurements of thermal conductivity and dynamic viscosity," *International Communications in Heat and Mass Transfer*, vol. 92, pp. 51–55, 2018.

[125] N. A. C. Sidik, M. Khakbaz, L. Jahanshaloo, S. Samion, and A. N. Darus, "Simulation of forced convection in a channel with nanofluid by the lattice boltzmann method," *Nanoscale research letters*, vol. 8, no. 1, p. 178, 2013.

[126] M. H. Esfe, A. A. A. Arani, A. H. Niroumand, W.-M. Yan, and A. Karimipour, "Mixed convection heat transfer from surface-mounted block heat sources in a horizontal channel with nanofluids," *International Journal of Heat and Mass Transfer*, vol. 89, pp. 783–791, 2015.

[127] S. Foroutani and A. Rahbari, "Numerical investigation of laminar forced convection heat transfer in rectangular channels with different block geometries using nanofluids," *Thermal Science*, vol. 21, no. 5, pp. 2129–2138, 2017.

List of Publications

The following papers have been published from this thesis:

1. Swati Sharma, Dilip K. Maiti, Md. Mahbub Alam and Bhupendra K. Sharma, "Nanofluid ($H_2O - Al_2O_3/CuO$) flow over a heated square cylinder near a wall under the incident of Couette flow", **Journal of Mechanical Science and Technology**, 32 (2), (2018), 659–670.

2. Dilip K. Maiti and Swati Sharma, "Roles of nanofluids, temperature of base fluids and pressure gradient on heat transfer enhancement from a cylinder: uniformly heated/heat flux" , **Journal of Heat Transfer (ASME)**, 141, (2019), 062402.

3. Swati Sharma, Dilip K. Maiti, Md. Mahbub Alam and Bhupendra K. Sharma, "Nanofluid flow and heat transfer from heated square cylinder in the presence of upstream rectangular cylinder under Couette-Poiseuille flow", **Wind and Structures**, 29 (1), (2019), 65–74.

Paper Presented in Conferences

1. Presented a paper "Heat Transfer Study of Nanofluid Flow around Heated Square Cylinder in Wall Proximity" at the **National Conference on "Computational Mathematics and Operational Research"** organised by B.K.Birla Institute of Technology and Science, Pilani, during October, 15-16, 2016.

2. Presented a paper "Numerical Investigation of Base Fluid and Temperature Effect on Heat Transfer Around Square Cylinder in Wall Proximity" in **International conference in Applicable Mathematics-2018** held in University of Delhi during Feb, 19-20, 2018.

3. Presented a paper "Heat Transfer Enhancement Around a Square Cylinder Under the Incident of CouettePoiseuille Flow" in **6th European Conference on Computational Mechanics (Solids, Structures and Coupled Problems) (ECCM 6)**

and the 7th European Conference on Computational Fluid Dynamics (ECFD 7) held in Glasgow, United Kingdom, 11 – 15 June 2018.

4. Presented a paper "Heat Transfer Enhancement from a Heated Square Cylinder due to Nanofluid and Presence of an Inline Upstream Rectangular Cylinder" in **International Conference on Applied and Computational Mathematics 2018** during November 23-25, 2018 at IIT Kharagpur.

Workshops Attended

1. Short term training program on "**Computational Fluid Dynamics (CFD-2015)**", Department of Applied Mechanics, MNIT Allahabad, June 22 - 26, 2015.

2. Short term program on "**Mathematical Modeling and Computational Techniques in Nanofluids**", Department of Mathematics, NIT Kurukshetra, September 21 - 25, 2015.

3. National Conference on Mathematics "**GOOGOL 2017**", Birla Ballika Vidyapeeth, Pilani, April 15 - 16, 2017.

4. National Workshop on "**Improving Synergy between Teaching and Research in Indian Academia**", Teaching Learning Centre, BITS PILANI, Pilani Campus, March 26 - 27, 2018.

Brief Biography of the Supervisor

Prof. Bhupendra Kumar Sharma is an Associate Professor and Head, Department of Mathematics, Birla Institute of Technology and Science, Pilani, (BITS Pilani) Pilani Campus, Rajasthan, India. He obtained his M.Sc. (1999), M. Phill (2000) and Ph. D. (2006) from Department of Mathematics, University of Rajasthan, Jaipur. He was awarded NET-JRF (Junior Research Fellowship, CSIR) in 2001 and Senior Research Fellowship in 2003. His research interest includes Heat and Mass Transfer, Arterial Blood Flow, Magnetic Targeting Drug Delivery, Porous Medium, Boundary Layer Theory, Micro-polar Fluid, Differential Equations etc. He has published more than 60 publications in the international/national journals of repute, and authored two books on Engineering Mathematics. He is associate editor, member of editorial board, advisory board of a number of journal of reputes. Prof Sharma is a member of various academic and management committees of many institutes/universities such as advisory committee, selection committee etc. He has also participated in many conferences and workshops.

Brief Biography of the Co-supervisor

Prof. Dilip Kumar Maiti is a professor and Head of the Department in Department of Applied Mathematics and Oceanography, Vidyasagar University, Midnapore, WB. He received his Ph.D. degree in the year 2005 from IIT Kharagpur. He was top 20% awardees of CSIR-NET (2001) for the Shyama Prasad Mukherjee (SPM) Fellowship Test-2002. His research interests are in the areas of Heat Transfer from Cylinder/s in Isolated/Tandem Arrangement, Heat and Mass Transfer in Cavity and Micro Channel flow, Nanofluid flow past bluff bodies. He successfully completed 2 major projects financially supported by DST, India. He has visited various foreign institutes to present his research work (UK, Switzerland, Canada and China). He was selected by Indian National Science Academy (INSA) and approved by Chinese academy of science (CAS) to work in China under International collaboration/Exchange Programme of INSA, New Delhi in 2012.

Brief Biography of the Candidate

SWATI SHARMA, is working as a research scholar in the Department of Mathematics, BITS PILANI, Pilani Campus since January, 2015. She did her Bachelor's in Mathematics from MIRANDA HOUSE, University of Delhi and Master's in Mathematics from HINDU COLLEGE, University of Delhi. Then She did Bachelor's in Education from Maharishi Dayanand University. She has qualified GATE in 2013. She was awarded Direct SRF, CSIR in 2019. Her research interests are in the areas of Heat Transfer from Cylinder/s in Isolated/Tandem Arrangement, Nanofluid flow past bluff bodies and Numerical methods Till date, she has published 3 papers in peer-reviewed international journals and presented 4 papers in international/national conferences.